Wagging the Pacific Dog by its Indian Tail? A west Indian Ocean Precursor to El Niño

Claudia Elisabeth Wieners

Wagging the Pacific Dog by its Indian Tail? A west Indian Ocean Precursor to El Niño

Kwispelt de Indische staart met de Pacifische hond? Een Voorbode voor El Niño in de westelijke Indische Oceaan

(met een samenvatting in het Nederlands)

Proefschrift

ter verkrijging van de graad van doctor aan de Universiteit Utrecht op gezag van de rector magnificus, prof.dr. G.J. van der Zwaan, ingevolge het besluit van het college voor promoties in het openbaar te verdedigen op

woensdag 21 maart 2018 des ochtends te 10.30 uur

door

Claudia Elisabeth Wieners

geboren op 26 april 1989

te Frankfurt am Main, Duitsland

Promotoren: Prof. dr. W.P.M. de Ruijter
               Prof. dr. ir. H.A. Dijkstra

Don't blame me! Blame El Niño!

Contents

List of Figures

List of Tables

List of frequently used acronyms

CESM Community Earth System Model

CP Central Pacific (El Niño type)

EEOF Extended Empirical Orthogonal Function (in MSSA)

EIO East Indian Ocean

ENSO El Niño/Southern Oscillation

EP East Pacific (El Niño type)

EPe East Pacific, eastward propagating (El Niño type)

EPw East Pacific, westward propagating (El Niño type)

GCM Global Circulation Model

HR High Resolution (CESM simulation)

IOB Indian Ocean Basinwide warming

IOD Indian Ocean Dipole

LR Low Resolution (CESM simulation)

MC Maritime Continent

MJO Madden-Julian Oscillation

MSSA Multi-channel Singular Spectrum Analysis

OLR Outgoing Longwave Radiation

OBS observational data

SSH Sea Surface Height

SST Sea Surface Temperature

WIO West Indian Ocean

WWV Warm Water Volume

ZC Zebiak-Cane (model)

English Summary

Climate scientists still struggle to predict major El Niño/Southern Oscillation (ENSO) events at more than about 9 months lead time. However, previous studies (e.g. Izumo et al., 2010) suggest that the Indian Ocean, in particular the Indian Ocean Dipole mode (IOD; positive IOD events involve west Indian Ocean warming and cooling off Sumatra) may add skill to ENSO predictions at up to 14 years lead time. In this thesis, the possible causal relationship between Indian Ocean Sea Surface Temperature (SST) anomalies and ENSO is analysed, using observational data, experiments with an intermediate complexity model, and the output of a global circulation model.

An analysis of the observational record yields a negative correlation between the west Indian Ocean SST in boreal summer-autumn and ENSO 1.5 years later. A specially designed statistical test, the 'common cause test', shows that this correlation is significantly stronger than one would expect, based on the influence of ENSO on the Indian Ocean (west Indian Ocean cooling tens to occur abut 1/2 year after La Niña) and the cyclicity of ENSO (La Niña tends to be followed by El Niño after 2 years). This suggests that a cool west Indian Ocean in boreal summer may pre-condition the Pacific to generate an El Niño event in next year's winter. No significant correlation is found between the east Indian Ocean and ENSO.

A further analysis of observational data suggest two possible mechanisms for this interaction.

State-dependent noise mechanism A cool west Indian Ocean favours intraseasonal wind variability over the west Pacific in boreal winter-spring, which in turn may excite El Niño development by initialising a downwelling Kelvin wave.

Atmospheric bridge mechanism A cool west Indian Ocean is accompanied by easterly winds over the west Pacific which lead to an accumulation of warm water in the west Pacific warm pool. A high ocean heat content, in turn, is a prerequisite for El Niño.

Both mechanisms may co-occur. They favour El Niño events with large SST anomalies near the South American coast (East Pacific or EP El Niños) because EP events require a strong west Pacific warm pool.

The observational evidence for the atmospheric bridge mechanism is found not entirely satisfying, because after subtracting the effect of lingering ENSO-related SST anomalies, the Pacific easterly wind signal associated with a cool west Indian Ocean only reaches 80% confidence - possibly because the wind data is too noisy. However, the correlation between west Indian Ocean SST and the warm water volume reaches 95% confidence.

An easterly wind response to the east of a cool anomaly is an unexpected result, as negative SST anomalies are expected to cool the overlying air and thus induce pressure increase and surface divergence (Gill response). Therefore a cool west Indian Ocean should

be accompanied by westerlies over the Pacific. However, we hypothesise that the initial uplift generated by the Gill response over the warm pool region around Indonesia can be nonlinearly amplified due to convection and latent heat release in this very warm and moist area. If the convection becomes strong enough, it may induce surface convergence and thus easterlies over the Pacific.

We test this hypothesis using the Zebiak-Cane (ZC) model. Originally, this is an intermediate-complexity model including only the tropical Pacific. We extend the model with a very simplified Indian Ocean and an idealised convection feedback above Indonesia. For a sufficiently large convective feedback strength, a cool west Indian Ocean is indeed found to induce easterlies over the Pacific. However, a warm east Indian Ocean (which tends to co-occur with west Indian Ocean cooling) can induce much stronger easterlies, suggesting that the east Indian Ocean may have more impact on ENSO than the west, which contradicts the results from the common cause test.

To resolve the discrepancy regarding the relative importance of the west and east Indian Ocean, output from a global circulation model (the Community Earth System Model/CESM) was analysed. In the low resolution simulation (LR; 1° for both ocean and atmosphere), ENSO is too periodic, so that the Indian Ocean cannot add much predictive skill and thus the common cause test yields negative results. In the high resolution simulation (HR, 0.1° for the ocean and 0.5° for the atmosphere) the east Indian Ocean seems to have a stronger impact on Pacific winds. However, CESM (both HR and LR) is strongly biased in the sense that in boreal autumn east Indian Ocean variability is too strong by a factor of around 3, which might obscure signals from the west Indian Ocean. The reason for the bias seems to be an overly strong sensitivity of the SST to thermocline variability, which in turn may be linked to biases in the mean temperature profile. Thus the CESM results can neither support nor falsify our hypothesis over the convective feedback over Indonesia.

The Indian Ocean may also influence ENSO by long term temperature trends, rather than interannual variability. In recent decades, the Indian Ocean has probably warmed relative to the Pacific. The possible effects of this warming are investigated with a convection-free version of the ZC model. It is found that Indian Ocean warming induces an easterly wind contribution over the Pacific, which in turn leads to a steeper thermocline slope, a stronger mean zonal SST gradient, and stronger mean upwelling. These changes are favourable for ENSO variability. Stronger mean upwelling enhances the impact of thermocline anomalies on the SST, a shallower thermocline increases the SST impact of upwelling anomalies, and a stronger SST gradient leads to stronger advection. In addition, we find that these changes in the Pacific background state also lead to a shift of ENSO-related SST anomalies towards the Central Pacific (CP El Niños). This effect particularly interesting, because it offers a possible explanation for the increased frequency of CP El Niños in recent decades in terms of the observed Indian Ocean warming.

To summarise, although the Indian Ocean certainly does not 'dictate' ENSO, it may have some impact, and taking into account Indian Ocean variability and long-term trends may improve ENSO predictions. However, the underlying mechanisms are not yet completely understood.

Samenvatting in het Nederlands

Klimaatwetenschappers worstelen nog steeds om sterke El Niño's en La Niña's met meer dan ca. 9 maanden van tevoren te voorspellen. Echter, eerdere studies (bijv. Izumo et al., 2010) suggereren dat voorspellingen van het El Niño/Southern Oscillation (ENSO) fenomeen tot 14 maanden van tevoren verbeterd kunnen worden door informatie over de Indian Ocean Dipole (IOD; de IOD is positief als de westelijke Indische Oceaan warm en het gebied ten westen van Sumatra koud is) mee te nemen. In dit proefschrift worden de mogelijke causale samenhangen tussen de zeeoppervlaktemperatuur (sea surface temperature/SST) in de Indische Oceaan en ENSO geanalyseerd, waarvoor observaties, doelgerichte experimenten met het Zebiak-Cane-model, en de resultaten van een globaal klimaatmodel, namelijk het Community Earth System Model (CESM), worden gebruikt.

Observaties vertonen een negatieve correlatie tussen de SST in de westelijke Indische Oceaan in de boreale zomer tot herfst en ENSO anderhalf jaar later. Dit zou in principe door de periodiciteit van ENSO (La Niña wordt na twee jaar met een verhoogde kans door El Niño gevolgd) en de invloed van ENSO op de Indische Oceaan (de westelijke Indische Oceaan koelt enkele maanden na een La Niña vaak af) verklaard kunnen worden. Echter, een specifiek ontwikkelde statistische test, de 'gemeenschappelijke oorzakentest', laat zien dat de gemeten correlatie significant sterker is dan men puur op basis van de periodiciteit van ENSO en diens invloed op de westelijke Indische Oceaan zou verwachten. Dit duidt erop dat een koude anomalie in de westelijke Indische Oceaan tijdens de zomer bevorderlijk is voor het optreden van El Niño in de winter anderhalf jaar later. Voor de oostelijke Indische Oceaan bestaat geen dergelijke significante correlatie.

Uit verdere analyses van observaties komen twee mogelijke interactiemechanismes naar voren:

Toestandsafhankelijke ruis Een koude westelijke Indische Oceaan in de zomer en najaar is gunstig voor een verhoogde windvariabiliteit op tijdschalen van enkele weken (ruis) over de westelijke Stille Oceaan in de daarop volgende winter en lente. Deze windvariabiliteit kan een warme Kelvingolf genereren, die de ontwikkeling van El Niño initieert.

Atmosferische brug Een koude westelijke Indische Oceaan wordt vergezeld van oostenwinden boven de westelijke Stille Oceaan. Door deze oostenwinden wordt voor de Indonesische kust warm water opgehoopt, dat als reservoir voor een opwarming van de oostelijke Stille Oceaan tijdens de volgende El Niño dient.

Beide mechanismes kunnen gezamenlijk optreden. Zij zijn bevorderen vooral El Niño's met een sterke temperatuuranomalie nabij de Zuid-Amerikaanse kust (zogeheten East Pacific of EP El Niño's), omdat juist voor de ontwikkeling van EP El Niño's een groot warmwatervolume nodig is.

Helaas is het oostenwindsignaal over de Stille Oceaan tijdens de koude anomalie in de westelijke Indische Oceaan relatief onduidelijk. Nadat de invloed van lokale SST-anomaliën in de oostelijke Stille Oceaan (restanten van een La Niña) eruit is gefilterd, heeft het resterende signaal nog maar een significantie van 80%. Dit komt mogelijk doordat er relatief veel ruis op de winddata zit. De correlatie tussen de SST anomalie in de westelijke Indische Oceaan en het warmwatervolume in de Stille Oceaan (een geïntegreerd maat voor de zonale wind en dus minder ruisgevoelig) haalt een significantie van 95%.

Oostenwinden ten oosten van een koude anomalie zijn bovendien een onverwacht resultaat. Koude SST-anomaliën zorgen voor een afkoeling van de erboven liggende lucht, en dus voor een stijgende luchtdruk en divergente winden aan het oppervlak (Gill-respons). Men zou dus verwachten dat een koude westelijke Indische Oceaan juist westenwinden boven de Stille Oceaan veroorzaakt. Echter, het gebied rond Indonesië heeft een heel warme en vochtige achtergrondtoestand. Onze hypothese is dat het opstijgen van lucht, dat door het Gill-respons boven Indonesië wordt geïnitieerd, door convectie en het vrijkomen van latente warmte niet-lineair versterkt kan worden. Als deze positieve terugkoppeling sterk genoeg is, worden bij Indonesië convergente winden geïnduceerd, waardoor de wind boven de Stille Oceaan oostelijk wordt. Deze hypothese wordt verder onderzocht met behulp van het Zebiak-Cane (ZC) model. Aan dit model, dat oorspronkelijk alleen de tropische Stille Oceaan bevat, worden hier een simpele Indische Oceaan en een geïdealiseerde convectieve terugkoppeling boven Indonesië toegevoegd. Als deze terugkoppeling voldoende sterk is, kunnen koude anomaliën in de westelijke Indische Oceaan inderdaad oostenwinden boven de Stille Ocean veroorzaken. Echter, een opwarming voor de westkust van Sumatra (die dankzij de IOD vaak samen met een afkoeling in de westelijke Indische Oceaan optreedt) kan binnen het model nog veel sterkere oostenwinden veroorzaken. Dit zou kunnen betekenen dat de oostelijke Indische Oceaan meer invloed op ENSO heeft dan de westelijke - in tegenstelling tot de eerdere resultaten uit de 'gemeenschappelijke oorzakentest'.

Om de relatieve invloed van de oostelijke Indische Oceaan en westelijke Indische Oceaan verder te onderzoeken, worden de resultaten van twee CESM-simulaties geanalyseerd, één met een lage resolutie (LR; 1° voor oceaan en atmosfeer) en één met een hoge resolutie (HR, 0.1° in de oceaan en 0.5° in de atmosfeer). In LR is ENSO te periodiek, zodat de Indische Oceaan weinig informatie over ENSO kan toevoegen, waardoor de 'gemeenschappelijke oorzakentest' negatieve resultaten geeft. In HR lijkt de oostelijke Indische Ocean, vergeleken met de westelijke Indische Oceaan, een sterkere invloed op de winden boven de Stille Oceaan te hebben. Echter, in beide CESM-simulaties is de amplitude van de SST-variabiliteit in de oostelijke Indische Oceaan ongeveer een factor 3 te groot ten opzichte van observaties en zou dus signalen vanuit de westelijke Indische Oceaan kunnen maskeren. De reden voor de overdreven SST-variabiliteit bij Sumatra is een overgrote gevoeligheid van de SST voor schommelingen in de thermoclinediepte, die waarschijnlijk door afwijkingen in het gemiddelde temperatuurprofiel wordt veroorzaakt. De CESM-resultaten kunnen dus onze hypothese omtrent de convectieve terugkoppeling noch bevestigen noch ontkrachten.

Ook temperatuurveranderingen op lange termijn in de Indische Oceaan kunnen ENSO beïnvloeden. In de afgelopen decennia is de Indische Oceaan waarschijnlijksterker opgewarmd dan de Stille Oceaan. De mogelijke effecten van deze relatieve opwarming worden onderzocht met behulp van een convectievrije versie van he ZC-model. Een warmere Indische Oceaan leidt tot sterkere gemiddelde oostenwinden boven de Stille Oceaan, wat een sterkere thermoclinehelling, een sterkere zonale SST-gradiënt en een grotere opwaartse

snelheid langs de evenaar tot gevolg heeft. Deze veranderingen versterken de ENSO-gerelateerde variabiliteit. Een sterkere gemiddelde opwaartse snelheid maakt de SST gevoeliger voor thermoclineschommelingen, een ondiepere thermocline zorgt voor een grotere gevoeligheid voor schommelingen in de verticale snelheid, en een grotere temperatuurgradiënt bevordert anomale temperatuuradvectie. Daarnaast verandert ook het spatiale patroon van ENSO: De temperatuuranomaliën verschuiven westwaarts en lijken meer op Central Pacific (CP) El Niño's. In de afgelopen decennia komen steeds vaker CP El Niños voor. Volgens onze modelresultaten zou dit met de opwarming in de Indische Oceaan samen kunnen hangen.

Al is de Indische Oceaan zeker niet in staat om ENSO 'aan te sturen', lijkt het toch mogelijk dat hij een zekere invloed uitoefent. Daarom zouden ENSO-voorspellingen ervan kunnen profiteren als met de Indische Oceaan rekening wordt gehouden. Echter, verder onderzoek zal nodig zijn om de onderliggende processen volledig te begrijpen.

Feynman's Recipe (Prologue)

Richard P. Feynman describes a simple recipe by which we can find new laws of nature.

'In general, we look for a new law by the following process: First we guess it; then we compute the consequences of the guess to see what would be implied if this law that we guessed is right; then we compare the result of the computation to nature, with experiment or experience, compare it directly with observation, to see if it works. If it disagrees with experiment, it is wrong. [...] That's all there is to it.'

In climate science, we have to content ourselves with a poor men's version of this grand recipe. Suppose we want to understand how the Indian Ocean might influence the mighty El Niño. We, too, can let observations inspire us to guess a new 'law', or rather a mechanism. We can put our guess into a conceptual or intermediate-complexity model to convince ourselves that the guess may work in principle, and compute the consequences. But then the trouble starts. By lack of sufficiently long observational records and Pacific-Ocean-sized laboratories, we have to compare the results of our computation to the surrogate nature of General Circulation Models - and can only hope that the GCMs represent reality sufficiently well to allow a fruitful comparison.

Chapter 1

Introduction

Major El Niño/Southern Oscillation (ENSO)[1] events have a strong influence around the globe and can cause substantial damage such as flooding in Peru and draught in Indonesia; early predictions of strong El Niños and La Niñas can be of great value to reduce damage (Zebiak et al., 2015). Therefore understanding the processes leading to major ENSO events and improving the skill of predictions, especially at long lead times, is vital.

This study treats the question whether Sea Surface Temperature (SST) variations in the Indian Ocean affect the ENSO phenomenon in the Pacific Ocean via atmospheric processes ('the atmospheric bridge' and state-dependent noise). A particular focus lies on the role of southwest Indian Ocean SST anomalies and their possible impact via a convective feedback above the Maritime Continent, at lags of up to 1.5 years.

In this introduction, first a brief overview on ENSO is given (section 1.1), followed by a description of the seasonal cycle and main modes of variability in the Indian Ocean (section 1.2). Section 1.3 provides an overview of previous studies on the possible influence of the Indian Ocean on ENSO. Finally, in section 1.4, an outline of this thesis is presented.

1.1 El Niño - Southern Oscillation

The background state of the equatorial Pacific arises from the interplay of the externally induced Hadley circulation, which can be thought of as generating weak zonally independent easterly winds, and a climatological version of the Bjerknes feedback (Dijkstra and Neelin, 1995): The easterlies generate shallow westward currents which lead to an accumulation of warm surface water, and thus a deep thermocline and high SSTs in the west and a shallow thermocline, stronger upwelling and low SSTs in the east. This zonal temperature gradient in turn strengthens the easterly winds.

Against this background state, one of the strongest modes of interannual variability (Philander, 1990) takes place: The El Niño/Southern Oscillation (ENSO) phenomenon. A measure for its strength is the Nino3.4 index (defined in Fig. 1.1). It captures, for example, the big El Niño events of 1982/83 and 1997/98 (see Fig. 1.2a), but also shows that ENSO behaves rather irregularly, making it potentially hard to predict. Note that throughout this thesis, a year in which an ENSO event develops is labeled as 'year 1' (i.e. the ENSO event peaks in the boreal winter of year 1/2). Season names always refer to boreal seasons, unless specified otherwise. The basic processes involved in ENSO are well understood and involve a fast positive feedback and a delayed negative feedback on east

---

[1]A list of frequently used acronyms is provided on page xii.
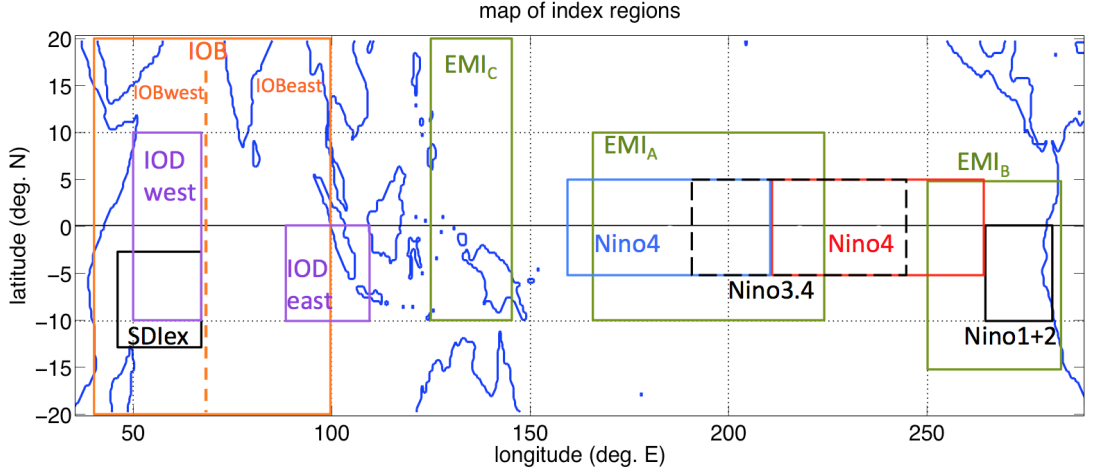
Index	Region / Definition	Index	Region / Definition
IODwest	$10°N - 10°S; \ 50^\circ - 70°E$	Nino4	$5°N - 5°S; \ 160°E - 150°W$
IODeast	$0°S - 10°S; \ 90^\circ - 110°E$	Nino3.4	$5°N - 5°S; \ 170°W - 120°W$
IOD (1)	IOD=IODwest-IODeast	Nino3	$5°N - 5°S; \ 150°W - 90°W$
IOBwest	$20°N - 20°S; \ 40^\circ - 70°E$	Nino1+2	$0°N - 10°S; \ 90°W - 80°W$
IOBeast	$20°N - 20°S; \ 70° - 100°E$	EMI_A	$10°N - 10°S; \ 165°E - 140°W$
IOB (2)	IOB=(IOBwest+IOBeast)/2	EMI_B	$5°N - 15°S; \ 110°W - 70°W$
SDIex	$3°S - 13°S; \ 45^\circ - 70°E$	EMI_C	$20°N - 10°S; \ 125°E = 145°E$
AOeast (3)	$5°N - 5°S; \ 15°W - 15°E$	EMI (4)	$EMI = EMI_A - (EMI_B + EMI_C)/2$

(1) Indian Ocean Dipole; also known as Dipole Mode Index (DMI) in the literature
(2) Indian Ocean Basinwide warming; also known as BasinWide Index (BWI) in the literature
(3) Atlantic Ocean east (not shown in figure)
(4) "El Niño Modoki Index"

Figure 1.1: *Illustration of the indices used in this thesis. The indices are the monthly mean SST averaged over the corresponding box. Occasionally, other variables such as Sea Surface Height are used. The computation of the IOD and IOB index are explained in the table. The IOB region can be split into an eastern and western half (IOBeast and IOBwest).*
The table gives the exact boundaries boundaries as well as the definition of the composite indices IOD and EMI.
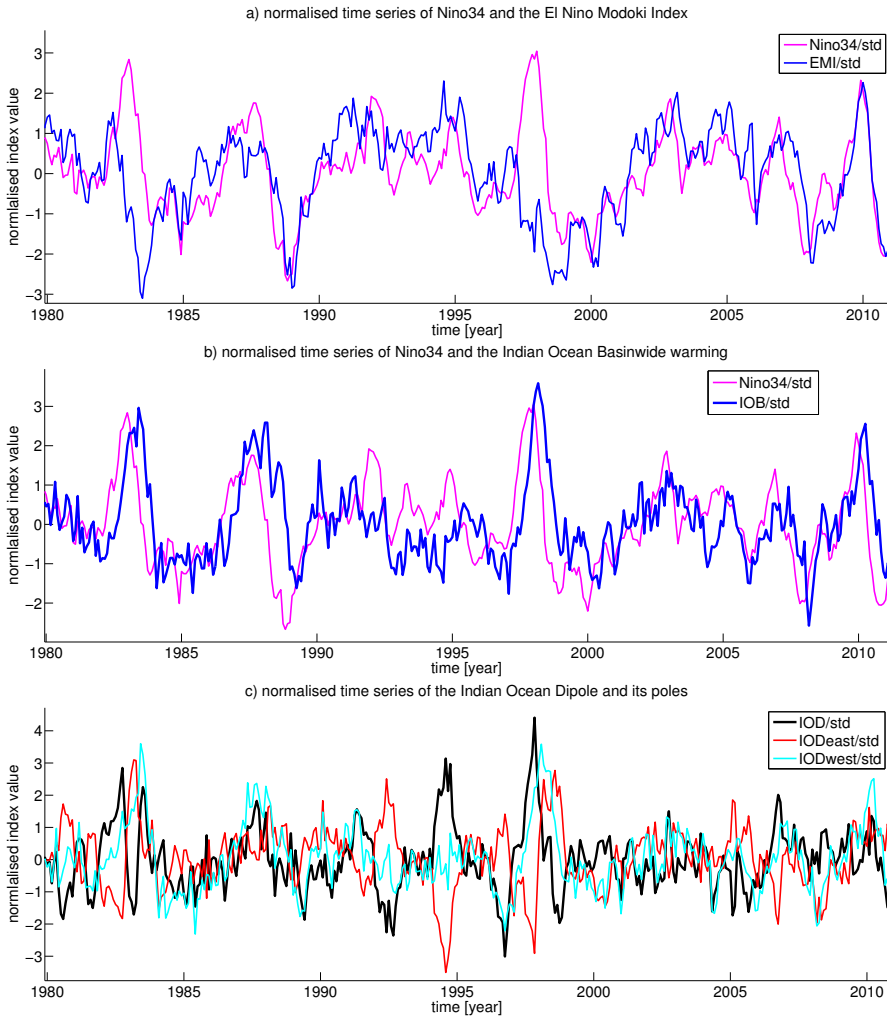
Figure 1.2: *Time series of various indices, normalised by their respective standard deviation. Plot a) shows Nino3.4 (a standard measure for ENSO strength) and EMI. Note that for the El Niños of 1982 and 1997, the EMI is rather low (EP events), while in 2009 it is high (CP event). Plot b) shows Nino3.4 and the IOB; Indian Ocean warming (cooling) follows El Niño (La Niña) after a few months. Plot c) depicts the IOD and its poles. Note that some IOD events occur independently of strong ENSO events (e.g. 1994). The SST data was taken from Met Office Hadley Centre (2017) (see also Rayner et al. (2003)), for the years 1948-2016 and detrended with a running mean technique (see section 2.1.1). The indices are defined in Fig. 1.1.*

Pacific SST anomalies, which together lead to oscillatory behaviour. The fast positive 'Bjerknes' feedbacks include the zonal advection feedback (warm anomalies in the east Pacific cause enhanced westerly wind anomalies which lead to eastward currents advecting water from the west Pacific warm pool), the thermocline feedback (the westerly anomalies lower the thermocline in the east Pacific, so that the water that is upwelled to the surface becomes less cold) and the upwelling feedback (the westerly anomalies lead to reduced upwelling along the equator). On the time scale of several months, the ocean adjustment due to equatorial wave processes provides a delayed negative feedback (Neelin et al., 1998; Jin, 1997a,b): The warm water accumulated in the east Pacific is "discharged" polewards as coastal Kelvin waves, whereas an upwelling Rossby wave initiated by the westerly winds reflects at the Indonesian coast and travels eastward as upwelling Kelvin wave. Meinen and McPhaden (2000) showed that a sufficiently high Pacific warm water volume (WWV; the volume of water warmer than $20°C$ between $5°N - 5°S$ and $120°E - 80°W$) is relevant for the occurrence of El Niño events: A sufficient heat reservoir must be present in the West Pacific in order to warm the East Pacific. The heat is then discharged polewards during El Niño (see also Wyrtki, 1975; Jin, 1997b).

The formulation of the Zebiak-Cane (ZC) model (Zebiak and Cane, 1987) was a breakthrough in understanding ENSO dynamics. In the ZC model, the (steady or seasonal) background climate (e.g., provided by observations) becomes unstable when the strength of the Bjerknes's feedback processes exceeds a critical value. Tyically, the strength of the Bjerknes feedback is represented by he 'coupling strength' μ which determines how strongly the atmosphere responds to a certain SST anomaly. This transition form a stable to an unstable state is referred to as a Hopf bifurcation (steady background state) or a Neimark-Sacker bifurcation (seasonal background state) and occurs at a critical value μ_{crit}. When $\mu > \mu_{crit}$, interannual time scale oscillatory motion develops spontaneously (Bejorano and Jin, 2008; Fedorov and Philander, 2000) and the associated spatial pattern is usually referred to as the ENSO mode. When $\mu < \mu_{crit}$, the ENSO mode is damped.

Even if the ENSO mode is slightly damped, variability may be excited by 'noise', i.e. by processes at time scales considerably smaller than that of ENSO; this noise impact may explain the irregularity of ENSO (Kleeman, 2008). In particular, noise can be provided by intraseasonal spells of westerly winds (Keen, 1982), such as those associated with the Madden–Julian Oscillation (MJO; see also section 1.3) (Madden and Julian, 1971; Zhang, 2005). "Bursts" of westerly winds over the west Pacific generate equatorial Kelvin waves, which affect the thermocline in the eastern Pacific, favouring the development of an El Niño (Kessler et al, 1995; McPhaden et al., 2006). Kessler and Kleeman (2000) emphasise that in order to obtain a long-scale signal from short-scale wind perturbations, nonlinear rectification processes are needed. They find that even purely oscillatory short-scale winds can favour El Niño, for example by evaporative cooling of the Pacific warm pool due to higher wind speeds, leading to westerly wind anomalies, and by causing eastward equatorial currents due to non-linear advection of zonal momentum by Ekman convergence. Note that westerly (easterly) winds lead to Ekman convergence (divergence) of eastward (westward) momentum along the equator and thus stronger eastward (weaker westward) currents, so in both cases an eastward contribution is generated. Westerly Wind Bursts may in turn be modulated by ENSO (Eisenman et al., 2005), as they are favoured by a more extended Pacific Warm Pool which often precedes El Niño.

ENSO is strongly phase-locked to the seasonal cycle, with its strongest variability in winter. The causes for this phase-locking are still controversial; suggestions include changes in the SST-atmosphere coupling strength associated with shifts of the ITCZ and changes in east Pacific upwelling (Tziperman et al., 1997), and seasonal variations in

the damping of east Pacific SST anomalies caused by cloud shading (Dommenget and Yu, 2016). Upcoming ENSO events can be relatively well predicted from early summer onwards (which amounts to detecting an event that is already growing), while predictions in or before boreal spring are more difficult (Barnston et al., 2012); this phenomenon has been termed the Spring Predictability Barrier. Obviously, an ambition of climate scientists is to improve the skill of ENSO predictions beyond the Spring Predictability Barrier.

Two types, or flavours, of El Niño events have been distinguished (Ashok et al., 2007; Larkin and Harrison, 2005; Kao and Yu, 2009; Kug and Kang, 2009). One type, which we will refer to as central Pacific (CP) El Niño (also known as El Niño Modoki), is characterised by warm anomalies in the central Pacific, whereas eastern Pacific (EP) El Niños have the strongest warm anomalies in the eastern Pacific (see Fig. 1.3). The El Niño Modoki Index (EMI; see Fig. 1.1) can be used to distinguish both types; for example, in 1982/83 and 1997/97 the EMI was low, while in 2009/10 it was high (see Fig. 1.2a). The different flavours of temporal ENSO development and spatial patterns may arise as a result of a variation of the strength of the different Bjerknes feedbacks (thermocline, zonal advection, and upwelling feedback), which amplify sea surface temperature (SST) perturbations. Kao and Yu (2009) report that the CP El Niño temperature signal reaches less deep than that of EP El Niños and suggest that CP El Niños might be more dominated by local winds and SST advection, whereas for EP El Niños thermocline processes and the WWV are important as well. Yu and Kim (2010) find that CP El Niños can occur during recharged, neutral, or discharged states of the WWV.

The strength of the feedback processes determining the stability and flavour of ENSO depends on the background state, which can be influenced by processes outside of the Pacific basin. In Dijkstra and Neelin (1995), these external processes were limited to a zonally averaged wind stress τ_{ext}^x, thought of as the zonal component of the Hadley circulation. It was shown that stability properties of the background state of the ZC model depend strongly on τ_{ext}^x. Links between El Niño flavours and the Pacific background state have been investigated using global climate models. Yeh et al. (2009) use CMIP3 runs to suggest that increased CO_2 concentrations lead to weakened trade winds, thermocline flattening, and enhanced CP El Niño activity. Observations indeed show more frequent CP El Niños in recent decades (Ashok et al., 2007), but McPhaden et al. (2011) found strengthening trades and thermocline steepening in observations for 1980–2010.

1.2 Indian Ocean variability and its response to ENSO

The Indian Ocean has a rather complex background state with marked asymmetry across the equator and an intense seasonal cycle; this is due to the Asian landmass forming the northern boundary of the Indian Ocean and giving rise to the Asian Monsoon. A review on the Indian Ocean climatology can be found in section 2 of Schott et al. (2009). In the context of this thesis, an important aspect of the Indian Ocean climatology is the absence of sustained easterly winds along the equator, which one would expect due to the Hadley circulation. In fact, in the annual mean, the zonal winds along the equator are slightly westerly. Therefore the Indian Ocean lacks a cold tongue in the east, but actually has an area of very high SSTs there, which is part of the Indo-Pacific warm pool. Watanabe (2008) uses a simple model to explain this in terms of convergence over the Maritime Continent: Mean easterlies and a strong Bjerknes feedback in the (zonally wide)
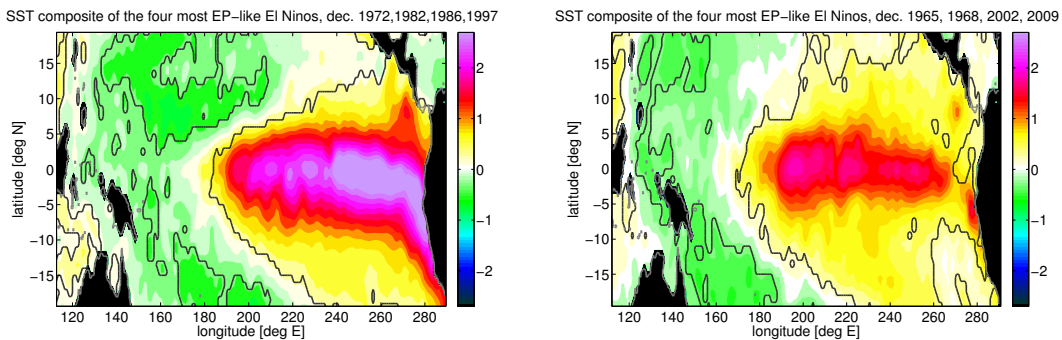
Figure 1.3: *Composites of December SST during the four most EP-like El Niños and the four most CP-like El Niños since 1948. Grey lines represent coast lines, and black lines encircle areas where the anomalies are significant at 90% confidence. El Niño winters were defined as winters wherein the Nino3.4 index in NDJF exceeds 0.9 standard deviations; for defining El Niño types, the four events with the lowest (EP) and highest (CP) El Niño Modoki Index (EMI) were used. The indices are defined in Fig. 1.1. The SST data was taken from Met Office Hadley Centre (2017), for the years 1948-2016.*

Pacific leads to warming in the west Pacific and convergence over the Maritime Continent, which gets enhanced by a positive feedback (convergence leads to convection, latent heat release, and hence stronger convergence). As the Indian Ocean is zonally rather narrow and thus has a weak Bjerknes feedback, the convergence effect generates a westerly wind contribution over the Indian Ocean which overcomes the easterly contribution by the Hadley circulation.

The winds over the equatorial Indian Ocean show a strong seasonal cycle, dominated by the Asian Summer Monsoon. In boreal summer and autumn, the southeasterly trade winds shift northwards and in particular lead to strong southeasterlies along the west coast of Sumatra, which give rise to coastal upwelling due to Ekman dynamics. In this season, the SST off Sumatra is sensitive to thermocline depth variations, and Bjerknes feedbacks can occur. Another dynamically active region is the Seychelles Dome (SD) around $8°S, 50°E$ (see Fig. 1.4). Here, cyclonal winds lead to a shallow thermocline, upwelling, low SSTs, and a strong air-sea coupling (Xie et al., 2002) throughout the year, though a semi-annual cycle can be observed in the Seychelles Dome heat budget (Yokoi et al., 2008).

There are thought to be two major modes of variability influencing the Indian Ocean on interannual timescales, namely ENSO and the Indian Ocean Dipole (IOD; also known as Indian Ocean Zonal Mode, IOZM), although the latter may not be independent of ENSO. Their indices are defined in Fig. 1.1. El Niño is followed by Indian Ocean Basinwide warming (IOB; also abbreviated BWW in the literature) with a lag of about 3 months; La Niña is followed by Indian Ocean cooling (see Fig. 1.2b). Klein et al. (1999) found that the IOB variability is mainly caused by anomalous surface heat fluxes: During El Niño, convection over the Indian Ocean is suppressed and thus increased solar radiation can heat the ocean. However, in the Seychelles Dome, additional contributions to the warming occur (Xie et al., 2002; Schott et al., 2009): During El Niño, negative SST anomalies occur in the west Pacific (see Fig. 1.3, both a and b) which induce positive sea level pressure anomalies and easterly winds extending over the east Indian Ocean. This leads to an anticyclonal wind curl which forces a downwelling Rossby wave. The Rossby
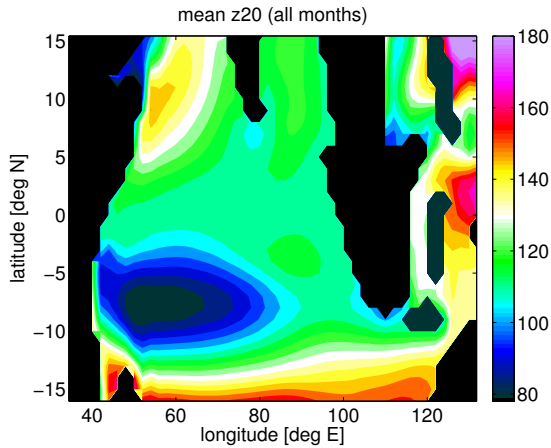
Figure 1.4: *The mean depth of the $20°C$ isotherm (proxy for the thermocline depth) in m in the Indian Ocean. Note the area of shallow thermocline around $8°S, 60°E$, referred to as the Seychelles Dome. The data is available at Bureau of Meteorology (2017) for 1960-2016, and the mean is taken over all calendar months.*
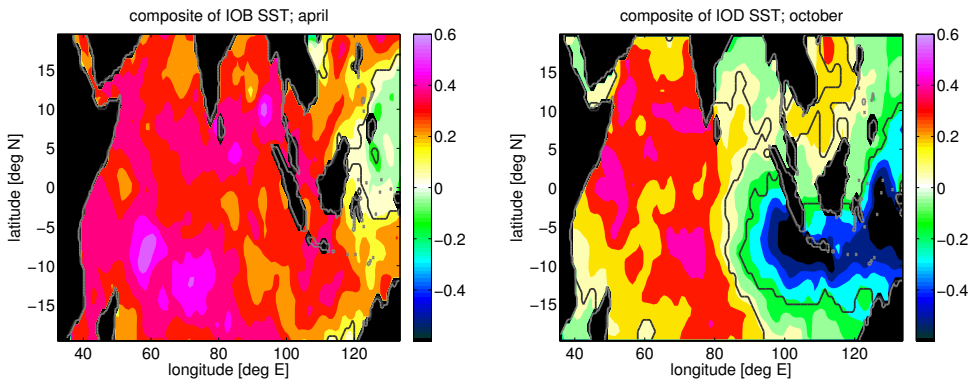
Figure 1.5: *SST composite of positive IOB years in April (left) and positive IOD years in October (right). Grey lines represent coast lines, and black lines encircle areas where the anomalies are significant at 90% confidence (in the IOB case, the warming is significant over nearly the whole Indian Ocean). The SST data was taken from Met Office Hadley Centre (2017), for the years 1948-2016. Positive IOB (IOD) years are defined as years where the anomaly of IOB(FMA) (IOD(ASON)) exceeds 0.9 standard deviations.*

wave leads to downwelling in the Seychelles Dome region, where due to the climatological upwelling and shallow thermocline the SST is sensitive to thermocline variations, and causes a warm anomaly. The same process occurs with opposite sign during La Niña. Yet Seychelles Dome variability is not entirely dominated by ENSO; Tozuka et al. (2010) suggest that it is more strongly tied to the IOD (note that the western pole of the IOD overlaps with the Seychelles Dome region).

A positive IOD is characterised by warm SST anomalies in the west Indian Ocean and cool anomalies off Sumatra. IOD events develop in the course of the summer and peak in autumn (Xie et al., 2002), i.e. they occur while the mean winds along the coast of Sumatra favour upwelling. It has been discussed (Schott et al., 2009, and references therein) whether the IOD is really an independent climate mode or an expression of ENSO. El Niño is associated with easterlies over the east Indian Ocean which can lead to upwelling anomalies and cooling there. Indeed, many positive (negative) IOD events co-occur with El Niño (La Niña), especially if the ENSO event develops early in the season, but strong IOD events have also been found in absence of El Niño (e.g. 1994; see Fig. 1.2c).

1.3   Possible Impacts of the Indian Ocean on ENSO

El Niño may not only influence adjacent regions like the tropical Indian Ocean, but also in turn be influenced by them. In particular, along the equator, far-reaching influence in the zonal direction is possible due to the lack of geostrophic balance. Dayan et al. (2014) suggest that only the Indian Ocean SST, mostly the IOB in spring, produces statistically significant zonal wind anomalies in the Pacific, while SST anomalies in the Atlantic and the extra-tropical Pacific do not. However, Wright (1986) and Ham et al. (2013) suggest that both north and equatorial Atlantic SST initial conditions increase forecasting skill for ENSO. Frauen and Dommenget (2012) and Dommenget et al. (2006) suggest that the effect of decoupling the Atlantic on the spectral properties of ENSO (standard deviation and period) is much lower than for decoupling the Indian Ocean. The reason for this may be that the Atlantic—at least the Atlantic equatorial SST—does not show a consistent response to ENSO (Jansen et al., 2009; Chang et al., 2006), so the Atlantic influence does not occur at a fixed phase relation to ENSO and is unlikely to systematically affect the amplitude or period of ENSO.

This does not hold for Indian Ocean variability; as mentioned in the previous section, the Indian Ocean Dipole and especially the Indian Ocean Basinwide warming are influenced by ENSO and therefore typically do occur at a certain phase relation with ENSO. The IOB is thought to dampen ENSO and increase its frequency, as a warming Indian Ocean causes easterlies over the west Pacific (Gill, 1980) which counteract the westerlies associated with the ongoing El Niño and initiate a switch to La Niña, as found in may studies using GCMs and observations (Kug and Kang, 2006; Kug et al., 2006; Santoso et al., 2012; Kajtar et al., 2016). The IOB does not offer much additional predictive skill, possibly because the IOB depends so strongly on ENSO that it can be regarded as part of the ENSO cycle (Xie et al., 2009; Izumo et al., 2013).

The relation between the IOD and ENSO is less clear. It has been argued that the wind response to an IOD outside the Indian Ocean is small, because the contributions by the individual poles are of similar magnitude and opposite sign and thus cancel out. Yet it was suggested that a positive IOD co-occurring with El Niño (i.e. in autumn/winter of year 1) can indirectly strengthen it by reducing the damping effect of the IOB (Annamalai et al., 2005; Santoso et al., 2012). Izumo et al. (2015) proposed a mechanism by which the

IOD[2] in autumn(year 0) can impact ENSO in winter(1/2): In autumn(0), the wind effects of the cool western and warm eastern Indian Ocean over the west Pacific cancel, but in the spring(1), when the eastern pole also cools (such as to yield a pure IOB pattern), the resulting westerlies cause a downwelling oceanic Kelvin wave that might initiate El Niño, without being partially compensated by the delayed negative feedback that would arise if the IOB-induced westerlies had already been present in autumn. However, Izumo et al. (2010, 2013) suggest that a negative IOD is associated with easterlies over the west Pacific, because the effect of the SST in this region is amplified by a convection feedback in this warm and moist region. (Note that although we use a negative IOD as example, a positive IOD might likewise induce La Niña at ca. 1.5 years lag.) They also show that the IOD adds predictive skill at 14 months lead time, i.e. across the spring predictability barrier.

The Indian Ocean might also influence ENSO by causing changes in the atmospheric noise characteristics, e.g. the amplitude, period or spatial extent of intraseasonal winds. Izumo et al. (2010) suggest that the zonal wind variability in the west Pacific increases after a negative IOD event. One possible source of wind noise is the Madden-Julian Oscillation (MJO; see Zhang (2005) for a review), an intraseasonal ocean-atmosphere coupled mode with a preferred period of 30-100 days. Its active phase essentially consists of a large cluster of thunderstorms which forms over the west Indian Ocean and travels eastward at a speed of about $5m/s$. Underneath and to the west of the convective cluster, westerly wind anomalies prevail, while to the east, the anomalies are easterly. Upon reaching the west Pacific, the convective signal of the MJO vanishes but the wind anomalies remain and propagate east at the phase speed of a dry atmospheric Kelvin wave (about $30m/s$). Izumo et al. (2009) found two components of the MJO, a high-frequency one (period $30 - 50$ days) centred around the equator and a low-frequency one (period $55 - 100$ days) centred around $8°S$. Following a negative IOD event, the low-frequency component is strengthened, while the high-frequency component diminishes. For this, Izumo et al. (2009) offer two explanations: first, the shallow thermocline in the Seychelles Dome region (the onset region of the low-frequency MJO) enables a stronger air-sea coupling, or second, the IOD may create a favourable atmospheric background state for the low-frequency MJO. Wilson et al. (2013) also suggest that during a negative IOD event, low-level convergence and high humidity over the east Indian Ocean favour convection and thus the MJO. It should be noted that the MJO, or at least its propagation behaviour over the Pacific, is also influenced by ENSO (Zhang, 2005, and references therein). In particular, the MJO tends to propagate further into the Pacific when the Warm Pool extends far to the east, i.e. prior to the onset of El Niño. Thus it is hard to disentangle the influence of the IOD on the MJO, the influence of ENSO on MJO and the influence of the MJO on ENSO.

The Pacific and Indian Ocean may not only influence each other via the atmosphere ('atmospheric bridge' or state-dependent noise) but also via an 'oceanic bridge', e.g. variability in the Indonesian Throughflow (ITF), which transports relatively warm water from the Pacific into the Indian Ocean. Yuan et al. (2011, 2013) suggest that upwelling anomalies may propagate eastward from the Indian to the Pacific Ocean through the ITF. However, Kajtar et al (2015) performed an experiment with a closed ITF. They found that although the Indian Ocean modes and to a lesser extent ENSO are somewhat de-

---

[2]Note that, throughout this study, by a positive IOD we mean a warm west and cool east Indian Ocean, as obtained when regressing autumn Indian Ocean SST only onto the IOD index (Saji et al., 1999), rather than mainly a cool eastern pole, as Izumo et al. (2015) and Shinoda et al. (2004) obtain by partial regression of SST onto IOD and IOB. See also Fig. 1.5. Izumo et al. (2015) classify "our" IOD as a combination of IOD and IOB.

formed due to changes in the background state, Indo-Pacific interaction still takes place. This suggests that at least part of the Indo-Pacific interaction is transferred via the atmosphere. It may be difficult to assess the potential influence of the ITF due to the complex geometry and the short high-quality time series available. Because of this lack of data, this thesis will deal with the atmospheric interaction mechanisms only, although a potentially important role of the ITF cannot be dismissed.

The amplitude, period and spatial pattern of ENSO also depend on the background state (e.g. the mean zonal wind) over the Pacific. Changes in Indian Ocean temperature on decadal and longer time scales might impact the Pacific background state. Luo et al. (2012) used observational data and 163 climate model simulations and found that a substantial Indian Ocean warming, as observed in recent decades, favours easterly winds over the western Pacific, which can cause a more La Niña-like background state. Using HadISST data at $1°$ resolution (Rayner et al., 2003; Met Office Hadley Centre, 2012), the linear warming trend of the basinwide warming index (IOB; $20°N - 20°S$; $40 - 100°E$) for 1970-2011 is $1.2K/100yr$ whereas for 1900-1969 this trend is $0.3K/100yr$. For the Nino3.4 region, the corresponding trends are $0.2K/100yr$ (1970-2011) and $-0.2K/100yr$ (1900-1969). Though the discrepancies between datasets for the tropical Pacific are large (Deser et al., 2010), the Indian Ocean seems to be warming relative to the Pacific, which may influence the background wind field of the Pacific and thereby affect ENSO.

1.4   Research Questions and Outline of this thesis
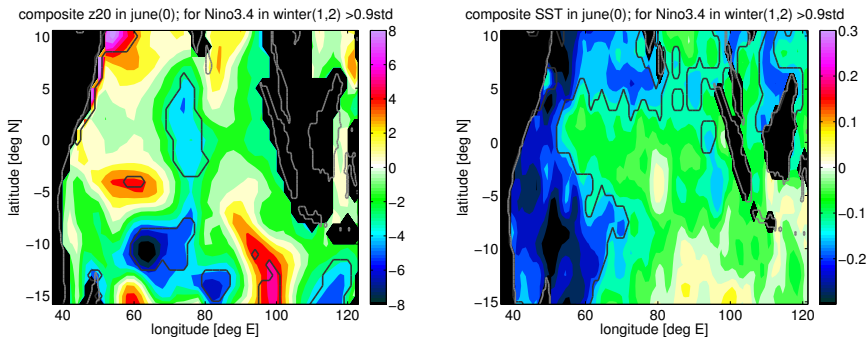
Figure 1.6: *Composite of the thermocline depth (z20; left) in m and Sea Surface Temperature (right) in K in June of year 0 preceding El Niño in winter (1-2). I.e. the years 0 were included into the composites if Nino3.4 averaged over November (year 1) - February (year 2) exceeds 0.9 standard deviations. Grey lines are coast lines; black lines encircle areas in which the deviation is significantly different from zero at 90% confidence (two-tailed). The SST data was taken from Met Office Hadley Centre (2017), for the years 1948-2016, while the z20 data was taken from Bureau of Meteorology (2017) and is available for 1960-2016.*

The studies in this thesis were triggered by a composite (Fig. 1.6) of the south west Indian Ocean thermocline depth (represented by the depth of the $20°C$ isotherm, z20) or Sea Surface Temperature (SST) in boreal summers ('summer in year 0') 1.5 years prior to El Niño, i.e. prior to winters (November (year 1) - February (year 2)) in which Nino3.4 exceeds 0.9 standard deviations.

Fig. 1.6 suggests that El Niño tends to be preceded by a shallow thermocline and low SST in the Seychelles Dome region with 1.5 years lead time. In other words, the thermocline depth and the SST in this region might act as a precursor to ENSO. However, as discussed in section 1.2, the Seychelles Dome region is probably also influenced by ENSO. Therefore care must be taken to disentangle cause and consequences, and it must be tested whether the Seychelles Dome region provides any additional predictive skill compared to basing a prediction of subsequent ENSO behaviour on previous ENSO-related variables only. - From these considerations the following two research questions arise:

1) Does the summer variability in the Seychelles Dome region (or possibly other regions in the Indian Ocean) contain any independent information about ENSO 1.5 years later, e.g. about probability, the amplitude, or the flavour of upcoming events?

2) If so, by which physical mechanism may the summer Seychelles Dome anomalies influence ENSO development at 1.5 years lag?

As mentioned in section 1.2, the Indian Ocean SST has increased the last 4-5 decades. The frequency of CP El Niño events has also increased (Ashok et al., 2007). This leads to the third research question:

3) How do long-term changes in Indian Ocean SST affect ENSO stability and flavour? In particular, could there be a connection between Indian Ocean SST trends and the frequency of CP El Niños?

The first question is mainly addressed in chapter 2. In section 2.2 a statistical test (the 'common cause test') is employed to test whether the negative correlation between summer Seychelles Dome variability and ENSO after 1.5 years is stronger than one would expect, based on the influence of ENSO on the Seychelles Dome and on itself (ENSO cyclicity). In addition, in section 2.3.2 we investigate whether a cool Seychelles Dome favours particular El Niño flavours.

To answer the second question, additional data analysis is used to propose two mechanisms that might explain the observations (section 2.4): State-dependent noise and the atmospheric bridge. The latter raises some concerns that need to be resolved. A key point of the atmospheric bridge mechanism is that a cool Seychelles Dome is associated with easterly wind anomalies over the (west) Pacific. However, the observational data is too noisy to clearly distinguish between the influence of Indian and Pacific SST signals on the wind. In addition, easterly winds to the east of a cool SST anomaly is contrary to the Gill response (which suggests air subsidence and surface divergence, especially in the zonal direction, over a cool anomaly near the equator, see (Gill, 1980)). These two points raise doubts about whether the atmospheric bridge mechanism is realistic. To shed some light on this question, an intermediate complexity model - an Indo-Pacific extension of the Zebiak-Cane model (in a version by Van der Vaart et al. (2000)) with a simple convective feedback, described in chapter 3 - will be used to better understand this wind response in chapter 5. In chapter 6, an attempt will be made to verify the results by comparing them to a 100 year simulation of both a high and a low resolution version of a Global Circulation Model (GCM), namely the Community Earth System Model (CESM).

The third research question is addressed in chapter 4 by using a convection-free version of the Indo-Pacific Zebiak-Cane model. The same model is used to confirm the results concerning the impact of the IOB on ENSO (see section 1.3) found in earlier studies using GCMs and observations.

The thesis ends with a summary, conclusions and outlook (chapter 7).

Chapter 2

Data Analysis[1]

2.1 Introduction and Methods

As mentioned in section 1.4, El Niño events peaking in the (boreal) winter of year 1-2 tend to be preceded by low sea surface heights in the Seychelles dome region and and low sea surface temperatures in the Seychelles Dome in the summer-autumn of year 0 (see Fig. 1.6), i.e. at roughly 1.5 years lead time. This finding suggests that the Seychelles Dome region, or more generally the west Indian Ocean might potentially act as a precursor to ENSO and add some skill to long-range ENSO predictions. In this chapter, observational data will be analysed in order to further investigate the statistical significance of the relation and obtain some hints about the underlying physical mechanisms.

After a brief description of the data used and some technical remarks about statistical significance testing (section 2.1.1) and the Multi-channel Singular Spectrum Analysis (MSSA) method (section 2.1.2), correlation-based techniques are employed to test whether the west Indian Ocean really adds independent information on ENSO development (section 2.2). Next, the spatio-temporal patterns related to ENSO are computed using MSSA (section 2.3.1), and the relation between ENSO types and the Seychelles Dome is investigated (section 2.3.2). Finally, evidence for underlying mechanisms of an Indian Ocean - ENSO interaction is presented (section 2.4). The chapter ends with a summary and conclusions.

2.1.1 Data, indices, and significance tests

For this study we made use of zonal wind data, both monthly and daily, at 2.5° resolution, available for the years 1948-2013, from the NCEP reanalysis data (Kalnay et al., 1996; NOAA/OAR/ESRL PSD , 2014). Also the monthly mean HadISST SST data at 1° resolution available for the years 1870-2011 were used (Rayner et al., 2003; Met Office Hadley Centre, 2012); unless stated otherwise, SST data were used for the period 1948-2011. In addition, a monthly mean Warm Water Volume (WWV; the volume of water warmer than $20°C$ in $5°N - 5°S$ and $120°E - 80°W$) time series was taken from the TAO Project Office, NOAA/PMEL (NOAA/PMEL Tropical Atmosphere Ocean Project, 2014), which is available from 1980 onwards, and Sea Surface Height (SSH) anomaly data for October 1992 - August 2013 was used. This satellite altimeter product is produced and

---

[1]This chapter is based on the article Wieners, C.E., W.P.M de Ruijter, W. Ridderinkhof, A. von der Heydt, and H.A. Dijkstra, 2016: Coherent tropical Indo-Pacific interannual climate variability. J. Climate, 29, 4269-4291

distributed by AVISO as part of the Ssalto ground processing segment (AVISO/SSALTO, 2014). The data are provided as weekly 'snapshots' of the state of the ocean on a certain day. Monthly data were obtained by linearly interpolating to daily values and then taking a monthly average.

In addition to standard ENSO and IOD indices, we define an 'extended Seychelles Dome Index' (SDIex) as the monthly-mean SST averaged over $3-13°$S, $45-70°$E. This area is chosen slightly larger than the actual Seychelles Dome region, 1) to include more data points to reduce measurement errors in this data-sparse region, and 2) because the SST anomalies around the Seychelles Dome usually extend further north than the Seychelles Dome itself. We denote hIND, where 'IND' is an index (e.g., 'hSDIex' and 'SDIex'), when SSH is used for the index instead of SST. Index regions are defined with help of Fig. 1.1.

We also define a field we call 'burstiness', which is a measure for the intraseasonal variability of the zonal wind. It is computed at each location $\vec{x}$ by taking the variance over 3 months of the 5-daily mean zonal wind on 850hPa, u:

$$B(\vec{x}, m) = \sum_{p \in P_m} \frac{1}{N_{P_m}} (u(\vec{x}, p) - \bar{u}(\vec{x}, m, p))^2, \qquad (2.1)$$

where $B(\vec{x}, m)$ is the burstiness at location $\vec{x}$ in month m, P_m the set of all 5-day blocks p in months $m-1$, m, and $m+1$, N_{P_m} the number of elements in P_m, and $\bar{u}(\vec{x}, m, p)$ is linear fit of u at $\vec{x}$ over the interval P_m. Subtracting $\bar{u}$ should remove the influence of long-term trends, and using 5-daily wind suppresses synoptic-scale signals. Izumo et al. (2010) used a similar concept, but using a band-pass filter and wind stress. We used $850hPa$ wind because it is less sensitive to orographic effects.

In all applications of correlations, regressions and composites, the analysis is performed for each calendar month m separately, such as to take into account phase locking to the seasonal cycle. Anomalies Q_a of a quantity Q are computed by subtracting a 'background value' Q_b from the data, which captures variability on time scales much longer than ENSO time scales: $Q_a(y, m) = Q(y, m) - Q_b(y, m)$ where y is the year. For the relatively short time series of WWV and the SSH data, $Q_b(y, m)$ is computed by taking the linear trend over all years, with m fixed. For other quantities, a running-mean like technique is used in order to account for possible non-linear trends, i.e.

$$Q_b(y, m) = \frac{\sum_{k=-y_1}^{y_2} w_k Q(y+k, m)}{\sum_{k=y_1}^{y_2} w_k}, \qquad (2.2)$$

where $y_1 = y_2 = 10$ and $w_k = 1$ if $|k| \le 5$, and otherwise $w_k = 1/2$. The results presented below do not strongly depend on the details of the detrending.

Unless stated otherwise, significance of quantities C obtained by correlation, regression, or composite analysis is tested in a non-parametric way by re-calculating C with N_{shuf} surrogate data sets in which the years were randomly shuffled. When the true C is greater or smaller than $(100 - s/2)\%$ of the surrogate C, then C is significant at $s\%$ confidence (two-tailed). A value $\tilde{N}$ for N_{shuf} is considered sufficiently large when $\tilde{N}/2$ and $\tilde{N}$ yield the same limits for C; a typical value is $N_{shuf} = 2000$.

In a composite analysis, when investigating whether a quantity Q in a set of years Y_1 differs significantly from Q in a set Y_2, it is tested whether the auxiliary variable

$$R \equiv \frac{1}{N_1} \sum_{i \in Y_1} Q(i) - \frac{1}{N_2} \sum_{i \in Y_2} Q(i). \qquad (2.3)$$

differs significantly from zero, where N_i is the number of years in Y_i.

2.1.2 Multi-channel Singular Spectrum Analysis (MSSA)

The Multichannel Singular Spectrum Analysis (MSSA) technique (Plaut and Vautard, 1994) is able to determine covarying spatio-temporal patterns in multivariate data. It is a generalisation of purely spatial Empirical Orthogonal Function (EOF) analysis and purely temporal Singular Spectrum Analysis (SSA). Both for the calculation of the statistical modes and for the significance test against red noise, we follow Allen and Robertson (1996).

The MSSA analysis is applied to a data set consisting of SST, zonal wind and burstiness fields. We consider data from a band extending from 20°N to 20°S and $0-360$°E. The spatial resolution is 2° meridionally and 4° zonally for SST, 2.5° and 5° for the zonal wind and 2.5° and 2.5° for the burstiness. The time resolution is 1 month and the window length is approximately 10 years (120 lag values). Prior to computing the MSSA modes, the data is detrended as in eq. 2.2, the seasonal cycle is subtracted and a binomial low-pass filter

$$X'(t) = \frac{\sum_{m=-M}^{M} a_m X(t + m\Delta t)}{\sum_{m=-M}^{M} a_m} \; ; \; a_m = \frac{(2M)!}{(m+M)!(M-m)!} \tag{2.4}$$

with $M = 4$, $\Delta t = 1$ month is applied, damping signals with periods of 9 months to half of the original amplitude (Mitchell et al., 1966). The data of each of the fields are normalised by the standard deviation over space and time of each field in order to avoid the weight of the fields to depend on the units in which they are measured.

In order to reduce the computational effort, and to obtain uncorrelated (at lag zero) data for the MSSA/significance test, the data are pre-filtered by first computing ordinary EOFs over the combined data set (Allen and Robertson, 1996). The first N_{eof} EOFs (containing 90% of the variance) are selected and the corresponding time series are used as variables in the MSSA procedure. For calculating the properties of the red noise surrogate data used in the significance test, the method described in section 4.3 of Allen and Smith (1996) is used. We will refer to the spatio-temporal patterns found by MSSA as Extended EOFs (EEOFs) and the corresponding time series as Principal Components (PCs).

Both the data-adaptive and noise-adaptive test described in Allen and Robertson (1996) are applied. The former serves for identifying potentially significant EEOFs and their PCs, while the noise adaptive test is used to check whether there is really improbably high variance in the dominant frequencies of the PCs (Allen and Robertson, 1996). In the significance tests, 2400 surrogate data sets were used.

2.2 Correlations and the effects of ENSO cyclicity

In this section we show that the Seychelles Dome contains information linearly independent of ENSO, and how the Seychelles Dome relates to the IOD and IOB. When correlating the SSH in the Indian Ocean in spring-autumn (year 0) to Nino3.4 in Dec. (year 1), i.e. with a lag around 1.5 years, one finds a strong negative correlation in the Seychelles Dome area for April-Aug.(Fig. 2.1a; see also 1.6a). For the SST data a similar signal can be found, though it is spread out over most of the west Indian Ocean (see Fig. 1.6b).

A negative correlation between SDIex in August-October and Nino3.4 in next year's July-January reaches values down to -0.48 (Fig. 2.1c). Already in April, values below -0.35 are reached, so El Niño in boreal winter(1/2) is preceded by a cool Seychelles Dome in summer(year0) ($> 95\%$ significant using Student's t-test).
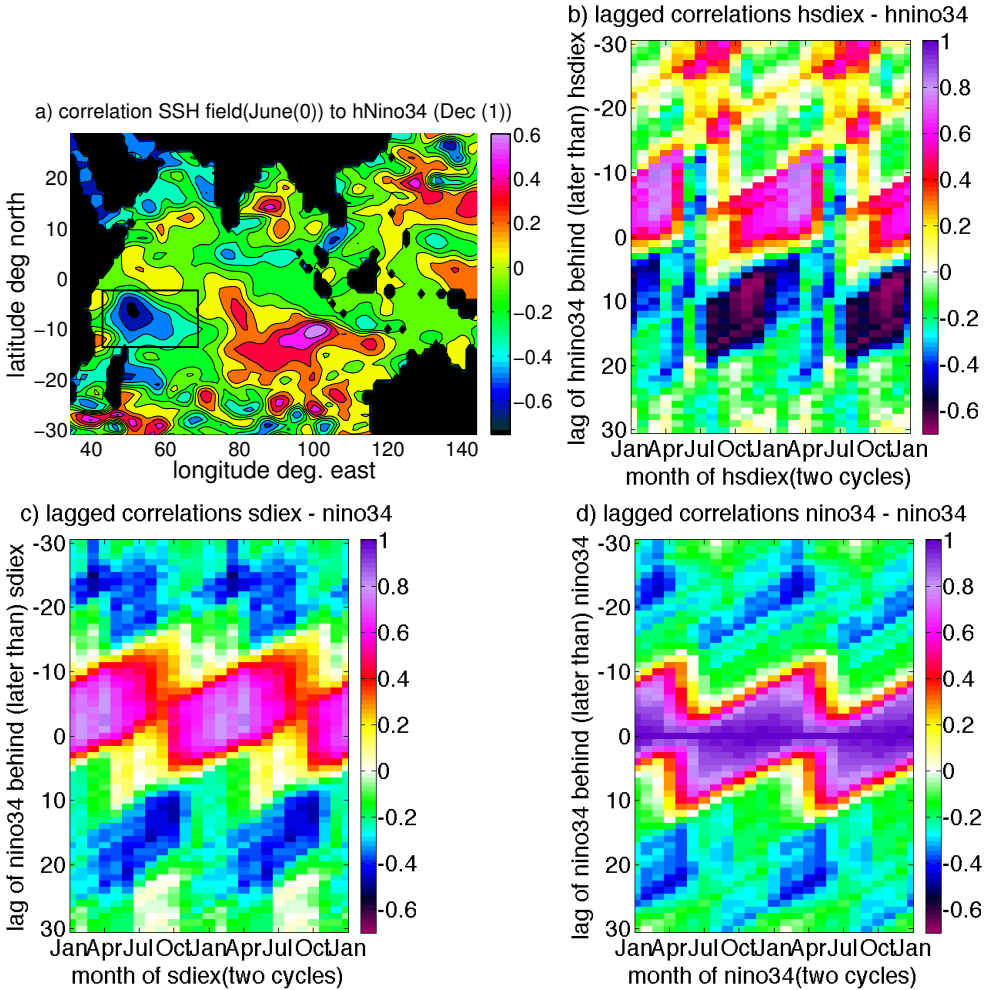
Figure 2.1: *(a) correlation of the SSH field in June (year 0) with the hNino34 index in Dec (year 1). The black box represents the area in which SDIex and hSDIex are computed. (b) Lagged correlation between hSDIex and hNino3.4, where a positive lag (in months) means that hNino3.4 is taken at a later time. 'Month of hSDIex=August and lag=+16' means the time series of hSDIex in August is correlated to hNino3.4 16 months later (December next year). Two annual cycles are shown for convenience. (c) same as (b) but for SDIex and Nino3.4. (d) same as (b) but for Nino3.4 correlated to itself. SST data is taken for 1948-2011, while SSH data covers the period of 1993-2012. Using a Student's t-test, correlations exceeding 0.25 (0.21) are significant at 95% (90%) confidence for the SST time series used in plots (c) and (d), while for the shorter SSH time series used in plot (b), correlations should exceed 0.44 (0.38).*
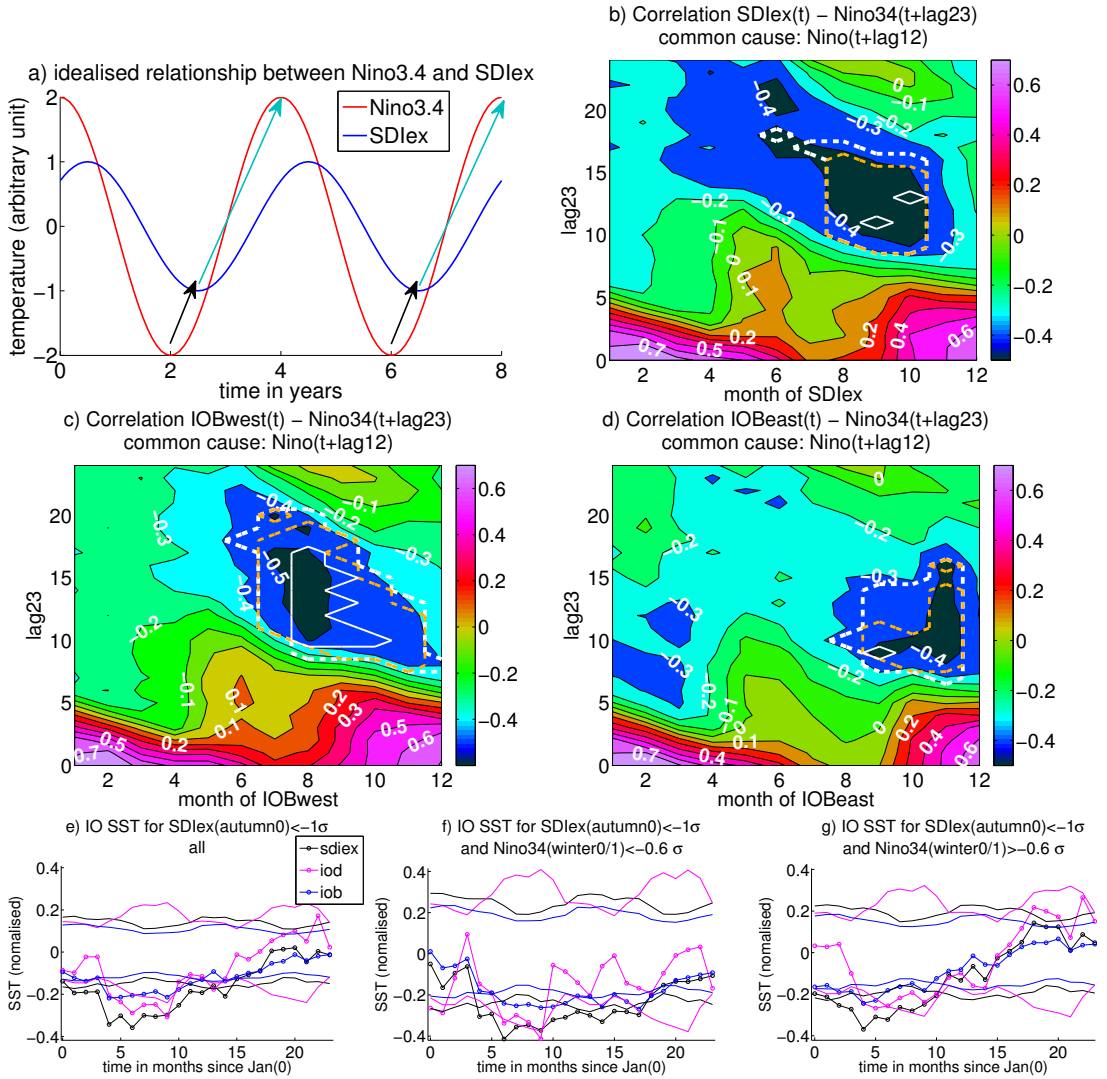
Figure 2.2: *(a) Illustration of possible influences between Nino3.4 and SDIex (see text). (b) Results of the common cause test for the correlation of SDIex at a certain calendar month with Nino3.4 lag_2 months later. Colours denote the correlation, while the white dashed, orange dashed, and white solid lines encircle values which are significant at 90%, 95% and 99% confidence in the common cause test against Nino3.4 at lag_1 months later than SDIex. $lag_1 \in \{-10, -9, ..., +4\}$ and the test is only considered passed if the correlation is significant for each value of lag_1. (c) and (d) are as (b) but replacing SDIex by IOBwest and IOBeast, respectively. (e)-(g) show composites of SDIex (black), IOD (magenta) and IOB (blue) for all years with SDIex(JJASO(0))$< -1\sigma$ (plot (e)), or with the additional constraint that Nino3.4(ND(0),JF(1)) $< [>] -0.6\sigma$ (plot (f) [(g)]). Lines with circles show the actual data, while bare lines show the 95% confidence limits. The years(0) in plot(f) are 1954,1964,1984,1985 and in plot (g) 1965,1971,1974,1989,1996,2004.*

For comparison, Fig. 2.1d shows a negative autocorrelation of Nino3.4 of around -0.45 at lags around 22 months, caused by the cyclicity of ENSO with a mean period of around 4 years. The SDIex from October (year 0) to August (year 1) is also strongly linked to the state of ENSO in the boreal winter of year 0/1. For SDIex in April, this correlation reaches values of 0.83, while in August-October the correlation to Nino3.4 at short lags is still up to 0.5. Mature El Niños are known to be associated with anticyclonic winds in the southeast tropical Indian Ocean, causing downwelling Rossby waves which arrive in the southwest Indian Ocean several months later, lower the thermocline and hence increase SST (Xie et al., 2002; Schott et al., 2009).

This raises the question as to whether the negative correlation between SDIex and Nino3.4 at ≈ 1.5 years lag could be exclusively explained by ENSO's positive influence on the Seychelles Dome at lags around -5 months, together with ENSO cyclicity. To illustrate this, suppose that Nino3.4 were perfectly sinusoidal with a period of 4 years, and SDIex were completely determined by ENSO and would follow Nino3.4 as a lagged and possibly rescaled copy, say six months later (Fig. 2.2a). Then a cool Seychelles Dome would appear half a year after La Niña (black arrows in Fig. 2.2a). This cool Seychelles Dome event would automatically be followed by an El Niño after 1.5 years (light blue arrows), without any influence being exerted by the Seychelles Dome on ENSO.

In order to check whether the Seychelles Dome contains any (linearly) independent information from ENSO, we perform a significance test against the null hypothesis H0: 'The negative correlation between Seychelles Dome and Nino3.4 after 1.5 years is due to the influence of ENSO on the Seychelles Dome and ENSO cyclicity.' This is more generally formulated as:

'*H0: The correlation between two time series z_2 and z_3 does not significantly differ from what one expects, knowing only their correlations to a third time series z_1, i.e. $corr(z_2, z_3)$ is near $corr(z_1, z_2) \times corr(z_1, z_3)$.*' A more rigorous formulation will follow below. The test to falsify this null hypothesis, henceforth referred to as 'common cause test', is validated against the output of a conceptual model in the Appendix. The test consists of the following steps:

Let z_2 and z_3 be two time series, say, SDIex in calendar month m (i.e. we take one value per year) and Nino3.4 at a lag l_{23} later, while z_1 is the time series of the suspected common cause, say Nino3.4 in month $m + l_{12}$ (l_{12} is typically negative, i.e. z_1 is taken at an earlier time than z_2). All time series are assumed to have zero mean.

1. Perform a linear fit of z_2 and z_3 onto z_1 and write $z_2 = a_1 z_1 + Z_2$; $z_3 = a_3 z_1 + Z_3$ where a_2 and a_3 are linear fit parameters and Z_2 and Z_3 the residual time series.

2. Reject H0 if the following conditions both hold: (a) Z_2 explains a significant percentage of variance of z_3 and (b) Z_3 explains a significant percentage of the variance of z_2. This is equivalent to requiring that both $corr(z_3, Z_2)$ and $corr(z_2, Z_3)$ are significant.

The significance test of $corr(z_2, Z_3)$ and $corr(z_3, Z_2)$ can be performed as described in section 2.1.1. There is no canonical way to assign a single significance level to the common cause test, which tests two conditions. To be conservative, we consider the test passed at $s\%$ significance if *both* conditions are met at $\geq s\%$ significance.

As Z_2 and Z_3 by construction are uncorrelated to z_1, it can be shown that both condition (a) and (b) can never be fulfilled if $corr(Z_2, Z_3)$ is not significant. In addition, condition (a) will not be fulfilled if z_3 is dominated by z_1, i.e. $std(az_1) \gg std(Z_3)$, and likewise, condition (b) ensures that z_2 is not dominated by z_1. It can be shown that if $corr(Z_2, Z_3) = 0$, then $corr(z_2, z_3) = corr(z_1, z_2) \times corr(z_1, z_3)$.

Note that the common cause test is deliberately allowed to be passed in some cases where $\text{corr}(z_2, z_3) = 0$, namely if the contribution by z_1 is 'large' but cancelled by the contribution of Z_2 and Z_3, i.e., the actual correlation is much weaker than one would expect based on the common cause. One can supplement the common cause test by an ordinary significance test of $\text{corr}(z_2, z_3)$ to detect these cases. In our data, this situation never occurred.

In order to prevent a passing of the test due to a wrong choice of l_{12}, values in $\{-10, -9, ..., +4\}$ were used. Positive values of l_{12} should in particular be included when using the IOD as z_2, as the IOD might be influenced by a growing ENSO event peaking several months after the IOD itself. A correlation is considered significant only when passing the significance test for *all* values of l_{12}. Polynomial rather than linear fits of the z_2 and z_3 data to z_1 at up to fourth order have also been performed, but do not improve the fit significantly, so only linear fits are used.

The correlation between SDIex in August-October and Nino3.4 after roughly 10-15 months is significant against our null hypothesis at 95% confidence; locally even 99% are reached (Fig. 2.2b). When omitting the very strong 1997/98 El Niño, 95% confidence are still reached (not shown). These results indicate that the Seychelles Dome indeed contains independent information on ENSO.

To investigate whether SSH data yields better results than SST - SSH is less influenced by processes other than ocean dynamics, such as surface fluxes - the above analysis was repeated using hSDIex and hNino3.4 or hNino3 (which is more cyclic than hNino3.4). In the common cause test, the resulting correlations of hSDIex (Aug-Sept) to hNino3 are significant at 95% confidence (98% for hNino3.4; not shown). Correlations can reach values as low as -0.74 (Fig. 2.2b), but similarly strong values can be reached using SST data in only the years where SSH data is available, so it cannot be concluded that SSH performs better.

To check the relation between Seychelles Dome and IOD/IOB, the common cause test was repeated with other Indian Ocean indices than SDIex. For IODwest, IOB (both not shown) or IOBwest (Fig. 2.2c), slightly stronger correlations are obtained and 99% confidence are reached at more points than for SDIex. For IOBeast (Fig. 2.2d), significant correlations occur about 2 month later and weaker than for IOBwest, probably because the cold signal in the Indian Ocean spreads eastward in time. IODeast never reaches significant values, and the IOD performs less well than IODwest. So it is the west Indian Ocean in late boreal summer-autumn that carries most information about ENSO, though the region of strongest correlations is not confined to the Seychelles Dome. The significant results for IOB may seem contradictory to the results by Xie et al. (2009); Izumo et al. (2013) that the IOB offers little predictive skill for ENSO. However, it is mainly the IOB in spring that is determined by ENSO (correlations for IOB in April and the previous winter's Nino3.4 reach 0.85; for IOB in September, only correlations up to 0.37 are reached). In addition, the IOB in autumn might be dominated by the western half of the Indian Ocean; the correlation between IOB and IODwest in autumn exceeds 0.85, while in the IODeast, SST anomalies of opposite sign frequently occur, due to the IOD variability.

While Annamalai et al. (2005) suggest that a negative autumn IOD (including a cool west Indian Ocean) does not by itself have a strong impact on the Pacific, because its eastern and western poles are so close that their influence on Pacific wind cancels, Izumo et al. (2015) suggest that a negative IOD in autumn(0) influences the Pacific by postponing the formation of a full negative IOB and associated westerlies over the Pacific until next spring, thus preventing a delayed negative feedback through ocean adjustment. However, the IOB in spring(1) is strongly influenced by Nino3.4(winter 0/1). Indeed,
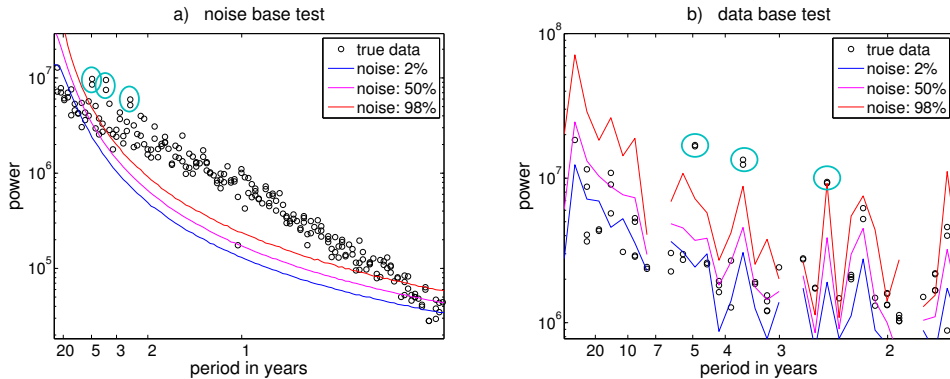
Figure 2.3: *Spectra of the variance against period in the noise base (a) and the data base (b). The black circles correspond to the data, while the red (magenta, blue) lines denote the power under which 98% (50%, 2%) of the surrogates lie. The high-frequency parts are cut off from the plots. Significant pairs of EEOFs are marked by blue circles.*

Fig. 2.2e-g suggest that a cool autumn SDIex is only followed by a significant spring IOB in case of a co-occurring La Niña. Therefore the mechanism of Izumo et al. (2015) may be dependent of a bi-annual component of ENSO (La Niña occurring in winter(0/1) and El Niño in winter(1/2). This does not exclude, however, that the IOD adds predictive skill according to the mechanism of Izumo et al. (2015), in such winters where the IOB is active.

2.3   Indo-Pacific Co-varying modes of Variability

2.3.1   Multi-channel Singular Spectrum Analysis: Indo-Pacific ENSO modes

To investigate the spatio-temporal patterns of the Tropical Indo-Pacific, an MSSA (see section 2.1.2) is performed simultaneously to the SST, zonal wind and burstiness fields. The lag window is 120 months (roughly 2 ENSO periods), and $N_{eof} = 70$ EOFs are included in the pre-filtering step. To test the robustness of the results below, we repeated the MSSA with (i) 30 instead of 70 EOFs, (ii) lag windows of 100 or 140 months, (iii) a low-pas filter with ($M = 2$ and $M = 6$ in (2.4)) and (iv) taking data only between 40°E and 290°E, i.e. omitting the Atlantic. The results were hardly affected.

The power spectra (Fig. 2.3) show (oscillatory pairs of) significant EEOFs. In the data adaptive test (Fig. 2.3b), three pairs with periods in the interannual band extend above the 98% level: EEOF2,3 with a period of 4.9 years and explaining 9.6% of the variance, EEOF4,5 with 3.6 years and 7.4%, and EEOF8,9 with 2.5 years and 5.3%. At all of these periods there is an enhanced variance also in the noise base test (Fig. 2.3a), compared to the variances in neighbouring frequencies.

Fig. 2.4a shows that the correlation between the sum of the three oscillatory modes and the original (detrended and low-pass filtered) data is high (up to 0.85) in the central-east Pacific and also in most of the Indian Ocean, in particular the Seychelles Dome (up to 0.68), while correlations in the Atlantic, the warm pool and the southeast Indian Ocean are much weaker. The sum of the three modes captures all major El Niño and La Niña
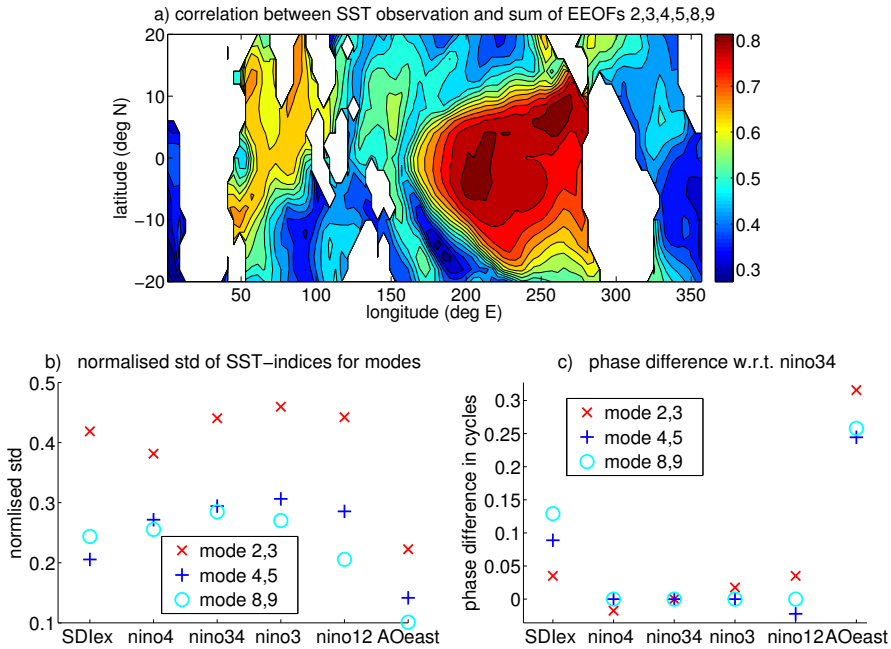
Figure 2.4: *(a) Correlation between the full SST data used for the MSSA and the re-constructed time series resulting from the three significant MSSA oscillations EEOF2,3, EEOF4,5 and EEOF8,9. (b) Standard deviation of SST-based indices for the three significant oscillations. The values are normalised by the corresponding value obtained by including all EEOFs (e.g. for EEOF2,3 and Nino3.4, the plot shows $std(Nino3.4\ for\ EEOF2,3)/std(Nino3.4\ for\ all\ EEOFs))$ (c) Phase relations of SST-based indices to Nino3.4. The plot shows the lag for which the correlation between an index I and Nino3.4 becomes maximal, divided by the period of the corresponding EEOF. A value of $+1/4$ means that I peaks $1/4$ period later than Nino3.4.*
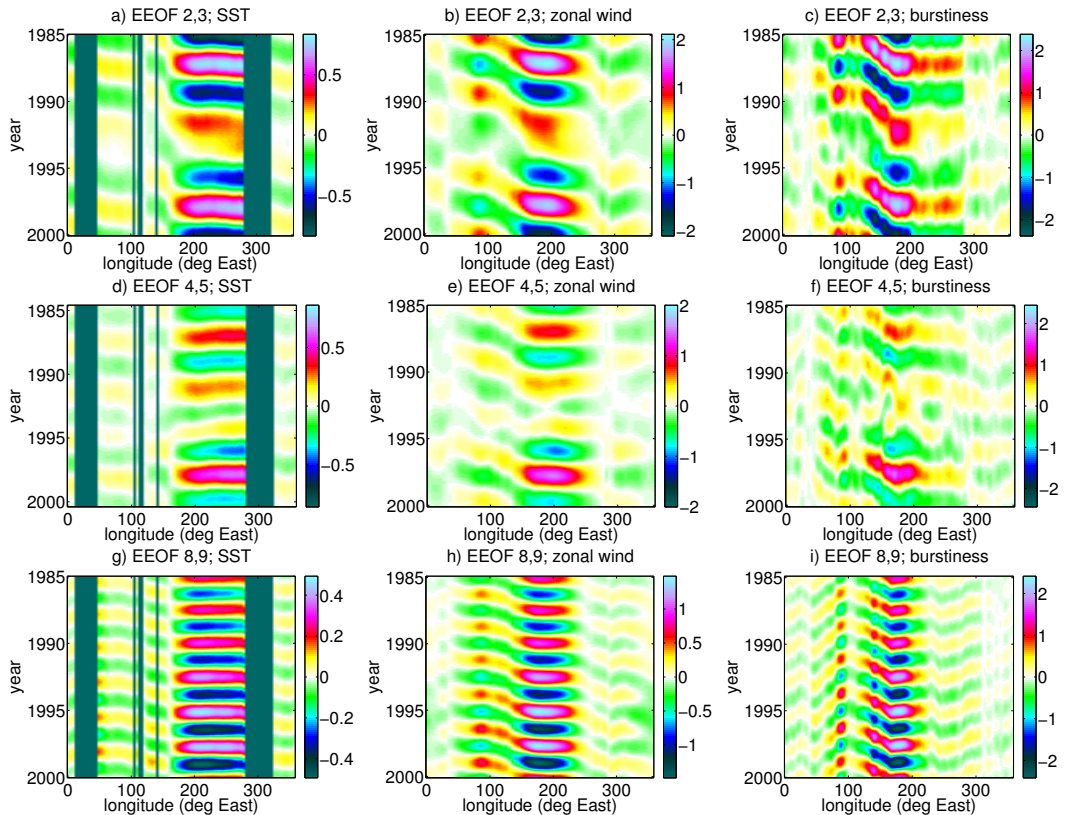
Figure 2.5: *Hovmöller diagrams of the reconstructed time series of the significant oscilla-tions EEOF 2,3 (a-c), EEOF4,5 (d-f) and EEOF8,9 (g-i) obtained by an MSSA of SST (a,d,g), zonal wind (b,e,h) and burstiness (c,f,i). Data is averaged over the region $5°N$ - $5°S$ and only the years 1985-2000 are shown.*

events, though the asymmetry between warm and cold events is reduced (not shown). Fig. 2.4b shows the standard deviation of several ENSO indices, SDIex and AOeast (see Fig. 1.1) as obtained by reconstructing the time series for a certain oscillatory pair of EEOFs, divided by the value obtained when considering *all* EEOFs in the reconstruction (this normalisation ensures that the relative importance of the contributions from the oscillating pairs can be estimated). The figure demonstrates that also the individual oscillations have stronger signals in the Niño indices and SDIex than in the Atlantic - they represent 'Indo-Pacific ENSO modes', while much of the Atlantic variability is contributed by other modes. Fig. 2.4c shows the lag for which the correlation between some SST-based index and Nino3.4 becomes maximal, divided by the period of the corresponding oscillation. All oscillations found here are dominated by an ENSO-like SST signal in the Pacific (Fig. 2.5 a,d,g), i.e. a strong oscillation in the east and central Pacific, to which the SST in the west Pacific is in anti-phase. The normalised standard deviation of SDIex is also high for all three oscillations (Fig. 2.4b), with SDIex signals lagging Nino3.4 by $\approx 0.04 - 0.13$ periods (Fig. 2.4c, Fig. 2.5a,d,g), while the Atlantic signal is much weaker.

The zonal wind field (Fig. 2.5b,e,h) has its strongest signal in the east Indian Ocean and west to central Pacific. For all significant oscillations, SST maxima (minima) in the

central/east Pacific are accompanied by westerly (easterly) winds on the equator around 190°E (EEOF2,3), 200°E (EEOF4,5), or 175°E (EEOF8,9), which are nearly in phase with the SST signal, peaking at most 1 month earlier. This wind pattern is typical for ENSO. During the peak of El Niño (La Niña) a patch of easterlies (westerlies) forms in the Indian Ocean around 0°N, 90°E, consistent with the SST difference between the west Indian Ocean and the Indonesian Seas. The wind anomaly moves eastward, temporarily weakening above Indonesia, and reaches the west Pacific slightly before Nino3.4 passes through zero. It then rapidly spreads eastwards and strengthens along with the SST anomaly forming the next La Niña (El Niño). Wind anomalies propagating from the Indian Ocean to the Pacific are consistent with Clarke (2003); Kug et al (2010). During and after El Niño (La Niña), a diverging (converging) wind anomaly is thus present above Indonesia, which may help to deplete (build up) the west Pacific warm pool Wyrtki (1985); Jin (1997a). A positive WWV anomaly in turn is a precursor to El Niño (Meinen and McPhaden, 2000).

The burstiness (Fig. 2.5c,f,i) is positive (negative) in the Pacific east of 150°E during El Niño (La Niña), with strongest values occurring at 10°N (not shown). To the west of 150°E, negative (positive) anomalies are found. During the decay of El Niño (La Niña) the positive (negative) anomaly moves southeastwards (meridional propagation component not shown) and decays, while the negative (positive) one propagates eastward, reaching the west Pacific before Nino3.4 becomes negative (positive). High (low) zonal wind variability is thus present in the west Pacific prior to the onset of El Niño (La Niña), consistent with McPhaden et al. (2006) and Kug et al (2010) who suggest that strong zonal wind variability is a precursor to El Niño. West Pacific burstiness may be influenced by the Indian Ocean (Izumo et al., 2009; Wilson et al., 2013).

Fig. 2.6 shows that the SST evolution in the early stages of El Niño is not the same for all three modes. The early stages of evolution are represented by the moment where Nino3.4 switches from negative to positive values (Fig. 2.6a,d,g), and three (for EEOF2,3 and EEOF4,5) or two (EEOF8,9) months after Nino3.4 the switch to positive values (Fig. 2.6b,e,h). The mature El Niño phase is represented by the moment where Nino3.4 reaches its maximum (Fig. 2.6c,f,i). For EEOF2,3 (Fig. 2.6a-c) there is a slight warm anomaly in the west Pacific when Nino3.4 switches from negative to positive. South of the equator between Peru and about 225°E, a cool anomaly (remnants of the previous La Niña) is found to the southwest of the warm anomaly. Three months later, the warm anomaly has intensified and spread further east, and the narrow band along the South American coast south of the equator begins to warm, too. For EEOF4,5 (Fig. 2.6d-f) the evolution is almost the other way around, with El Niño starting along the Peruvian coast and growing westward. However, the mature El Niño phase looks very similar to that of EEOF2,3 with a strong warm anomaly along the Cold Tongue which extends till about 160°E, and the strongest anomalies along the Peruvian coast. For EEOF8,9 (Fig. 2.6g-i) El Niño starts as a warm anomaly in a narrow band along the equator, while cool anomalies (remnants of the previous La Niña) are found polewards of it. The warm anomaly intensifies and broadens polewards, without zonal propagation. The fully grown El Niño is similar to the other modes, except that its maximum lies at 210°E, rather than near the coast.

EEOF8,9 shares some properties with the CP El Niño described in the literature: It is not propagating and it has a shorter period than the other ENSO modes, namely 2.5 years. Both findings agree well to those of Kao and Yu (2009), but the spatial pattern of the EEOF8,9 El Niño does not resemble the horseshoe pattern found in that paper. However, the CP Niño composites of Kug and Kang (2009) and Ashok et al. (2007) do
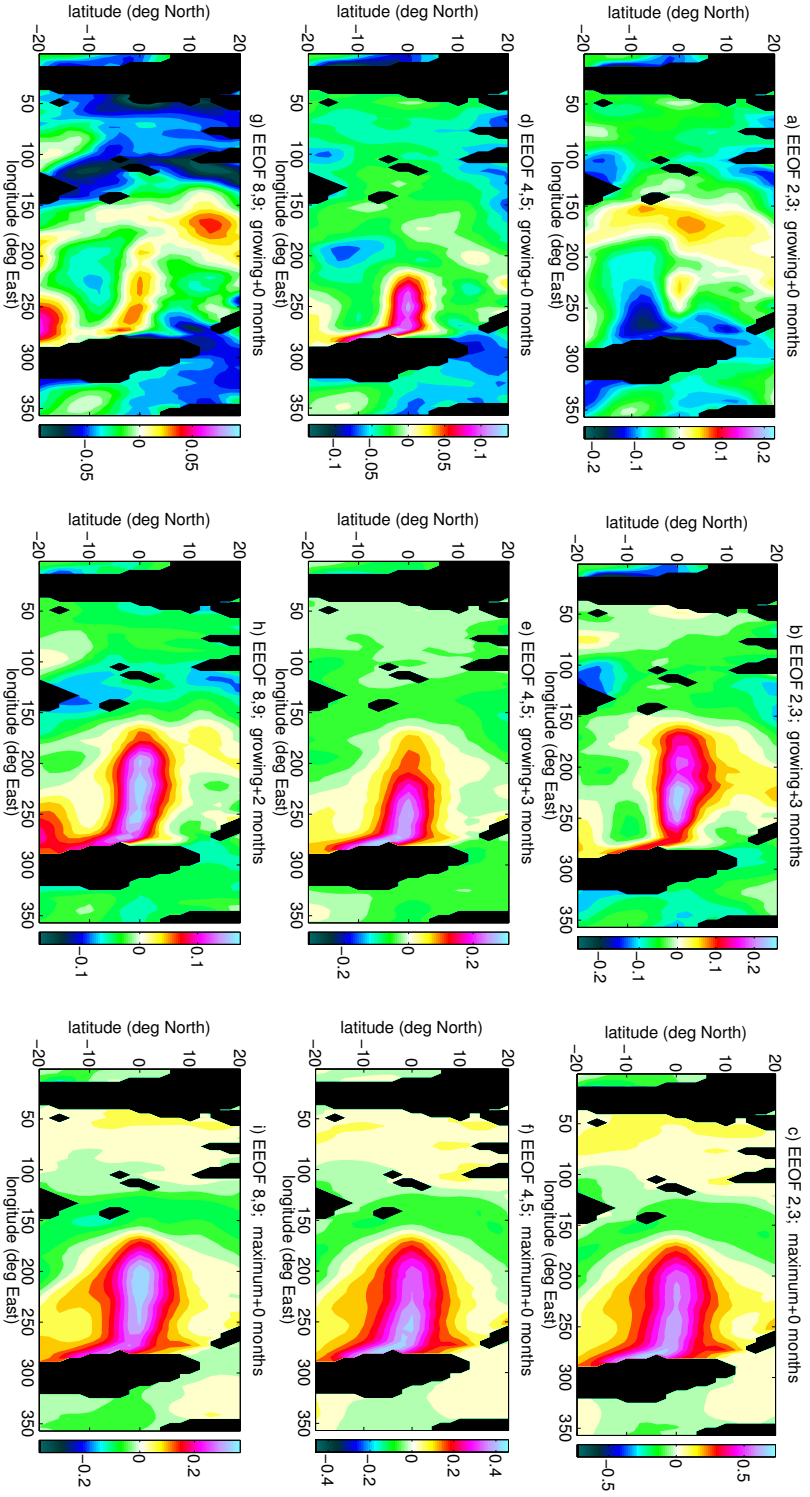
Figure 2.6: *The development of an El Niño in the three significant oscillations EEOF 2,3 (a-c), EEOF4,5 (d-f) and EEOF8,9 (g-i) from the MSSA. For each oscillation, a composite of the SST field is given at three stages of the ENSO cycle: For the moment where Nino3.4 is increasing and passes through zero (a,d,g), three (for EEOF2,3 and 4,5) or two (EEOF8,9) months later (b,e,h), and for the moment where Nino3.4 is maximal (c,f,i). Note that the colour scale is not the same for all plots.*

not show a pronounced horseshoe pattern either, but warm anomaly centred at about 190°E, i.e. 20° further west than for our EEOF8,9.

EEOF2,3 and EEOF4,5 represent EP El Niños, of which the former shows eastward initial growth (EPe), and the former westward growth (EPw). All modes are 'Indo-Pacific ENSO modes'; there are no significant pure Pacific or pure Indian Ocean modes.

2.3.2 ENSO types and the Seychelles Dome

In this subsection a composite analysis is used to investigate whether the ENSO types found in the MSSA - CP, EPe and EPw - interact in a different way with the Seychelles Dome.

We introduce the shorthand notation $I(m) > \sigma$ to denote that the anomaly of index I in the set of calendar months m for some selected years is larger than the standard deviation σ of I in m over all available years.

The El Niños (defined as winters in year 1/2 wherein $Nino3.4(Nov(1) - Feb(2) > 0.9\sigma)$ are split into three categories:

- CP Niños: $EMI(Nov(1) - Feb(2)) > 1.2\sigma$ (1968/69, 1994/95, 2009/10).

- EPw Niños: Not CP and in addition: $Nino12(April(1) - Sept(1)) > 1\sigma$ (1957/58, 1965/66, 1972/73 and 1997/98)

- EPe Niños: Not CP and not EPw (1982/83, 1986/87, 1991/92 and 2002/03)

The exact values of the thresholds were chosen such as to generate roughly equally large groups. Note that our distinction between EPe and EPw is concerned with the initial stages of the event (as opposed to Santoso et al. (2013)). EPw events show a warm anomaly in the east Pacific during spring and summer(1) (Fig 2.7d) which is significantly different from zero (95% confidence) and from the other types (90% confidence; see also Fig 2.7e,f). In Jan(2), there is no significant difference between EPe and EPw events, but between CP and EP events (Fig 2.8i): CP events are centred more in the central Pacific and extend less far east. So sorting the El Niños into CP, EPe and EPw events is sensible. It should be noted that the sorting into EPe and CP events is quite sensitive to small changes in the criteria (i.e. events easily change between these groups), while the distinction between EPw events and others, which can be made using Nino12(Apr(1)-Sep(1)) only, is more robust.

EPw events are preceded by a cool Indian Ocean anomaly in July-October(0) (Fig 2.7a) which is significantly different from zero (95% confidence) and is particularly strong in and to the southeast of the Seychelles Dome. EPe events are also preceded by a slight cool Indian Ocean anomaly, but it is not significant (Fig 2.7b). CP events are preceded by a significant warm anomaly around $70°E$ and cool anomalies to the east and west thereof (Fig 2.7c). The cool anomaly around the Seychelles Dome for EPw events is significantly stronger than for EPe and CP events (90% confidence). It is also significantly stronger than for the union of EPe and CP events, so the result that EPw events are preceded by the coolest Seychelles Dome is sensible despite the fact that the distinction between CP and EPe is not very robust. Compared to the union of EPe and CP events, EPw events are preceded by significantly lower (more negative) values of SDIex (90% confidence in Jul-Oct, 95% in Aug-Sep), a lower IODwest (90% in Sep-Nov, 95% in Sep), IOBwest (90% in Aug-Dec, 95% Sep-Nov) and IOB (90% in Aug-Dec, 95% Sept-Oct) and IOD (> 90% in Juli, Sep, Oct, 95% Juli, Sep). Fig 2.9 illustrates that all EPw El Niños are preceded by an autumn(0) SDIex below -0.9σ, while this is only the case for one EPe and no CP event.
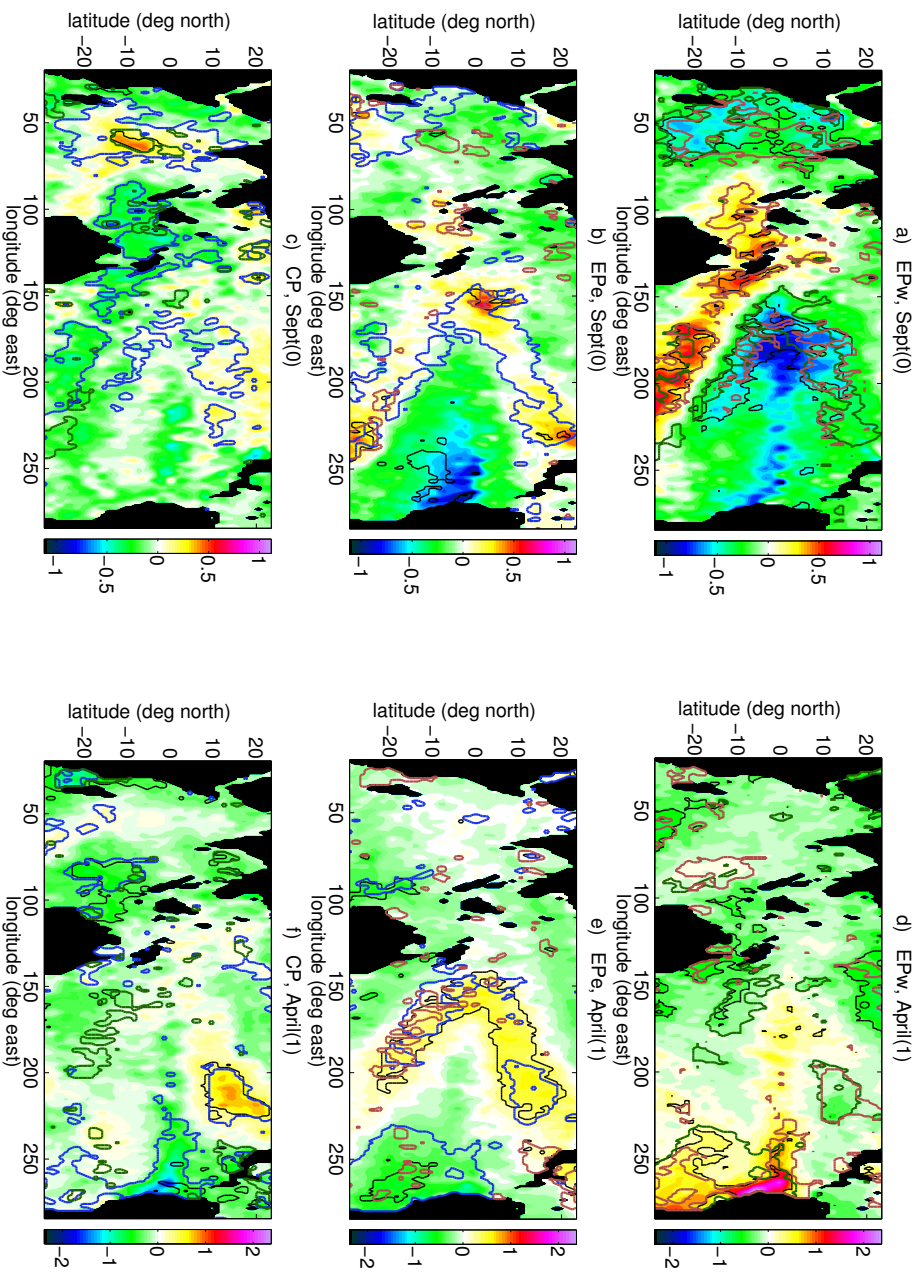
Figure 2.7: *Composites of the SST field in September of year 0 (left) and April of year 1 (right) for EPw (a,d), EPe (b,e) and CP (c,f) El Niños. The thin solid black line denotes the 95% confidence level (two-tailed) of the corresponding SST field against zero. The thicker red (blue, green) line marks regions where the SST is different from the CP (EPw, EPe) case at 90% confidence. This figure is continued in Fig. 2.8.*
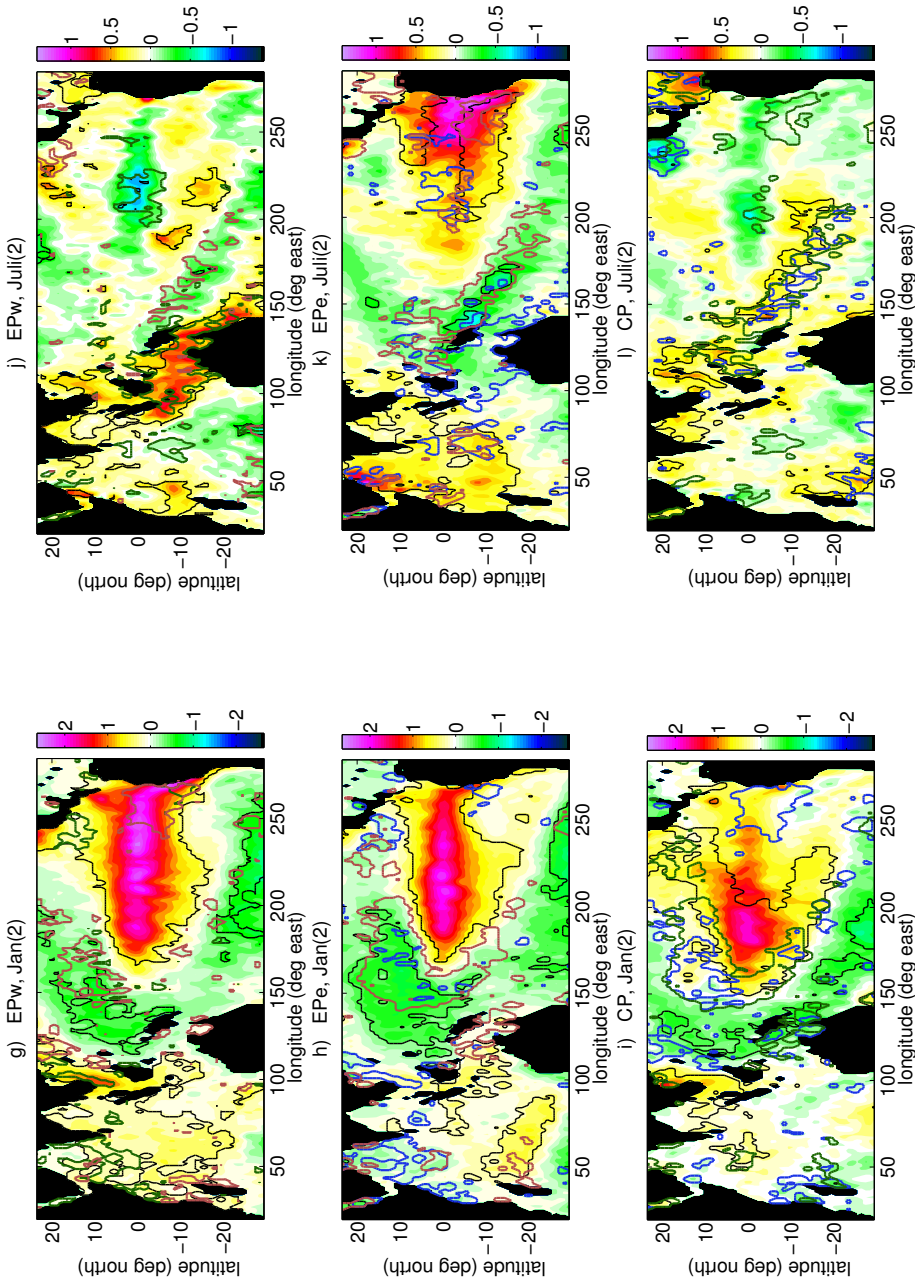
Figure 2.8: *This figure is a continuation from Fig. 2.7. Composites of the SST field in January (left) and July (right) of year 2 for EPw (g,j), EPe (h,k) and CP (i,l) El Niños. The thin solid black line denotes the 95% confidence level (two-tailed) of the corresponding SST field against zero. The thicker red (blue, green) line marks regions where the SST is different from the CP (EPw, EPe) case at 90% confidence.*
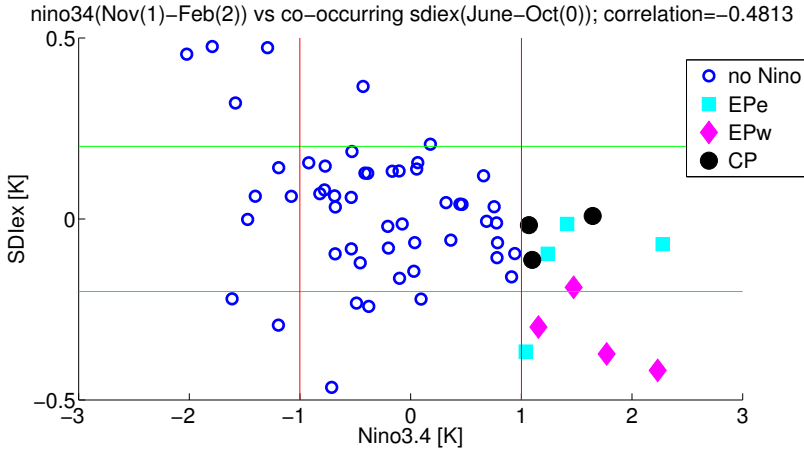
Figure 2.9: *Scatter plot of SDIex(Aug-Nov(year 0)) vs Nino3.4 (Nov(1)-Feb(2)). The El Niño events are marked according to their class as EPe (light blue square), EPw (pink diamond) or CP (black circle). The classification is performed as in section 2.3.2. La Niñas are not marked as they cannot properly be categorised. The horizontal green (vertical red) lines are at $\pm 1\sigma(SDIex)$ ($\pm 1\sigma(Nino3.4)$).*

For La Niñas, no criterion could be found that divides the events into a CP and EP type which differ significantly (90% confidence). When dividing the La Niñas (i.e. $Nino3.4(Nov(1) - Feb(2)) < -1\sigma$) into events with or without an early cooling against the Peruvian coast (threshold: $Nino12(Apr - Sept(1)) < -0.75\sigma$), the two groups hardly differ (90% confidence is reached in March-July(1); for El Niño, the confidence is 98% in April-Sept(1)). No significant differences in the preceding Indian Ocean indices can be detected. Note that the subdivision into westwards and eastward growing La Niñas can be expected to be problematic because 1) La Niñas typically have a relatively weak signal in Nino1+2 and 2) often 2-3 La Niñas occur in a row, so it is hard to distinguish whether a signal in spring/summer belongs to the previous of following event. The result that La Niñas are hard to classify is in line with Kug and Ham (2011). Wiedermann et al. (2016) attempt to classify CP and EP La Niñas by means of an abstract network-based climate index (which performs well at distinguishing CP and EP El Niños), but January SST composites of their 'EP' La Niñas look in fact more CP-like than their 'CP' La Niña events (not shown).

All El Niño types are followed by a positive anomaly in the IOB (95% confidence) in spring(2), so they all cause basin wide warming (not shown); the difference between the ENSO types is not significant. In case of the EP El Niños, the Indian Ocean remains warm until late summer(2), with a maximum at the Seychelles Dome (Fig 2.8j-l). So all ENSO types show interaction with the Indian Ocean at least via the link between ENSO and the following IOB, hence it is reasonable that in the MSSA all significant oscillations (not only the EPw one) have a signal in the Indian Ocean.

However, a cool west Indian Ocean event seems to favour EPw El Niños while for La Niñas, a classification into EPe, EPw and CP events is not useful. Mechanisms by which the west Indian Ocean can influence ENSO will be discussed in the next section.

2.4 Evaluation of Mechanisms

The results of the previous section suggest that the Indian Ocean and the Pacific ENSO signal are strongly linked, which may be due to mutual influence. Since much research has been done on the influence of ENSO on the Seychelles Dome (section 4.1 of Schott et al., 2009; Xie et al., 2002), we will focus here on influences of the Seychelles Dome onto ENSO. As we have seen in section 2.3.1, for all significant MSSA modes during and after a La Niña or cool Seychelles Dome event, zonal winds converge over Indonesia, while later on, westerly winds propagate from the Indian Ocean to the Pacific, hinting at an 'atmospheric bridge' mechanism (section 2.4.1). In addition, the burstiness was found to have a positive (negative) anomaly prior to the onset of El Niño (La Niña). These changes in wind variability might be influenced by the Indian Ocean through a 'state-dependent noise' mechanism (section 2.4.2).

2.4.1 The atmospheric bridge

The concept of influence of the Indian Ocean on the Pacific transmitted by large-scale atmospheric processes ('atmospheric bridge') is more than a decade old (Clarke, 2003; Annamalai et al., 2005; Chen and Caine, 2008) and has been thought to arise from the IOD (Izumo et al., 2010), the IOB (Santoso et al., 2012), or a combination of both (Izumo et al., 2015). Nevertheless it seems useful to investigate further the link between Seychelles Dome and ENSO, because our correlation analysis in section 2.2 showed that the west Indian Ocean contains more information on ENSO than the east Indian Ocean, and in order to link west Indian Ocean influence to different ENSO types.

In order to identify possible large-scale mechanisms specifically related to the west Indian Ocean, we made composites of SST and zonal wind for the five years between 1948 and 2010 with the strongest negative SDIex anomaly in JJASO(0). The selected 'years 0' are 1964, 1971, 1984, 1985, 1996. The results in Fig. 2.11 are consistent with the MSSA results discussed above, but performing this separate composite analysis allows us to check significance of some relations suggested by the MSSA technique. Fig. 2.11a shows that in July of year 0, the main part of the Indian Ocean is significantly cooler than normal, with the largest deviation of $0.8K$ in the Seychelles Dome region. In the equatorial Pacific, remnants of a previous La Niña can be seen, surrounded by warmer anomalies (the 'horseshoe pattern', (Wang et al, 1999)), especially in the southwest Pacific under the south Pacific Convergence Zone. From March to October, the wind to the west of Indonesia is westerly, while to the east of Indonesia, above the west Pacific, it is easterly (Fig. 2.11b).

Unless these easterlies are caused locally in the Pacific (e.g. by the decaying La Niña; this will be tested below), this result seems contradictory, because to the east of a cool anomaly westerly winds should be expected (Gill, 1980), as illustrated in Fig. 2.10a. However, we hypothesise that a non-linear convection feedback above Indonesia may overcome the Gill response over the Pacific: The weak initial uplift generated over Indonesia by the Gill response might be amplified by vigorous convection and latent heat release, since the air around Indonesia is very moist and warm. The latent heat release might trigger further uplift and surface convergence, which, if strong enough, would lead to an inflow (easterly winds) from the Pacific. In order to check whether the easterly wind anomaly is related to the state of the Seychelles Dome or caused by the La Niña conditions in the Pacific, we compute the wind field associated to the current state of ENSO (obtained by regressing the zonal wind to Nino3.4) and subtract this ENSO-induced wind from the composites. The remaining wind $U_r(\vec{x}, m)$ at a position $\vec{x}$ in month m for a composite
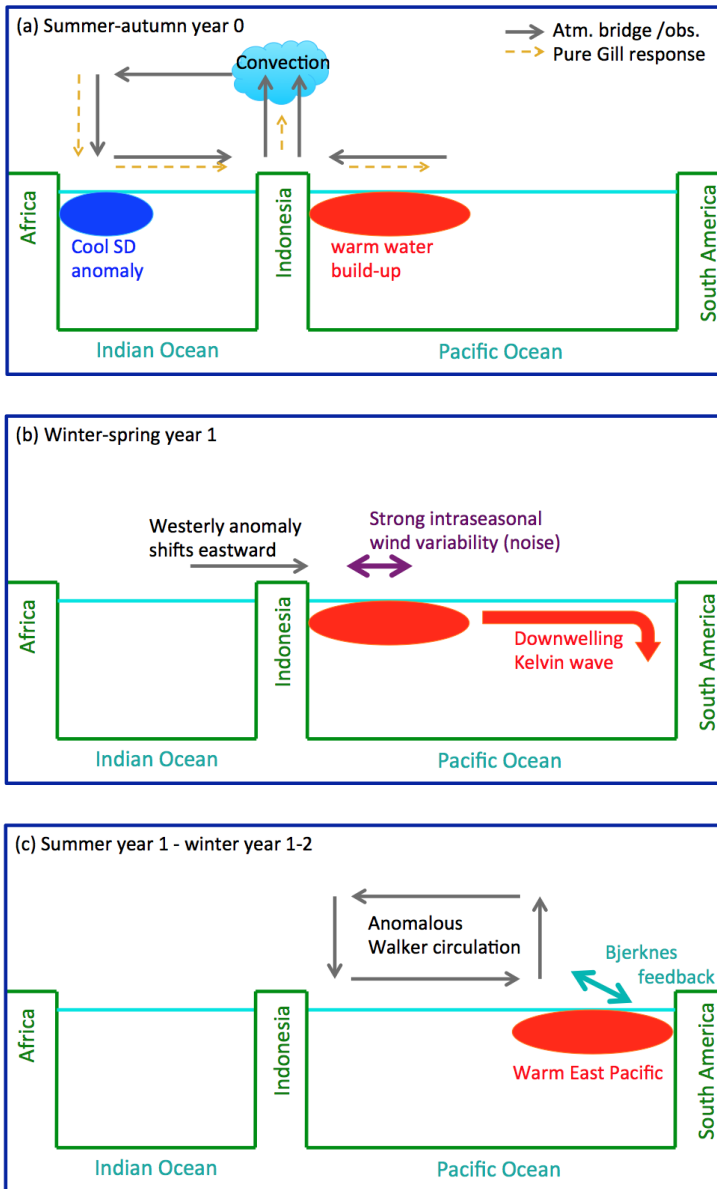
Figure 2.10: *The combined atmospheric bridge and state-dependent noise mechanism by which a cool Seychelles Dome may affect El Niño development. In summer/autumn of year 0, the Seychelles Dome is cool (a). In absence of convection effects above Indonesia, one would expect a pure Gill response, i.e. subsidence over the Seychelles Dome, and westerly winds and a weak uplift to the east of the cool anomaly (orange dashed arrows). However, observed winds are more consistent with the 'atmospheric bridge mechanism' (grey arrows) in which the uplift above Indonesia is enhanced by convection, leading to surface convergence and thus easterlies over the West Pacific. These easterlies create a strong warm pool in the west Pacific. During winter - spring of year 1 (b), anomalous westerlies propagate towards the west Pacific, and the zonal wind variability in the west Pacific is anomalously high, so intraseasonal spells of westerly winds can initiate a downwelling Kelvin wave early in the year. This leads to a strong warming in the east Pacific and the development of a westward growing east Pacific El Niño during the next summer/autumn (c).*
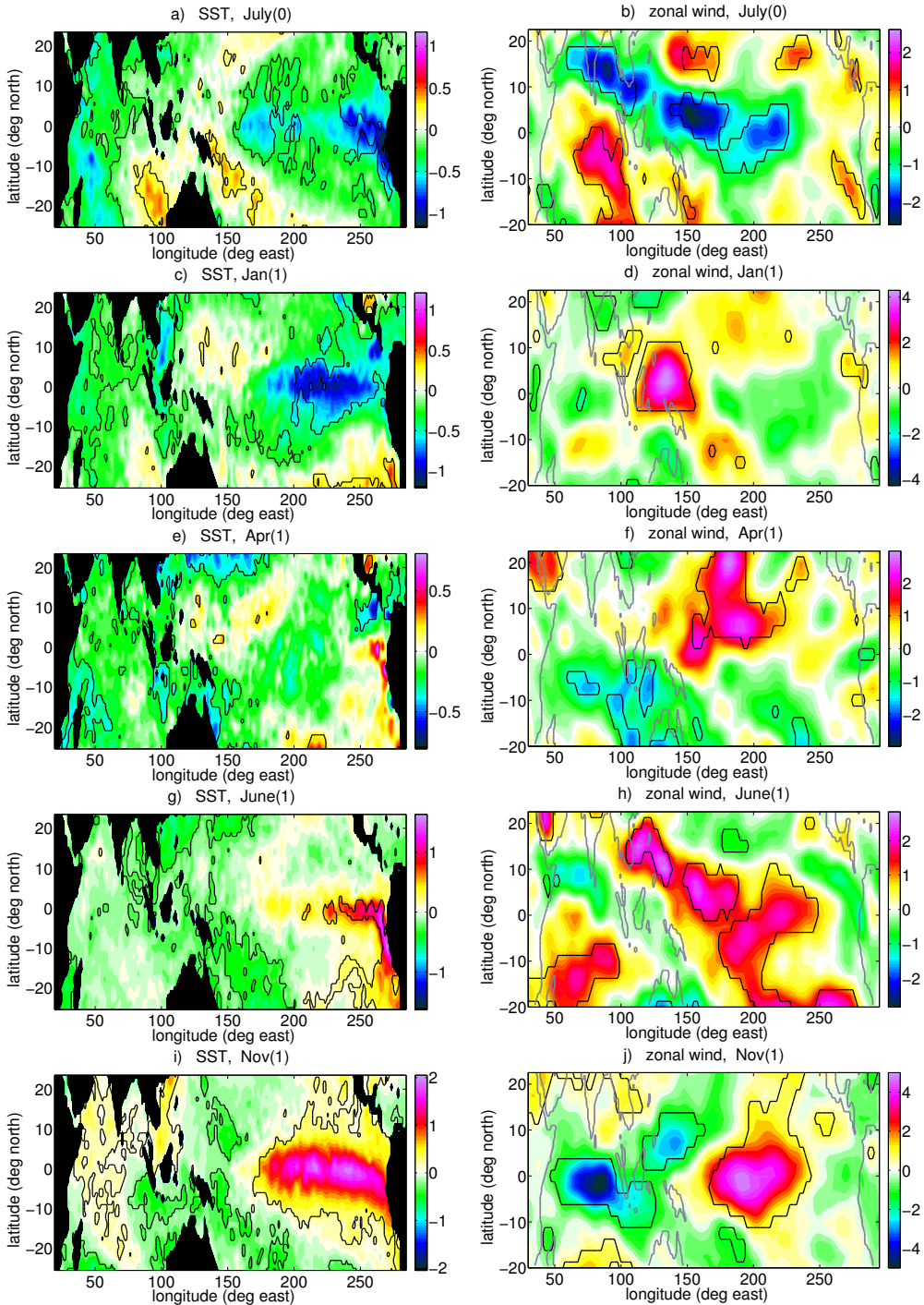
Figure 2.11: *Composites of the SST (in K, left) and zonal wind (in m/s, right) following the five coolest Seychelles Dome events (defined for June-October of year 0). Plots are given for the months: July of year 0 (a,b), January 1 (c,d), April 1 (e,f), June 1 (g,h), and November 1 (i,j). Black lines mark the 90% confidence limits. Note that the colour scale differs for each panel.*
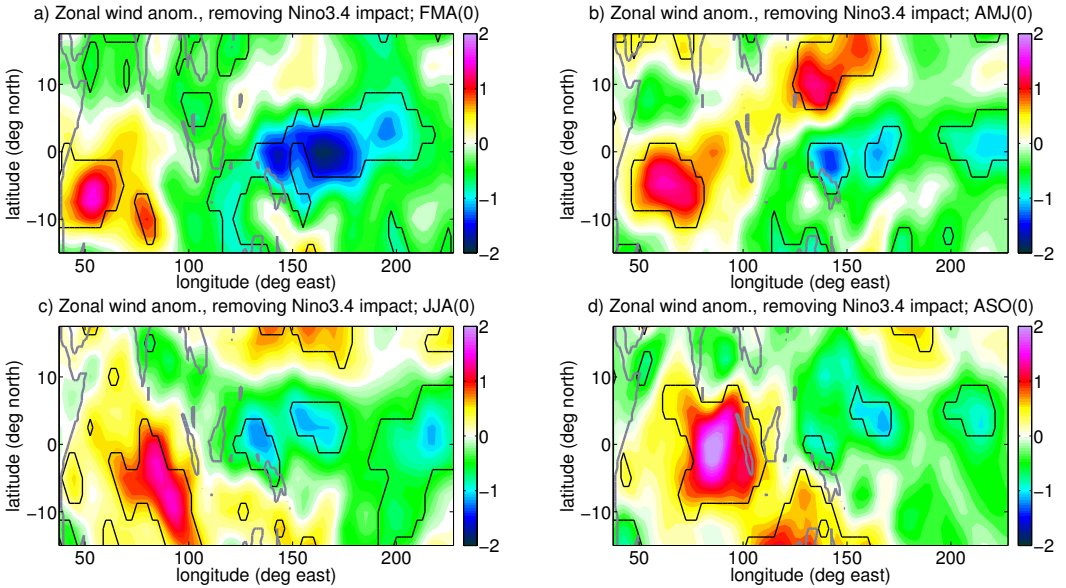
Figure 2.12: *Composites of the zonal wind (in m/s) in the five coolest Seychelles Dome events (defined for June-October of year 0) minus the zonal wind associated with the ongoing La Niña, i.e. $U_r(\vec{x}, m)$ as defined in the text. A 3 months running mean has been applied to the zonal wind. The plots show the situation in a) FMA, b) AMJ, c) JJA and d) ASO of year 0. Black lines mark the 80% confidence limits (two-tailed).*

over a set Y of N_Y years is thus obtained by

$$U_r(\vec{x}, m, Y) = \frac{1}{N_Y} \sum_{i \in Y} U(\vec{x}, m, i) - A(\vec{x}, m) Nino3.4(m, i), \qquad (2.5)$$

where $U(\vec{x}, m, i)$ is the zonal wind at $\vec{x}$ in month m and year i, and $A(\vec{x}, m)$ the regression coefficient in $\vec{x}$ and m. A running mean over 3 months was applied to the zonal wind prior to computing A and U_r, such as to obtain a clearer signal. Throughout the first 8 months of year 0, the easterlies in the equatorial west to central Pacific are stronger than expected based on the Nino3.4 values, i.e. $U_r < 0$ (Fig. 2.12). The magnitude of U_r is similar to that of $A \times$ Nino3.4. However, significance is not very high with only 80% confidence (two-tailed). In March, May and July, 90% is reached, but in June confidence drops below 80%. These results are in line with the convective 'atmospheric bridge' mechanism, but not with a very high confidence.

Easterly winds in the west Pacific are thought to influence next year's El Niño by increasing the Pacific Warm Water Volume (Izumo et al., 2010), which in turn is a prerequisite for an El Niño event (Jin, 1997a; Meinen and McPhaden, 2000). We find that the Warm Water Volume (WWV) is indeed negatively correlated to previous SDIex. This correlation is strongest (-0.73) for SDIex in November and WWV around 5 months later, but values below -0.45 (significant at 98% confidence according to a two-tailed Student's t-test) are found throughout the year. However, the influence of ENSO on the WWV is also strong. Therefore we test the significance of the lagged correlation between SDIex and WWV by using the common cause test of section 2.2, with Nino3.4 as the common cause. It turns out that the correlation between SDIex (Aug-Nov) and WWV (around

5 months later) is significantly stronger than expected from ENSO's influence on SDIex and WWV (95% confidence; figure not shown). Since the WWV acts to some extent as an integrated (and thus probably less noisy) measure of the zonal winds in the previous months, this result supports the notion of an easterly wind response to a cool Seychelles Dome. - Using IODwest instead of SDIex gives very similar results. IODeast never gives correlations significant at 90% confidence. The full IOD yields significant correlations (95% confidence) slightly earlier than IODwest and SDIex, namely for IOD in June-Oct. This suggests that a cool west Indian Ocean is indeed followed by an enhanced WWV after a few months. This result cannot be explained by the IOB-based mechanism proposed by Santoso et al. (2012) and Izumo et al. (2015), which only involves westerlies over the Pacific.

In October, the easterly anomaly over the west Pacific starts moving southeastwards and decaying (not shown), while the westerlies above the Indian Ocean shift eastwards and reach the west Pacific in Dec(year 0) - Jan (year 1) (see Fig. 2.11d). Meanwhile, the 'horseshoe' warm anomaly in the southwest Pacific has spread eastwards towards the end of year 0 and then moves northwards along the South American coast, weakening (Fig. 2.11c,e). In April of year 1, the water near the Peruvian coast starts warming (Fig. 2.11e), reaching significant values in May; in June the anomaly starts growing westward along the equator (Fig. 2.11g). The westerly winds move to the central Pacific and increase along with the SST anomaly (Fig. 2.11f,h,j), hinting at a Bjerknes feedback. The eastward propagation of the wind anomalies in winter/spring(year 1) and the following increase is consistent with the MSSA results.

Despite the fact that this eastward propagation of winds has long been known (Barnett, 1984; Clarke, 2003), to our knowledge the underlying mechanism is still uncertain. Gill (1983) and Barnett et al. (1991) suggest mechanisms by which coupled SST-wind anomalies can propagate eastwards on the Pacific, but they depend on the local background state. Latif and Barnett (1995) conclude that the eastward propagation on global scales around the tropics is coincidental, while White and Cayan (2000) describe a 'global ENSO wave' possibly based on SST- atmosphere feedbacks. Another candidate might be a transition from IOD to IOB: A negative IOD causes westerlies over the Indian Ocean, while a subsequent IOB can cause westerlies over the west Pacific, as shown by Izumo et al. (2015); together these effects can explain the propagation of the westerlies from the Indian to west Pacific Ocean. On the other hand, Fig. 2.2e-g suggest that the IOD-IOB transition mostly occurs in ENSO years, and Fig. 2.11d shows strong westerlies over the far west Pacific even though there is no strong IOB signature in Fig. 2.11c-e, so the IOD-IOB transition may not be the whole explanation for the propagation of winds.

The processes described above may favour a westwards moving EP El Niño. First, EP El Niños need a large WWV to develop (Meinen and McPhaden, 2000), while Kao and Yu (2009) suggest that CP events have a smaller vertical extent and are more dominated by winds and horizontal SST advection than by thermocline processes. Yu and Kim (2010) find that CP events can take place in a recharged, neutral or discharged WWV state. Hence an increase in WWV associated with a cool Seychelles Dome would favour EP events, but should not influence CP events. Second, eastward growing and CP El Niños are initiated later in the year than westward growing El Niños. Harrison and Schopf (1984) attributed the eastward propagation of the 1982/83 El Niño to the fact that westerly wind forcing occurred in boreal summer (not spring) of 1982, i.e. at a time when the climatological zonal SST gradient in the central Pacific is strongly negative and hence anomalous eastward currents can cause strong zonal advection in the central Pacific. The westward growing El Niño of 1997-98, for which thermocline depth and

upwelling played a vital role (Vialard et al., 2001), started in spring. In the composites in Fig. 2.11d it can be seen that a westerly anomaly reaches the west Pacific as early as January (year 1), where it can induce downwelling Kelvin waves leading to a warming at the Peruvian coast in spring (Fig. 2.11e).

A similar analysis for the five warmest Seychelles Dome years in June-Oct(year 0), i.e. in the years 1961, 1972, 1983, 1987 and 1998, yields a significant La Niña signal in winter(1/2) with 95% confidence (the El Niño signal following a cool Seychelles Dome also reaches 95% confidence). The cold anomaly starts being significant in April (1) and extends from Peru to 160°E without initial westward growth. It is not possible to detect westerly winds in the west Pacific in summer/autumn(0) which are significantly stronger than what one would expect from the Nino3.4 signal at the same time.

Since the observational evidence for the atmospheric bridge mechanism is not completely satisfying, the effect will be further investigated in chapter 5 by using an intermediate complexity model, and in chapter 6 by using output from a GCM.

2.4.2 State-dependent noise
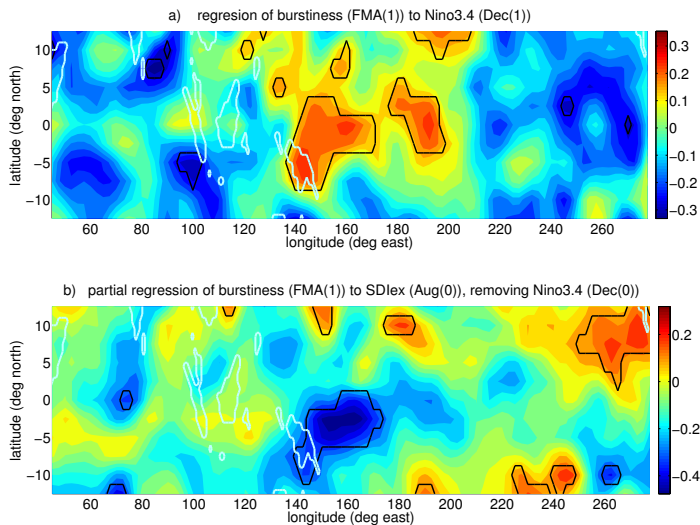
Figure 2.13: *Regressions between the burstiness field and various SST-based indices. Indices and local burstiness time series are normalised to unit standard deviation. Thick black lines denote the 95% confidence level. Plots show: (a) regression of Nino3.4 in December to the burstiness in previous FMA; (b) partial regression of burstiness in FMA onto SDIex in previous July, removing Nino3.4 in previous December.*

The Indian Ocean might also influence ENSO by altering the characteristics of short-scale atmospheric processes above the Pacific. By short-scale 'noise' we mean processes of time scales much smaller than that of ENSO itself, but long enough to influence ENSO (e.g. by triggering Kelvin waves), i.e. roughly of intraseasonal time scales. In the MSSA we have seen that burstiness anomalies propagate from the Indian Ocean into the Pacific, with positive anomalies in the west Pacific during the onset of El Niño.

In order to investigate possible effects of the Seychelles Dome or IOD on the burstiness, we regress the burstiness in February-April (FMA) onto the SDIex in previous
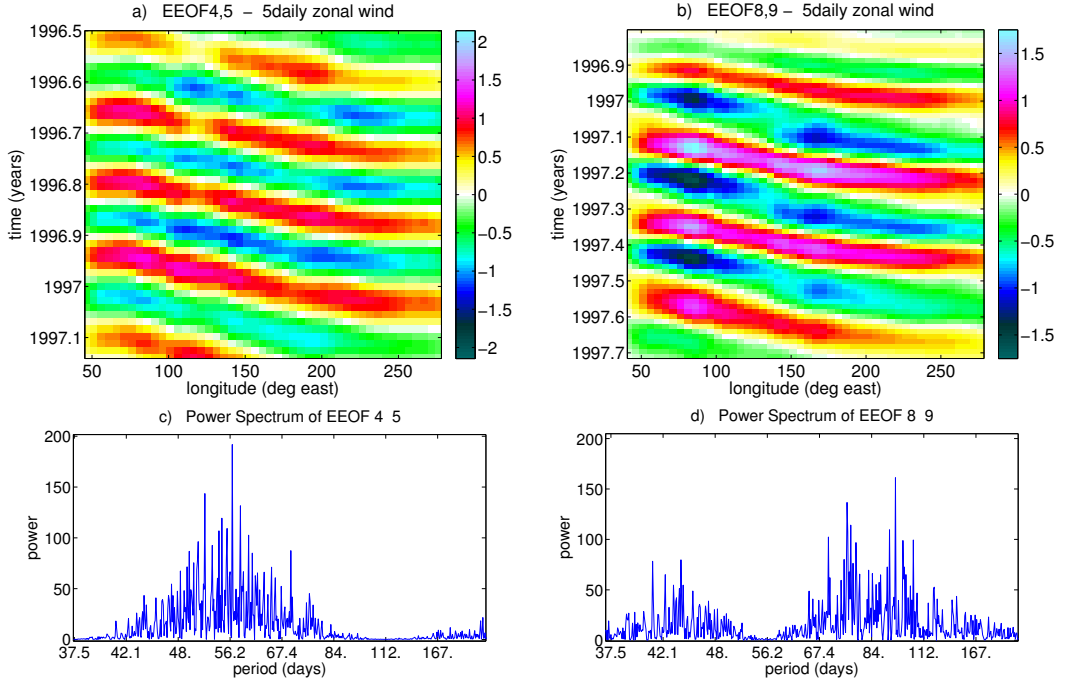
Figure 2.14: *(a-b) Hovmöller plots of (sections of) the reconstructed time series of EEOF4,5 (a) and EEOF8,9 (b) of the 5-daily zonal wind, averaged over the latitude band $5°N-5°S$. (c-d) Power spectra of the PCs belonging to EEOF4,5 (c) and EEOF8,9 (d).*

summer/autumn. Direct influence by the previous ENSO is removed by taking a bilinear regression:

$$\tilde{B}(\vec{x}, t_1) = a(\vec{x})\tilde{S}(t_2) + b(\vec{x})\tilde{N}(t_3) + R, \tag{2.6}$$

where $\tilde{B}(\vec{x}, t_1)$ is the normalised burstiness in location $\vec{x}$ and time t_1 (FMA of year 1), $\tilde{S}(t_2)$ is the normalised SDIex at time t_2 (within June-Nov(0)) and $\tilde{N}$ is the normalised Nino3.4 index at time t_3 (Dec(0)). Normalisation is performed point-wise by dividing by the standard deviation, e.g. $\tilde{B}(\vec{x}, t_1) = B(\vec{x}, t_1)/\sigma(B(\vec{x}))$. The coefficients a and b are local regression coefficients and R the residual; due to the normalisation, a and b are in $[-1, 1]$. In order to investigate the influence of the burstiness on ENSO, we also regressed Nino3.4 in Sep(1)-Jan(2) to the previous FMA burstiness field.

Fig. 2.13a shows that El Niño in December is preceded by a positive burstiness anomaly around the equator at $140 - 200°E$ in FMA. On the other hand, the regression of the burstiness onto SDIex in the previous July (Fig. 2.13b) is negative in a region around $2.5°S, 140°E$, overlapping with the region of positive regression to Nino3.4. These results are consistent with the MSSA of section 2.3.1 and robust against shifting lags by 1-2 months or using JFM or MAM burstiness. They suggest a possible causal link between a cool Seychelles Dome and El Niño via enhanced burstiness.

In order to investigate the relation between Seychelles Dome, intraseasonal wester-lies and ENSO further, and to understand the mechanisms underlying the burstiness, an MSSA (see section 2.1.2) of the 5-daily zonal wind field between 20°N and 20°S is performed. In the pre-filtering step the first 50 EOFs are included, accounting for 80% of
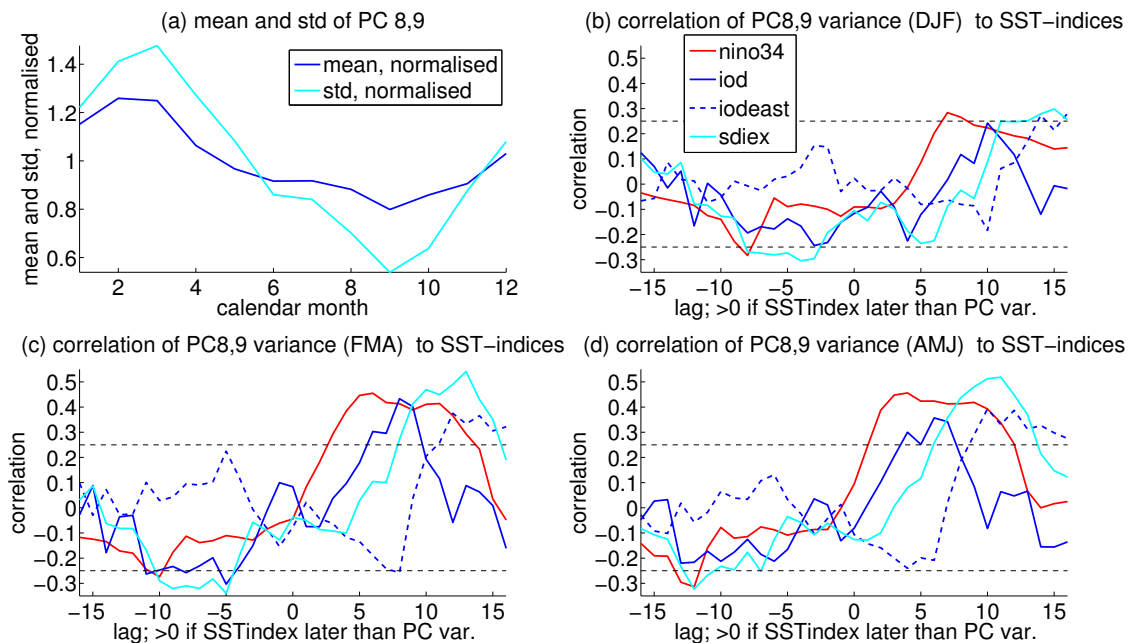
Figure 2.15: *(a) Seasonal cycle of the running variance of PC 8 and 9. The dark blue line is the mean over all years of the running variance in a 3-months block centred at a certain calendar month; the bright blue line is the standard deviation over all years. (b)-(d): correlation of PC8+9 running variances to Nino3.4 (red), IOD (dark blue, solid), IODeast (dark blue, dashed), and SDIex (light blue). The PC running variance is given in months DJF (b), FMA (c), and AMJ (d). The black dashed horizontal lines indicate the 95% confidence limits.*

the variance. The length of the lag window is 120 days. The results are robust against a 20% variation in the number of EOFs included or the length of the time window.

We obtain two significant oscillatory pairs which both span the Indian Ocean and PO: EEOF4,5 and EEOF 8,9. The Hovmöller plots in Fig. 2.14a,b show that the phase velocity in the Indian Ocean and west Pacific is about 60 degrees/15days $\approx$ 5m/s and increases in the central/east Pacific. The PC's of the first pair have a period of about 53 days (Fig. 2.14c), while those of the second pair (Fig. 2.14d) have a dominant period of about 80 days with a relatively strong first harmonic (40 days). About 70% of the power of this mode lies at periods longer than 55 days, the local minimum of the power spectrum. Both the dominant periods observed and the behaviour of the phase velocity are characteristic for the Madden-Julian Oscillation (MJO).

The relationship between the two oscillating pairs and ENSO/IO variability is checked by correlating the variance of the corresponding PC's over blocks of 3 months (henceforth referred to as the pair's 'running variance') to Nino3.4, SDIex, and IOD. Correlations between the running variance and monthly SST-based indices are significant at 95% confidence when outside $\approx \pm 0.25$, as was checked using the non-parametric technique from section 2.1.1. The running variance of EEOF4,5 has hardly a significant correlation to ENSO, IOD or SDIex (not shown). However, there is a significant negative correlation between the running variance of EEOF8,9 in OND-AMJ, and SDIex in previous summer-autumn (lags -5 to -10 months) which is strongest (-0.34) for the running variance in JFM-FMA (Fig. 2.15b-d). In addition, the running variance of the PC's in DJF-MJJ is positively correlated to the following autumn/winter Nino3.4 (lags around +3 to +12 months), with values above 0.45 being reached in FMA-AMJ. Correlations between running variance in FMA-AMJ and the following SDIex (i.e. at lags around 12 months) are significantly positive, too. Applying the common cause test from section 2.2 confirms that the negative correlation between SDIex in July-October and EEOF8,9 running variance in the following DJF-AMJ is significant (90% confidence) against the null-hypothesis that the correlation is caused by a possible influence of ENSO on SDIex and the running variance of EEOF8,9 (not shown). Using IOD instead of SDIex yields slightly weaker correlations which are not significant at 90% confidence in the 'common cause test'. While the western pole of the IOD yields results very similar to those using SDIex (not shown), the eastern pole never yields significant correlations at negative lags.

These findings suggest that modifications of long-period MJO variability by the west Indian Ocean might at least partly explain the interannual variability in the burstiness in boreal winter-spring (the time where the interannual variability of mode EEOF8-9 variance is strongest, see Fig. 2.15a). This result is in line with Wilson et al. (2013), who demonstrated from observations that the MJO is slightly strengthened (considerably weakened) in negative (positive) IOD years and link these observations to increased air moisture content, wind convergence and reduced sea level pressure above Indonesia in years following a negative IOD. Izumo et al. (2009) find that the low frequency (period > 55days) part of boreal winter MJO signal is weakened after a positive IOD, possibly due to the IOD's influence on the mean state of the atmosphere or enhanced sea-atmosphere coupling in the Seychelles Dome region during negative IOD (i.e. cool SD/shallow thermocline). Intraseasonal westerlies such as provided by the MJO can generate anomalous eastward currents leading to zonal SST advection, and generate intraseasonal downwelling Kelvin waves which help lowering the east Pacific thermocline (Zhang, 2005; Kessler et al, 1995; McPhaden et al., 2006).

Our analysis not only confirms earlier results with different techniques (MSSA, common cause test), but suggests that one mode - the long-period MJO mode EEOF8,9

- provides a link between Seychelles Dome in summer-autumn(year 0) and El Niño in autumn-winter(year 1). In addition, we find that it is the west Indian Ocean, rather than the east, which influences the MJO. Finally we remark that the negative correlation between EEOF8,9 running variance and the previous SDIex peaks earlier than the positive correlation between running variance and the later Nino3.4, though there is some overlap for running variance around FMA. So the Seychelles Dome-induced impact of the MJO on ENSO occurs early during the time where ENSO is sensitive to such a forcing. As discussed in section 2.4.1, such an early westerly wind forcing is likely to stimulate a westward-growing EP El Niño.

2.5   Summary and Conclusions

A Multi-Channel Singular Spectrum Analysis (MSSA) of SST, zonal wind and burstiness (intraseasonal wind variability) of the tropical oceans yields three significant oscillatory modes, all of which show an ENSO signal in the Pacific and a strong SST variability in the west Indian Ocean, but only weak signals in the Atlantic. No pure Pacific or Indian Ocean mode is found, suggesting that the Pacific ENSO cycle and the Indian Ocean closely interact.

The Pacific ENSO signals in the two MSSA modes with periods of 4.9 and 3.6 years (EEOF2,3 and EEOF4,5) are strongest in the east Pacific (Nino3-Nino1+2 region). In the former mode the SST anomaly starts in the central Pacific and spreads eastward ('EPe event'), while in the latter, the anomaly grows from the South American coast to the west ('EPw'). The third mode (EEOF8,9) has a period of 2.5 years and the ENSO signal is strongest around 150°W and shows no zonal propagation. This non-propagating behaviour and a maximum away from the South American coast are properties of CP El Niños, though a typical CP El Niño peaks still further west. In all significant modes, El Niño (La Niña) is followed by a warm (cool) Seychelles Dome 2-4 months later, which reflects the influence of ENSO onto the west Indian Ocean (Xie et al., 2002), but might also feed back on ENSO.

In particular, the SDIex in summer-autumn is negatively correlated to Nino3.4 $\approx$ 1.5years later. This correlation is significant against the null hypothesis that it is caused by ENSO's influence on the Seychelles Dome and ENSO's cyclicity. The various ENSO types are differently influenced by the Seychelles Dome. A composite analysis shows that EPw El Niños are preceded by cool west Indian Ocean anomalies which are significantly stronger than for other El Niño types. La Niñas cannot be sorted into EPe, EPw and CP events.

Based on these results, two mechanisms were investigated by which the Seychelles Dome may influence ENSO (Fig. 2.10). In the 'atmospheric bridge' mechanism, subsidence over a cool Seychelles Dome leads to westerlies over the Indian Ocean and enhanced convection above Indonesia, causing easterlies (rather than the westerlies one would expect as part of the Gill response) over the west Pacific. These easterlies favour the build-up of a strong warm pool. While the zonal wind signal, after subtracting the influence of a decaying La Niña, is significant only at 80% confidence, the Seychelles Dome SST in August-November is significantly negatively correlated to the warm Water Volume (WWV) around 5 months later (95% confidence against the null hypothesis that the correlation is caused by ENSO influence on Seychelles Dome and WWV). Since the WWV is to some extent an integrated measure of the zonal wind over the last few months, this result supports the hypothesis that a cool Seychelles Dome might be associated with easterlies over the Pacific. The enhanced warm pool can be activated during the next

spring/summer, when the patch of westerly winds has propagated from the Indian to the Pacific. This propagation may in some cases be explained by a transition from a negative IOD in autumn (causing westerlies over the Indian Ocean) to a negative IOB in spring (causing westerlies over the west Pacific), but since the propagation may occur in absence of a strong IOB signal in spring (Fig. 2.11c-f), additional processes may play a role. The mechanism for this eastward propagation of wind anomalies remains an open issue.

In the 'state-dependent noise' mechanism a cool Seychelles Dome in summer leads to an enhanced wind variability during the next early spring, as was confirmed by regressing FMA (year 1) burstiness onto SDIex in August (year 0). An MSSA over 5-daily zonal wind data suggests that interannual variability in the low-frequency part of the MJO might be a source of the burstiness variation. Intraseasonal wind variability in the west Pacific is known to force intraseasonal Kelvin waves that may induce El Niño development (Kessler et al, 1995; McPhaden et al., 2006).

Both mechanisms favour the development of westward growing EP El Niños. First, because EP El Niños need a sufficient WWV to develop, while CP El Niños do not, and second because both the westerly wind anomaly that propagates into the west Pacific and the enhanced burstiness after a cool Seychelles Dome event in summer-autumn (year 0) reach the west Pacific in late winter to early spring (year 1). At this time of the year, westerly wind forcing is more likely to create SST anomalies in the east Pacific through downwelling Kelvin waves, than advection-induced anomalies in the central Pacific, because the zonal SST gradient in the central Pacific is typically weak in spring. The 'atmospheric bridge' and 'state dependent noise' mechanisms might be interrelated, since large-scale westerlies as found in the west Pacific from spring (year 1) onwards and zonal wind variability might re-enforce each other (Kug et al, 2010).

From observational data it cannot be decided which mechanism is more relevant and in fact also other mechanisms might play a role, such as variability in the Indonesian Throughflow induced by SSH anomalies in the southeast Indian Ocean (Yuan et al., 2011, 2013). Modelling studies are necessary to disentangle cause and consequences, especially concerning influences on the WWV, and investigate important issues such as how the wind anomalies propagate from the Indian Ocean to the Pacific on interannual time scales and how this might influence the burstiness. The hypothesis that a non-linear convection feedback over Indonesia can lead to a reversal of the Gill response will be tested with the aid of an intermediate complexity model in chapter 5.

The results presented here strongly suggest that the interannual variability in the Indian Ocean and Pacific is quite coherent. Although there is no one-to-one relationship between the Seychelles Dome SST variations and ENSO, a better understanding of this connection might provide a valuable additional ingredient for ENSO prediction at longer lead times. For example, it might be worthwhile to take Seychelles Dome or west Indian Ocean SST into account in statistical models, and in dynamic models, a good initialisation and/or data assimilation in this region might help to improve predictions. Finally, long-term changes in the (west) Indian Ocean, such as the recent warming of the Indian Ocean, might potentially affect the properties of ENSO. This will be investigated in chapter 4.
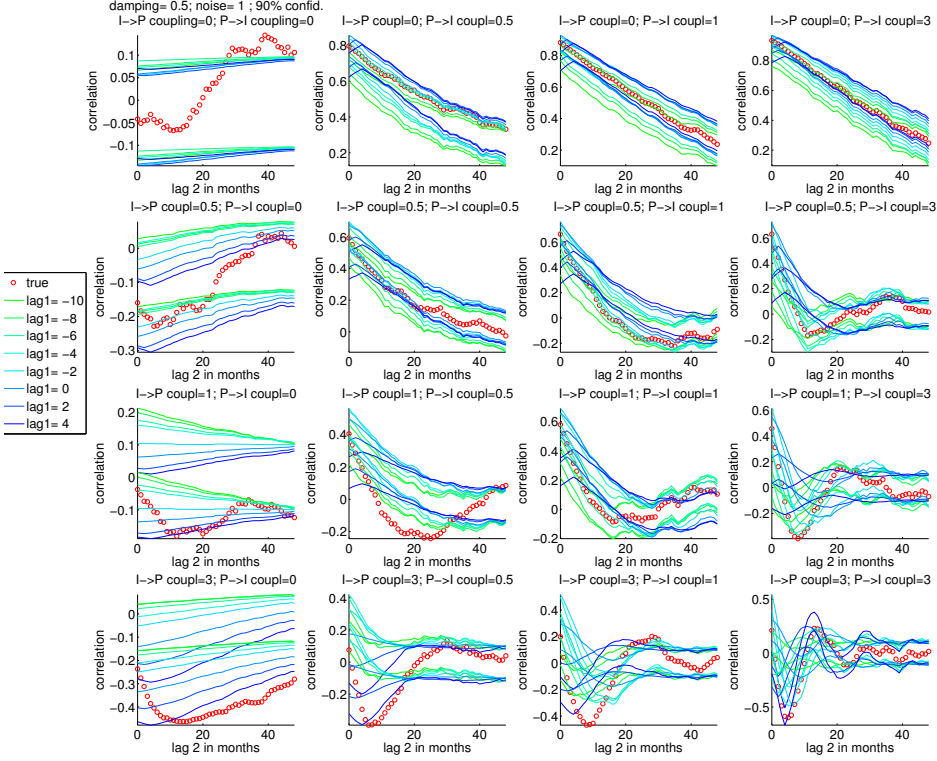
Figure 2.16: *Results of the 'common cause test' for 250 years of toy model data, with $k_{damp} = 0.5$, $k_{noise} = 1.0$. k_{IP} increases from left to right and k_{PI} increases from top to bottom; both range from 0 to 3. Red circles denote the true correlation between T_I and T_P at lag_2 (positive when T_P is later), while green and blue lines denote the regions within which 90% of the surrogate data lies, for various values of lag_1 (in months; negative when the T_P value used as common cause is earlier than T_I.*

Appendix to Chapter 2: Evaluating the common cause test

In order to validate the common cause test, we apply it to data generated by the conceptual recharge oscillator model in Jansen et al. (2009), namely

$$\frac{d}{dt} \begin{pmatrix} T_P \\ h_P \\ T_I \end{pmatrix} = \begin{pmatrix} -2\gamma_P & \omega_0 & c_{PI} \\ -\omega_0 & 0 & c_{h,PI} \\ c_{IP} & 0 & -2\gamma_I \end{pmatrix} \begin{pmatrix} T_P \\ h_P \\ T_I \end{pmatrix} + \begin{pmatrix} \eta_{TP} \\ \eta_{hP} \\ \eta_{TI} \end{pmatrix}$$

where T_P, h_P and T_I are the SST in the (east) Pacific, the Pacific thermocline depth and the Indian Ocean SST, respectively. The parameters are fitted from observations. We generated time series for a model with adapted coefficients,

$$\frac{d}{dt} \begin{pmatrix} T_P \\ h_P \\ T_I \end{pmatrix} = \begin{pmatrix} -2k_{damp}\gamma_P & \omega_0 & k_{PI}c_{PI} \\ -\omega_0 & 0 & k_{PI}c_{h,PI} \\ k_{IP}c_{IP} & 0 & -2k_{damp}\gamma_I \end{pmatrix} \begin{pmatrix} T_P \\ h_P \\ T_I \end{pmatrix} + k_{noise} \begin{pmatrix} \eta_{TP} \\ \eta_{hP} \\ \eta_{TI} \end{pmatrix}$$

where k_{damp} and k_{noise}, the scaling factors controlling damping and noise strength, are $\in \{0.5, 1, 2\}$ and k_{PI} (k_{IP}), controlling the influence on the Pacific (Indian) Ocean exerted by the Indian (Pacific) Ocean, are $\in \{0, 0.3, 0.5, 1, 2, 3\}$. In Fig. 2.16, results are given for $k_{damp} = 0.5$, $k_{noise} = 1$.

For all values of k_{damp}, k_{noise} and k_{IP}, increasing k_{PI} clearly makes the correlations more significant, while increasing k_{IP} has no systematic influence on significance. The passing of the test for some lags with $k_{IP} = k_{PI} = 0$ is an artefact of this particular noise realisation (not shown). This suggests that the test is capable of detecting influence from the Indian Ocean on the Pacific in presence of ENSO cyclicity and ENSO influence on the Indian Ocean.

Chapter 3

The Indo-Pacific Zebiak-Cane model

In order to investigate some aspects of Indo-Pacific interaction further, an intermediate complexity model based on the Zebiak-Cane model (Zebiak and Cane, 1987) will be used. To be precise, the model used in this study is an extension of the fully coupled (i.e. generating its own background state) version of the Zebiak-Cane model by Van der Vaart et al. (2000) and Van der Vaart (1998), which is briefly described in section 3.1. The Zebiak-Cane model includes the tropical Pacific and was designed to model interannual variability associated with ENSO. The Ocean component consists of a linear reduced-gravity model with an embedded Ekman layer in which the Sea Surface Temperature (SST) is defined. The atmosphere is based on the Gill model and consists of one shallow-water layer and reacts instantaneously to SST-induced heating.

In order to study Indo-Pacific interaction in a Zebiak-Cane framework, a natural extension to the model would be to use two separate ocean basins coupled by one overlying atmosphere which can react to the SST in one basin by generating winds felt in the other basin. This model version is described in section 3.2, but it turns out not to work well, as will be explained in section 3.3. Therefore a simplified model version was designed in which the internal dynamics of the Indian Ocean are neglected. Instead, the Indian Ocean SST varies according to prescribed spatial patterns whose variability depends entirely on ENSO (see section 3.4). Based on the findings in chapter 2, we are particularly interested in the effect of nonlinear convection above the Maritime Continent. Therefore in section 3.5 the atmospheric equations are extended by a simple convection scheme. In the sections describing various model versions (3.1, 3.2, 3.4, and 3.5), first an overview over the the physical formulation of the model is given, followed by a subsection about the spatial discretisation intended for readers interested in the technical aspects. Section 3.6 briefly describes the time discretisation, which is the same for all model versions, and gives an overview of the continuation method used to investigate the stability of equilibrium solutions.

3.1   The single-basin model

The following section is a brief summary of the original Pacific-only model; for more details see Van der Vaart et al. (2000) and Van der Vaart (1998).

a)

b)
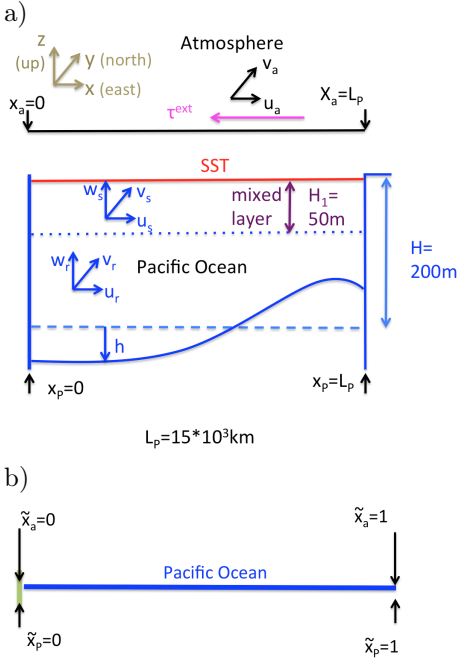
Figure 3.1: *a) Setup of the Pacific-only Zebiak-Cane model. Note that the dimensional meridional coordinate y is the same for the ocean and atmosphere and is zero at the equator. b) Definition of non-dimensional zonal coordinates for the Pacific-only model.*

3.1.1   Physical formulation

A sketch of the original model configuration by Van der Vaart et al. (2000) is given in Fig. 3.1. The meridional coordinate y is zero at the equator. The ocean consists of a shallow water reduced gravity model on an equatorial β-plane. It contains an active upper layer with a zonal velocity u_r and meridional velocity v_r and a deep lower layer at rest, separated by a thermocline at depth $H + h$ where $H = 200m$ is the equilibrium depth. The vertical velocity w_r is determined by mass conservation. The frictional damping is assumed to be linear and the long-wave limit is applied (neglecting the small terms $(\partial_t + \epsilon_o^*)v_r$). The ocean is forced by a wind stress $\tau = (\tau_x, \tau_y)$. This yields the dimensional equations:

$$(\partial_t + \epsilon_o^*)u_r - \beta y v + g' \partial_{x_P} h = \tau_x / \rho H$$
$$\beta y u + g' \partial_y h = 0$$
$$(\partial_t + \epsilon_o^*)h + H(\partial_{x_P} u + \partial_y v) = 0 \qquad (3.1)$$

where $\partial_s f$ is a shorthand for $\partial f / \partial s$. The dimensional model parameters are given in Table 3.1. The effect of meridional wind stress on the shallow water equations has been neglected. At the eastern boundary, at $x_P = L_P$, the zonal velocity is zero. At the western boundary, at $x_P = 0$, this condition cannot be fulfilled in the long wave approximation, hence the mass flux across the boundary is set to zero. The boundary conditions thus become

$$\int_{-\infty}^{\infty} u(0, y, t) dy = 0; \quad u(L_P, y, t) = 0 \quad \forall y.$$

parameter	meaning
$L_P = 1.5 \times 10^7 m$	length Pacific Ocean
$L_I = 0$ or $7.5 \times 10^6 m$	length Indian Ocean (*)
$L_{MC} = 0$ or $3.75 \times 10^6 m$	length Maritime Continent (*)
$L_a = L_I + L_{MC} + L_P$	length atmosphere
$H = 200m$	background thermocline depth
$H_1 = 50m$	mixed layer depth
$c_o = \sqrt{g'H} = 2m/s$	Kelvin wave speed (ocean)
$c_a = 30m/s$	Kelvin wave speed (atmosphere)
$\epsilon_o^* = 0.42 yr^{-1}$	damping coefficient ocean dynamics
$\epsilon_a^* = 0.22 day^{-1}$	damping coefficient atmosphere dynamics
$\epsilon_s^* = 0.44 day^{-1}$	damping coefficient Ekman
$\epsilon_T^* = 2.9 yr^{-1}$	damping coefficient SST
$\tau_0 = -1.1 \times 10^{-2} Nm^{-2}$	standard background wind strength
$y_0 = 1.5 \times 10^6 m$	reference length scale used in τ_{ext}
$T_0 = 30°C$	radiative equilibrium SST
$T_{s0} = 23°C$	subsurface temperature at $h = h_0$
$h_0 = 30m$	offset of $T_{sub}(h)$
$H_* = 40m$	steepness of $T_{sub}(h)$
$\tilde{H} = 50m$	reference height computing vertical temperature gradient
$R_o = 3.0 \times 10^5 m$	Rossby radius (ocean)
$R_a = 1.5 \times 10^6 m$	Rossby radius (atmosphere)
$\beta = 2.23 \times 10^{-11} (ms)^{-1}$	equatorial beta parameter (meridional derivative Coriolis param.)
$\alpha_T = 3 \times 10^{-3} m^2/Ks^3$	atm. geopotential tendency/SST anom. (scales wind response)
$\gamma_\tau^0 = 1.6 \times 10^{-8} s^{-1}$	(wind stress/ ρH) / wind anomaly (**)
$\mu_0^* = \alpha_T \gamma_\tau^0$	air-SST coupling strength (**)
ΔT	unit SST anomaly
$\gamma_c = 1.02 c_a^2$	convection feedback strength
$c^{0b} = -0.25 L_a/c_a$	background divergence strength

(*) The lengths L_I and L_{MC} used in the individual model versions can be inferred from the corresponding configuration sketches.

(**) For γ_τ and μ^* other values than the standard values γ_τ^0 and μ_0^* are often used, as explained in the corresponding chapters. When not using the standard value, the subscript or superscript 0 is dropped.

Table 3.1: *Dimensional parameters of the Zebiak-Cane model.*

Embedded in the upper layer of the shallow water model is a surface mixed layer of depth $H_1 = 50m$ with Ekman dynamics. The Ekman velocities obey

$$\epsilon_s u_s - \beta y v_s = \frac{H_2}{H_1} \frac{\tau_x}{\rho H}$$

$$\epsilon_s v_s + \beta y u_s = \frac{H_2}{H_1} \frac{\tau_y}{\rho H} \qquad (3.2)$$

where $H_2 = H - H_1$. The equations can be solved for u_s and v_s in terms of the wind stress. The total horizontal velocity in the surface layer is given by $(u_1, v_1) = (u_r + u_s, v_r + v_s)$. The vertical velocity at the lower boundary of the surface layer is determined by mass conservation and obeys $w_1 = H_1(\partial_{x_P} u_1 + \partial_y v_1)$.

The Sea Surface Temperature (SST) T is defined in the well-mixed surface layer and evolves as

$$\partial_t T + u_1 \partial_{x_P} T + v_1 \partial_y T + \frac{w_1}{\tilde{H}} \mathcal{H}(w_1)[T - T_{sub}(h)] + \epsilon_T^*(T - T_0) = 0 \qquad (3.3)$$

where $\mathcal{H}$ is the Heaviside function: $\mathcal{H}(s) = \begin{cases} 1 & \text{if } s > 0 \\ 0 & \text{else} \end{cases}$, so vertical advection only affects the SST if the vertical velocity is upward, while downwelling has no effect (because loosing water from the mixed layer will not affect the mixed layer temperature, while import of cold water from below does). T_0 is a prescribed radiative equilibrium temperature, and the T_{sub}, the temperature just below the mixed layer, is parameterised as

$$T_{sub}(h) = T_{s0} + (T_0 - T_{s0}) \tanh(\frac{h + h_0}{H_*}). \qquad (3.4)$$

i.e. the shallower the thermocline, the colder T_{sub}. The SST is thus influenced by zonal and meridional advection (second and third term in (3.3)), upwelling into the mixed layer (fourth term) and a linearised atmospheric heat flux (fifth term). Again, parameters are provided in Table 3.1.

The atmosphere is modelled as a Gill model (Gill, 1980), i.e. it obeys linear shallow water equations in a steady state on an equatorial β plane. The atmosphere is heated by SST deviations from T_0:

$$\epsilon_a^* u_a - \beta y v_a + \partial_{x_a} \phi_a = 0$$
$$\beta y u_a + \partial_y \phi_a = 0$$
$$\epsilon_a^* \phi_a + c_a^2(\partial_{x_a} u_a + \partial_y v_a) = -Q \qquad (3.5)$$

where (u_a, v_a) is the wind velocity and ϕ_a is the geopotential and

$$Q = \alpha_T(T - T_0) \qquad (3.6)$$

is the heating.

The wind stress is assumed to depend linearly on the wind:

$$\tau = (\gamma_\tau u_a + \tau_{ext}, \gamma_\tau v_a)$$

where $\tau_{ext} = \tau_0 \exp(-y^2/2y_0^2)$ is a weak external, zonally independent, easterly wind stress which is though of a being generated by the Hadley circulation. This wind stress is the only external forcing needed; it will cause a shallowing of the thermocline and thus cooling in the east Pacific, which in turn causes additional easterlies. Thus with some relatively modest τ_{ext}, the mode generates its own background state with a cold tongue in the east Pacific.

parameter	meaning	value (Gill)	value (conv.)
$\epsilon_o = \epsilon_o^* L_P/c_o$	ocean damping	0.1	0.1
$\epsilon_s = \epsilon_s^* L_P/c_o$	surface layer damping	37.5	37.5
$\epsilon_a = \epsilon_a^* L_a/c_a$	atm. damping	1.875	2.19
$\epsilon_T = \epsilon_T^* L_P/c_o$	SST damping	0.1	0.1
$\alpha_w = H_1/\hat{H}$	upwelling scale	0.1	0.1
$\eta_1 = H/H_*$	T_{sub} sharpness	5.0	5.0
$\eta_2 = h_0/H_*$	T_{sub} set-off	0.5	0.5
δ_w	sharpness Heaviside	5.0×10^{-2}	5.0×10^{-2}
δ_s	scales Ekman contribution	0.2	0.2
δ_0	scales ∂_t terms	1	1
F_0	scale τ_{ext} formula w.r.t tau0?	0.2	0.2
$\alpha = R_o/R_a$	ratio Rossby radii	0.2	0.2
$\Lambda_P = R_p/L_P$	aspect ratio ocean	2×10^{-2}	2×10^{-2}
$\Lambda_a = R_a/L_a$	aspect ratio atmosphere	6.7×10^{-2}	0.57×10^{-2}
$\gamma_s = (H - H_1)/H_1$	a depth ratio	3	3
$\tilde{\alpha}_T = \frac{L_a \Delta T}{c_a^3}\alpha_T$	SST-wind coupling	2.50	2.92
$\tilde{\gamma}_{\tau 0} = \frac{L_P c_a}{c_o^2}\gamma_\tau$	wind-windstress coupling (**)	1.80	1.80
$\tilde{\mu}_0 = \alpha_T\gamma_\tau L_a L_P \Delta T/(c_a^2 c_o^2)$	coupling strength (*) (**)	4.50	5.25
$\tilde{\gamma}_c = \gamma_c/c_a^2$	non-dim. convection parameter	/	1.02

(*) Van der Vaart (1998)has an error here; with $L_a = L_P$, as is the case in the Pacific-only model, the correct value is 3.0.
(**) Other values than the reference values are frequently used, as shall be explained in the corresponding chapters. When not using the standard value, the subscript $_0$ is dropped.

Table 3.2: *Non-dimensional parameters of the Zebiak-Cane model. The numerical values are for the Gill-based 1.5 basin model are given in the column titled 'value (Gill)', whereas the values for the model with convective feedback are given in the column titled 'values (conv.)'. Mostly these values differ because L_a differs for both configurations.*

3.1.2 Spatial discretisation

The model equations are first non-dimensionalised. Non-dimensional quantities are marked by a tilde. For the Pacific ocean quantities, $(x_P, y) = (L_P\tilde{x}_P, R_P\tilde{y}_P)$ is used for the co-ordinates, $t = \frac{L_P}{c_o}\tilde{t}$ for time, $(u, v, w) = c_o(\tilde{u}, \frac{R_P}{L_P}\tilde{v}, \frac{H_1}{L_P}\tilde{w})$ for the velocity (both Ekman and reduced gravity contributions) and $h = H\tilde{h}$ for the thermocline deviations. The atmospheric quantities are non-dimensionalised by $(x_a, y) = (L_a\tilde{x}_a, R_a\tilde{y}_a)$, $(u_a, v_a) = c_a(\tilde{u}_a, \frac{R_a}{L_a}\tilde{v}_a)$ and $\phi = c_a^2\tilde{\phi}$ (see Table 3.2 for dimensional parameters). The SST is non-dimensionalised with $T = (\Delta T)\tilde{T}$, $T_{sub} = (\Delta T)\tilde{T}_{sub}$ and $T_0 = (\Delta T)\tilde{T}_0$. In the Pacific-only case considered here, the zonal coordinates of the ocean and atmosphere are the same, as $L_a = L_P$ (see Fig. 3.1b). The non-dimensional meridional coordinates are zero on the equator and obey $y_a = y_P R_P/R_a = \alpha_P y_P$.

The bulk equations and boundary conditions for the reduced-gravity Pacific Ocean dynamics are:

$$(\delta_0 \partial_{\tilde{t}} + \epsilon_o)\tilde{u}_r - \tilde{y}_P \tilde{v}_r + \partial_{\tilde{x}_P} \tilde{h} = F_0 \tilde{\tau}_{ext}^x + \tilde{\mu} \tilde{u}_a$$

$$\tilde{y}_P \tilde{u}_r + \partial_{\tilde{y}_P} \tilde{h} = 0$$

$$(\delta_0 \partial_{\tilde{t}} + \epsilon_o)\tilde{h} + \partial_{\tilde{x}_P} \tilde{u}_r + \partial_{\tilde{y}_P} \tilde{v}_r = 0$$

$$\int_{-\infty}^{\infty} \tilde{u}_r(0, \tilde{y}_P, \tilde{t}) d\tilde{y}_P = 0; \quad \tilde{u}_r(1, \tilde{y}_P, \tilde{t}) = 0 \qquad (3.7)$$

and for the embedded surface Ekman layer

$$\epsilon_s \tilde{u}_s - \tilde{y}_P \tilde{v}_s = \gamma_s (F_0 \tilde{\tau}_{ext}^x + \tilde{\mu} \tilde{u}_a)$$

$$\epsilon_s \tilde{v}_s + \tilde{y}_P \tilde{u}_s = \gamma_s \Lambda_0 (F_0 \tilde{\tau}_{ext}^y + \tilde{\mu} \tilde{v}_a) \qquad (3.8)$$

The SST equation becomes

$$\delta_0 \partial_{\tilde{t}} \tilde{T} + \tilde{u}_1 \partial_{\tilde{x}_p} \tilde{T} + \tilde{v}_1 \partial_{\tilde{y}_p} \tilde{T} + \alpha_w \tilde{w}_1 \mathcal{H}(\tilde{w}_1)(\tilde{T} - \tilde{T}_{sub}(\tilde{h})) + \epsilon_T (\tilde{T} - T_0) = 0 \qquad (3.9)$$

where $\vec{\tilde{u}}_1 = \vec{\tilde{u}}_r + \delta_s \vec{\tilde{u}}_s$, $\mathcal{H}$ is a mollified Heaviside function, $\mathcal{H}(s) = \frac{1}{2}(1 + \tanh(s/\delta_w))$ and $(\Delta T)\tilde{T}_{sub}(h) = T_{so} + (T_0 - T_{so}) \tanh(\eta_1 \tilde{h} + \eta_2)$.

Finally, the atmosphere obeys

$$\epsilon_a \tilde{u}_a - \tilde{y}_a \tilde{v}_a + \partial_{\tilde{x}_a} \tilde{\phi} = 0$$

$$\tilde{y}_a \tilde{u}_a + \partial_{\tilde{y}_a} \tilde{\phi} = 0$$

$$\epsilon_a \tilde{\phi} + \partial_{\tilde{x}_a} \tilde{u}_a + \partial_{\tilde{y}_a} \tilde{v}_a = -\tilde{Q}(x_a, y_a, t) \qquad (3.10)$$

where $\tilde{Q}$ is the heating due to deviations of the SST from radiative equilibrium, i.e. $\tilde{Q} = \tilde{\alpha}_T (\tilde{T} - \tilde{T}_0)$.

Since for the remainder of this section (3.1.2) all quantities are non-dimensional, the tildes denoting non-dimensional variables will be dropped here in order to simplify the notation.

As shown in Van der Vaart (1998), the model state can be reduced to two sets of independent variables, namely $r \equiv (u_r + h)/2$ and Q (or $T - T_0$). The winds only depend on the heating and can thus be derived from Q; the Ekman velocities in turn are derived from the wind stress; and u_r, v_r and h can be derived from r, Q and τ_{ext}, as will be specified below.

To solve the above equations on the domain $(x, y) \in [0, 1] \times (-\infty, \infty)$, a pseudo-spectral method is employed. The quantities Q and r can be decomposed as

$$Q(x_P, y_p) = \sum_{ij} f_{ij}(x_P, y_P)q_{ij} , \quad r(x_P, y_P) = \sum_{ij} f_{ij}(x_P, y_P)r_{ij} \qquad (3.11)$$

with the shorthand $\sum_{ij} = \sum_{i=0}^{n_x} \sum_{j=0}^{n_y}$. The functions f_{ij} are given by

$$f_{ij} = \tilde{C}_i(x_P)\psi_j(y) \qquad (3.12)$$

where $\tilde{C}_i(x) = C_i(2x - 1)$ with C_i being the i-th Chebyshew polynomial, and ψ_j the j-th Hermite function. The f_{ij} form an orthogonal basis. The q_{ij} and r_{ij} form the

$2(n_x + 1)(n_y + 1)$-dimensional space vector $\mathbf{z} = (r_{ij}, q_{ij})$. The variables are evaluated at the collocation points $(x_{P,k}, y_{P,l})$ with k and l ranging from 0 to n_x and n_y, respectively, and $x_{P,k} = 0.5 \times [1 - \cos(\pi k/n_x)]$ and $y_{P,l}$ is the l-th root of the $(n_y + 1)$-th Hermite function. Atmospheric quantities are evaluated at the same physical locations as ocean quantities, though these points are then expressed in terms of the atmospheric coordinates x_a, y_a. Van der Vaart et al. (2000) find only small differences between $n_x = 11, n_y = 21$ and $n_x = 17, n_y = 41$. Throughout this study, $n_x = 15, n_y = 31$ is used.

The atmospheric equations (3.10) can be solved by expressing the heating $Q(x_a, y_a)$ in atmospheric coordinates, rewriting $u_a \equiv R + S$ and $\phi_a = R - S$ and expanding R, S, v_a and Q meridionally in Hermite functions: $X(x_a, y_a) = \sum_{j=0}^{n_a} X_n(x_a)\psi_n(y_a)$ for $X = R, S, v_a, Q$. Using the recurrence relations for Hermite functions, the equations (3.10) can be reformulated as

$$(\epsilon_a + \partial_{x_a})R_0(x_a) + \frac{1}{2}Q_0(x_a) = 0 \qquad (3.13)$$

$$R_1(x_a) = 0$$

$$((2n - 1)\epsilon_a - \partial_{x_a})R_n(x_a) + \frac{n-1}{2}(Q_n(x_a) + \sqrt{\frac{n}{n-1}}Q_{n-2} = 0 \qquad ; n \geq 2$$

where $Q_n(x_a) = \int Q(x_a, y_a)\psi_n(y_a)dy_a$. In the Pacific-only model, the only heating is from Pacific SST anomalies $T - T_0$. The total heating effect can thus be expressed as a linear combination of the effects of individual modes (i, j), obtained by putting $q_{ij} = 1$ and all other $q = 0$ in (3.11), thus $R_n(x_a) = \sum_{ij} R_n^{ij}(x_a)q_{ij}$. Using (3.12), the effect of the (i, j)-th mode of Q is given by

$$R_0^{ij}(x_a) = -\frac{1}{2}e^{-\epsilon_a x_a}c_j^0 \int_0^{x_a} e^{\epsilon_a x'_a}\tilde{C}_i(x_P(x'_a))dx'_a$$

$$R_0^{ij}(x_a) = 0 \qquad (3.14)$$

$$R_n^{ij}(x_a) = -\frac{n-1}{2}e^{\epsilon_a(2n-1)x_a}[c_j^n + \sqrt{n/(n-1)}c_j^{n-2}]\int_{x_a}^1 e^{-\epsilon_a(2n-1)x'_a}\tilde{C}_i(x_P(x'_a))dx'_a \quad ; n \geq 2$$

where $c_j^n = \int_{-\infty}^{\infty} \psi_j(y_P(y_a))\psi_n(y_a)dy_a$ is the projection of the j-th Hermite function of the Pacific basin onto the n-th atmospheric Hermite function.

From the R_n, one can obtain the S_n and hence express the winds in terms of the heating coefficients q_{ij}. The zonal wind at x_a, y_a is given by

$$u_a(x_a, y_a) = \sum_{ij} \mathcal{A}^{ij}(x_a, y_a)q_{ij} \qquad (3.15)$$

where $\mathcal{A}^{ij}$ is the contribution of the (i, j)-th SST mode to the zonal wind:

$$\mathcal{A}^{ij}(x_a, y_a) = \sum_{n=0}^{n_a}\{R_n^{ij}(x_a) - \sqrt{\frac{n+2}{n+1}}R_{n+2}^{ij}(x_a)\}\psi_n(y_a). \qquad (3.16)$$

Similarly, the meridional wind can be expressed as

$$v_a(x_a, y_a) = \sum_{ij} \mathcal{B}^{ij}(x_a, y_a)q_{ij} \qquad (3.17)$$

with

$$\mathcal{B}^{ij}(x_a, y_a) = \sqrt{2}\tilde{C}_i(x_P(x_a))c_j^1\psi_0(y_a) +$$
$$2\sum_{n=1}^{n_a}\{\sqrt{2(n+1)}[\epsilon_a R_{n+1}^{ij}(x_a) + \frac{1}{4}\tilde{C}_i(x_P(x_a))][c_j^{n+1} + \sqrt{\frac{n}{n+1}}c_j^{n-1}]\psi_n(y_a)\}.$$

$$(3.18)$$

The Ekman velocities depend only on the wind stress, so (3.8) can be rewritten as

$$(u_s(x_P, y_P), v_s(x_P, y_P)) = \sum_{ij}(u_s^{ij}(x_P, y_P), v_s^{ij}(x_P, y_P))q_{ij} + (u_s^{ext}(x_P, y_P), v_s^{ext}(x_P, y_P))$$

$$(3.19)$$

where $\mathbf{u}_s^{ext}$ is the contribution from the external wind stress and $(u_s^{ij}(x_P, y_P), v_s^{ij}(x_P, y_P))$ can be expressed as linear combinations of $\mathcal{A}^{ij}$ and $\mathcal{B}^{ij}$ (see Van der Vaart (1998)for details).

The oceanic shallow-water model (3.7) is solved by putting $u_r = s + r$, $h = r - s$, decomposing r meridionally into Hermite functions and eliminating s and v to yield the evolution equations for $r_j(x_P)$:

$$(\delta_0\partial_t + \epsilon_o + \partial_{x_P})r_0(x_P) - \frac{1}{2}\mathcal{F}_0(x_P) = 0$$

$$r_0(x_P = 0) - \sum_{j=2}^{n_y}\frac{\varepsilon_j}{j-1}r_j(x_P = 0) = 0$$

$$r_1(x_P) = 0$$

$$((2j-1)(\delta_0\partial_t + \epsilon_o) - \partial_{x_P})r_j - \frac{j-1}{2}(\mathcal{F}_j - \sqrt{\frac{j}{j-1}}\mathcal{F}_{j-2}) = 0\,,\ j \geq 2$$

$$r_j(x_P = 1) - \varepsilon_j r_0(x_P = 1) = 0\,,\ j \geq 2 \qquad (3.20)$$

with $\varepsilon_0 = 1$, $\varepsilon_1 = 0$, $\varepsilon_j = \sqrt{j/(j-1)}\varepsilon_{j-2}$, $j \geq 2$. Inserting $r_j(x_P) = \sum_{i=0}^{n_x}r_{ij}\tilde{C}_i(x_P)$ yields a set of coupled linear inhomogeneous ordinary differential equations in r_{ij}. The forcing terms are given by

$$\mathcal{F}_n(x_P) = F_0\tau_{ext}^x + \tilde{\gamma}_\tau\sum_{ij}a_n^{ij}(x_P)q_{ij} \qquad (3.21)$$

with the contribution $a_{ij}^n(x_P)$ from a unit SST perturbation in mode i, j in the Pacific is given by

$$a_n^{ij}(x_P) = \int_{-\infty}^{\infty}\mathcal{A}^{ij}(x_P, y_P)\psi_n(y_P)dy_P \qquad (3.22)$$

For a given set of q_{ij}, r_{ij}, the shallow water variables are given by

$$u_r(x_P, y_P, t) = \sum_{ij}u_r^{ij}(x_P, y_P)r_{ij}(t)$$

$$h(x_P, y_P, t) = \sum_{ij}h^{ij}(x_P, y_P)r_{ij}(t)$$

$$v_r(x_P, y_P, t) = \sum_{ij}v_r^{rij}(x_P, y_P)r_{ij}(t) + \sum_{ij}v_r^{qij}(x_P, y_P)q_{ij}(t) + v_r^\tau(x_P, y_P) \qquad (3.23)$$

a)
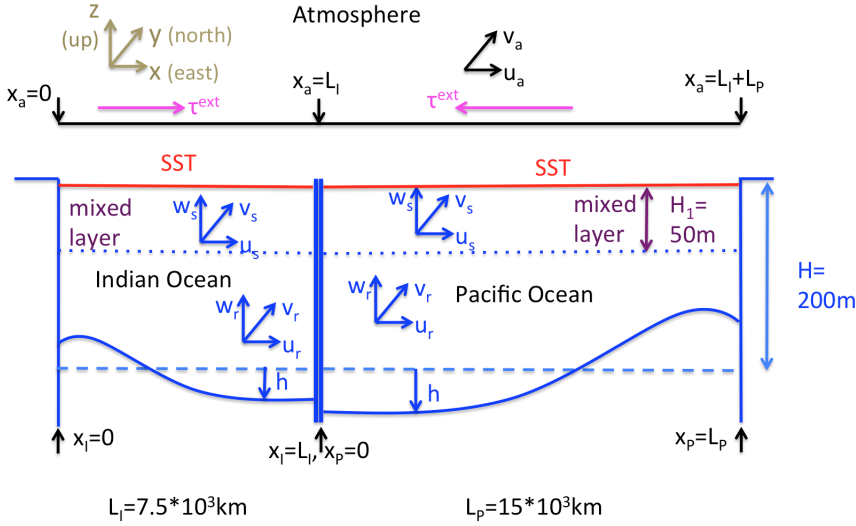
b)
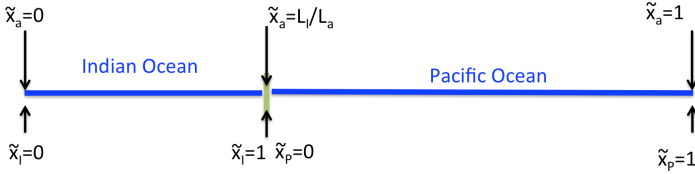
Figure 3.2: *a) Setup of the full double-basin Zebiak-Cane model. b): definition of non-dimensional zonal coordinates for the full double-basin model.*

where u_r^{ij}, h^{ij} and v_r^{rij} are linear combinations of the f_{ij}, while v_r^{qij} and v_r^τ (contribution to v_r due to external wind stress) can be expressed in terms of and $\mathcal{A}_{ij}$ and τ^{ext}, respectively, and the Hermite function ψ_n , as described in Van der Vaart (1998).

3.2 The full double-basin model

Although the full double-basin model does not work for simulating the Indo-Pacific system, as will be discussed in section 3.3, it seems useful to give a brief description. First, in order to understand why it does not work, and second, because a similar mathematical set-up might be useful for studying the interaction between the Pacific and the Atlantic.

3.2.1 Physical formulation

The full double-basin Zebiak-Cane model consists of two ocean basins separated by a zonally very thin and meridionally infinite wall, as shown in Fig. 3.2. The Indian Ocean has a length $L_I = L_P/2$; the Maritime Continent has a length $L_{MC} = 0$. Transformations between dimensional oceanic and atmospheric zonal coordinates (see Fig. 3.2a) now take the form: $x_a(x_I) = x_I$, $x_a(x_P) = L_I + x_P$. The dimensional meridional coordinate is the same for both basins and the atmosphere.

Each basin separately obeys (3.1) - (3.3). There is one atmosphere spanning both oceans and providing coupling between them, as heating by one basin can cause wind anomalies over the other. The atmosphere obeys (3.5), except that now $Q = Q_P + Q_I$, where $Q_P = \alpha_{T,P}(T_P - T_0)$ is non-zero only over the Pacific ($x_a > L_I$) and $Q_I = \alpha_{T,I}(T_I - T_0)$ is non-zero only over the Indian Ocean ($x_a < L_I$). Only Indo-Pacific coupling via the atmosphere is studied; the Indonesian Throughflow is ignored. It would be difficult to implement this, as it would require to generate completely new boundary conditions for the ocean basins.

3.2.2   Spatial discretisation

Once more, for the remainder of this section (3.2.2), only non-dimensional quantities are used and the tilde marking non-dimensional quantities is suppressed. The nondimensional zonal coordinates (see Fig. 3.2b) obey $\tilde{x}_a(\tilde{x}_I) = \frac{L_I}{L_a}\tilde{x}_I$ and $\tilde{x}_a(\tilde{x}_P) = \frac{L_I}{L_a} + \frac{L_P}{L_a}\tilde{x}_P$. Both basins have the same Rossby radius R_o, so $y_a = \alpha y_P = \alpha y_I$.

Solving the atmospheric equations is done in a similar way as for the single-basin model, except that there are now two sets of R_n^{ij}, namely one for heating from the Pacific (R_n^{Pij}) and one from the Indian Ocean (P_n^{Iij}). They are computed as follows:

$$R_0^{Iij}(x_a) = -\frac{1}{2}e^{-\epsilon_a x_a}c_j^0\int_0^{min(x_a,L_I/L_a)} e^{\epsilon_a x_a'}\tilde{C}_i(x_I(x_a'))dx_a'$$

$$R_0^{Iij}(x_a) = 0 \tag{3.24}$$

$$R_n^{Iij}(x_a) = -\frac{n-1}{2}e^{\epsilon_a(2n-1)x_a}[c_j^n + \sqrt{n/(n-1)}c_j^{n-2}]\times$$

$$\int_{min(x_a,L_I/L_a)}^{L_I/L_a} e^{-\epsilon_a(2n-1)x_a'}\tilde{C}_i(x_I(x_a'))dx_a' \qquad ; n \geq 2$$

and

$$R_0^{Pij}(x_a) = -\frac{1}{2}e^{-\epsilon_a x_a}c_j^0\int_{L_I/L_a}^{max(x_a,L_I/L_a)} e^{\epsilon_a x_a'}\tilde{C}_i(x_P(x_a'))dx_a'$$

$$R_0^{Pij}(x_a) = 0 \tag{3.25}$$

$$R_n^{Pij}(x_a) = -\frac{n-1}{2}e^{\epsilon_a(2n-1)x_a}[c_j^n + \sqrt{n/(n-1)}c_j^{n-2}]\times$$

$$\int_{max(x_a,L_I/L_a)}^1 e^{-\epsilon_a(2n-1)x_a'}\tilde{C}_i(x_P(x_a'))dx_a' \qquad ; n \geq 2$$

Note that the atmospheric coordinate x_a runs over the whole atmosphere, and therefore R_0^{Iij} can have non-zero values over the Pacific, while R^{Pij} with $n \geq 2$ can take non-zero values over the Indian Ocean.

From the R_n, one can obtain the S_n and hence express the winds in terms of the heating coefficients q_{ij}. The zonal wind at x_P, y_P is given by

$$u_a(x_a, y_a) = \sum_{ij}\mathcal{A}^{Pij}(x_a, y_a)q_{ij}^P + \sum_{ij}\mathcal{A}^{Iij}(x_a, y_a)q_{ij}^I \tag{3.26}$$

where $\mathcal{A}^{bij}$ is the contribution of the (i,j)-th SST mode in basin b to the zonal wind:

$$\mathcal{A}^{bij}(x_a, y_a) = \sum_{n=0}^{n_a}\{R_n^{bij}(x_a) - \sqrt{\frac{n+2}{n+1}}R_{n+2}^{bij}(x_a)\}\psi_n(y_a). \tag{3.27}$$

Similarly, the meridional wind can be expressed as

$$v_a(x_a, y_a) = \sum_{ij} \mathcal{B}^{Pij}(x_a, y_a)q_{ij}^P + \sum_{ij} \mathcal{B}^{Iij}(x_a, y_a)q_{ij}^I \tag{3.28}$$

with

$$\mathcal{B}^{Iij}(x_a, y_a) = \sqrt{2}\mathcal{H}(\frac{L_I}{L_a} - x_a)\tilde{C}_i(x_I(x_a))c_j^1\psi_0 +$$
$$2\sum_{n=1}^{n_a}\{\sqrt{2(n+1)}[\epsilon_a R_{n+1}^{Iij}(x_a) + \frac{1}{4}\mathcal{H}(\frac{L_I}{L_a} - x_a)\tilde{C}_i(x_I(x_a))]\times \tag{3.29}$$
$$[c_j^{n+1} + \sqrt{\frac{n}{n+1}}c_j^{n-1}]\psi_n(y_a)\}$$

and

$$\mathcal{B}^{Pij}(x_a, y_a) = \sqrt{2}\mathcal{H}(x_a - \frac{L_I}{L_a})\tilde{C}_i(x_P(x_a))c_j^1\psi_0 +$$
$$2\sum_{n=1}^{n_a}\{\sqrt{2(n+1)}[\epsilon_a R_{n+1}^{Pij}(x_a) + \frac{1}{4}\mathcal{H}(x_a - \frac{L_I}{L_a})\tilde{C}_i(x_P(x_a))]\times \tag{3.30}$$
$$[c_j^{n+1} + \sqrt{\frac{n}{n+1}}c_j^{n-1}]\psi_n(y_a)\}$$

where the Heaviside function $\mathcal{H}(s) = \begin{cases} 1 & \text{if } s > 0 \\ 0 & \text{else} \end{cases}$ ensures that the local heating terms only become non-zero when x_a is within the basin of which the contribution is considered.

The Ekman velocities now are influenced from wind contributions caused by heating in both basins. Therefore the Ekman velocity within each basin b is given by

$$(u_s^b(x_b, y_b), v_s^b(x_b, y_b)) = \sum_{ij}(u_s^{Iij}(x_b, y_b), v_s^{Iij}(x_b, y_b))q_{ij}^I + \tag{3.31}$$
$$\sum_{ij}(u_s^{Pij}(x_b, y_b), v_s^{Pij}(x_b, y_b))q_{ij}^P + (u_s^{ext}(x_b, y_b), v_s^{ext}(x_b, y_b))$$

where once again the $u_s^{bij}v_s^{bij}$ depend linearly on the $\mathcal{A}, \mathcal{B}$.

The ocean models for each basin b resemble (3.20-3.23), except there is now a wind stress forcing from both oceans:

$$\mathcal{F}_n(x_b) = F_0\tau_{ext}^x + \tilde{\gamma}_\tau \sum_{ij} a_{bn}^{Iij}(x_b)q_{ij}^I + \tilde{\gamma}_\tau \sum_{ij} a_{bn}^{Pij}(x_b)q_{ij}^P.$$

In addition, the meridional velocity in basin b now takes the form

$$v_r(x_b, y_b, t) = \sum_{ij} v_{br}^{rij}(x_b, y_b)r_{ij}^b(t) + \sum_{ij} v_{br}^{qIij}(x_b, y_b)q_{ij}^I(t) + \sum_{ij} v_{br}^{qPij}(x_b, y_b)q_{ij}^P(t) + v_{br}^\tau(x_b, y_b).$$

As mentioned before, this model turns out not to work well (see also section 3.3). Therefore a simplified representation of the Indian Ocean is introduced in section 3.4.
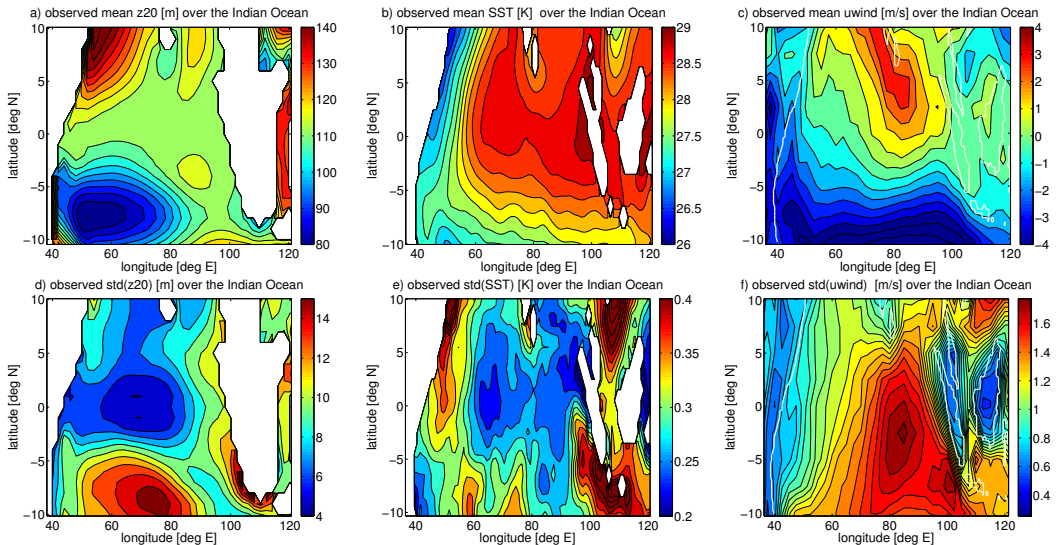
Figure 3.3: *Top row: The observed mean state of the Indian Ocean (averaged over all seasons), for the thermocline depth (z20; plot a), SST (b) and zonal wind speed (c). Bottom: the same but for the standard deviation instead of the mean. The data was detrended and the seasonal cycle was subtracted before computing the standard deviation.*

3.3 One model fits all? - Why the Zebiak-Cane framework does not capture Indian Ocean dynamics

The Zebiak-Cane model was designed to describe the dynamics of interannual variability in the Pacific, but turns out not to capture the dynamics of the Indian Ocean well. The first problem is to construct a reasonable climatology; this can be solved to some extend. However, even with a reasonable background state, interannual variability cannot be realistically modelled.

Compared to the tropical Pacific, the Indian Ocean has a complicated climatology which is heavily affected by the Asian monsoon and thus characterised by a strong seasonal cycle, meridional asymmetry across the equator, and off-equatorial variability, e.g. in the Seychelles Dome. In the annual mean, the winds along the equator are westerly in the central-east Indian Ocean (Fig. 3.3c). The westerly winds prevent the formation of an equatorial cold tongue in the east Indian Ocean, as opposed to what one finds in both the Pacific and Atlantic Ocean, where the Hadley circulation leads to mean easterlies. In boreal autumn, however, the Indian Ocean has easterly winds over the equator, leading to upwelling and cooling along the west coast of Sumatra.

As the ZC model is mainly designed to represent near-equatorial dynamics, we first attempt to generate a very crude setting, ignoring the meridional asymmetry and also the seasonal cycle. In order to roughly mimic observations (cf. Fig. 3.3), the mean state in the Indian Ocean should have a relatively small thermocline tilt along the equator, but off-equatorial thermocline ridges with relatively low SST in the west Indian Ocean (roughly representing the Seychelles Dome). This requirement may appear questionable because in nature such a thermocline ridge exists only on the southern hemisphere, but the Seychelles Dome is a region of high thermocline variability and reasonably high SST variability, and emerged from chapter 2 as a region with potential impact on ENSO, so

parameter	meaning
$L_I = 7.5 \times 10^6 m$	length Indian Ocean
$\epsilon_o^* = 0.11 yr^{-1}$	damping coeff. ocean dynamics
$\epsilon_T^* = 8.7 yr^{-1}$	damping coeff. SST
$\tau_0 = -1.1 \times 10^{-2} Nm^{-2}$	standard background wind strength
$\tau_{ext}^I = -3\frac{L_I - x_I}{L_I}\tau_0 \exp(y^2/2y_0^2)$	external wind stress
$h_0 = 0m$	offset of $T_{sub}(h)$
$H_* = 20m$	steepness of $T_{sub}(h)$
$\alpha_T = 3 \times 10^{-3} m^2/Ks^3$	coupling: geopotential tendency per SST anom.
$\gamma_\tau^0 = 1.6 \times 10^{-8} s^{-1}$	coupling: wind stress/ ρH per wind anomaly (*)
$\mu^0 = \alpha_T \gamma_\tau$	(*)

Table 3.3: *Parameter changes with respect to table 3.1 used to obtain a reasonable Indian Ocean climatology of Fig. 3.5 (in the absence of a Pacific Ocean and convection feedback).*

it seems sensible to include this phenomenon in our symmetrised model. The SST in the east should be near $30°C$. The winds along the equator should be weak westerlies.

A first attempt to fulfil these criteria could be to put $L_I = L_p/2$ and impose a westerly wind stress over the Indian Ocean,

$$\tau_{ext}^I = -\tau_0 \exp(y^2/2y_0^2) = -\tau_{ext}^P$$

(here τ_{ext}^P is the Pacific external wind stress). However, when increasing the coupling strength μ^* to values similar to the Pacific ones, the cool anomalies which for low μ^* are found in the west, move eastward (see Fig. 3.4). The mechanism for this shift is as follows: Westerly winds along the equator cause equatorial downwelling and off-equatorial upwelling. While upwelling cools the sea surface, downwelling does not lead to warming (see (3.3)). To the east (west) of a cool anomaly, westerlies (easterlies) arise which strengthen (weaken) the total wind stress and thus the off-equatorial upwelling. Thus increasing μ^* leads to additional cooling east of a cool anomaly; in other words, the cool anomaly is shifted eastward. The initial tilt of the thermocline (lower in the east than in the west) is reduced when increasing μ^*, which further favours the eastward shift. This experiment already suggests that the ZC model might have difficulties with oceans exhibiting mean westerly winds.

A way to remedy the eastward shift of the cool patches is to prescribe a zonally nonuniform wind stress, which is strongest in the west and zero in the east, e.g.

$$\tau_{ext}^I = -3\frac{L_I - x_I}{L_I}\tau_0 \exp(y^2/2y_0^2).$$

Some additional parameter changes were made (see table 3.3). The increase in ϵ_T^* serves to suppress unphysical high-frequency SST modes; the reduction in ϵ_o^* serves to roughly compensate for the impact of the increased ϵ_T^* on stability; and h_0 and H_* were changed such as to make T_{sub} more sensitive to thermocline changes near $h = 0$ (cf. (3.4)). The equilibrium state is not very sensitive to these parameter changes. Though this choice for τ_{ext} yields a reasonable SST and thermocline depth equilibrium state (see Fig. 3.5), it is not motivated by physical principles (as opposed to τ_{ext}^P in the Pacific, which can be thought of as being caused by the Hadley circulation).

Having constructed an acceptable climatology, the main problem with the double-basin model is that the Indian Ocean shows extremely little interannual variability -
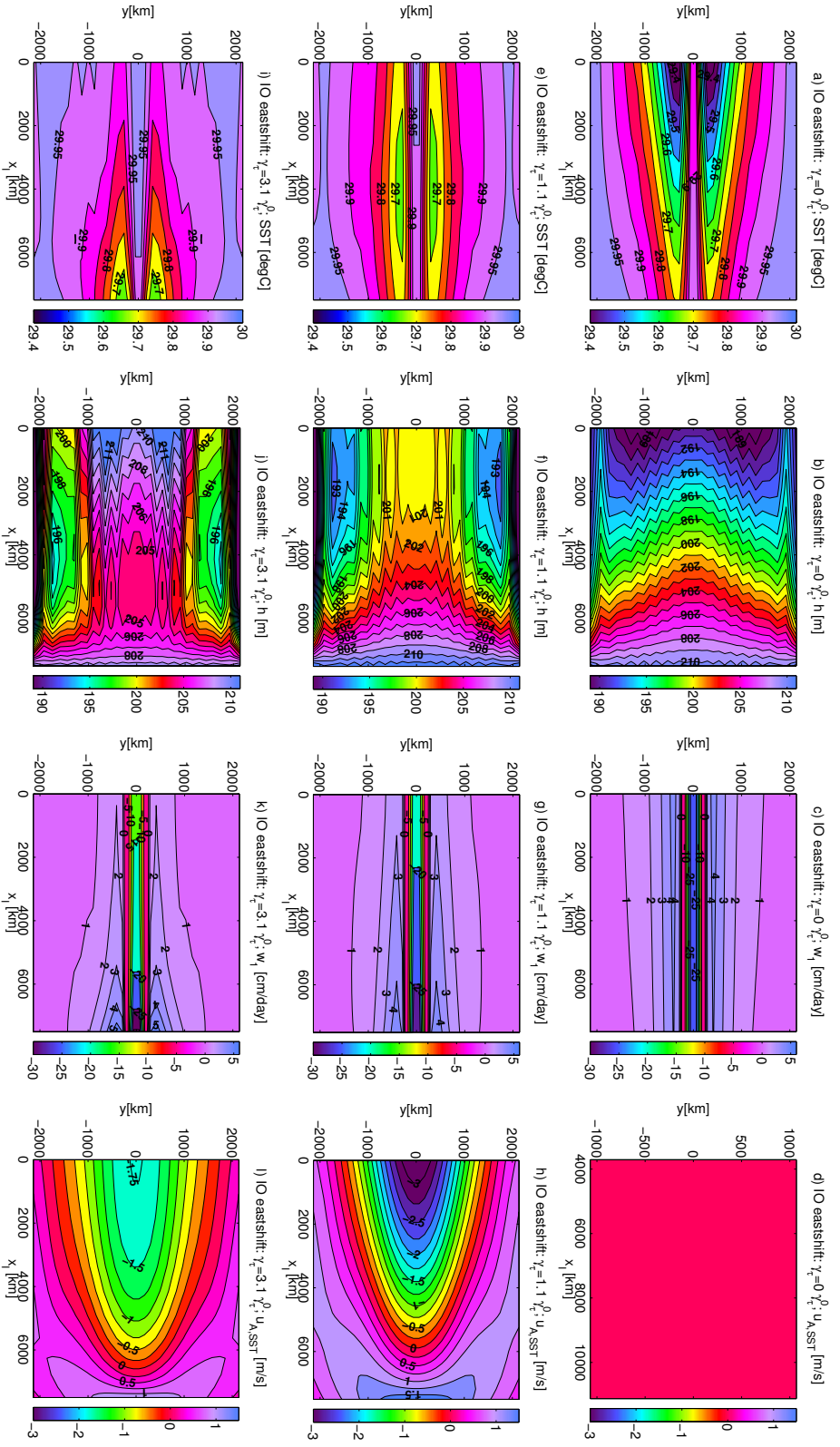
Figure 3.4: *Illustration of the eastward shift of the off-equatorial cool patches in the Indian Ocean for increasing coupling* γ_τ *at* $L_I = L_P/2$ *and zonally uniform external wind stress* $\tau_{ext}^I = -\tau_0 \exp(y^2/2y_0^2) = -\tau_{ext}^P$. *Other parameters are as for the standard Pacific (see table 3.1). Results are shown for* $\gamma_\tau = 0\gamma_\tau^0$ *(plots a-d),* $\gamma_\tau = 1.1\gamma_\tau^0$ *(plots e-h), and* $\gamma_\tau = 3.1\gamma_\tau^0$ *(plots i-l). The plots are the equilibrium states of the SST (a,e,i), thermocline depth (b,f,j), upwelling speed (c,g,k) and zonal wind induced by the SST (d,h,l).*
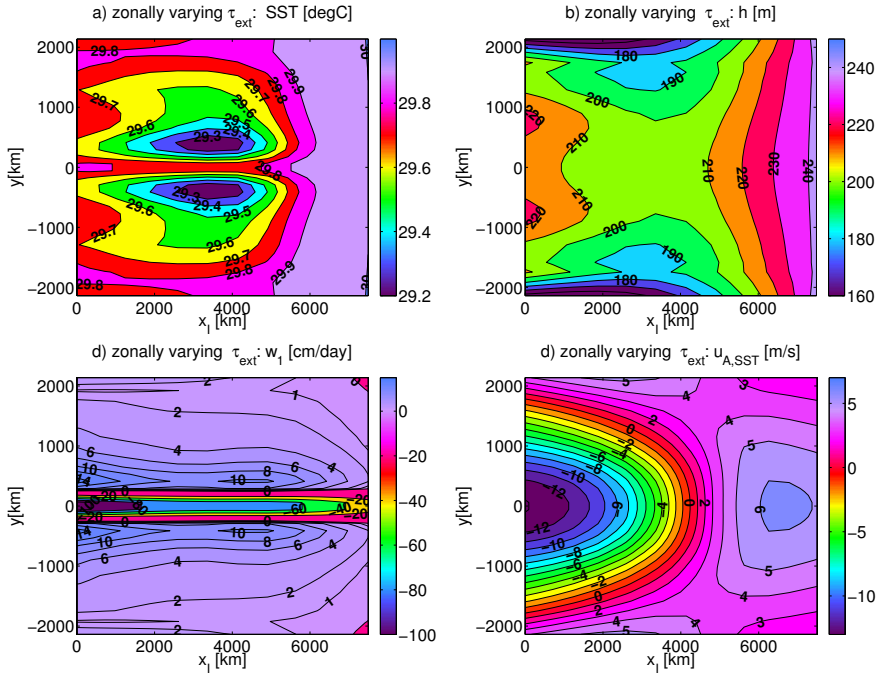
Figure 3.5: *The Indian Ocean equilibrium state in the absence of a Pacific, with a zonally varying, westerly external wind stress $\tau_{ext}^I = -3\frac{L_I - x_I}{L_I}\tau_0 \exp(y^2/2y_0^2)$. Parameters are as in table 3.1, except for those mentioned in table 3.3. All plots are for $\gamma_\tau = 1.94\gamma_\tau^0$. The plots are the equilibrium states of the SST (a), thermocline depth (b), upwelling speed (c) and zonal wind induced by the SST gradient (d).*

not even as a response to the Pacific ENSO cycle. A first difficulty is that the Pacific fails to produce easterly (westerly) anomalies over the Indian Ocean during El Niño (La Niña), as observations suggest Wang et al (1999). In observations, El Niño (La Niña) is accompanied by cool (warm) anomalies in the west Pacific which can cause easterlies (westerlies) over the east Indian Ocean. However, these SST anomalies are very small in the ZC model, because T_{sub} and thus T are very insensitive to variations in h if the thermocline is already very deep. This problem can be solved by adjusting the T_{sub} -parametrisation in the west Pacific, though the drawback is that this also affects the equilibrium state (i.e. a slight cool patch is formed in the west Pacific, where actually there should be a warm pool). An alternative method could be to insert a block of land in between the Indian and Pacific Ocean, similar to the geometry of Fig. 3.7, and prescribe that during El Niño (La Niña) negative (positive) temperature anomalies occur on that block. A third way is to include convection over the Maritime Continent (MC); after all, ENSO is associated with reduced convection and thus cooling over the MC. All these methods generate the desired wind response to ENSO over the east Indian Ocean, though the first two are rather ad-hoc.

However, even with a reasonable wind response, the Indian Ocean SST reacts very little to ENSO forcing. The main reason for this is that the equilibrium state has downwelling ($w_1 < 0$) on the equator, so that thermocline variations there will not impact the SST. The off-equatorial upwelling is much weaker than the equatorial downwelling, so SST response

to off-equatorial thermocline variations is possible but weak. Typically, the amplitude of the Indian Ocean SST signal reaches about 1/50 of the corresponding values in the Pacific cold tongue. Concerning the Seychelles Dome, it is believed that in nature its variability is partially externally forced: anticyclonic winds over the east Indian Ocean during El Niño cause a downwelling Rossby wave which leads to cooling in the Seychelles Dome a few months later (see Schott et al. (2009), section 4.1.2 and references therein). This delayed effect is not reproduced in the double-basin ZC model.

Since the ZC model apparently has difficulties with systems with mean westerlies, a possibility would be to focus on the boreal autumn season and study mainly the effect of east Indian Ocean SST variability enabled by the background upwelling off Sumatra during that season. We did not pursue this because we are interested in the effect of west Indian Ocean variability.

Indian Ocean SST variability is not only influenced by ocean dynamics (which are an important driving force for the Indian Ocean Dipole and Seychelles Dome variability), but also by radiative processes. These are thought to be responsible for Indian Ocean Basinwide warming (IOB) variability. In particular, El Niño is known (see Schott et al. (2009), section 4.1.2 and references therein) to cause reduced cloud cover and thus increased downward short-wave heat fluxes over the Indian Ocean. This effect is not included in the ZC model, but can be implemented by replacing T_0 by $T_0 + T_1(x_I, y_I, N)$ in (3.3), where T_1 is the radiation-driven impact of ENSO (represented by an El Niño index N) on the Indian Ocean SST. Note that (3.6) must not be altered, because only the SST evolution, but not the way in which the SST impacts the wind, is supposed to be affected. Unfortunately this approach leads to unrealistic spatial patterns of the SST variability, because the Indian Ocean warming leads to westerly wind anomalies over the west Indian Ocean, which lead to anomalous off-equatorial upwelling and hence reduced warming or even cooling over the off-equatorial west Indian Ocean. In principle, this problem could be mitigated by introducing warming over the African continent in phase with the Indian Ocean warming, so as to reduce the temperature gradient and hence the winds over the Indian Ocean, but this would require careful tuning and is not physically motivated.

From the model experiments described above, it can be concluded that the Zebiak-Cane model is not well suited to simulate the Indian Ocean (neither the IOD nor the IOB), both because it has difficulties with systems with mean westerlies, and because the Indian Ocean has complicated phenomena not captured by the Zebiak-Cane dynamics, in particular, strong off-equatorial variability, meridional asymmetry, and the Indian monsoon which gives rise to a very complicated seasonal cycle. However the main aim of this study is not to understand the subtle internal dynamics of the Indian Ocean, but the impact of the Indian Ocean on ENSO via the atmospheric bridge. Hence it seems acceptable to *prescribe* Indian Ocean variability - possibly in an ENSO-dependent way - based on observations and investigate their impact on ENSO.

Though this is outside the scope of the current thesis, it should be noted that the full double-basin Zebiak-Cane model might be useful to study the interaction between the Atlantic and Pacific Oceans. The dynamics in the Atlantic are more similar to the Pacific (and thus the Zebiak-Cane model); in particular, the Atlantic has easterly winds, a cold tongue and an ENSO-like phenomenon (the co-called Atlantic Niño).

3.4 Prescribing Indian Ocean SST patterns

3.4.1 Physical aspects

As the main interest of this study is not the subtle internal mechanisms of the Indian Ocean, but the impact of Indian Ocean SST variability on ENSO, a simplified version of the double-basin ZC model, called the Gill-based 1.5 basin ZC model, is introduced. This model will be used in chapter 4. Its geometry is exactly as in Fig. 3.2, except that the Indian Ocean has no mechanical variables (currents and thermocline depth). Instead, the dynamics of the Indian Ocean are neglected, and its SST varies as

$$T_I = T_0 + \sum_{m=1}^{n_I} T_m^{0I}(x_I, y) A_m(t) \tag{3.32}$$

where the $T_m^{0I}(x_I, y)$ are fixed spatial patterns which might, for example, represent the IOD or IOB, and $A_m(t)$ the time-dependent amplitude of that SST anomaly which may be influenced by ENSO. Its evolution equation is adapted from the conceptual model of Jansen et al. (2009) and is of the form

$$\frac{dA}{dt} = a_0 \cos(\psi)(N - \bar{N}) + \frac{a_0}{\omega} \sin(\psi) \frac{dN}{dt} + a_c + a_d A + R(t). \tag{3.33}$$

Here N is an El Niño index specified in (3.37) and $\bar{N}$ its equilibrium value, so that $N - \bar{N} > 0$ ($N - \bar{N} < 0$) signifies El Niño (La Niña) conditions. The parameter a_0 determines how strongly A depends on ENSO and ψ can be used to change the phase relation between N and A. For example, if $\psi = 0$ ($\psi = 180°$) one would expect A to peak shortly after El Niño (La Niña), though the exact phase relation also depends on the other parameters and the amplitude of A. The factor $1/\omega$, where ω is the angular frequency of the ENSO cycle, was inserted because for sinusoidal oscillations N and $(dN/dt)/\omega$ have the same amplitude. $a_d < 0$ is a damping factor and $R(t)$ a noise term. a_c is a constant, and if $a_0 = 0, R = 0$, then A will equilibrate to $A = a_c/a_d$. Note that if $R = 0$ and $a_c = 0$ and the model is in equilibrium (which implies $N = \bar{N}, dN/dt = 0$) the equilibrium solution for A is $A = 0$, so the Indian Ocean will not influence the equilibrium over the Pacific.

Temperature anomalies in the Indian Ocean can affect the atmosphere (see (3.5)), leading to additional wind contributions (pure Gill-response) which extend over the Pacific. For details, see (3.34)-(3.36).

3.4.2 Spatial discretisation

The numerical implementation of the Gill-based 1.5 basin model is very similar to the original single-basin model. The state space of independent variables is expanded by adding the n_I new variables A_m, thus the state vector becomes $\mathbf{z} = (r_{ij}, q_{ij}, A_m)$ and has $2(n_x + 1)(n_y + 1) + n_I$ dimensions. Once again, for the rest of this section (3.4), all variables and coordinates are non-dimensional without being marked by a tilde.

Winds over the Indian Ocean need not be computed, because there are no oceanic variables (currents, thermocline depth) that might be influenced by such winds. The wind over the Pacific now also gets a contribution from the Indian Ocean SST and takes

the form

$$(u_a(x_a,y_a), v_a(x_a,y_a)) = \sum_{ij}(\mathcal{A}^{Pij}(x_a,y_a), \mathcal{B}^{Pij}(x_a,y_a))q_{ij} + \sum_{m=1}^{n_I}(u_a^{Im}(x_a,y_a), v_a^{Im}(x_a,y_a))$$

(3.34)

where $\mathcal{A}^{Pij}, \mathcal{B}^{Pij}$ are the contributions from the Pacific SST from (3.27, 3.30). The Indian Ocean contributions are given by

$$u_a^{Im}(x_a,y_a) = \sum_{n=1}^{n_a}\{R_n^{Im}(x_a) - \sqrt{\frac{n+2}{n+1}}R_{n+2}^{Im}(x_a)\}\psi_n(y_a)$$

$$v_a^{Im}(x_a,y_a) = 2\sum_{n=1}^{n_a}\sqrt{2n+2}\epsilon_a R_{n+1}^{Im}(x_a)\psi_n(y_a)$$

(3.35)

where the R_n^{Im} are given by

$$R_0^{Im} = -\frac{1}{2}e^{-\epsilon_a x_a}\int_0^{min(x_a,L_I/L_a)}e^{\epsilon_a x_a'}T_{m,n}^{I0}(x_a')dx_a'$$

(3.36)

$$R_1^{Im} = 0$$

$$R_n^{Im} = -\frac{n-1}{2}e^{(2n-1)\epsilon_a x_a}\int_{min(x_a,L_I/L_a)}^{L_I/L_a}e^{-\epsilon_a(2n-1)x_a'}\times$$

$$[T_{m,n}^{0I}(x_a') + \sqrt{\frac{n}{n-1}}T_{m,n-2}^{0I}(x_a')]dx_a', \ \ n \geq 2$$

where $T_{m,n}^{0I}(x_a)$ is the projection of $T_m^{0I}(x_a,y_a)$ onto the n-th Hermite function $\psi_n(y_a)$.

The additional wind contributions (u_a^{Im}, v_a^{Im}) generate contributions (u_s^{Im}, v_s^{Im}) to the Ekman velocities and to the wind stress forcing acting on the Pacific (see (3.22)) and v_r which all can be computed in the same way as contributions from Pacific-induced winds.

The El Niño index N is defined based on heating coefficients q_{ij} with low i and j (i.e. coefficients associated with large spatial scales) in the Pacific, namely as

$$N(t) = q_{00}(t) + q_{10}(t) - \frac{1}{2}q_{20}(t).$$

(3.37)

In other words, N measures how well the current SST field projects onto the spatial pattern given in Fig. 3.6. Using an index based on low-order (i.e., large spatial scale) SST modes only, rather than the mean SST over a sharp spatial box like Nino3, reduces numerical errors in our pseudo-spectral implementation of the ZC model.

3.5 Convection feedback

The model version described in section 3.4 cannot be used to simulate the atmospheric bridge mechanism proposed in section 2.4.1, because the atmospheric component only includes a (linear) Gill response but lacks convective feedback above Indonesia. Therefore we introduce a last version of the ZC model, which will be referred to as convective 1.5 basin ZC model. It is an expansion of the Gill-based 1.5 basin model which includes a non-linear convection feedback over the Maritime Continent and part of the Indian Ocean. This model will be used in chapter 5. The geometrical set-up is given in Fig. 3.7.
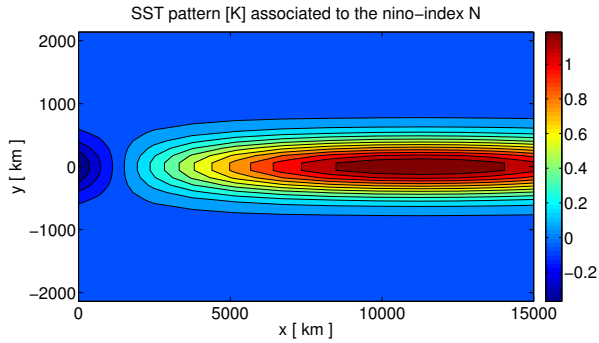
Figure 3.6: *The spatial pattern of Pacific SST associated with the El Niño index N. High positive values of N mean that the SST anomaly in the Pacific projects strongly onto this pattern (El Niño conditions).*
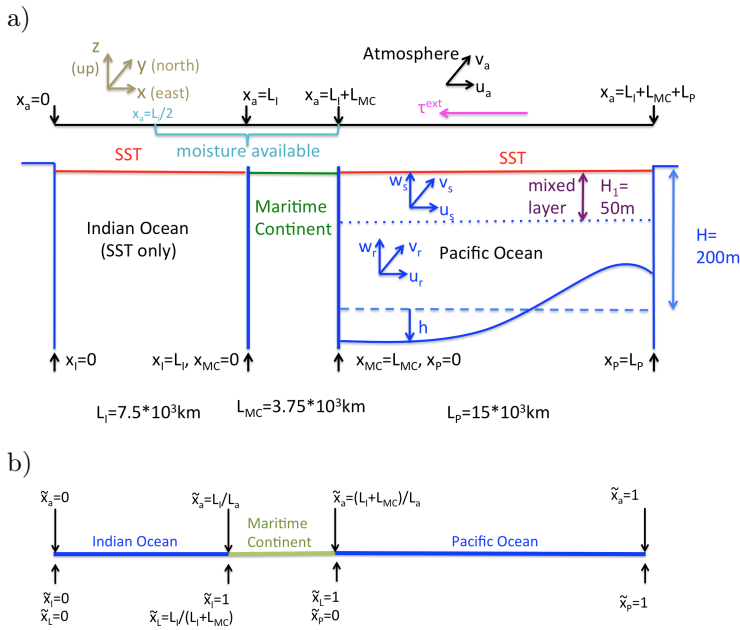
Figure 3.7: *a) Setup of the convective 1.5 basin Zebiak-Cane model. b): definition of non-dimensional zonal coordinates for the moist model.*

3.5.1 The physics of the convection feedback

Similar to Zebiak (1986); Zebiak and Cane (1987), we assume that convective heating can take place if there is converging horizontal wind and moisture, because wind convergence near the ground leads to upward motion and - if sufficient moisture is present - condensation and latent heat release. Together with the SST-induced heating Q^T, this convective heating Q^c contributes to the total heating Q which will in turn influence the wind (see (3.5)), leading to even stronger convergence. Writing the wind divergence as $c(x_a, y) = \partial_{x_a} u^a + \partial_y v^a$, the convective heating Q^c can be parameterised as

$$Q^c(x_a, y) = \gamma_c m(x_a, y) \times \begin{cases} [\mathcal{M}(-c(x_a, y) - c^b(x_a, y))]^\kappa & \text{if} - c(x_a, y) - c^b(x_a, y) < C_0 \\ a_\kappa [\mathcal{M}(-c(x_a, y) - c^b(x_a, y))]^{\tilde{\kappa}} - b_\kappa & \text{else} \end{cases}$$

(3.38)

where γ_c is a scaling parameter and m takes values between 0 and 1 and is a measure for moisture availability ($m = 1$ means that sufficient moisture is present for vigorous convection, while $m = 0$ means that convection is not possible). The field c^b is a prescribed background divergence, and

$$\mathcal{M}(z) = \begin{cases} z & \text{if } z > 0 \\ 0 & \text{if } z \leq 0 \end{cases}$$

i.e. convergence leads to heating while divergence does not lead to cooling. a_κ and b_κ are chosen such that Q^c is continuous and differentiable at $-c(x_a, y) - c^b(x_a, y) = C_0$. As opposed to Zebiak and Cane (1987), who have $\kappa = \tilde{\kappa} = 1$, we use $\kappa = 1.5$. This supports strong heating anomalies at locations where the mean convergence is high, which is in line with observations. In order to avoid numerical problems, we let the convective heating grow slower if the convection is very large, represented by setting $\tilde{\kappa} = 0.5$. This is qualitatively in line with Gadgil et al. (1984), who suggest that convection does not increase if the SST is above a certain threshold (although others disagree (Roxy, 2013)). In order to avoid having very small-scale convective features, the divergence field is slightly smoothed (see section 3.5.2).

As we are interested in the effect of the Indian Ocean on ENSO, modified by convection over the Maritime Continent and over the east Indian Ocean, we let the moisture availability m obey

$$m(x_a, y) = \begin{cases} (2x_a - L_I)/L_I & \text{if } L_I/2 < x_a < L_I \\ 1 & \text{if } L_I < x_a < L_I + L_{MC} \\ 0 & \text{else} \end{cases}$$

i.e. $m(x_a, y) = 1$ over the Maritime Continent and linearly decreases to zero when moving westwards over the east Indian Ocean. Although the west Pacific is part of the Warm Pool region, nonlinear convection there is neglected, as it would require careful tuning to implement it. The reason is that the fully coupled model does not have a natural background convergence associated with the Hadley cell (recall that the Hadley cell is only incorporated in τ_{ext}). On the other hand, the cold tongue in the east Pacific causes a wind divergence over the equator and thus off-equatorial convergence. In order to compensate this effect, a strong, but carefully tuned background convergence would have to be inserted over the Pacific. In addition, SST variability in the west Pacific is underestimated in our model, so the SST-induced convection anomalies can be expected to be small. Finally, the original Pacific-only model of section 3.1 generates reasonable ENSO variability in absence of west Pacific convection.

The background divergence c^b serves to include the convergence associated with the Hadley circulation over the Maritime Continent and east Indian Ocean and is given by

$$c^b(x_a, y) = c^{b0}(2x_a - L_I)/2L_I \times \exp(-(y^2/2\alpha_y^2)) \text{ for } L_I/2 < x_a < L_I + L_{MC} \quad (3.39)$$

with $c^{b0} = -0.025c_a/L_a$ and $c_a = 30m/s$ the atmospheric Kelvin wave phase speed (see Table 3.1) and $\alpha_y = R_a = 1500km$. The linear increase of c^b with x_a serves to compensate roughly the effect of the cold tongue cooling, which is extends to the Maritime Continent. Over the Pacific and west Indian Ocean c^b need not be specified as $m = 0$ there.

Some of the parameterisations described here may seem somewhat arbitrary. To test the robustness of our results, the simulations presented below in sections 5.2 and 5.3 were repeated with $\kappa \in \{1.0, 1.25, 1.75, 2.0\}$, $m = 1$ over the whole east Indian Ocean, and c_b zonally independent over the east Indian Ocean or the Maritime Continent or both. In all cases, the results are qualitatively similar (not shown). In sections 5.2 and 5.3, $-c(x_a, y) - c^b(x_a, y) < C_0$ in (3.38), so the results do not depend on C_0 provided it is not too small (i.e. $C_0 \geq 0.89$). The results in section 5.4 do not change qualitatively when using $C_0 \in \{0.89, 1.25, 1.5, 2.0\}$.

The scaling parameter γ_c takes values in the order of c_a^2, as will be specified below. This is in agreement with Zebiak (1986) who finds that in the rotation-free case $\gamma_c \lesssim c_a^2$ for $\kappa = 1$ (in Zebiak's notation: $\beta \equiv \gamma_c/c_a^2 \lesssim 1$). Due to the smoothing of c and the presence of rotation, our model allows values a little larger than $\gamma_c = c_a^2$. In the convective case, the atmospheric continuity equation in (3.5) becomes

$$\epsilon_a^* \phi + c_a^2(\partial_{x_a} u^a + \partial_y v^a) = -Q = -Q^T - Q^c \quad (3.40)$$

where $Q^T = \alpha_T(T - T_0)$ and Q^c is defined in (3.38). As opposed to Zebiak and Cane (1987), we do not solve this equation iteratively, but by adding c to the state vector of independent variables. Details on the implementation of the convective feedback are provided in section 3.5.2.

In the linear atmosphere model, the ocean-atmosphere coupling is characterised by $\alpha_T\gamma_\tau$, which determines how much wind stress is generated per surface heating anomaly. Only the product, but not the individual values of α_T and γ_τ matters, hence $\tilde{\alpha}_T = \alpha_T\Delta T L_a/c_a^3$, (the non-dimensionalised α_T) was arbitrarily put to unity by Van der Vaart (1998)(which amounts to scaling the dimensionless winds by $1/\tilde{\alpha}_T$). In the convective case, both wind stresses and winds (for the divergence) are needed, hence α_T cannot be scaled arbitrarily but is taken from Zebiak (1986).[1]

3.5.2 Spatial discretisation

Although $m = 0$ is used over the Pacific in all experiments performed with this model, here the more general case is treated where $m \neq 0$ is allowed over the Pacific. In this section (3.5.2) all quantities are non-dimensional. The non-dimensional zonal coordinates are illustrated in Fig. 3.7b. Atmospheric divergence is scaled with c_a/L_a. As mentioned in section 3.1.2, the convection-free model is discretised using a pseudo-spectral method, and the heating caused by Pacific SST anomalies, namely $Q^T = \frac{\alpha_T L_a \Delta T}{c_a^3}(T - T_0) \equiv \tilde{\alpha}_T(T - T_0)$, can be decomposed as

$$Q^T(x_P, y_P) = \sum_{ij} f_{ij}(x_P, y_P)q_{ij}^T \quad (3.41)$$

---

[1]Zebiak and Cane (1987)have a typo, in their appendix α_T is a factor 10 too large.

The f_{ij} form an orthogonal basis, and the variables are evaluated at the collocation points (x_{Pk}, y_{Pl}) with k and l ranging from 0 to n_x and n_y, respectively. We introduce a shorthand, $Q_{kl}^T = Q^T(x_{Pk}, y_{Pl})$. Now with a finite number of base functions and collocation points, (3.41) actually amounts to a matrix multiplication,

$$Q_{kl}^T = \sum_{ij} F_{kl,ij} q_{ij}^T$$

with $F_{kl,ij} = f_{ij}(x_k^P, y_l^P)$. The decomposition is a bijection, hence one can also write

$$q_{ij}^T = \sum_{kl} P_{ij,kl} Q_{kl}^T$$

where P is the inverse of F.

As explained before, the winds at the (k, l)-th Pacific collocation point are very efficiently computed from the heating coefficients q_{ij}^T and the amplitudes A_m of the m-th Indian Ocean SST pattern:

$$(u_{kl}^a, v_{kl}^a) = \sum_{ij} (\mathcal{A}_{kl,ij}, \mathcal{B}_{kl,ij}) q_{ij}^T + \sum_{m=1}^{n_I} (\mathcal{A}_{kl,m}^I, \mathcal{B}_{kl,m}^I) A_m \tag{3.42}$$

where $\mathcal{A}_{kl,ij}$ and $\mathcal{B}_{kl,ij}$ are the zonal and meridional wind at the (k, l)-th Pacific collocation point in case only the SST mode ij is excited ($q_{ij}^T = 1$), and $(\mathcal{A}_{kl,m}^I, \mathcal{B}_{kl,m}^I)$ are the contributions of the m-th Indian Ocean SST pattern. Winds over the Indian Ocean or Maritime Continent (MC) need not be computed, as they have no effect (no ocean dynamics can be forced by wind here).

In Zebiak and Cane (1987), the convection feedback is computed iteratively. In our implicit implementation of the model, this would require numerical approximations of the Jacobian, or actually $\mathcal{J}$ and $\mathcal{K}$ as defined below in (3.50). Instead, the divergence $c = \partial_{x_a} u^a + \partial_{y_a} v^a$ is added to the state vector, which takes the form $\mathbf{z} = (r_{ij}, q_{ij}^T, c_{ij}, A_k)$. This requires additional, implicit diagnostic equations for c.

The divergence needs to be defined both on Pacific collocation points and over the Indian Ocean and MC, because convective heating over the Indian Ocean or MC can lead to wind anomalies over the Pacific. The Indian Ocean and MC can be mathematically treated as one entity, because their surface temperature is not determined by ocean dynamics, but parametrised. Hence they will collectively be referred to as 'land'. A superscript ^{L} is used to indicate that a quantity is defined over 'land'.

Grid points over land have the same y-coordinates as over sea (i.e. the Pacific), whereas in the x-direction, $n_x^L + 1 = 18$ equidistant points are used. Their nondimensional atmospheric coordinates are $x_k^a = \frac{k(L_I + L_{MC})}{n_x^L L_a}$; $k \in \{0, 1, ..., n_x^L\}$. The base functions over land are of the form

$$f_{ij}^L(x_L, y_L) = \psi_j(y_L) \times \begin{cases} 1 & \text{if } i = 0 \\ \cos(2\pi m x_L) & \text{if } i = 2m - 1; \ m \in \{1, ..., N_c\} \\ \sin(2\pi m x_L) & \text{if } i = 2m; \ m \in \{1, ..., N_s\} \end{cases}$$

where $(N_c, N_s) = ((n_x^L + 1)/2, (n_x^L - 1)/2)$ for odd n_x^L and $(N_c, N_s) = ((n_x^L)/2, (n_x^L)/2)$ for even n_x^L. With these base functions, SST- or convection-induced heating over land can be decomposed in the same way as over the Pacific:

$$Q_{kl}^{LT} = \sum_{ij} F_{kl,ij}^{L} q_{ij}^{LT} \quad , \quad q_{ij}^{LT} = \sum_{kl} P_{ij,kl}^{L} Q_{kl}^{LT}$$

$$Q_{kl}^{Lc} = \sum_{ij} F_{kl,ij}^{L} q_{ij}^{Lc} \quad , \quad q_{ij}^{Lc} = \sum_{kl} P_{ij,kl}^{L} Q_{kl}^{Lc}$$

where $F_{kl,ij}^{L} = f_{ij}^{L}(x_{Lk}, y_{Ll})$, P^{L} is the inverse of F^{L}, and Q^{LT} is determined by the prescribed Indian Ocean SST patterns: $Q_{kl}^{LT} = \tilde{\alpha}_T \sum_{m=1}^{n_I} T_m^{0I}(x_{Lk} y_{Ll}) A_m$. These projections of surface temperature and convection induced heating make it possible to keep using the efficient computation of winds and divergence in terms of the q_{ij}, similar to (3.42).

Now it is possible to write the wind divergence in a similar fashion as (3.42), only that the divergence is needed both above land and above sea. As for the wind, the divergence is influenced by heating both over land and over sea.

The divergence over sea becomes

$$c_{kl} = \sum_{ij} \mathcal{C}_{kl,ij}^{PP}(q_{ij}^{T} + q_{ij}^{c}) + \sum_{ij} \mathcal{C}_{kl,ij}^{PL}(q_{ij}^{LT} + q_{ij}^{Lc}) \tag{3.43}$$

where $\mathcal{C}_{kl,ij}^{PP}$ and $\mathcal{C}_{kl,ij}^{PL}$ are the wind divergence in the Pacific location (x_k^P, y_l^P) caused by heating associated with the ij-th base function in the Pacific and over land, respectively. Analogously the divergence over land becomes

$$c_{kl}^{L} = \sum_{ij} \mathcal{C}_{kl,ij}^{LP}(q_{ij}^{T} + q_{ij}^{c}) + \sum_{ij} \mathcal{C}_{kl,ij}^{LL}(q_{ij}^{LT} + q_{ij}^{Lc}). \tag{3.44}$$

As the convection feedback has a tendency to amplify short-scale features, a slight spatial smoothing has been applied to the $\mathcal{C}$ (e.g. over sea, $\mathcal{C}$ would be a smoothed version of $\partial_{x^a}\mathcal{A} + \partial_{y^a}\mathcal{B}$).

Now we use $Q_{kl}^{c} = A_\kappa \tilde{\gamma}_c m_{kl} [\mathcal{M}(-c_{kl} - c_{kl}^{b})]^\kappa - B_\kappa$ over sea and $Q_{kl}^{Lc} = A_\kappa \tilde{\gamma}_c m_{kl}^{L} [\mathcal{M}(-c_{kl}^{L} - c_{kl}^{Lb})]^\kappa - B_\kappa$ over land with

$$\begin{cases} \kappa = 1.5, \ A_\kappa = 1, \ B_\kappa = 0 & \text{if } -c_{kl} - c_{kl}^{b} < C_0 \\ \kappa = 0.5, \ A_\kappa = a_\kappa, \ B_\kappa = b_\kappa & \text{else} \end{cases}$$

where $\tilde{\gamma}_c = \gamma_c/c_a^2$ is the non-dimensional equivalent of γ_c and a_κ and b_κ have been defined after (3.38). This yields implicit, diagnostic equations for the state variables c_{kl} and c_{kl}^{L}:

$$c_{kl} = \sum_{ij} \mathcal{C}_{kl,ij}^{PP} \{ q_{ij}^{T} + \sum_{k'l'} P_{ij,k'l'} \tilde{\gamma}_c m_{k'l'} (A_\kappa [\mathcal{M}(-c_{k'l'} - c_{k'l'}^{b})]^\kappa - B_\kappa) \}$$

$$+ \sum_{ij} \mathcal{C}_{kl,ij}^{PL} \{ q_{ij}^{LT} + \sum_{k'l'} P_{ij,k'l'}^{L} \tilde{\gamma}_c m_{k'l'}^{L} (A_\kappa [\mathcal{M}(-c_{k'l'}^{L} - c_{k'l'}^{Lb})]^\kappa - B_\kappa) \} \tag{3.45}$$

$$c_{kl}^{L} = \sum_{ij} \mathcal{C}_{kl,ij}^{LP} \{ q_{ij}^{T} + \sum_{k'l'} P_{ij,k'l'} \tilde{\gamma}_c m_{k'l'} (A_\kappa [\mathcal{M}(-c_{k'l'} - c_{k'l'}^{b})]^\kappa - B_\kappa) \}$$

$$+ \sum_{ij} \mathcal{C}_{kl,ij}^{LL} \{ q_{ij}^{LT} + \sum_{k'l'} P_{ij,k'l'}^{L} \tilde{\gamma}_c m_{k'l'}^{L} (A_\kappa [\mathcal{M}(-c_{k'l'}^{L} - c_{k'l'}^{Lb})]^\kappa - B_\kappa) \}.$$

The equations for the total wind over the Pacific have to be extended with the convective heating contribution:

$$(u_{kl}^{a}, v_{kl}^{a}) = \sum_{ij} (\mathcal{A}_{kl,ij}^{PP}, \mathcal{B}_{kl,ij}^{PP})(q_{ij}^{T} + q_{ij}^{c}) + \sum_{ij} (\mathcal{A}_{kl,ij}^{PL}, \mathcal{B}_{kl,ij}^{PL})(q_{ij}^{LT} + q_{ij}^{Lc}).$$

The winds over 'land' have no influence on any dynamics and are not explicitly computed.

3.6   Temporal discretisation and continuation

All model versions described above can either be integrated in time to generate transient simulations, or their equilibrium solutions and linear stability can be analysed using continuation methods. In the latter case, the forcing is constant in time, and noise terms set to zero.

3.6.1   Transient simulations

Time integration is performed employing an implicit scheme. Let the time steps all be of length Δt, and let $\mathbf{z}$ denote the state vector, $\partial_t \mathbf{z}$ its time derivative, and $\mathbf{f}$ all external forcings (e.g. external wind stress, noise terms). The the model equations can be formally written as

$$\mathcal{G}(\partial_t \mathbf{z}, \mathbf{z}, \mathbf{f}) = 0. \tag{3.46}$$

Suppose that at time step n the solution is known to be $\mathbf{z}_n$ and we want to compute $\mathbf{z}_{n+1}$. Then (3.46) can be evaluated at time $(n+\frac{1}{2})\Delta t$, using the approximations $\mathbf{z}_{n+1/2} \approx (\mathbf{z}_n + \mathbf{z}_{n+1})/2$ and $\partial_t \mathbf{z}|_{n+1/2} \approx (\mathbf{z}_{n+1} - \mathbf{z}_n)/\Delta t$. Now (3.46) can be solved iteratively with a Newton scheme. For the exact (and unknown) solution $\mathbf{z}_{n+1}$ the following would hold at time $(n + \frac{1}{2})\Delta t$:

$$0 = \mathcal{G}((\mathbf{z}_{n+1} - \mathbf{z}_n)/\Delta t, \; (\mathbf{z}_{n+1} + \mathbf{z}_n)/2, \; f_{n+1/2}) \tag{3.47}$$

Let $\mathbf{z}_{n+1}^i$ the result of the i-th iteration towards the exact solution. Then a Taylor expansion of (3.47) in the current error $\mathbf{z}_{n+1} - \mathbf{z}_{n+1}^i$ around the current estimate can be made:

$$\begin{aligned} 0 =& \mathcal{G}((\mathbf{z}_{n+1}^i - \mathbf{z}_n)/\Delta t, \; (\mathbf{z}_{n+1}^i + \mathbf{z}_n)/2, \; f_{n+1/2}) \\ &+ (\frac{1}{\Delta t}\partial_1\mathcal{G} + \frac{1}{2}\partial_2\mathcal{G})(\mathbf{z}_{n+1} - \mathbf{z}_{n+1}^i) + \mathcal{O}(||\mathbf{z}_{n+1} - \mathbf{z}_{n+1}^i||^2) \end{aligned} \tag{3.48}$$

where $\partial_1\mathcal{G}$ is the derivative of $\mathcal{G}$ to its first argument, $\partial_t \mathbf{z}$, and $\partial_2\mathcal{G}$ is the derivative of $\mathcal{G}$ to its second argument, $\mathbf{z}$ (both have a matrix form, as $\mathbf{z}$ and $\mathcal{G}$ are vectors). Neglecting terms of quadratic order, 3.48 can be solved for $\mathbf{z}_{n+1}$. The result will be the next estimate of the iteration. When convergence is reached, i.e. when the right hand side of (3.47) is small enough in some suitable norm, the solution at the next time step is computed, using $\mathbf{z}_{n+1}$ as initial guess.

3.6.2   Equilibrium solutions and linear stability

One might also be interested in solutions to 3.46 with time-independent forcing $\mathbf{f}$ and $\partial_t \mathbf{z} = 0$, i.e. equilibrium solutions $\bar{\mathbf{z}}$, and their linear stability. In particular, it might be interesting how an equilibrium state and its stability depend on a certain model parameter p. This can be achieved using the pseudo-arclength continuation method by Keller (1977), nicely summarised in Meijer et al. (2009). The basic idea is that if at steps n and $n-1$ the parameter and the equilibrium solutions were $(\bar{\mathbf{z}}_n, p_n)$ and $(\bar{\mathbf{z}}_{n-1}, p_{n-1})$, then the next pair is first estimated to be

$$(\bar{\mathbf{z}}_{n+1}, p_{n+1}) \quad = \quad (\bar{\mathbf{z}}_n, p_n) + \gamma(\bar{\mathbf{z}}_n - \bar{\mathbf{z}}_{n-1}, p_n - p_{n-1}) \tag{3.49}$$

where γ is chosen such that the step size is constant: $||\gamma((\bar{\mathbf{z}}_n - \bar{\mathbf{z}}_{n-1}, p_n - p_{n-1}))|| = \Delta$ with some suitable norm $|| \cdot ||$. To refine this initial guess and make it obey the equilibrium condition $\mathcal{G}_{p_{n+1}}(0, \bar{\mathbf{z}}_{n+1}, \mathbf{f}) = 0$, a Newton-Raphson method is used with the additional constraint that the corrections to the initial guess are orthogonal to $(\bar{\mathbf{z}}_n - \bar{\mathbf{z}}_{n-1}, p_n - p_{n-1})$ such that the step size is unchanged to first order.

To investigate the linear stability of an equilibrium solution $\bar{\mathbf{z}}$ at parameter value p, a small perturbation $\mathbf{z}'$ around the equilibrium solution is introduced, i.e. $\mathbf{z} = \bar{\mathbf{z}} + \mathbf{z}'$. Neglecting terms of higher than linear order, (3.46) now takes the form

$$\mathcal{K}\partial_t \mathbf{z}' + \mathcal{J}\mathbf{z}' = 0 \tag{3.50}$$

where $\mathcal{K}$ and $\mathcal{J}$ are the (matrix-valued) derivative of $\mathcal{G}$ to its first and second argument, respectively, both evaluated at $(\bar{\mathbf{z}}, p)$ with time-independent $\mathbf{f}$. Solutions to (3.50) take the general form $\mathbf{z}'(t) = \sum_k \mathbf{y}^k e^{\sigma^k t}$ where $\mathbf{y}^k$ is the k-th generalised eigenvector of the generalised eigenvalue problem

$$\mathcal{K}\sigma\mathbf{y} + \mathcal{J}\mathbf{y} = 0 \tag{3.51}$$

and $\sigma^k = \sigma_r^k + i\sigma_i^k$ its (complex) generalised eigenvalue. If all real parts of the eigenvalues σ_r^k are negative, then the amplitudes of all perturbations $\mathbf{z}'$ decay in time and thus the equilibrium solution $\bar{\mathbf{z}}$ is stable.

As shown by Van der Vaart et al. (2000), the original single-basin model has a Hopf bifurcation in the coupling strength μ^*. If $\mu^* < \mu_H^*$, then all eigenvalues have real parts below zero and stable equilibrium exists. However, if the coupling becomes too strong, a complex conjugate pair of eigenvalues crosses the imaginary axis, destabilising the stationary solution and giving rise to an oscillation (limit cycle) whose period near the Hopf bifurcation is given by $P = \frac{2\pi}{\sigma_i}$. This oscillation is the ENSO mode.

Chapter 4

The influence of large-scale Indian Ocean SST variability on ENSO Stability and Flavour[1]

4.1 Introduction

In this chapter, the influence of large-scale Indian Ocean SST variability (i.e. the Indian Ocean Basin-wide warming or IOB) on ENSO will be investigated, using the Gill-based 1.5 basin model introduced in section 3.4. The IOB is the dominant mode of variability in the Indian Ocean and its most prominent response to ENSO, but might also feed back on the Pacific.

   Not only interannual variability, but also long-term temperature trends in the Indian Ocean might influence ENSO by changing the background state of the Pacific (Luo et al., 2012). The Indian Ocean has shown a substantial warming over the last few decades. As mentioned in the introduction, HadISST data (Rayner et al., 2003; Met Office Hadley Centre, 2012), shows a linear warming trend of the IOB index (SST averaged over $20°N - 20°S$, $40 - 100°E$) of $1.2K/100yr$ for 1970-2011, whereas for 1900-1969 this trend is $0.3K/100yr$. For comparison, the corresponding values for Nino3.4 are $0.2K/100yr$ and $-0.2K/100yr$. Thus the Indian Ocean seems to be warming relative to the Pacific, although the uncertainties are large, in particular for the tropical Pacific (Deser et al., 2010). Ashok et al. (2007) have suggested that in recent decades central Pacific (CP) El Niños have become more frequent, compared to the classical east Pacific (EP) El Niños.

   In this chapter, two questions will be treated:

1. Can the recent long-term Indian Ocean warming trend explain the more frequent occurrence of CP El Niños?

2. How does ENSO-induced IOB variability feed back on ENSO?

After briefly describing the behaviour of the system in absence of Indian Ocean influence as a reference case (section 4.2), the first and second question will be addressed in sections 4.3 and 4.4, respectively.

---

[1]This chapter is based on the article Wieners, C.E., W.P.M de Ruijter, and H.A. Dijkstra, 2017: The influence of the Indian Ocean on ENSO stability and flavour. J. Climate, 30, 2601– 2620
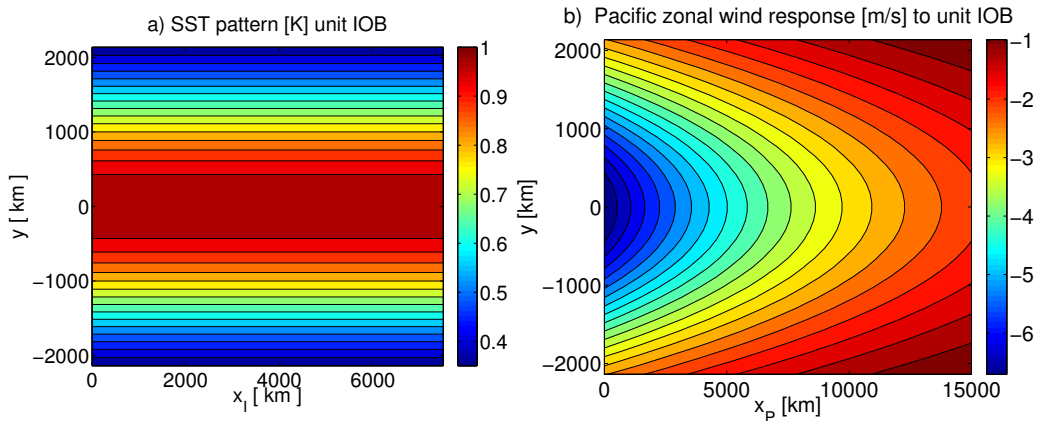
Figure 4.1: *a) The IOB-related Indian Ocean SST pattern $T^{0I}_{IOB}(x_I, y)$; the zonal coordinate x_I ranges from the east coast to the west coast of the Indian Ocean and $y = 0$ on the equator. b) The zonal wind response over the Pacific Ocean associated with T^{0I}; here coordinates are Pacific coordinates ($x_P = 0$ on the Pacific west coast).*

Both questions can be tackled using the Gill-based 1.5 basin model introduced in section 3.4, i.e. disregarding the effect of a non-linear convection feedback, owing to the large Gill response to zonally uniform Indian Ocean SST anomalies. This will be justified in section 5.3. On the other hand, for smaller-scale Indian Ocean variability such as the Indian Ocean Dipole (IOD), nonlinear convection might play an important role, hence these will not be addressed here, but will be investigated in chapter 5, using the convective 1.5 basin model.

As only one Indian Ocean mode is considered, namely the IOB, (3.32) takes the form

$$T_I = T_0 + T^{0I}_{IOB}(x_I, y)A_{IOB}(t) \qquad (4.1)$$

where T^{0I}_{IOB} is the spatial pattern of the SST anomaly and A_{IOB} a time-dependent amplitude which may depend on ENSO. Since we only treat one Indian Ocean mode in this chapter, the subscript 'IOB' in T^{0I}_{IOB} and A_{IOB} will be dropped for the rest of chapter. The spatial pattern T^{0I} obeys $T^{0I}(x_I, y) = 1\text{K} \times \exp[-(y/y_0)^2/2]$, i.e. it is zonally independent and Gaussian in the meridional direction. A plot is shown in Fig. 4.1a. The amplitude A is here assumed to evolve in a purely deterministic way, hence the noise term in (3.33) is dropped, yielding

$$\frac{dA}{dt} = a_0 \cos(\psi)(N - \bar{N}) + \frac{a_0}{\omega} \sin(\psi)\frac{dN}{dt} + a_c + a_d A \qquad (4.2)$$

where N is the El Niño index defined in (3.37), $\bar{N}$ its equilibrium value, and ω the angular frequency of the ENSO cycle. ψ is a constant used to set the phase relation between N and A. Temperature anomalies $T_I - T_0$ in the Indian Ocean lead to a Gill response in the atmosphere, as described in (3.34)-(3.36), which causes a wind contribution over the Pacific Ocean (see Fig. 4.1b).

In order to simplify the notation, the Pacific dimensional zonal coordinate x_P will be simply denoted by x and takes the value 0 at the west coast and $1.5 \times 10^7 km$ at the east coast of the Pacific. The model parameters are given in Tables 3.1 and 3.2.
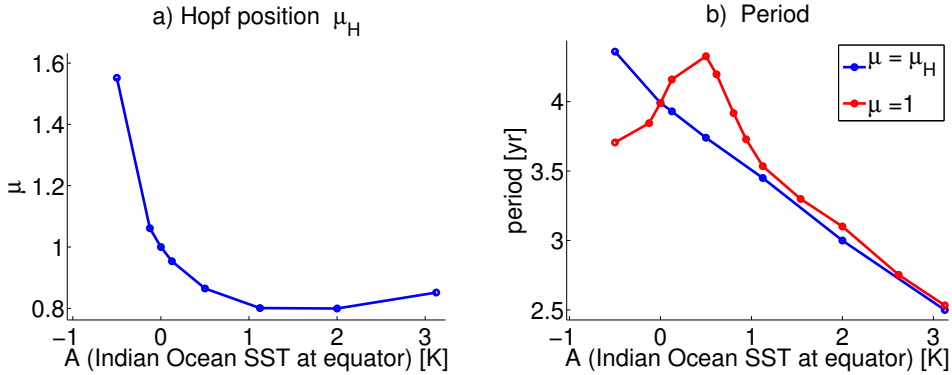
Figure 4.2: *Dependence of (a) the position of the Hopf bifurcation μ_H and (b) ENSO period at $\mu = 1$ (red) and $\mu = \mu_H$ (blue) on the (time-independent) Indian Ocean SST. $A(t) = +1$ amounts to an Indian Ocean SST of $1K$ above radiative equilibrium at the equator.*
The reference case of section 4.2 corresponds to the points at $A = 0$.

4.2 Reference case

In the reference case, the effect of the Indian Ocean is switched off, i.e. $A = 0$ and hence $T_I = T_0$. The results are then the same as for the original Pacific-only ZC model by Van der Vaart et al. (2000). For the parameters as in 3.1, the Hopf bifurcation of the ENSO mode (the generalised eigenvector to (3.51) with the largest real part) occurs at $\tilde{\mu} = 4.16 \equiv \tilde{\mu}_{H0}$, where $\tilde{\mu}$ is the (non-dimensional) coupling strength determining how much the wind stress is affected by a certain SST anomaly (see Table 3.2). To simplify the notation, for the rest of this chapter coupling strengths will be expressed through their ratio with $\tilde{\mu}_{H0}$, i.e. in terms of $\mu \equiv \tilde{\mu}/\tilde{\mu}_{H0}$. The symbol μ_H will be used to denote the value of μ at which a Hopf bifurcation occurs for general A (i.e. for $A = 0$, $\mu_H = 1$). The period P of the ENSO mode at $A = 0$ and $\mu = \mu_H$ is 4.0 years (see Fig. 4.2b).

The SST, thermocline depth and upwelling equilibrium fields at $A = 0$ and $\mu = 1$ are shown in Fig. 4.3d-f. The equilibrium state has a cold tongue with the lowest temperature $\bar{T}_m = 25°C$ at $x = \bar{x}_m = 1.36 \times 10^4 km, y = 0$. The thermocline becomes as shallow as $167m$ ($33m$ above the reference value $H = 200m$) at the east coast, and the strongest equatorial upwelling of 100cm/day occurs at $x \approx 1.18 \times 10^4 m$.

The SST field of the eigenvector at this Hopf bifurcation (the generalised eigenvector in (3.51) with the largest real part) is plotted in Fig. 4.4c-d. In order to characterise the zonal shape of SST anomalies, we define a measure

$$\tilde{\gamma}_{EM} \equiv \tilde{T}_E / \tilde{T}_M, \tag{4.3}$$

where $\tilde{T}_E$ is the equatorial amplitude of the SST anomaly at the east coast, while $\tilde{T}_M$ is the largest equatorial SST amplitude found (typically at the position $\tilde{x}_M \approx 1.3 \times 10^4 km, \tilde{y}_M = 0$). So $\tilde{\gamma}_{EM}$ measures the strength of the ENSO signal near the east coast; the lower the value of $\tilde{\gamma}_{EM}$, the weaker the coastal signal. In addition, we define the phase difference between the signal at the coast and at $x = \tilde{x}_M$ as

$$\Delta\phi_{EM} = \phi_E - \phi_M, \tag{4.4}$$
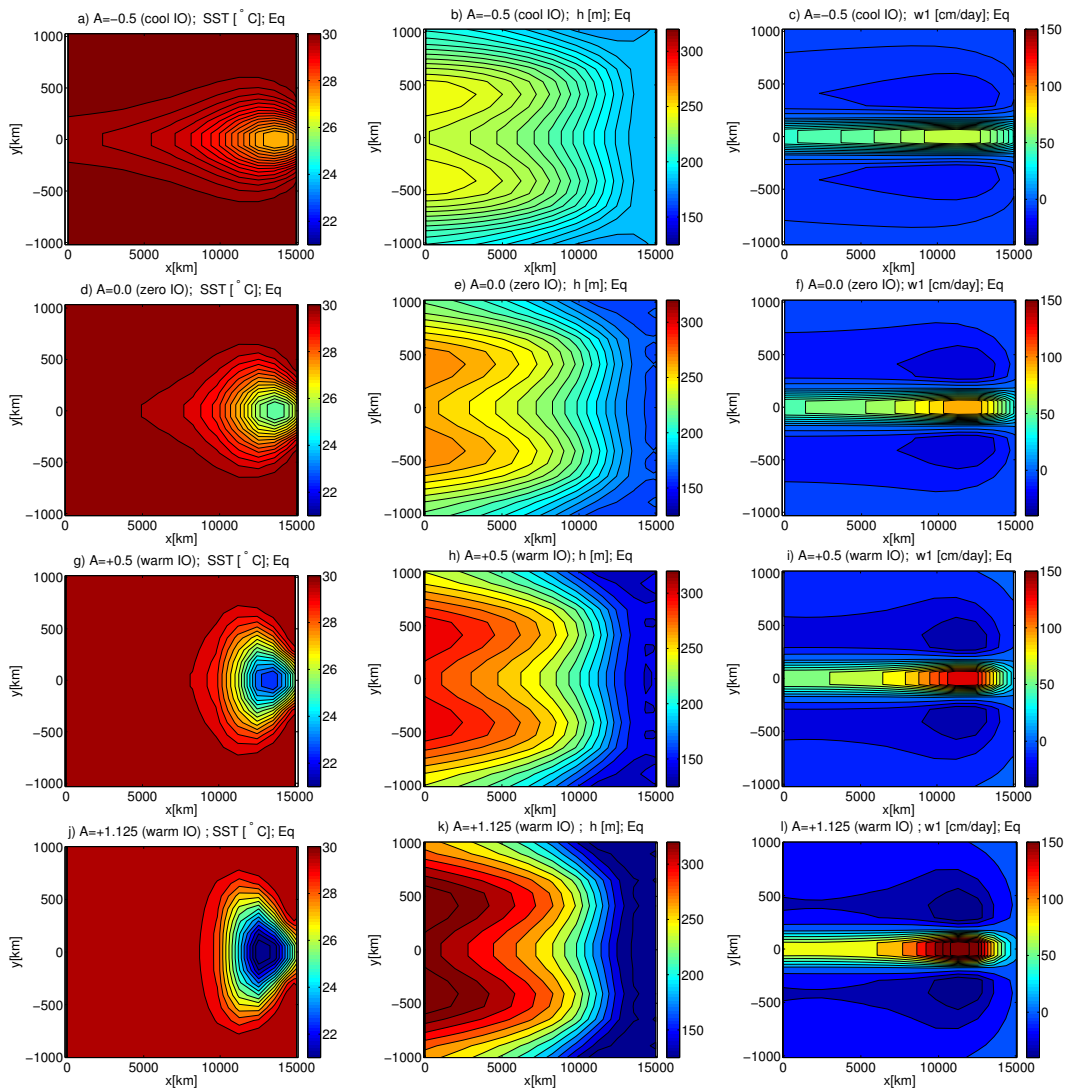
Figure 4.3: *Equilibrium solutions for the constant Indian Ocean cases at* $\mu = 1$. *(a) SST (in °C), (b) thermocline depth (in m below sea level), and (c) upwelling (in cm/day) for* $A = -0.5$. *(d-f) The same but for* $A = 0$ *(the reference case of section 4.2); (g-i) the same but for* $A = +0.5$; *(j-l) the same but* $A = +1.125$.
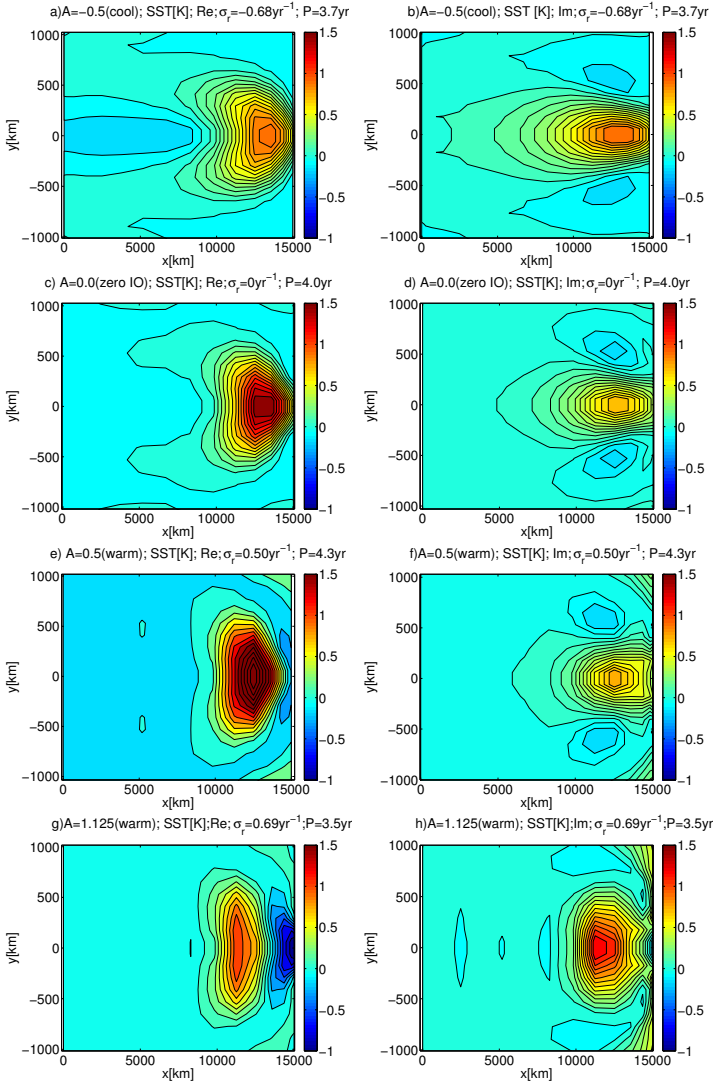
Figure 4.4: *The SST pattern of the ENSO eigenvectors for constant Indian Ocean simulations at $\mu = 1$. (a) real part and (b) imaginary part for $A = -0.5$; (c) and (d) the same but for $A = 0.0$ (the reference case of section 4.2); (e) and (f) the same but $A = +0.5$; (g) and (h) the same but $A = +1.125$. The growth rate σ_r is the real part of the eigenvalue, the period P is given by $2\pi/\sigma_i$, where σ_i is the imaginary part of the eigenvalue. In all plots, $\sigma_i > 0$, so the imaginary part of the eigenvector leads the real part by $90°$ or $1/4\,P$.*

A	-0.5	0.0	$+0.5$	$+1.125$
$\sigma_r[yr^{-1}]$	-0.67	0.0	$+0.5$	$+0.69$
$\tilde{x}_M[10^4 km]$	1.32	1.29	1.26	1.17
$\tilde{\gamma}_{EM}$	0.56	0.36	0.15	0.61
$\Delta\phi_{EM}[P]$	0.02	0.03	0.27	0.39
$\bar{T}_m[°C]$	27.7	25.1	22.4	20.1
$\bar{x}_m[10^4 km]$	1.37	1.36	1.33	1.28
$\bar{\gamma}_{Em}$	0.80	0.70	0.56	0.38
$\bar{\gamma}_{Em,upw}$	0.53	0.36	0.19	0.085
$(\lambda_{zadv})/(\lambda_{thc}+\lambda_{upw})$	0.16	0.27	0.54	0.84

Table 4.1: *The measures characterising the ENSO mode and the mean state in the cold (A = −0.5), zero (A = 0) and warm (A = 0.5, A = 1.125) Indian Ocean cases, all at $\mu = 1$. The first four measures describe the ENSO mode: σ_r is the growth factor, $\tilde{x}_M$ the zonal coordinate of the maximal SST amplitude, $\tilde{\gamma}_{EM}$ the ratio between the SST amplitude at the east coast and at $\tilde{x}_M$, and $\Delta\phi_{EM}$ the lag between the SST at the east coast and at $\tilde{x}_M$ (positive if the coastal signal is leading), measured in ENSO periods P (for values of P, see Fig. 4.2). The next four measures characterise the background state: $\bar{T}_m$ is the lowest SST in the cold tongue, $\bar{x}_m$ the zonal location of $\bar{T}_m$, $\bar{\gamma}_{Em}$ the ratio between the mean SST at the coast and $\bar{T}_m$, and $\bar{\gamma}_{Em,upw}$ is defined as $\bar{\gamma}_{Em}$ but for the mean upwelling $\bar{w}_1$ rather than SST. Finally, $(\lambda_{zadv})/(\lambda_{thc}+\lambda_{upw})$ is the ratio between the contributions of zonal advection and thermocline+upwelling processes to the Bjerknes feedback.*

which is positive if the signal at the east coast is leading. The reference case has $\tilde{\gamma}_{EM} = 0.36$, i.e. the ENSO amplitude at the coast is only about $1/3$ of the amplitude at $\tilde{x}_M = 1.29 \times 10^4 km$. The phase difference is $\Delta\phi_{EM} = 10° = 0.03P$, i.e. the coastal and off-shore signal are nearly in phase.

A measure similar to $\tilde{\gamma}_{Em}$ can be defined to characterise the shape of the background cold tongue:

$$\bar{\gamma}_{Em} \equiv (\bar{T}_E - T_0)/(\bar{T}_m - T_0) \qquad (4.5)$$

where $\bar{T}_E$ is the equilibrium SST at $(x = L_P, y = 0)$, and $\bar{T}_m$ the lowest temperature found in the cold tongue of the background state, at $x = \bar{x}_m$. For the equilibrium state, $\bar{\gamma}_{Em} = 0.7$ and $\bar{x}_m = 1.35 \times 10^4 km$. The El Niño index N of the equilibrium state takes the value $\bar{N}_{ref} = -4.19$.

4.3   Constant Indian Ocean SST

We first consider the case where the Indian Ocean SST deviation $T_I - T_0$ is non-zero but constant. This is achieved by putting $a_0 = 0$ in (4.2) and yields $T_I(y = 0) - T_0 = A = -a_c/a_d$. The effect on ENSO stability is analysed by performing a continuation, first in a_c, then in μ, starting from $a_c = 0$, $\mu = 1$ (the reference case). As shown in Fig. 4.2a, the Hopf bifurcation shifts to higher (lower) values of μ for a cool (warm) Indian Ocean. For $A \lesssim -0.5K$, the Hopf bifurcation value shifts to large values of μ indicating a strong stabilisation. At $A \approx 2$, μ_H reaches a minimum of 0.80 and then slowly increases again. The period at $\mu = 1$ (red curve in Fig. 4.2b) has a maximum of 4.3 yr for $A \approx 0.5$. For $\mu = \mu_H$ the period is lower (higher) than at $\mu = 1$ for warm (cool) Indian Ocean (blue curve in Fig. 4.2b). As a constant warm Indian Ocean adds a constant easterly wind
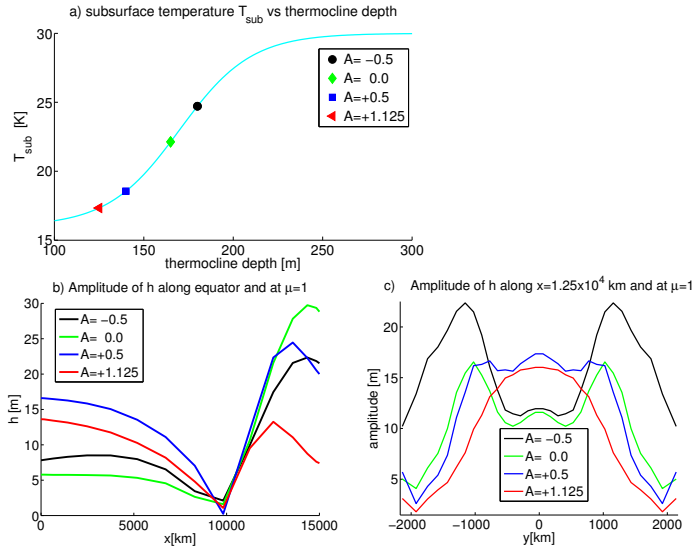
Figure 4.5: *a) Dependence of the subsurface temperature T_{sub} on thermocline depth h. The markers denote the conditions found at the east coast on the equator for the $A = -0.5$ (black circle), $A = 0$ (green diamond), $A = 0.5$ (blue square) and $A = 1.125$ (red triangle); b) amplitudes of h along the equator (obtained from the ENSO eigenvector) for $A = -0.5$ (black), $A = 0$ (green), $A = 0.5$ (blue) and $A = 1.125$ (red). c) same as b but along $x = 1.25 \times 10^4 km$.*

stress, which is similar to increasing τ_{ext}, the results are in qualitative agreement with those in Van der Vaart et al. (2000), who found that μ_{crit} first decreases, then saturates with τ_{ext} and that both for very low and very high τ_{ext} the period decreases (see their Fig. 14) at fixed μ. They also found that the period increases with μ.

The value of T_I does not only affect stability but also the spatial patterns of the associated SST anomalies. Fig. 4.4 shows the SST patterns of the ENSO mode, for $A \in \{-0.5, 0.0, 0.5, 1.125\}$. In order to exclude the influence of μ itself, all plots are for $\mu = 1$. So for $A = -0.5$ the ENSO mode is damped (the real part of the eigenvalue, σ_r, is negative; see Table 4.1), whereas for $A > 0$ the ENSO mode grows. For a cool Indian Ocean, SST anomalies are zonally more elongated, while for a warm Indian Ocean, they are more compact and detached from the east coast.

To quantify this, the results for the position of maximal SST amplitude x_M, the ratio between coastal and maximal ENSO amplitude $\tilde{\gamma}_{EM}$, (see (4.3)), and the phase difference $\Delta\phi_{EM}$ (see (4.4)) are given in Table 4.1. With increasing A, x_M shifts westwards, and the SST anomaly directly at the coast is nearly in phase with the signal at x_M for cool and neutral Indian Ocean, but weakens when A is increased. For a very warm Indian Ocean, the coastal signal becomes stronger again, but the phase difference approaches 0.5, i.e., the SST at the coast has a minimum shortly after the SST at x_M reaches its maximum. So while for low Indian Ocean temperatures the ENSO mode resembles the EP El Niño pattern, increasing the Indian Ocean temperature leads to a more CP-like ENSO mode.

In the y-direction, SST anomalies broaden with increasing A, while the amplitude of thermocline depth anomalies (Fig. 4.5c) becomes narrower from $A = +0.5$ to $A = +1.125$. For lower A such a statement is hard to make since at least for $A = -0.5$ a mid-

latitude basin mode (Cessi and Paparella, 2001) with strong off-equatorial h-variability is mixed into the ENSO mode. The narrowing of the h anomalies between $A = 0.5$ and 1.125 explains the decreasing period (Fig. 4.2b), as broader h signals indicate a stronger contribution from higher, and hence slower, Rossby modes (Kirtman, 1997).

T_I also affects the mean state (Fig. 4.3, Table 4.1). The cold tongue in the east Pacific is much weaker for the cool Indian Ocean than for the warm Indian Ocean. The zonal position $\bar{x}_m$ of the SST minima slightly shifts westward with increasing A, and like the SST anomalies, the equilibrium cold tongue becomes more zonally confined with increasing A, as reflected by the decrease in $\bar{\gamma}_{Em}$ (see (4.5)). In addition, the cold tongue becomes wider in the meridional direction. The equilibrium solution of the thermocline has a similar spatial pattern for all cases, but the thermocline slope is far greater for warm Indian Ocean. Likewise, the equilibrium upwelling is strongest for the warm Indian Ocean. The strongest upwelling is found at $x = 1.13 \times 10^4$km in all cases, but again the ratio between coastal and maximal value, $\bar{\gamma}_{Em,upw}$, strongly decreases with increasing A.

These results can be understood using the fact that a warm Indian Ocean enhances the mean easterlies over the Pacific, causing a stronger background equatorial upwelling $\bar{w}_1$ and a steeper thermocline (Fig. 4.3). In case of stronger $\bar{w}_1$, thermocline anomalies have a stronger effect on the SST, enhancing the thermocline feedback. This explains the shift of the Hopf bifurcation to lower μ in the warm Indian Ocean case, as a weaker SST-atmosphere coupling suffices to generate self-sustained oscillations if other components of the Bjerknes feedback are strengthened. In addition, a steeper thermocline and stronger $\bar{w}_1$ strengthen the cold tongue (Fig. 4.3). For a very cool Indian Ocean with $T_{IO} \lessapprox -0.5K$ the background state cold tongue in the east Pacific cannot maintain itself but shifts to the west Pacific. Increasing easterlies also strengthen poleward surface currents (Ekman transport), and hence meridional advection, which explains the meridional broadening of both the anomalous and the equilibrium SST signal with increasing A.

These arguments are confirmed with the analysis of the Bjerknes feedback terms (Fig. 4.6; for computational details, see Appendix of this chapter). The thermocline term, which is due to anomalies in $T - T_{sub}(h)$, is dominant and increases with A. The upwelling feedback due to anomalies in w_1 also increases from $A = -0.5$ to $A = 0$. The ratio of zonal advection to the sum of thermocline and upwelling terms, $(\lambda_{zadv})/(\lambda_{thc} + \lambda_{upw})$, strongly increases with A (Table 4.1) until for $A = 1.125$ advection contributes almost as strongly to the growth factor as thermocline and upwelling processes. The fact that advection does not actually become stronger than vertical processes may be due to the fact that the ZC-model is quite thermocline-feedback dominated. Partially, this increase in zonal advection terms is explained by stronger equilibrium currents and a more intense cold tongue. In addition, since for high A the SST anomalies become more zonally confined, the zonal SST gradients increase relative to the magnitude of the SST signal (larger $(\partial_x T)/T$). Zonal winds and currents increase accordingly. Both the increase in SST gradients and zonal currents (anomalous or equilibrium) leads to increased zonal advection. Meridional advection, which mainly leads to a poleward extension of SST signals generated at the equator, is hardly affected by A. The stronger meridional equilibrium currents are partially compensated by decreased meridional SST gradients due to broader signals.

To understand the increase in μ_{crit} for very large A (Fig. 4.2a) and the changes in spatial patterns we consider the parametrisation of T_{sub}, the temperature of upwelled water. According to (3.4), $T_{sub}(h)$ becomes saturated for very high or low h. For a shallow thermocline, as found in the eastern Pacific in the warm Indian Ocean cases, dT_{sub}/dh is considerably smaller than in the cool Indian Ocean case (Fig. 4.5a), which reduces the
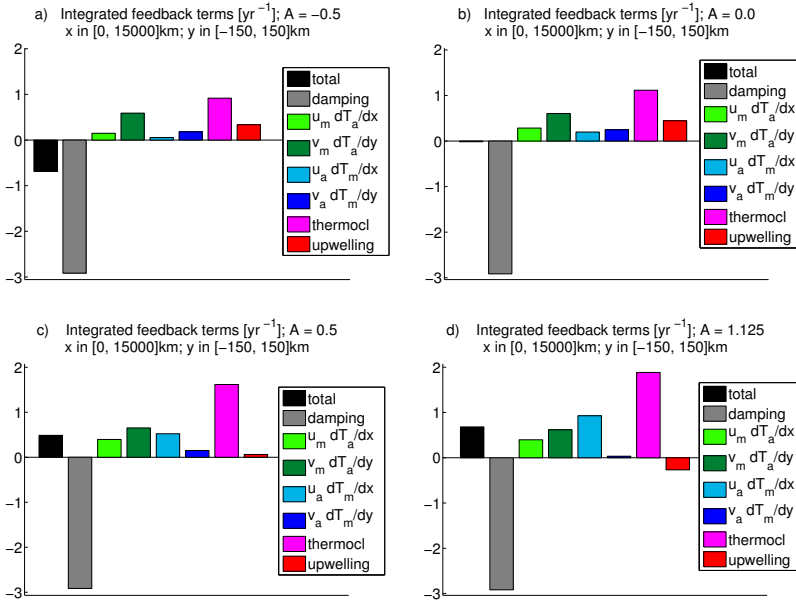
Figure 4.6: *Bjerknes feedback contributions for (a) $A = -0.5$, (b) $A = 0$, (c) $A = 0.5$, (d) $A = 1.125$, all at $\mu = 1$. In all plots, the bars indicate (from left to right) the total growth factor (black), damping (grey), zonal and meridional advection of SST anomalies by equilibrium currents (light and dark green), zonal and meridional advection of equilibrium SST by anomalous currents (light and dark blue), $T - T_{sub}$ anomalies (thermocline feedback; magenta) and upwelling anomalies (red).*

influence of h anomalies on the SST. This reduction in the thermocline feedback explains why μ_{crit} does not decrease further when A is increased beyond ≈ 2.

For cool and zero Indian Ocean, thermocline anomalies have a relatively strong effect near the east coast as their amplitude peaks near the coast (Fig. 4.5b). Here, dT_{sub}/dh is large and the background upwelling $\bar{w}_1$ at the coast is not much weaker than off-shore. For warmer Indian Ocean, the amplitude of the h anomaly and dT_{sub}/dh near the coast decrease and the difference in $\bar{w}_1$ between the coast and $x = 1.13 \times 10^4$km increases, so the coastal SST amplitudes weaken relative to the off-shore ones (lower $\tilde{\gamma}_{EM}$). If the thermocline is quite shallow and T_{sub} is near saturation in the whole eastern Pacific (say, east of $x = 1.2 \times 10^4$km), the location of the strongest SST amplitude (x_M) is dominated by the amplitude of the upwelling w_1. Equatorial upwelling tends to be stronger (weaker) to the west (east) of cool SSTs because of the SST-induced easterlies (westerlies). This further increases the westward shift of x_M and the reduction in $\tilde{\gamma}_{EM}$, as the warm (cool) off-shore SST anomalies during El Niño (La Niña) cause upwelling (downwelling) and hence cooling (warming) near the coast.

For $A = 1.125$ this effect is so strong that the coastal signal is nearly in anti-phase with the off-shore variability. This is in line with Kao and Yu (2009), who find that CP El Niños are more dominated by local wind, while EP El Niños are more related to thermocline processes. It also explains the negative contribution of upwelling feedback to the growth factor for $A = 1.125$ (Fig. 4.6d). The upwelling anomalies have their strongest effect on SST near the east coast (strong zonal SST gradients and hence strong winds) and are nearly in anti-phase with the main, offshore, El Niño signal. Locally, the upwelling term does enhance the (coastal) SST signal.

Similar arguments can be used to explain how T_{sub} saturation and the effect of low (equilibrium) SSTs in the cold tongue on the wind and hence the upwelling lead to a more off-shore cold tongue for warm Indian Ocean.

We confirmed that the Indian Ocean-induced decrease in μ_H leads to a significant increase in ENSO variability by performing time integrations at $\mu = 0.86$ (below the Hopf bifurcation for $A = 0$) and with a simple wind noise (spatially Gaussian, centred around $x_P = L_P/2$, $y_P = 0$, temporally white noise at a time step of 2.5weeks, and a standard deviation of $1.5F_0$). The resulting standard deviation of N was found to be 0.79 for $A = -0.5$, 1.57 for $A = 0$, and 2.93 for $A = +1$.

4.4   Covarying Indian Ocean SST

Next, the case is considered wherein T_I co-varies with the Pacific ENSO cycle, but has no constant offset (i.e. $a_c = 0$ in (4.2)). The most realistic phase relation between ENSO and Indian Ocean SST is that T_I peaks a few months after N. However, in order to better understand the behaviour of the coupled Indo-Pacific system, four cases are considered, wherein T_I peaks shortly after the maximum of N (i.e. during the decay of El Niño; this case will be referred to as ED case), shortly after the minimum of dN/dt (i.e. during the growth of La Niña; the LG case), after the minimum of N (i.e. during the decay of La Niña; the LD case) or after the maximum of dN/dt (i.e. during El Niño growth; the EG case). The ED case is the most realistic one.

For the ED and LD cases, the phase parameter ψ in (4.2) takes the values 0 and 180°, respectively, so (4.2) becomes

$$\frac{dA}{dt} = \pm a_0(N - \bar{N}) + a_d A, \tag{4.6}$$
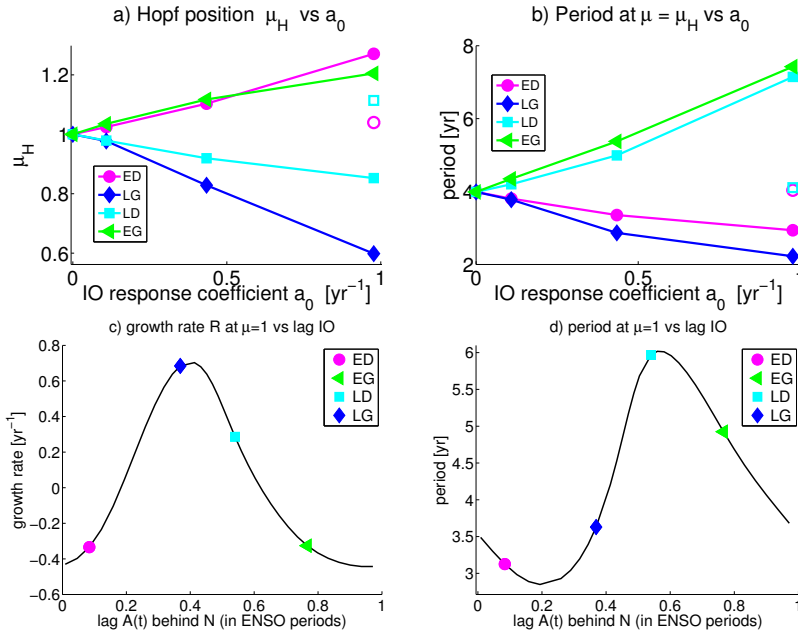
Figure 4.7: *Effect of co-varying T_I on (a) the position of the Hopf bifurcation μ_H and (b) the period of the ENSO mode at $\mu = \mu_H$. Magenta circles: ED case (T_I peaks shortly after the maximum of the El Niño index N); blue diamonds: LG case (T_I peaks after minimum of dN/dt); cyan squares: LD case (T_I peaks after minimum of N); green triangles: EG case (T_I peaks after maximum of dN/dt). The unfilled magenta circles (cyan squares) correspond to the control of the ED (LD) cases, as explained in the text. Panels (c) and (d) show the growth rate and period for $a_0 = 0.43yr^{-1}$ and $\mu=1$ versus the lag ϕ between A and N. A lag value of 1/4 means that A peaks 1/4 period later than N. Positive (negative) values of σ_r indicate growth (damping). Coloured markers denote the results for the ED (magenta circle), LG (dark blue diamond), LD (cyan square) and EG (green triangle) cases.*

where the upper (lower) sign corresponds to the ED (LD) case, and $a_0 > 0$ scales the effect of the Indian Ocean. If one performs a continuation in a_0 from $a_0 = 0$ and choses $\bar{N}$ to equal the N value at $a_0 = 0$, then $A = 0$ remains the equilibrium solution for A (in physical terms, A is zero-mean), so the Indian Ocean does not affect the equilibrium state. But the eigenvectors and eigenvalues - hence the stability of the equilibrium - are affected. As we start our continuation from the Hopf bifurcation of the reference case, $\bar{N} = \bar{N}_{ref} = -4.19$ is chosen.

For the EG and LG cases, ψ in (4.2) takes the values $90°$ and $270°$, respectively, so (4.2) becomes

$$\frac{dA}{dt} = \pm\frac{a_0}{\omega}\frac{dN}{dt} + a_d A, \tag{4.7}$$

where the upper (lower) sign corresponds to the EG (LG) run and ω is the angular frequency of the ENSO mode. The factor $1/\omega$ in (4.7) ensures that the effect of ENSO on A has the same scale in (4.6) and (4.7), since in a harmonic oscillation N and $1/\omega \, dN/dt$ have the same amplitude. As ω is not known a priori, the value of the reference case is chosen, i.e., $\omega = \omega_{ref} \equiv 2\pi/(4.0\,yr)$. Again, $A = 0$ in the equilibrium solution and the Indian Ocean only affects the stability of the equilibrium state.

For all co-varying Indian Ocean cases, $a_d = 3.8\text{yr}^{-1}$ is chosen. It can be shown that with $\omega = \omega_{ref}$ this leads to a phase difference (ϕ) between N and A of $\phi = \arctan(-\omega/a_d) = 22° + n \times 90°$ where $n = 0, 1, 2, 3$ in the ED,LG,LD,EG case, respectively. For example, in the EG case, as long as the period remains close to the 4yr of the reference run, the Indian Ocean SST peaks about 3 months (1/16 period) after N. Also, for $a_0 = 0.98\text{yr}^{-1}$ the amplitude of $T_I(x, y = 0, t)$ is about 1/4 of the amplitude of N.

As can be seen from Fig. 4.7a, the ENSO mode is stabilised for the ED and EG cases and destabilised or the LD and LG cases. At $a_0 = 0.98\text{yr}^{-1}$, μ_H increases to 1.27 and 1.21 for the ED and EG cases, respectively, while for the LD and LG cases, μ_H is reduced to 0.85 and 0.60, respectively. By construction, the period at $\mu = \mu_H$ (Fig. 4.7b) of the ENSO mode is 4.0yr for $a_0 = 0$. For ED and LG, the period at the Hopf bifurcation is reduced to 2.9yr and 2.24yr, respectively, while in the LD and EG cases the period increases to 7.1yr and 7.4yr, respectively.

Performing a continuation in μ away from $\mu = 1$ can cause $\bar{N}$, the true equilibrium value of N, to deviate from $\bar{N}_{ref}$, the estimate for $\bar{N}$ used in (4.6). In the ED and LD cases, this leads to a non-zero equilibrium solution of A, with a value of $\mp a_0(\bar{N} - \bar{N}_{ref})/a_d$. In order to estimate whether the shifts in μ_H (Fig. 4.7a) and period at $\mu = \mu_H$ (Fig. 4.7b) in the ED and LD cases are due to the constant or to the oscillatory contribution to A, a control case was performed with

$$\frac{dA}{dt} = \pm a_0(\bar{N} - \bar{N}_{ref}) + a_d A, \tag{4.8}$$

i.e., with a constant A equal to the error arising from the shift in $\bar{N}$. The results of these control cases for $a_0 = 0.98yr^{-1}$ are shown as unfilled markers in Fig. 4.7a,b. The period in the control cases hardly differs from the 4yr obtained in the reference case, while μ_H changes from $\mu_H = 1$ in the reference case to 1.04 (ED control) and 1.11 (LD control). However, the difference in μ_H between the full ED (LD) case and the corresponding control case is still positive (negative), so apparently the co-varying, zero-mean contribution of A indeed increases (reduces) μ_H, i.e., dampens (destabilises) the ENSO mode.

In order to estimate the optimal lag ϕ between N and A for which ENSO is most strongly destabilised/stabilised, a set of cases is considered with

$$\frac{dA}{dt} = \cos(\psi)\,a_0(N - \bar{N}_{ref}) + \sin(\psi)\frac{a_0}{\omega}\frac{dN}{dt} + a_d A, \tag{4.9}$$

for $\psi \in [0, 360°]$. Fig. 4.7c,d show the growth rate σ_r and the period P, respectively, at $a_0 = 0.43\mathrm{yr}^{-1}$ and $\mu = 1$, against ψ. (If P were not affected, then ϕ, the phase difference between A and N, would obey $\phi = \psi + 22° = \psi + 0.06\,P$; but in reality there are slight deviations in that relation since P depends on ψ.) The ENSO mode is most strongly damped if $\phi = 0.95\,P$, i.e. the Indian Ocean SST peaks $0.05\,P$ before N; this situation is between the EG and ED case. The strongest destabilisation occurs if A peaks $0.41\,P$ later than N, which close to the LG case. The period of the ENSO mode at $\mu = 1$ is shortest if A lags N by $0.19\,P$, and longest for a lag of $0.56\,P$. Since the observed phase relation between A and N is close to the ED case, these results suggests that the Indian Ocean damps ENSO and shortens its period, since in observations the lag between the Basin Wide Warming mode and Nino3.4 is about 3 months and $P \approx 4\mathrm{yr}$, i.e. the lag is roughly $0.1\,P$.

Again, the above results can be understood in terms of the easterlies induced by a warm Indian Ocean. If the A and N peaks nearly coincide, then easterlies (westerlies) are induced during El Niño (La Niña), opposing the westerlies (easterlies) induced by the Pacific SST anomalies. To overcome this damping effect, higher coupling strength in the Pacific is needed, hence μ_H is increased in the EG and ED cases. Similarly, if A and N are in anti-phase, the Indian Ocean-induced winds re-enforce those of the Pacific, the ENSO mode is destabilised and μ_H decreases. Concerning the periods, if the lag between N and A is about $1/4$ period, the Indian Ocean generates easterlies (westerlies) when the winds induced by Pacific SST switch from westerly to easterly (from easterly to westerly), i.e. the switch in wind direction is facilitated and can occur earlier, and hence the period decreases. If, however, the lag is about $3/4$ periods, the change in wind direction is delayed and the period is lengthened.

Next, we turn to the influence of T_I on the spatial pattern of the ENSO mode. In order to exclude the strong influence of μ on $\tilde{\gamma}_{EM}$, we evaluate $\tilde{\gamma}_{EM}$ at $\mu = 1$ and $a_0 = 0.43\mathrm{yr}^{-1}$. For the reference case with $a_0 = 0$, we found $\tilde{\gamma}_{EM} = 0.36$. Adding a co-varying Indian Ocean affects $\tilde{\gamma}_{EM}$ only slightly. The values are 0.34 (ED), 0.43 (LG), 0.39 (LD) and 0.31 (EG). By construction, as long as $\mu = 1$, the background state is independent of a_0. These changes in $\tilde{\gamma}_{EM}$ can be explained as follows. The winds induced by the Indian Ocean extend till the Pacific east coast (Fig. 4.1b). If A peaks during El Niño, the Indian Ocean generates easterlies and hence upwelling near the coast, where the Pacific-induced wind signal is quite weak. So the Indian Ocean-induced winds lead to a slight cooling/reduced warming near the coast during El Niño. Hence the coastal SST signal is weakened and $\tilde{\gamma}_{EM}$ is reduced in the EG and ED cases, whereas for the LG and LD cases, $\tilde{\gamma}_{EM}$ increases. The changes in $\tilde{\gamma}_{EM}$ observed here are much weaker than those associated with changes in the background state, i.e. for constant T_I. So apparently the background state affects the spatial pattern of ENSO more strongly than the co-varying Indian Ocean.

These arguments are confirmed by a Bjerknes analysis (Fig. 4.8). The differences in stability between the four cases are mainly due to changes in the thermocline and upwelling feedback. The thermocline feedback is strongest in the LG case. The Indian Ocean-induced easterlies, peaking shortly after N becomes negative, cause an additional tilt in the thermocline some time later, which roughly coincides with, and re-enforces, La Niña. The upwelling term is about twice as strong for LG and LD than for EG and ED, because for LG and LD, the Indian Ocean-induced easterlies lead to additional upwelling nearly instantaneously, causing additional cooling during La Niña.
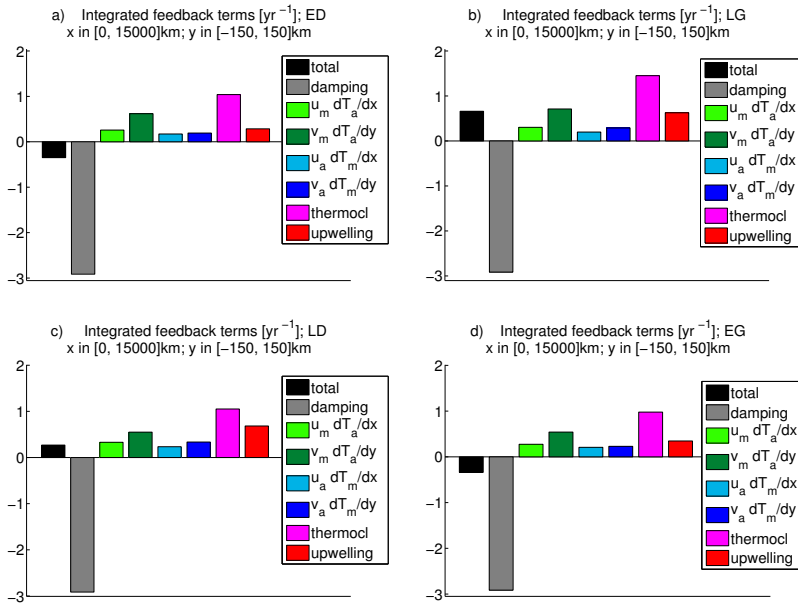
Figure 4.8: *Bjerknes feedback contributions for (a) the ED case (b) the LG case (c) the LD case and (d) the EG case, all at $\mu = 1$. In all plots, the bars indicate (from left to right) the total growth factor (black), damping (grey), zonal and meridional advection of SST anomalies by equilibrium currents (light and dark green), zonal and meridional advection of equilibrium SST by anomalous currents (light and dark blue), $T - T_{sub}$ anomalies (thermocline feedback; magenta) and upwelling anomalies (red).*

4.5 Summary and Conclusions

We have investigated the effect of Indian Ocean (IO) SST on ENSO using the Gill-based 1.5 basin extension of the Zebiak-Cane model (see section 3.4). In this model, the Indian Ocean's zonally independent SST either co-varies with ENSO or is constant. Continuation methods were used to determine the changes in growth rate and spatial pattern of the ENSO mode in the Pacific (PO) under influence of the Indian Ocean, in particular focussing on the critical conditions where the growth rate is zero (Hopf bifurcation).

For the co-varying cases (section 4.4), we found that - depending on the lag between ENSO and Indian Ocean SST - the growth rate and period of the ENSO mode are affected by the Indian Ocean. The findings can be explained by bearing in mind that a warm Indian Ocean leads to easterlies above the Pacific. If a warm Indian Ocean coincides with El Niño (La Niña), the ENSO-related winds are reduced (enhanced), leading to a damping (growth) of the ENSO mode. This shifts the Hopf bifurcation to higher (lower) values of the coupling strength. If a warm Indian Ocean occurs during the transition from El Niño to La Niña (from La Niña to El Niño), the ENSO-induced switch in wind direction is facilitated (hampered) and the period decreases (increases). In particular, in the most realistic scenario where El Niño is followed by a warm Indian Ocean after a few months, the Indian Ocean dampens El Niño (shift of the Hopf bifurcation to higher coupling strengths) and shortens the period. This result agrees with that in Frauen and Dommenget (2012), who find that decoupling the Indian Ocean by setting it to climatological values leads to a higher Nino3 standard deviation and longer periods. Kug and Kang (2006), Kug et al. (2006), Santoso et al. (2012) suggest that Indian Ocean warming during the mature phase of El Niño causes easterlies over the Pacific which help terminate the event (accelerated phase shift). Annamalai et al. (2005) argue that easterlies due to Indian Ocean warming during the early phase of El Niño hamper its growth. As the above studies rely solely on either GCMs and/or observations, we think that it is useful to confirm their suggested mechanisms using a simple model, as was done here.

We investigated the effect of long-term trends in the Indian Ocean SST by putting the Indian Ocean SST to a constant value different from the radiative equilibrium temperature T_0 (section 4.3). It was found that with a warm Indian Ocean, the ENSO mode is destabilised and acquires properties usually associated with central Pacific (CP) El Niños. The ratio between the off-shore and coastal SST variability decreases. In case of a very warm Indian Ocean ($T - T_0 = 1.125K$ on the equator), the coastal signal again increases in strength, but is now nearly in anti-phase with the offshore signal. This pattern qualitatively agrees with a strong El Niño Modoki Index (EMI) variability (Ashok et al., 2007). For a cool Indian Ocean, the ENSO mode is stabilised and becomes less CP-like.

The intensification of ENSO in the warm Indian Ocean case can be explained by the stronger mean easterlies and equatorial upwelling, as well as a more tilted thermocline, which lead to stronger positive thermocline and upwelling feedbacks. At the eastern coast, however, the temperature T_{sub} of the cool upwelling water becomes saturated if the thermocline is too high there, leading to a reduced sensitivity to thermocline variability and weaker signals at the coast. The effect is enhanced by wind anomalies to the east of the strongest SST anomalies, which lead to vertical velocity and temperature anomalies out of phase with the main off-shore signal. These results for constant Indian Ocean are particularly interesting because they offer a possible explanation for the observed increase in CP activity in the last four decades (Ashok et al., 2007) in terms of the observed rapid warming of the Indian Ocean. On the other hand, the predicted intensification of ENSO with increased Indian Ocean SST has not been identified in observations. Indeed Lübbecke

and McPhaden (2014)find that the Bjerknes index, as constructed from observations, is lower for 2000-2010 than for 1980-1999. However, 11 years is a very short period to construct the Bjerknes index from data, as regressions have to be made between different variables, and their study does not include the very strong El Niño of 2015-16. Still, it cannot be excluded that our model overestimates the instability (and variability) of CP ENSOs. For example, Philip and Van Oldenburg (2006) suggest that SST damping might increase in a warming climate due to enhanced cloud feedbacks which are not included in our model.

Our mechanism differs from the suggestions in Yeh et al. (2009), who link the increase in CP activity found in CMIP-3 projections to decreasing trade winds and a shoaling thermocline in the central Pacific. Note, however, that McPhaden et al. (2011) found a steepening thermocline and increasing trades in observations for 1980-2010, which is in agreement with our warm Indian Ocean case. The GCM experiments by Luo et al. (2012) also suggest that easterlies induced by Indian Ocean warming might lead to a more La Niña-like background state, although they explain the shift to stronger CP activity by hypothesising that a steeper thermocline suppresses warm Kelvin waves. Unfortunately our prediction of a cooling cold tongue is difficult to compare with observations, because datasets strongly disagree on SST trends in the tropical Pacific Deser et al. (2010). However, Fig. 2 of their paper seems to suggest that the east-central Pacific has at least warmed less than other parts of the tropical ocean.

Note that increasing easterlies over the Pacific can also be caused by a strengthening of the Hadley circulation or warming in the Pacific Warm Pool. To estimate the latter effect we performed simulations where the Pacific was warmed over $0 < x_P < L_P/3$. The effect on ENSO stability and spatial pattern is very similar to the constant Indian Ocean case (not shown). In HadISST data for 1970-2011, the equatorial Indian Ocean ($10°S - 10°N, 40 - 100°E$) and the Pacific Warm Pool ($10°S - 10°N, 130 - 180°E$) warm at a similar rate of $1.3K/yr$ (see also Weller et al. (2016)), hence the Pacific Warm Pool might have a significant effect as well. Pacific Warm Pool and Indian Ocean warming might not be independent: The Pacific Warm Pool warming may be partly a response to Indian Ocean-induced easterlies, and these easterlies may in turn push relatively warm Pacific Warm Pool water into the Indian Ocean via the Indonesian Throughflow (Lee et al., 2015). It might be interesting to investigate whether a significant positive feedback exists between these processes, in particular because according to some studies (Meehl et al., 2013; England et al., 2014; Lee et al., 2015), increased heat uptake in the Indo-Pacific system might have contributed to the recent global warming hiatus.

The result that ENSO variability depends on the background state may also apply to GCMs (e.g. Guilyardi (2006)) and support the suggestion that a correct background state - also of the Indian Ocean - may be crucial for correct predictions of variability.

Of course, our model is highly idealised in representing the complex interactions within the tropical equatorial climate system. First, the atmospheric response to Pacific and Indian Ocean SST is linear, i.e. does not include a detailed representation of convection. Second, the shape of the subsurface temperature T_{sub} parameterisation, though it has shown to work well in Zebiak-Cane-type models, does not closely agree to observations. Therefore it is not clear a priori how strong the effect of the T_{sub}-saturation for extreme thermocline levels (see section 4.3) will be in reality. A comparison of our findings to results from more complex ocean models would be useful here.

Despite these caveats our results suggest that the Indian Ocean can affect ENSO amplitude and flavour, both through interannual variability and through long-term trends. Warming the PWP may have similar effects as warming the Indian Ocean. These results

offer a possible explanation for the recent increase in CP El Niño activity, and suggest that long-term Indian Ocean (and Pacific Warm Pool) trends may play a role for the future of ENSO variability.

Appendix to Chapter 4: The Bjerknes index in the Zebiak-Cane model

To compute Bjerknes feedback terms, the SST equation is linearised around the equilibrium solution (denoted here by a bar; anomalies are denoted by plain letters). As trial solution, $\delta\psi \exp[(\lambda + i\omega)t]$ is used, where δ is a small constant, $\lambda, \omega \in \mathbb{R}$ and $\psi \equiv \psi_r + i\psi_i$ the ENSO eigenvector. This yields

$$
\begin{aligned}
(\lambda + i\omega)(T_r + iT_i) = &-\epsilon(T_r + iT_i) \\
&- \bar{u}_1 \partial_x(T_r + iT_i) - \bar{v}_1 \partial_y(T_r + iT_i) - (u_{1r} + iu_{1i})\partial_x \bar{T} - (v_{1r} + iv_{1i})\partial_y \bar{T} \\
&- \alpha_w \mathcal{M}(\bar{w}_1) \times (T_r + iT_i - T'_{sub}(\bar{h})(h_r + ih_i) \\
&- \alpha_w \mathcal{M}'(\bar{w}_1) \times (w_{1r} + iw_{1i})(\bar{T} - T_{sub}(\bar{h})),
\end{aligned}
\tag{4.10}
$$

where the first line on the right hand side denotes damping, the second line advection, and the third and fourth line come from thermocline and upwelling anomalies, respectively.

Summarising the r.h.s. as $C_r + iC_i$, one can solve for the growth factor λ and the frequency ω and obtains

$$
\begin{aligned}
\lambda &= (C_r T_r + C_i T_i)/(T_r^2 + T_i^2) \\
\omega &= (C_i T_r - C_r T_i)/(T_r^2 + T_i^2).
\end{aligned}
\tag{4.11}
$$

This yields the real and imaginary parts of the eigenvalue ψ - no matter at which location the equation is evaluated. Including only certain processes in (4.10) will yield their contribution to λ and ω at a specific location. To obtain a more global result, we integrate (4.10) over $x = [0, L_P]$ and $y = [-R_P/2, +R_P/2]$ prior to solving for (contributions to) λ, i.e. C_r, C_i, T_r, T_i in (4.11) are replaced by their spatial integrals. Note that a mere rescaling of the temperature anomaly field T does not affect the damping term (for which $C \propto T$) and also has little effect on advection, because u_1, v_1 are dominated by the Ekman contributions which scale with T.

Chapter 5

The influence of Convection over Indonesia on the interaction between the Indian Ocean and ENSO[1]

In this chapter, the atmospheric bridge mechanism proposed in section 2.4.1 will be investigated using the convective 1.5 basin ZC model described in section 3.5.

5.1 Introduction

The results in section 4.4 suggest that the influence of the Indian Ocean Basinwide warming (IOB) interannual variability on ENSO is mainly damping; previous studies found that the IOB has little predictive skill on ENSO (Xie et al., 2009; Izumo et al., 2013). For the Indian Ocean Dipole (IOD), the situation is less clear. While some suggest that the IOD cannot strongly impact the Pacific because the wind contributions of both poles cancel due to their close proximity(Annamalai et al., 2005; Santoso et al., 2012), it was suggested by Izumo et al. (2010, 2013) that a negative (positive) IOD is associated with easterlies (westerlies) over the west Pacific, leading to warm water accumulation (depletion) in the Warm Pool, thus favouring next year's El Niño (La Niña). They suggest that the influence of the eastern pole (IODeast) dominates over IODwest, because IODeast lies in the Warm Pool region, where similar SST anomalies can trigger stronger convective responses (see Fig. 5.1c).

However, in section 2.2 it was found that IODeast in summer-autumn (year 0) does not yield significant correlations to ENSO in winter(1-2), whereas IODwest (or SDIex; these two areas overlap and yield very similar results) does yield significant results. This suggests that IODwest may have more predictive skill than IODeast. It was also found in section 2.4.1 that a cool IODwest may be associated with easterlies over the Pacific (though only at 80% confidence, possibly because wind data tends to be noisy) and, at a lag of around 5 months, with large Warm Water Volumes (95% confidence). This is

---

[1]This chapter is based on the article Wieners, C.E., H.A. Dijkstra, and W.P.M de Ruijter, 2017: The Influence of Atmospheric Convection on the Interaction between the Indian Ocean and ENSO. J. Climate
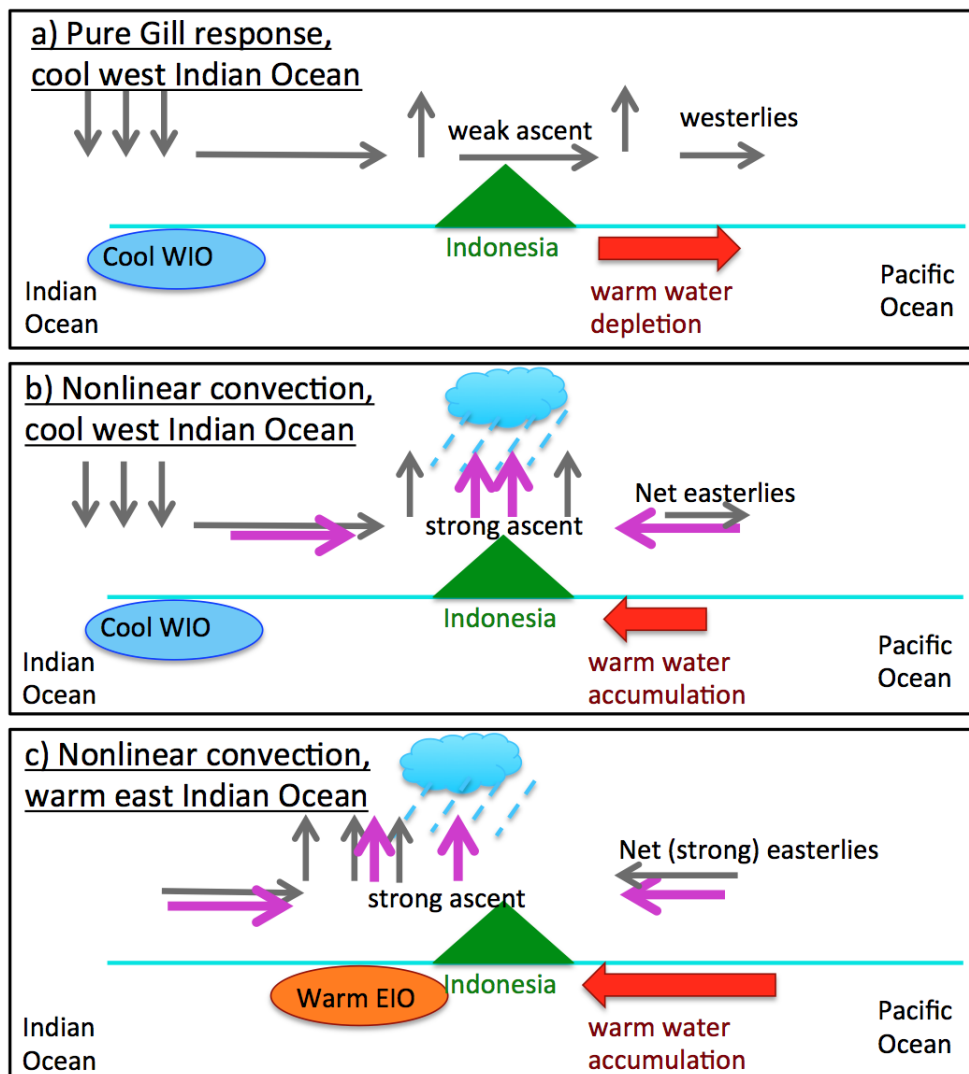
Figure 5.1: *Cartoon of the mechanisms to be investigated. a) Gill response (i.e. without convection effect above Indonesia) to west Indian Ocean (WIO) cooling. The low SST leads to cooling, subsidence and surface divergence of the air over the WIO, hence to the east of the WIO, westerly anomalies and upward motion prevail, extending to the west Pacific. The westerlies may cause a depletion of the west Pacific warm water volume. b) If the upward motion induced by the Gill response (grey arrows) is amplified by convective heating over the warm and moist Maritime Continent, surface convergence is induced there (purple arrows). If this effect is strong enough, it might overcome the Gill-induced westerlies and lead to net easterly anomalies over the west Pacific, which in turn may build up the warm water volume. c) If the SST anomaly is in the east Indian Ocean (EIO), i.e. if it close to or even overlaps with the region with a warm and moist background state, Gill response (grey) and convection-induced upward motion (purple) co-act; hence a warm east Indian Ocean is also expected to yield easterlies over the west Pacific.*

an unexpected result, seeing that the Gill response east of cool anomalies is a westerly wind (Gill, 1980), as illustrated in Fig. 5.1a. In chapter 2 we hypothesised that a cool IODwest might trigger enhanced convection above the Warm Pool, because the weak uplift generated in this region by the Gill response might be nonlinearly amplified by condensation and latent heat release in the prevailing warm and moist air masses (see Fig. 5.1b).

This hypothesis shall be tested in this chapter, using the convective 1.5 basin model introduced in section 3.5. Similar idealised models have been used to investigate the effect of convection on the Indo-Pacific climatology and its stability (Anderson and McCreary, 1985; Watanabe , 2008), but here the focus lies on the effect of Indian Ocean interannual variability on ENSO. First, it shall be investigated whether convection above the Maritime Continent can induce sufficiently strong wind responses as to overcome the contribution of the Gill response associated with IODwest SST anomalies (section 5.2). Next, the effect of other Indian Ocean modes will be addressed (section 5.3). While in these two sections linear stability analysis techniques are employed, transient simulations are used in section 5.4, allowing for the effects of finite amplitude perturbations and noise.

The Indian Ocean SST is again modelled according to (3.32), which is repeated here for convenience:

$$T_I = T_0 + \sum_{m=1}^{n_I} T_m^{0I}(x_I, y) A_m(t). \tag{5.1}$$

The spatial patterns $T_m^{0I}(x_I, y)$ (i.e. the Indian Ocean temperature anomalies associated with $A_m = 1$) used in this chapter are shown in Fig. 5.2. The IOB is a combination of west Indian Ocean heating (WIO) and IOBe (heating over the whole east Indian Ocean). IOD is a combination of 0.57×WIO and IODe; the latter represents a cooling centred south of the equator. IOB and IOD are simplifications of the observed patterns shown in Fig. 1.5. IODes is like IODe, except that the SST anomaly is shifted northward to be centred around the equator. No surface temperature anomalies occur over the Maritime Continent ($T_{MC} = T_0$).

Since constant Indian Ocean temperature deviations are not considered here, the constant term a_c in (3.33) is dropped and the evolution of each A_m takes the form

$$\frac{dA}{dt} = a_0 \cos(\psi)(N - \bar{N}) + \frac{a_0}{\omega} \sin(\psi) \frac{dN}{dt} + a_d A + R(t). \tag{5.2}$$

The constants a_0 and in particular ψ control ϕ_{TI}, the phase difference between A and the El Niño index N defined in (3.37), though there is no fixed relation between ψ and ϕ_{TI}, because the ENSO period might change under the influence of the Indian Ocean. The noise term R will be specified later. As in chapter 4, for $R = 0$ and in equilibrium, $N = \bar{N}$ and $dN/dt = 0$, hence $A = 0$, i.e. the equilibrium solution is not influenced by the Indian Ocean.

For the sake of notational compactness, the west Indian Ocean, east Indian Ocean and Maritime Continent shall be abbreviated as WIO, EIO and MC, respectively.

5.2 West Pacific Easterlies caused by a cool West Indian Ocean

To compare situations with and without convection in the absence of Indian Ocean SST anomalies, we first consider changes in the Pacific background state and the ENSO mode when increasing γ_c in (3.38) from zero to $\gamma_c = 1.02c_a^2$, while all $T_m^{0I} = 0$ in (5.1). This
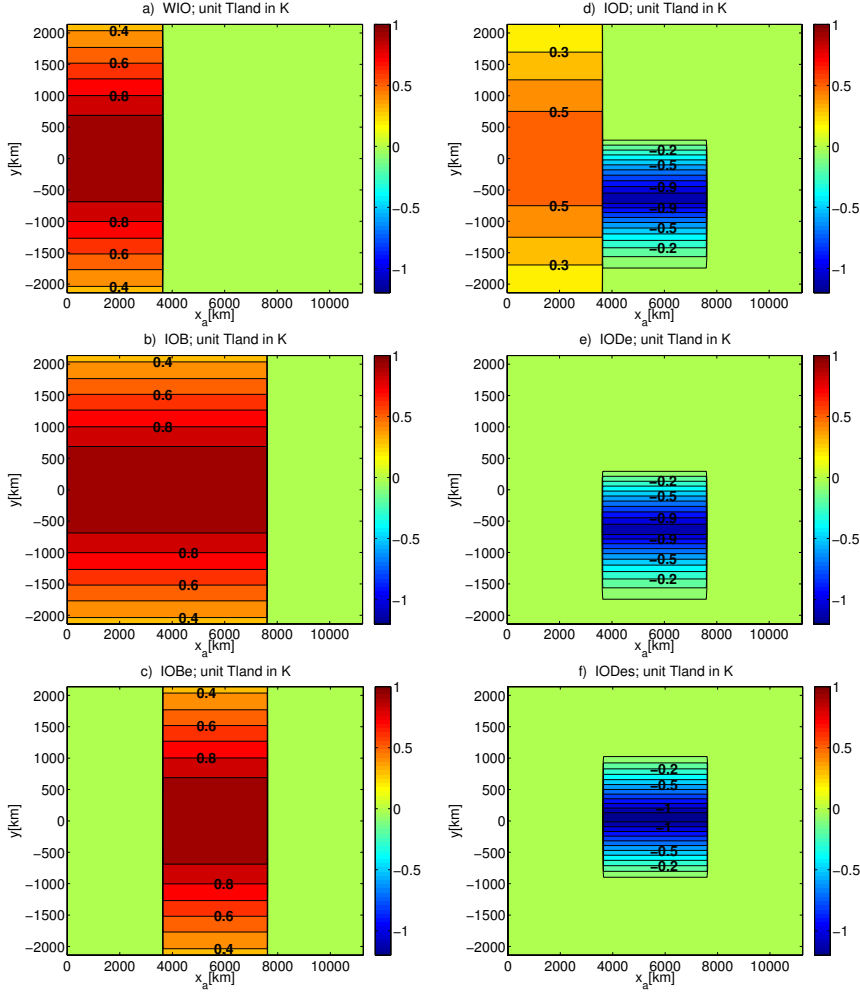
Figure 5.2: *The SST patterns in the Indian Ocean, T_m^{0I}, associated with $A_m = 1$ in (5.1). The patterns are associated with a) the warm west Indian Ocean (WIO), b) the Basin-wide warming (IOB), c) the eastern half of the IOB (IOBe), d) the Indian Ocean Dipole (IOD), e) its eastern half (IODe) and f) IODe shifted to the equator (IODes). IOB is a combination of WIO and IOBe; IOD is a combination of $0.57 \times$ WIO and IODe. The zonal axis covers the Indian Ocean and Maritime Continent (MC); the surface temperature deviations in the MC are always zero.*
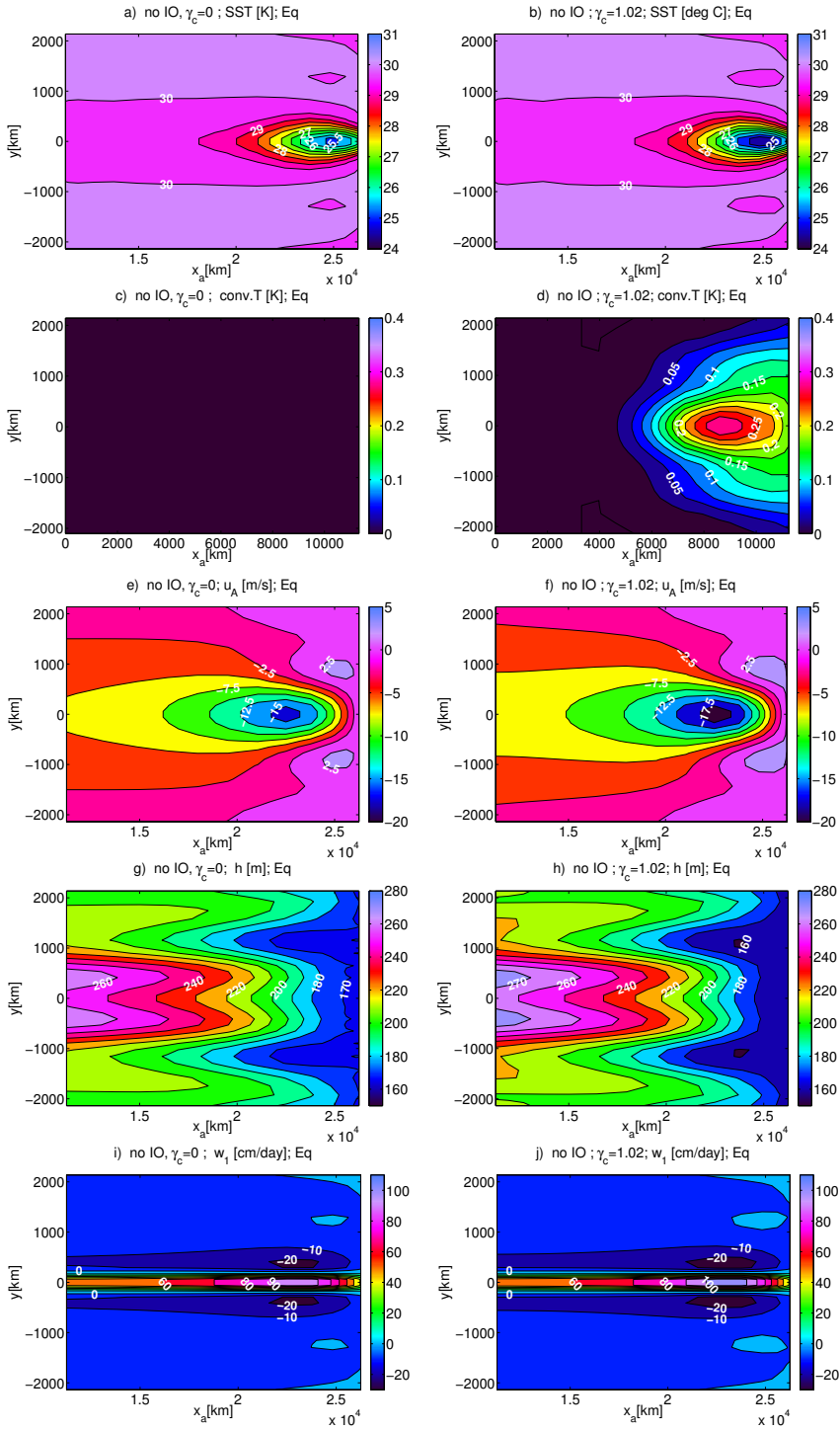
Figure 5.3: *The equilibrium state without ($\gamma_c = 0$; left column) and with ($\gamma_c = 1.02c_a^2$; right) convective heating. Plots a) and b) show the Pacific SST in °C, plots c) and d) the convective heating (rescaled to equivalent surface temperatures in K) over the Indian Ocean and Maritime Continent, plots e) and f) the Pacific zonal wind (in m/s), plots g) and h) the Pacific thermocline depth (in m), and plots i) and j) the upwelling w_1 (in cm/day) in the Pacific mixed layer. The zonal coordinate x_a is defined in Fig. 3.7b.*
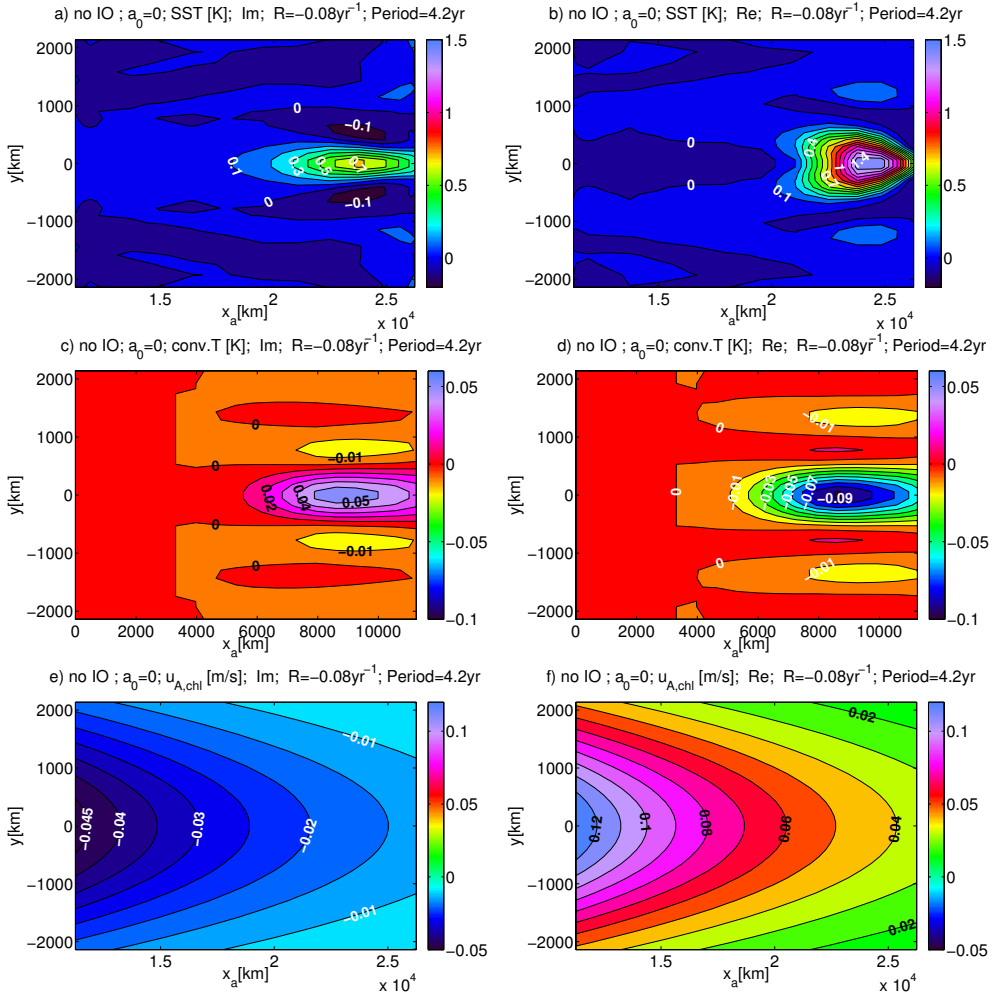
Figure 5.4: *The ENSO mode in the zero Indian Ocean case at $\gamma_c = 1.02c_a^2$. The left (right) column shows the imaginary (real) part of the eigenvector; the imaginary part is leading by 1/4 period. Plot a) and b) show the SST anomalies (in K) in the Pacific; c) and d) the convective heating anomalies (rescaled to the equivalent surface temperature in K) over the Indian Ocean and Maritime Continent, e) and f) the contribution of the convective heating to the zonal wind over the Pacific (in m/s). As this mode is an eigenvector of the generalised eigenvalue problem (3.51), it can only be computed up to an overall scaling factor. The zonal coordinate x_a is defined in Fig. 3.7b.*

a)

$\gamma_c = 1.02$	zero IO, $\gamma_c = 0$	zero IO	WIO	IOB	IOD	IOBe	IODe	IODes
$\sigma_r[yr^{-1}]$	-0.27	-0.08	-0.09	-0.88	0.50	-0.87	0.52	1.16
$P[yr]$	3.8	4.2	4.1	2.6	4.4	2.7	4.5	8.2
$\phi_{TI}[P]$	/		0.06	0.11	-0.08	0.11	-0.08	-0.03
$\phi_{uTI}[P]$	/		-0.44	-0.39	0.42	-0.39	-0.08	-0.03
$\phi_{uch}[P]$	/	0.12	0.08	-0.40	-0.06	-0.39	-0.05	-0.03
$U_{TI}[m/s]$	/		2.68	6.71	0.08	4.03	1.44	1.67
$U_{ch}[m/s]$	/	0.11 (*)	3.18	1.85	4.55	4.41	3.14	6.95

b)

$\gamma_c = 0.9$	zero IO, $\gamma_c = 0$	zero IO	WIO	IOB	IOD	IOBe	IODe	IODes
$\sigma_r[yr^{-1}]$	-0.27	-0.14	-0.26	-0.80	0.02	-0.62	0.14	0.23
$P[yr]$	3.8	4.0	3.6	2.8	3.9	3.0	4.0	4.0
$\phi_{TI}[P]$	/		0.07	0.11	-0.08	0.10	-0.10	-0.09
$\phi_{uTI}[P]$	/		-0.43	-0.39	0.39	-0.40	-0.10	-0.09
$\phi_{uch}[P]$	/	0.14	0.08	-0.40	-0.08	-0.41	-0.06	-0.06
$U_{TI}[m/s]$	/		2.68	6.71	0.08	4.03	1.44	1.67
$U_{ch}[m/s]$	/	0.03 (*)	1.21	0.62	1.49	1.59	0.95	1.38

(*) In the simulations with zero IO, $A = 0$, hence normalisation by A is not possible, and normalisation was performed with the El Niño index N. Typically, N is around 6 times as large as A, which means that U_{ch} is relatively small, but not negligible, in the zero Indian Ocean case.

Table 5.1: *Results of the linear stability analysis for various Indian Ocean (IO) configurations: no Indian Ocean SST anomaly and no convection ('zero IO, $\gamma_c = 0$'), no Indian Ocean SST anomaly but with convection ('zero IO'), warm west Indian Ocean following El Niño ('WIO'), Basin-wide warming following El Niño ('IOB'), pos. Indian Ocean Dipole preceding El Niño ('IOD)', warm eastern half of IOB following El Niño ('IOBe'); cool eastern pole of IOD preceding El Niño ('IODe') and cool eastern pole of IOD, shifted equatorwards, preceding El Niño ('IODes'). The first table a) shows results for $\gamma_c = 1.02c_a^2$, i.e. around the critical value, whereas the second table b) shows results for $\gamma_c = 0.90c_a^2$, well below the critical value. The measures denote: the growth factor of the ENSO mode (σ_r, positive/negative if perturbations grow/decay); the period (P); the phase difference between N and A measured in periods (ϕ_{TI}; positive if A peaks after El Niño); the phase difference between N and the wind response over the west Pacific (in $x_P = 0, y = 0$) to Indian Ocean surface heating and convective heating in periods (ϕ_{uTI} and ϕ_{uch}, respectively; positive if westerlies are induced after El Niño); the maximal zonal wind contribution in $x_P = 0, y = 0$ due to Indian Ocean SST and convection, normalised by A (U_{TI} and U_{ch}, respectively).*
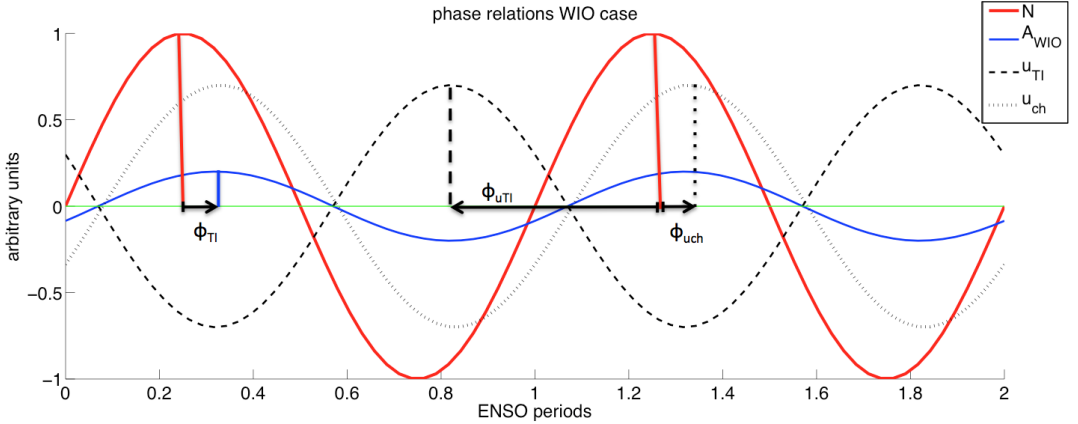
Figure 5.5: *Illustration of the phase relations in the WIO case. The solid red line denotes the El Niño index N, the solid blue line the amplitude A of the Indian Ocean SST pattern (here: WIO), and the black dashed and dotted lines the zonal wind contribution in the west Pacific ($x_P = 0, y = 0$) induced by Indian Ocean SST (u_{TI}) and convective heating (u_{ch}), respectively. The phase difference ϕ_{TI} between N and A is positive if A peaks later than N. The phase differences ϕ_{uTI} and ϕ_{uch} between N and the zonal winds induced by the Indian Ocean SST and convective heating, respectively, are positive if N is followed by westerlies. All phase differences are measured in ENSO periods.*

increase of γ_c causes changes in the equilibrium state (see Fig. 5.3). The negative background divergence c^b in (3.38,3.39) leads to heating and enhanced convergence over the MC (Fig. 5.3c-d). Note that in the figure, the convergence-induced convective heating anomaly Q_c is divided by α_T to rescale it to an equivalent surface temperature, i.e. the SST anomaly that would heat the atmosphere (in a Gill response) as much as Q_c. This heating in turn influences the atmosphere (see (3.40)) and leads to stronger easterlies over the (west) Pacific (Fig. 5.3e-f), which induce more La Niña-like background conditions with a cooler eastern Pacific (Fig. 5.3a-b), a steeper thermocline (Fig. 5.3g-h), and more equatorial upwelling (Fig. 5.3i-j).

The stability of the background state is determined by solving the linear stability problem (3.50) and determining the eigenvalue $\sigma_r \pm i\sigma_i$ of the generalised eigenvalue problem (3.51) with the largest real part. The corresponding eigenvector is referred to as the ENSO mode and the period of this mode is determined from $P = 2\pi/\sigma_i$. With increasing γ_c, the background state is destabilised as σ_r increases (see Table 5.1). The reason is that upwelling and thermocline feedbacks are strengthened as in the constant Indian Ocean-warming experiments in chapter 4. In Fig. 5.4, the anomalies associated with the oscillatory ENSO mode at $\gamma_c = 1.02c_a^2$ are shown. Note that stability analysis only yields the ENSO mode up to a normalisation constant; both the real (right panels) and imaginary (left panels) part of the eigenvector are plotted in Fig. 5.4.

In order to characterise the effect of nonlinear convection on the winds over the Pacific, we define the following measures (cf. Fig. 5.5): ϕ_{TI} is the phase difference between A, the time-dependent amplitude of the Indian Ocean SST (see (5.1)), and the El Niño index N. It is measured in ENSO periods P and is positive if A peaks after N. Similarly, ϕ_{uTI} and ϕ_{uch} are the phase difference between N and the zonal wind contribution at ($x_P = 0, y = 0$) caused by SST heating (Q^T) and convergence-induced heating (Q^c), respectively.

They are positive if westerly winds are induced after El Niño. The amplitudes of the Indian Ocean SST and convection-induced zonal winds per unit A at $(x_P = 0, y = 0)$ are denoted by U_{TI} and U_{ch}, respectively. In the cases with zero IO, i.e. $A = 0$, U_{ch} cannot be normalised per unit A, but is normalised by N. The amplitude of N is about 6 times as large as that of A when the Indian Ocean is active.

ENSO-mode related SST anomalies in the Pacific induce some relatively small anomalies in convective heating over the MC; their amplitude is $\approx 1/15$ of the amplitude of Pacific SST anomalies (compare Fig. 5.4a-b with Fig. 5.4c-d). El Niño (La Niña) is followed by a divergence (convergence) anomaly above the equatorial MC (Fig. 5.4c-d), which leads to cooling (heating). The Q^c anomalies are of opposite sign to the SST anomalies in the east Pacific, which enhances the zonal temperature gradient over the Pacific and leads to stronger wind responses (Fig. 5.4e-f), which is qualitatively similar to enhancing the coupling strength α_T. The wind contribution induced by nonlinear convection is not exactly in phase with N but lags by about 1/8 ENSO periods ($\phi_{uch} = 0.12$ in Table 5.1a), hence prolonging the westerlies (easterlies) associated with El Niño (La Niña). This may explain an increase in period seen in Table 5.1 (though changes in the background state can also affect the period).

In order to investigate the combined effect of the WIO anomalies and convection, we put $T^{0I} = T^{0I}_{WIO}$ in (5.1) and $\psi = 0°$, $R = 0$ in (5.2). As explained in section 5.1, if the Indian Ocean SST obeys (5.2) with $R = 0$, it remains zero in equilibrium and hence does not affect the equilibrium solution. So the background state for $\gamma_c = 1.02c_a^2$ in Fig. 5.3 remains unaltered throughout this and the following section. The linear stability analysis now yields an eigenmode involving both the ENSO mode and anomalies in the amplitude A of the WIO. The above parameter choices lead to a peak in WIO SST about 3 months or 0.06 ENSO periods ($\phi_{TI} = 0.06$ in Table 5.1a) after the peak in N, which agrees with observations. The amplitude of Indian Ocean SST (see Fig. 5.6c-d) is about 1/6 of the amplitude of N.

The heating parameter γ_c is next varied in order to determine whether it is possible to generate an easterly (westerly) wind response over the west Pacific in case of cool (warm) WIO SST anomalies. As can be seen in Fig. 5.6g-j, for $\gamma_c = 1.02c_a^2$ the zonal winds induced by Indian Ocean SST and nonlinear convection are of about equal magnitude and opposite sign. The value of γ_c for which the influence of the WIO variability on the wind over the Pacific becomes zero is referred to as $\gamma_{c,crit}$ below. Due to the small but non-zero influence of the east Pacific on MC convection, one cannot determine the value of $\gamma_{c,crit}$ exactly. For the case $\psi = 0$ presented here, U_{ch} is slightly larger than U_{TI} because the contributions to convective heating induced by ENSO and the WIO are roughly in phase; if one chooses $\psi = 180°$, U_{ch} is slightly smaller than U_{TI} (not shown). As one would expect, given the near-cancellation of the WIO-induced winds, both the spatial SST patterns and the period and growth factor of the ENSO mode (see Fig. 5.4a-b and Fig. 5.6a-b) change very little when adding WIO variability at $\gamma_c = \gamma_{c,crit}$.

U_{ch} becomes larger by a factor of about 5 when including the WIO (see Table 5.1a, bearing in mind that in the WIO case U_{ch} was normalised with A and in the zero Indian Ocean case with N, whose amplitude is ≈ 6 times as large as that of A). The relative smallness of the Pacific contribution is qualitatively in line with Watanabe and Jin (2002) and can be explained by the relatively large distance between the MC and the east Pacific, and also the fact that the Gill response is more zonally extended to the east of an SST anomaly than to the west. Hence, compared to Indian Ocean SST anomalies, east Pacific SST anomalies have relatively little effect on the divergence over the MC.

Fig. 5.6g-j also show that the winds due to WIO SST and convergence-induced heating
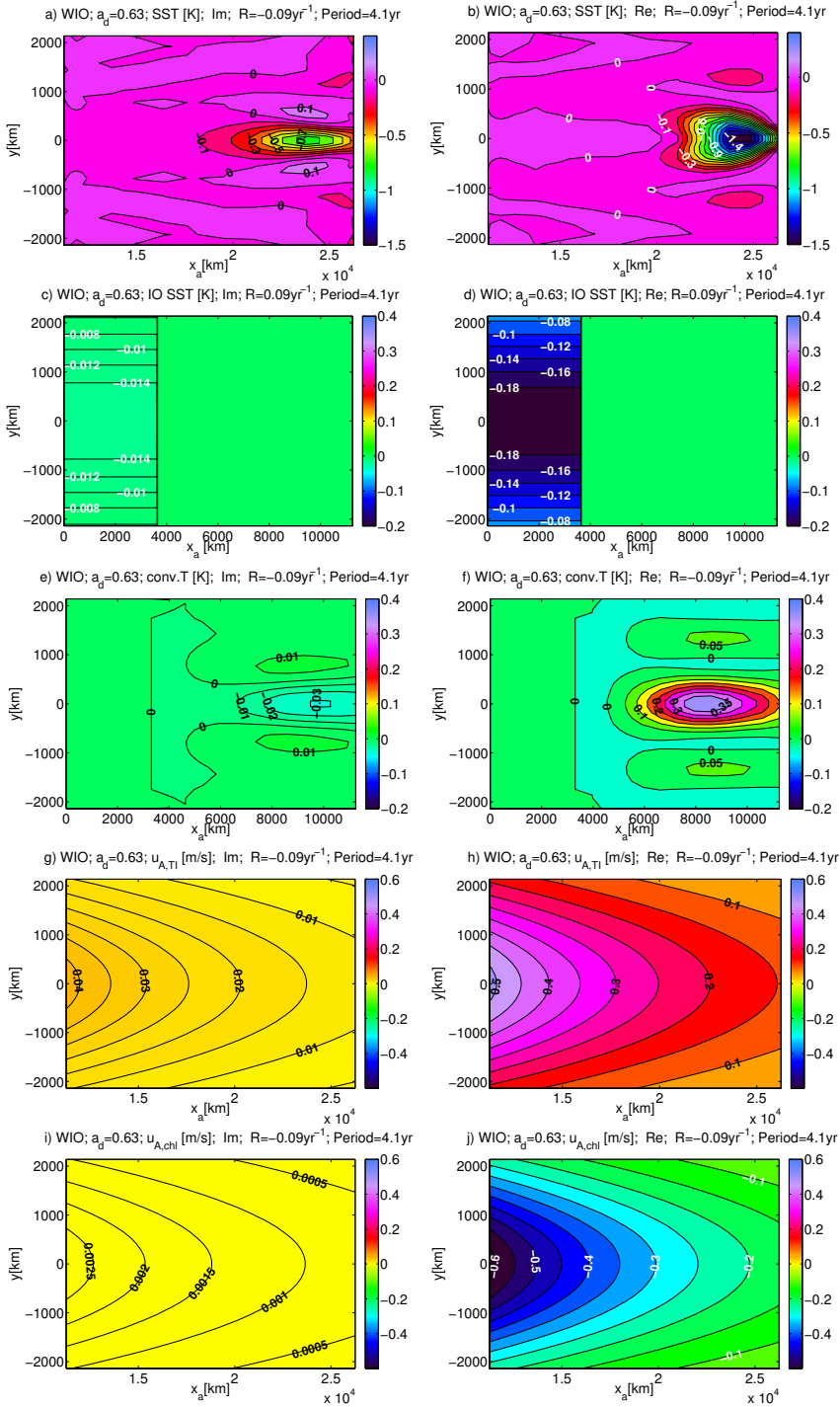
Figure 5.6: *The ENSO mode in the WIO case. The left (right) column shows the imaginary (real) part of the eigenvector; the imaginary part is leading by $1/4$ period. Plot a) and b) show the Pacific SST (in K), c) and d) show the Indian Ocean (IO) SST (in K), e) and f) show the convective heating (rescaled to the equivalent surface temperature in K) over the IO and Maritime Continent, g) and h) the contribution of the IO SST (pure Gill response) to the Pacific zonal wind (in m/s), i) and j) are as g) and h) but for convective heating instead of IO SST. The zonal coordinate x_a is defined in Fig. 3.7b.*

have exactly the same spatial pattern; this is a general feature of the Gill response to the east of a surface heating anomaly (Indian Ocean and MC). Fig. 5.6e-f show the convergence-induced heating (rescaled to equivalent temperature) which is positive when the WIO is cool.

If $\gamma_c < \gamma_{c,crit}$, a cool (warm) WIO anomaly generates a westerly (easterly) contribution to the wind over the Pacific. As A peaks shortly after El Niño ($\phi_{TI} > 0$), these winds counteract the winds associated with ENSO and dampen the ENSO mode (Table 5.1b). If $\gamma_c > \gamma_{c,crit}$, a cool (warm) WIO leads to easterlies (westerlies) and the growth factor of ENSO increases. For example, for $\gamma_c = 1.025c_a^2$ one obtains $\sigma_r = +0.04yr^{-1}$, as opposed to $-0.09yr^{-1}$ for $\gamma_c = 1.02c_a^2$, and the amplitudes U_{TI} and U_{ch} of the zonal wind contributions induced by Indian Ocean SST and convection, respectively, take the values $U_{TI} = 2.68m/s$, $U_{ch} = 4.10m/s$. These results suggest that it is possible, at least in principle, that a cool (warm) WIO leads to easterlies (westerlies) due to convection above the MC, as suggested in section 2.4.1. However, it is not clear whether such high values of γ_c are realistic.

5.3 The Wind Effect of IOB and IOD

The two dominant modes of Indian Ocean variability are the Indian Ocean Basinwide warming (IOB) and the Indian Ocean Dipole (IOD), and their effects on convection and Pacific winds are investigated in this section. For the IOB, $T^{0I} = T_{IOB}^{0I}$ (see Fig. 5.2) and $\psi = 0$ is chosen, i.e. the Indian Ocean warms over its full zonal width a few months after El Niño. The IOD is modelled with $T^{0I} = T_{IOD}^{0I}$ and $\psi = 60°$, i.e. a positive IOD occurs a few months before El Niño. For a better understanding of the contribution of the EIO, the eastern half of the IOB (IOBe) and eastern pole of the IOD (IODe) are also included, with $\psi = 0$ and $\psi = 60°$, respectively. IODes is like IODe but with the SST anomaly shifted towards the equator. For all these cases, R, a_d and a_0 are as in section 5.2 and $\gamma_c = 1.02c_a^2$. As $\gamma_c = 1.02c_a^2$ might be an unrealistically high value, the experiments are repeated with $\gamma_c = 0.9c_a^2$.

Table 5.1 summarises the results for the new cases considered. The spatial SST and thermocline patterns of the ENSO mode (not shown) do not differ strongly from the WIO case (as shown in Fig. 5.6a,b,e,f). The convergence-induced heating Q^c, taken at the phase where A is maximal, is shown in Fig. 5.7 for $\gamma_c = 1.02c_a^2$ and all cases considered. Note that maximal A coincides with a warm WIO, warm IOB, warm IOBe, positive IOD, cool IODe and cool shifted IOD for Fig. 5.7, respectively (see also Fig. 5.2). The fields are normalised by $|A|$, the amplitude of A.

While a warm WIO (Fig. 5.7a) is associated with a cool Q^c anomaly reaching $-1.1K$, a warm IOBe (Fig. 5.7c) yields a warm anomaly of $2.0K$. For the full IOB, the effects of WIO and IOBe partially cancel and Q^c only reaches $1.2K$ (Fig. 5.7b). This partial cancellation explains the relatively low value of $U_{ch} = 1.85m/s$ in Table 5.1a. In contrast, $U_{TI} = 6.71m/s$ is large for the IOB, because a large area is covered by warm SSTs. This dominance of the Gill response means that it is acceptable to study the effect of the IOB in a convection-free model, as was done in chapter 4. The two wind contributions are nearly in phase ($\phi_{uTI} \approx \phi_{uch}$) and the effect of the IOB is to induce easterlies (westerlies) during El Niño (La Niña) which damp the ENSO mode ($\sigma_r = -0.88yr^{-1}$, i.e. smaller than for the zero Indian Ocean case) and shorten the period, as the Indian Ocean-induced winds peak slightly after ENSO and facilitate the transition to the other ENSO phase.

A cool IODe (Fig. 5.7e) lead to a decrease in Q^c, up to $-2.4K$. In the full IOD (Fig. 5.7d), the effects of WIO and IODe are of the same sign, yielding an anomaly of
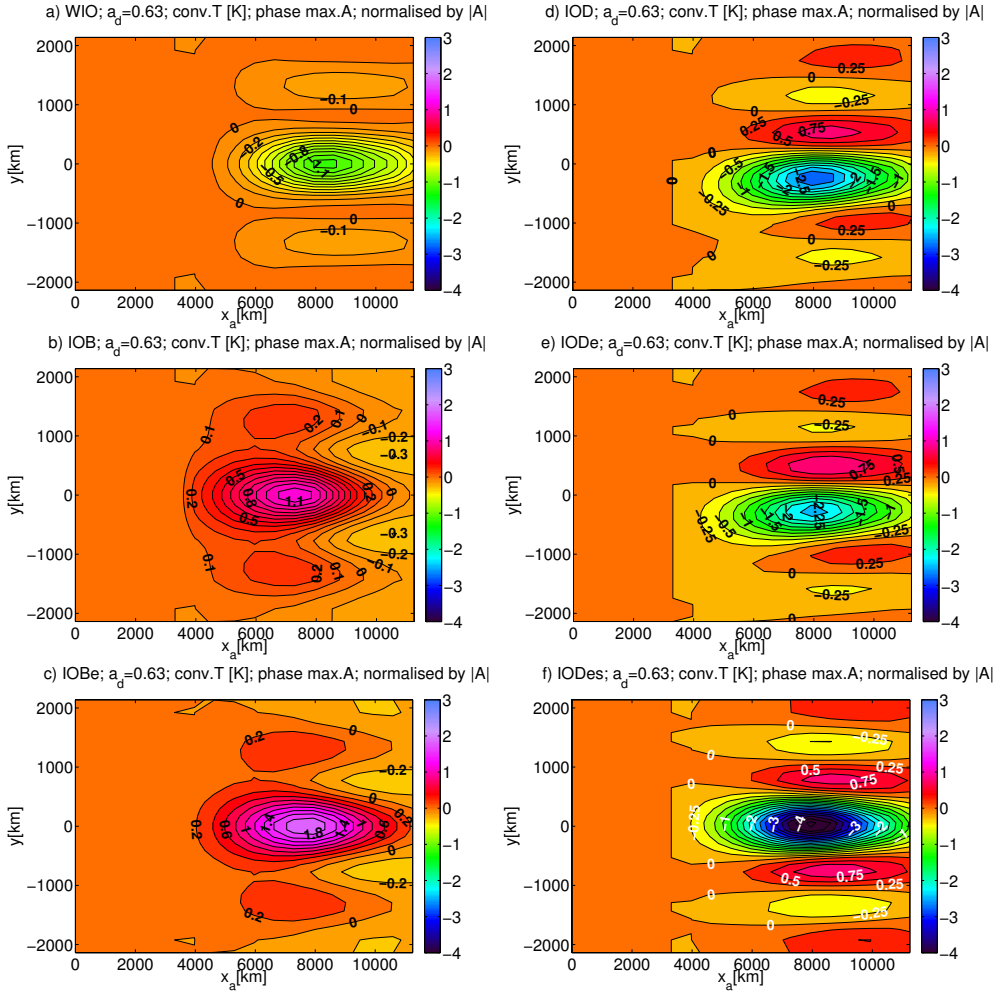
Figure 5.7: *The convective heating (rescaled to equivalent temperature) associated with the T_m^{0I} from Fig. 5.2, for $\gamma_c = 1.02c_a^2$. The patterns shown here are derived from the ENSO mode of a continuation experiment and show the convective heating in the moment of the ENSO cycle where A is maximal. The fields are normalised by $|A|$, the amplitude of A. The plots are for T_m^{0I} being a) west Indian Ocean warming (WIO), b) Basin-wide warming (IOB), c) the eastern half of IOB (IOBe), d) the Indian Ocean Dipole (IOD), e) its eastern pole (IODe) and f) IODe shifted onto the equator (IODes). The zonal coordinate x_a is defined in Fig. 3.7b.*

(a) list of parameters in the reference simulation (REF)

parameter	γ_τ	γ_c	$a_{0,IOD}$	$a_{d,IOD}$	ψ_{IOD}	η_{IOD}
value	$0.8\gamma_\tau^0$	$1.023c_a^2$	$0.26yr^{-1}$	$-3.78yr^{-1}$	$60°$	$1.01yr^{-1}$
parameter	η_τ		$a_{0,IOB}$	$a_{d,IOB}$	ψ_{IOB}	η_{IOB}
value	$0.55Nm^{-2}$		$0.84yr^{-1}$	$-3.78yr^{-1}$	0	$1.05yr^{-1}$

(b) list of the sensitivity experiments

Name	changes with respect to REF (table a)
REF	no change
IO*0	$T_{IOD}^{0I} \to T_{IOD}^{0I} \times 0,\ T_{IOB}^{0I} \to T_{IOB}^{0I} \times 0$
IOD*0	$T_{IOD}^{0I} \to T_{IOD}^{0I} \times 0$
IOD*0.5	$T_{IOD}^{0I} \to T_{IOD}^{0I} \times 0.5$
IOD*2	$T_{IOD}^{0I} \to T_{IOD}^{0I} \times 2$
IOB*0	$T_{IOB}^{0I} \to T_{IOB}^{0I} \times 0$
IOB*0.5	$T_{IOB}^{0I} \to T_{IOB}^{0I} \times 0.5$
IOB*2	$T_{IOB}^{0I} \to T_{IOB}^{0I} \times 2$
IODnoi	$a_{0,IOD} = 0;\ a_{d,IOD} = -1.39yr^{-1};\ \eta_{IOD} = 0.76yr^{-1}$

Table 5.2: *Settings for time integrations. Table (a) shows the settings for the reference case (REF). Other parameters are as in Table 3.1. Table (b) summarises the sensitivity studies by specifying the changes with respect to REF. Further explanations are given in section 5.4.*

-2.7K. (Recall that $T_{IOD}^{0I} = T_{IODe}^{0I} + T_{WIO}^{0I} \times 0.57$.) Fig. 5.7f illustrates that the impact of the IODe on Q^c would be ≈ 1.8 times higher if IODe were located on the equator. Since the Gill response to IOD forcing is very small ($U_{TI} = 0.08m/s$) due to cancellation of the contributions of the two poles, the wind effect above the Pacific is mainly due to the convergence-induced convection effect. The IOD leads to westerlies (easterlies) just before El Niño (La Niña), which increases the growth factor to $\sigma_r = +0.50yr^{-1}$. The period is not much affected, because the effect of IOD-induced winds on thermocline and SST lags a few months behind the winds themselves and thus peaks almost simultaneously with N. So the switch to La Niña (El Niño) is neither accelerated nor delayed. Since Annamalai et al. (2010) suggest that the marginal seas in the MC, whose SST develops in phase with the IODe during and IOD event also play an important role, we repeated the IOD experiment with IODe shifted eastward by $L_I/4$. The result (not shown) is qualitatively similar to the IOD experiment, but the convective winds are stronger ($U_{ch} = 8.5m/s$).

Though for the smaller value $\gamma_c = 0.9c_a^2$ the winds induced by the WIO are dominated by the Gill response ($U_{ch} < U_{TI}$ in Table 5.1b), it still holds that the IOB dampens ENSO and is dominated by Gill response, whereas the IOD destabilises the ENSO mode and its winds are induced by convergence-induced heating anomalies to which both the WIO and IODe contribute.

In the presence of IOB (IOD) influence, a higher (lower) coupling constant α_T is needed to obtain a self-sustained ENSO oscillation (i.e. the critical coupling associated with the Hopf bifurcation is shifted). The impact of Indian Ocean-induced winds on the Hopf bifurcation was discussed in section 4.4.
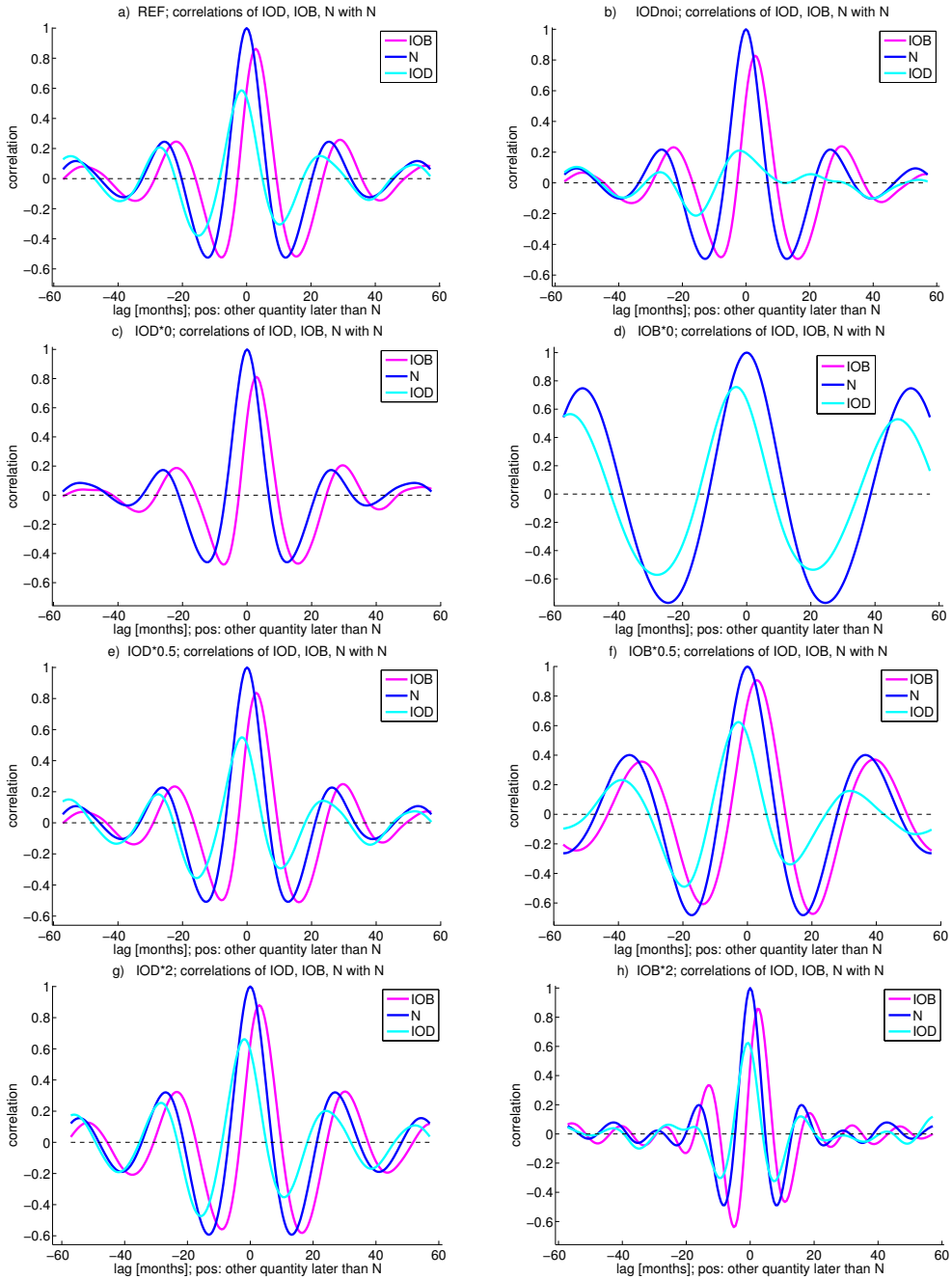
Figure 5.8: *Lagged correlations between IOB and the El Niño index N (purple), IOD and N (light blue) and N with itself (dark blue). Lags are in months and positive if N is taken at an earlier time than the other quantity.*

5.4 Transient Simulation

A linear stability analysis as performed in the previous sections only applies to the evolution of infinitesimal perturbations of the equilibrium state. In order to include finite amplitude anomalies and noise, we performed a set of simulations of 150 years each. In each of them, the seasonal cycle is neglected.

The most realistic simulation, referred to as the reference case REF, includes both the dominant Indian Ocean modes IOB and IOD. Hence (5.1) takes the form

$$T_I(x_I, y, t) = T_0 + T^{0I}_{IOD}(x_I, y)A_{IOD}(t) + T^{0I}_{IOB}(x_I, y)A_{IOB}(t) \qquad (5.3)$$

and T^{0I}_{IOD} and T^{0I}_{IOB} are as in Fig. 5.2. The evolution of the A is as in (5.2) with a noise term $R(t) = \eta r(t)$. Here η is a scaling factor and $r(t)$ is pink noise, i.e. at time step t_i, $r(t_i) = b_1 r(t_{i-1}) + b_2 s(t_i)$ where the $s(t_i)$ are normally distributed random numbers, and b_1 and b_2 are chosen such that r has a $1/e$-folding time of 2 months (i.e. rather long intraseasonal time scales) and unit standard deviation. In addition, noise is added to the zonal wind stress in the Pacific:

$$\tau^x_{noi} = \frac{\eta_\tau}{2}[1 - \cos(2\pi x_P/L_P)] \exp(-y^2/2\alpha^2_y)r(t)$$

where $\eta_\tau = 5.5 \times 10^{-3} Nm^{-2}$ and the $r(t)$ for the IOD, IOB and τ^x_{noi} are uncorrelated. The convection scaling parameter γ_c is put to $1.023c^2_a$, i.e. slightly above $1.020c^2_a$, so that a cool WIO should lead to easterlies over the west Pacific. The coupling parameter is put to $\gamma_\tau = 0.80\gamma^0_\tau$ (see Table 3.1), such that in absence of Indian Ocean influence ($A = 0$) the ENSO mode would be slightly damped.

A list of the parameter choices in the reference simulation is provided in Table 5.2a. The parameters for the Indian Ocean modes and Pacific noise are chosen such that the standard deviations of and correlations between the El Niño index and the IOB and IOD indices roughly resemble observed values. Using the HadISST data at $1°$ resolution (Rayner et al., 2003; Met Office Hadley Centre, 2017), we calculated standard deviations $\sigma(Nino3.4) \approx 1K$ in boreal winter, $\sigma(IOD_{obs}) \approx 0.35K$ (autumn), and $\sigma(IOB_{obs}) \approx 0.25K$ (spring). Here IOD_{obs} is the standard IOD index defined in Fig. 1.1, i.e., the SST anomaly (in K) averaged over $10°S - 10°N, 50 - 70°E$ minus the SST anomaly over $10 - 0°S, 90 - 110°E$ (Saji et al., 1999). The IOB_{obs} is the SST anomaly averaged over $20°S - 20°N, 40 - 100°E$ (Saji et al., 2006). The correlations between these indices are given by corr($Nino3.4, IOD_{obs}) \approx 0.6$ for $Nino3.4$ in boreal winter and IOD_{obs} in the previous boreal autumn, and corr($Nino3.4, IOB_{obs}) \approx 0.85$ for $Nino3.4$ in boreal winter and IOB_{obs} in the following spring.

Here we approximate Nino3.4 by N and define model IOD and IOB indices as $A_{IOD} \times [T^{0I}_{IOD}(\vec{x}_{WIO}) - T^{0I}_{IOD}(\vec{x}_{IODe})]$ and $A_{IOB} \times T^{0I}_{IOB}(\vec{x}_{IOB})$ where $\vec{x}_{IODe}$, $\vec{x}_{WIO}$ and $\vec{x}_{IOB}$ are the positions where the IODe, WIO and IOB have their strongest SST signal. Plots of the modelled lag-correlations (between IOD and N, IOB and N and the autocorrelation of N) for the REF case are provided in Fig. 5.8a. Values of the correlations at various local maxima and minima with the corresponding lags, as well as the standard deviations of the indices, are given in Table 5.3. Note that lags are defined as positive if N is leading. The value of the first peak at nonzero lag in the autocorrelation of N may serve to characterise how strongly periodic the ENSO cycle is, and the lag at which this peak occurs serves as proxy for the ENSO period.

As can be seen in Table 5.3, the standard deviations and correlations at small lags of these quantities in the REF case agree reasonably well to observations, however, std(N) is overestimated by a factor of 1.5 and the ENSO period is shorter than observed. The lags

	REF	IO*0	IOD*0	IOD*0.5	IOD*2	IOB*0	IOB*0.5	IOB*2	IODnoi
$\sigma(N)$[K]	1.58	2.99	1.46	1.57	1.84	3.59	2.03	1.86	1.53
$\sigma(IOB)$[K]	0.30	/	0.26	0.28	0.33	/	0.20	0.55	0.27
$\sigma(IOD)$[K]	0.32	/	/	0.16	0.68	0.40	0.33	0.34	0.36
corr(N, IOB)	0.86	/	0.81	0.83	0.88	/	0.90	0.86	0.83
lag(N, IOB)	2.3	/	2.6	2.5	2.3	/	2.9	2.5	2.6
corr(N, IOD)	0.58	/	/	0.55	0.66	0.75	0.62	0.62	0.21
lag(N, IOD)	-1.7	/	/	-1.7	-2.0	-3.2	-2.6	-0.6	-2.1
corr(N, IOD)	-0.38	/	/	-0.36	-0.47	-0.57	-0.50	-0.30	-0.21
lag(N, IOD)	-14.9	/	/	-15.6	-15.8	-28.0	-19.7	-9.1	-15.7
corr(N, N)	0.25	0.73	0.17	0.23	0.32	0.75	0.40	0.20	0.22
lag(N, N)	25.7	52.0	26.3	26.3	26.8	51.2	36.6	16.0	26.5

Table 5.3: *Results of the time integration sensitivity experiments. The labels of the simulations are explained in Table 5.2b. The measures provided here are the standard deviations of the El Niño index N, the model IOB and IOD indices (see section 5.4); the correlation between N and IOB at its global maximum and the corresponding lag (positive if N is leading); the correlation between N and IOD at its global maximum with its lag (positive it N is leading); the correlation between N and IOD at its local minimum at lags of around - 1/2 ENSO period, the value of this lag; the autocorrelation of N at the local maximum at a lag around one ENSO period, and the value of this lag (a proxy for the period). All lags are given in months.*

of corr(N, IOD) (for IOD events occurring a few months before ENSO) and corr(N, IOB) are also a bit shorter than in observations, but take reasonable values despite the lack of a seasonal cycle. As in observations, corr(N, IOD) has a minimum at -15 months lag, but the cause for this is different from reality. In observations, a cool WIO or negative IOD in autumn tends to be followed by El Niño after 15 months, without necessarily a La Niña occurring in between. In the simulations presented here, the negative IOD is first followed by La Niña, and, half a (short!) ENSO period later, by El Niño. In reality, only some negative IOD events are followed by La Niña in the same year (or rather, they co-occur with the developing La Niña; it is hard to disentangle cause and consequences from observations alone), but even a negative IOD occurring independently from La Niña can be followed by El Niño after 15 month. We hypothesise that this can be explained by the influence of the seasonal cycle, which is lacking in our simulations. In observations, a negative IOD occurring independently of ENSO may cause easterlies over the west Pacific, but this happens typically in boreal autumn (the IOD season), i.e. too late in the year to induce a major La Niña (though IOD events starting early in the season can re-enforce ENSO events (Luo et al., 2012). However, warm water is pushed to Indonesia and 'reloads' the Warm Water Volume, thus facilitating El Niño development in the next year.

Next, we decouple the Indian Ocean by multiplying T^{0I}_{IOB} and T^{0I}_{IOD} by zero (the IO*0 case). This leads to an increase in both $\sigma(N)$ and the ENSO period by a factor of ≈ 2 (see Table 5.3), so the net effect of the Indian Ocean is to damp the ENSO mode and shorten its period, which agrees to previous studies (Frauen and Dommenget, 2012; Kajtar et al., 2016). In order to understand in more detail how the IOD and IOB act on ENSO, a set of sensitivity studies was performed by increasing or reducing T^{0I}_{IOB} and T^{0I}_{IOD}, i.e., the magnitude of their spatial patterns. The equation for A (and hence the balance between

ENSO and noise influence on the Indian Ocean) remains unchanged. What is directly changed in this way, is the influence of the IOD or IOB on ENSO (and not vice versa). The numerical simulations are summarised in Table 5.2b and the results are provided in Table 5.3 and Fig. 5.8. It can be seen that the IOB has a strong damping effect on ENSO and shortens its period, while the IOD has little effect on the period but increases ENSO variability. The case IOB*2 is an exception because here the ENSO period is so much reduced that the peak impact of the IOB-induced easterlies (westerlies) occurs not shortly after nearly during El Niño (La Niña) but almost during the zero-crossing of N (the impact on SST lags a few months behind the winds), so the damping becomes less efficient. However, the noise contribution to IOB tends to enhance the variability both of IOB itself and ENSO, and this effect is amplified by doubling T_{IOB}^{0I}. In general, our findings agree with those in section 5.3 and suggest that the IOB has a larger influence than the IOD on the spectral properties of ENSO.

Increasing the influence of the IOD and decreasing that of the IOB both lead to stronger $\text{corr}(N, IOB)$, $\text{corr}(N, IOD)$ and $\text{corr}(N, N)$. This is because both lead to a larger ENSO amplitude, hence the impact of noise on IOD, IOB and the Pacific dynamics becomes relatively smaller, and correlations grow.

As mentioned, the IOB seems to have a stronger effect on ENSO period and standard deviation than the IOD, despite the fact that both have similar standard deviations in REF. One important reason is that the wind response per unit IOB is about 4.5 times as strong as the response per unit IOD. This was estimated by performing a partial regression of the total wind contribution due to Indian Ocean SST and convective heating onto N, IOB and IOD (not shown). The main reason for this increase is the large Gill response to IOB forcing (see Table 5.1), while the partial regression of $u_{ch}(x = L_I + L_{MC}, y = 0)$ onto N, IOB and IOD yields $0.04 m/sK$, $-0.44 m/sK$ and $0.36 m/sK$, respectively. Hence, IOD and IOB have a similar impact on convergence-induced convection. As in section 3a, the impact by ENSO on convection is smaller than that of the Indian Ocean, but not negligible.

Another potentially important factor is the timing of Indian Ocean-induced wind anomalies with respect to the ENSO cycle. The results in section 4.4 suggest that Indian Ocean-induced easterlies peaking slightly before El Niño (La Niña), i.e. slightly before N is maximal (minimal) are optimal for reducing (increasing) ENSO variability (the amplitude effect). Likewise, Indian Ocean-induced easterlies peaking slightly before the sign switch of N, i.e. the transition from La Niña to El Niño (from El Niño to La Niña) are optimal for increasing (shortening) the ENSO period (the period effect). The latter can explain why the IOD has so little influence on the period: It peaks slightly before El Niño. However, the timing of IOD influence is almost optimal for enlarging the ENSO amplitude. To be precise, the growth factor becomes largest if $\psi \approx 73°$ in (5.2), which corresponds to $\phi_{TI} \approx -0.11$ in Table 5.1 (not shown). Note that Luo et al. (2010) also find that the impact of the IOD on the ENSO amplitude is largest relatively early in the season, though their result is also influenced by the seasonal cycle.

A third factor is the regularity with which the Indian Ocean influence affects ENSO. We hypothesise that the effect of the IOD on the spectral properties of ENSO is reduced by the fact that the IOD is less strongly correlated to N, i.e. its influence does not occur as regularly within the ENSO cycle as that of the IOB. To test this hypothesis, one additional simulation is performed, in which the IOD is entirely driven by the noise and not affected by ENSO at all ($a_{0,IOD} = 0$ in (5.2)). In this simulation, labeled IODnoi, η_{IOD} and $a_{d,IOD}$ are chosen such that the standard deviation of IOD is similar to that in REF and the $1/e$-folding time of IOD is about a year. In the IODnoi case, $\sigma(N)$ is larger
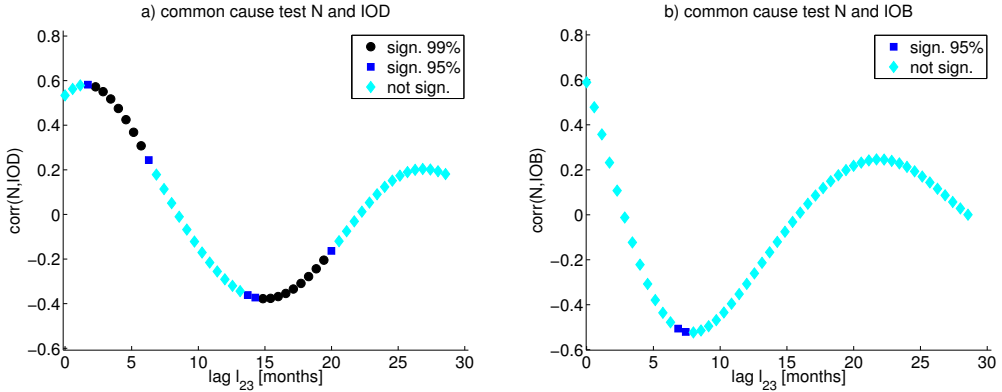
Figure 5.9: *Results of the common cause test for the REF simulation, using either the IOD (a) or IOB (b) as ENSO predictor. Black circles, dark blue squares and light blue diamonds denote values that are significant at* 99% *confidence (two-tailed), at* 95% *confidence or not significant, respectively. The lag* l_{23} *is positive if the predictor (IOD or IOB) leads ENSO.*

than in the IOD*0 case, but lower than for REF. Also, corr(N, IOD) at small negative lags is smaller for IODnoi than for REF (cf. Table 5.3). The positive corr(N, IOD) at small negative lags in IODnoi suggests that a positive (negative) IOD is likely to be followed by El Niño (La Niña), which is to be expected because a positive (negative) IOD leads to westerlies (easterlies) over the Pacific. On the other hand, compared to the IODnoi case, the equation for A_{IOD} in REF also tends to let the IOD peak shortly before N even if the influence of the IOD on ENSO were absent. The combination of these two effects - the influence of ENSO on the IOD and vice versa - leads to the higher corr(N, IOD) in the REF case. The reason for the higher $\sigma(N)$ in REF compared with IODnoi is that in REF, the influence of ENSO on the IOD helps to let IOD events occur during a phase of the ENSO cycle where they in turn support ENSO development. These results confirm the hypothesis that a higher corr(N, IOD) leads to a stronger impact of the IOD on the spectral properties of ENSO, but also suggest that the correlation between IOD and ENSO may partly be due to influence exerted by the Indian Ocean on the Pacific - not only vice versa. The high values of corr(N, IOB), however, must be dominated by the influence of N on the Indian Ocean, because the influence of the IOB on the Pacific mainly counteracts ongoing ENSO events.

The relative independence of the IOD on the ENSO cycle makes it potentially a better ENSO predictor than the IOB, which is so closely linked to ENSO that it gives little additional information beyond what is already available from N (Izumo et al., 2013). To confirm this, we performed the 'common cause test' of section 2.2 on the data of the REF simulation. This test investigates whether the correlation between two time series z_2 and z_3 is significantly different from what one expects, given their correlations to a third time series z_1. In other words, it tests whether corr(z_2, z_3) can be explained by the fact that both z_2 and z_3 are also correlated to the 'common cause' z_1. As argued in section 2.2, the test is passed if both corr(Z_2, z_3) and corr(z_2, Z_3) are significant, where $Z_k = z_k - a_{k1}z_1 - b_{k1}$ and a_{k1}, b_{k1} are obtained from a linear fit of z_k onto z_1.

Here, we use $IOD(t)$ or $IOB(t)$ as z_2, $N(t + l_{23})$, where l_{23} is a positive lag, as z_3, and $N(t + l_{12})$, where $l_{12} \leq 0$, as z_1. That is, supposing that at time t we want to predict ENSO a time l_{23} in advance, we check if the IOD or IOB contains additional information

compared to current or previous values of N, namely at time $t + l_{12}$. As the value of l_{12} at which $N(t + l_{12})$ contains the most information about $N(t + l_{23})$ is not known a priori, we try every value in $l_{12} \in [-P, 0]$, where P is the ENSO period, and consider the test passed only if it is passed for each individual l_{12}.

The results for REF are given in Fig. 5.9. It can be seen that the IOB, despite reaching higher values of $\text{corr}(z_2, z_3)$ never passes the test at 95% confidence (two-tailed) except at two points, while the IOD reaches 99% significance for lags of about 4 months and 4 months$+P/2$. At very small lags l_{23}, the test cannot be passed, because then for $l_{12} = 0, N(t + l_{12})$ is automatically very similar to $N(t + l_{23})$, due to ENSO persistence. In the other simulations (not shown), the IOD always passes the common cause test for lags of about 4 months and 4 months$+P/2$ at 99% significance (95% for IODnoi and IOB*2). For IOD*0, such a statement cannot be made. The IOB passes the common cause test at $l_{23} \approx 7$ months for the IOD*0.5 and IODnoi cases (95% confidence) and 99% for IOD*0 and the somewhat extreme case IOB*2, i.e. mainly for those cases where $\text{corr}(N, IOB)$ at small lags (see Table 5.3) are smaller than for REF, so that the IOB is less influenced by ENSO.

These results suggest that both the IOB and the IOD influence ENSO. The IOB has a stronger effect on the spectral properties of ENSO (damping and period shortening), because it is so strongly correlated to ENSO that its influence occurs at fixed phases of the ENSO cycle. The IOD enhances ENSO variability, hardly affects the period, and is - despite its much smaller wind response - a better ENSO predictor than the IOB because it is less strongly tied to the ENSO cycle. The IOB influence is dominated by the direct effect of the SST, but the strong IOD influence is made possible by the convergence-induced convection.

5.5 Summary and Discussion

Based on a Gill-model response, one would expect that a cool west Indian Ocean is accompanied by westerly anomalies over the west Pacific. Our results suggest that a sufficiently strong convective feedback over the east Indian Ocean and Maritime Continent weakens, and may in principle even revert, this wind response into easterly anomalies, as illustrated in Fig. 5.1. This is because west Indian Ocean cooling leads to subsidence over the west Indian Ocean and (weak) upward motion above the Maritime Continent. The latter leads to condensation and convective heating, which in turn leads to stronger upward motion and horizontal mass convergence, i.e. easterlies over the west Pacific. This is in line with the proposed mechanism in section 2.4.1. However, the reversal of the Gill response requires a very strong convection feedback (i.e. a high value of γ_c), and it is not clear, whether such values - or, in general, our simple representation of the convection - are realistic.

In observations, a cool west Indian Ocean in (boreal) autumn is often associated with a warm east Indian Ocean Saji et al. (1999) and warm marginal seas in the Maritime Continent Annamalai et al. (2010), thanks to the Indian Ocean Dipole. As a warm eastern pole of the IOD can also lead to enhanced convection above the east Indian Ocean and Maritime Continent, it is hard to disentangle the relative influence of both IOD poles. In fact, we find (Fig. 5.10a,b) that in our REF simulation the eastern IOD pole performs better than the western pole in the common cause test, though this is partially by design (choosing γ_c close to the value γ_{crit} minimises the wind impact of the west Indian Ocean). In observations, the western pole performs better (see Fig. 5.10c,d). Whichever pole is dominant, we find that a negative IOD is associated with easterlies over the west Pacific
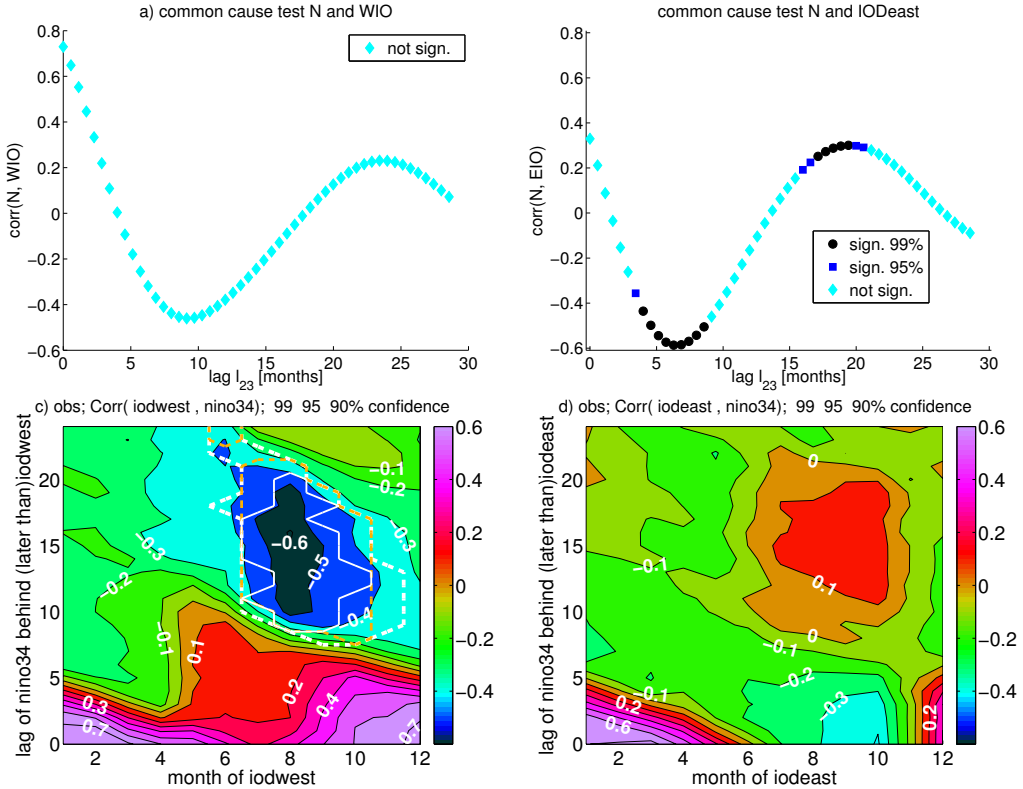
Figure 5.10: *Top row: Model results of the common cause test for the REF simulation, using either the WIO (a) or IODeast (b) as ENSO predictor. Black circles, dark blue squares and light blue diamonds denote values that are significant at 99% confidence (two-tailed), at 95% confidence or not significant, respectively. The lag l_{23} is positive if the predictor (IOD or IOB) leads ENSO. Bottom: The same but for observations. Since observations have a seasonal cycle, each month is treated separately: the x-axis represents the month where the IODwest or IODeast is taken (1 being January, etc), the y-axis shows the lag l_{23}, which is positive if the Indian Ocean leads. White dashed lines, orange dashed lines, and white solid lines encircle values which are significant at 90%, 95%, and 99%, respectively.*

which can either support an ongoing La Niña (e.g. Annamalai et al. (2010)), or enhance the west Pacific Warm Water Volume to favour El Niño development after about 15 months (see chapter 2, Izumo et al. (2010)). Our findings contradict studies suggesting that the IOD only has an indirect effect on ENSO, either by suppressing IOB variability which has a damping effect on the ongoing ENSO Annamalai et al. (2005); Santoso et al. (2012) or by strengthening (through removal of a delayed negative feedback) the effect of the spring IOB on next winter's ENSO (Izumo et al. (2015); note that our 'IOD' corresponds to the 'IOD+IOB' case in their Fig. 10e). These studies point out that due to their close proximity, the effects of the eastern and western pole of the IOD roughly cancel over the Pacific. Our results suggest that this is true for the direct SST heating effect, but not for convergence-induced convection over the Maritime Continent.

The sensitivity studies in section 5.4 suggest that the net effect of Indian Ocean variability is to dampen ENSO and shorten its period, which is in line with many previous studies Kug and Kang (2006); Kug et al. (2006); Santoso et al. (2012); Frauen and Dommenget (2012); Kajtar et al. (2016). The net effect of the Indian Ocean is dominated by the IOB, for which during El Niño we find that both the local heating and the convergence-induced convection lead to easterlies opposing the westerlies associated with El Niño (Table 5.1). However, as the IOB is strongly correlated with ENSO (the correlation between Nino3.4 in boreal winter and IOB in the following spring is about 0.85), the IOB does not offer ENSO-independent information and hence is not a useful precursor to ENSO (Izumo et al., 2013). On the other hand the IOD, which is less dependent on ENSO (the correlation between IOD in boreal autumn and Nino3.4 in the following winter is about 0.6) may be a useful ENSO predictor, as suggested by Izumo et al. (2010). The correlation between IOD and N passes the common cause test, whereas the correlation between IOB and N hardly does (see Fig. 5.9).

Our results do not fully capture the mechanism of Indian Ocean-ENSO interaction suggested by Izumo et al. (2010) and in chapter 2, wherein a cool west Indian Ocean or negative IOD favours El Niño after 15 months. Rather, a negative IOD is followed by La Niña after just a few months. In observations, IOD variability is typically highest in boreal autumn, which is too late in the year to induce a major La Niña (though Luo et al. (2010) suggest that a cool IODeast early in the season may support El Niño growth); instead, the IOD-induced easterlies lead to an increased west Pacific Warm Water Volume which favours El Niño in the following year. Our model lacks a seasonal cycle and its ENSO period is too short, therefore it does not capture this delay between IOD forcing and ENSO variability. However, a vital process - the easterly wind response to negative IOD forcing due to convection over the Maritime Continent - is represented.

As mentioned, a source of uncertainty in our model is the value of the convection parameter γ_c. For values around $\gamma_c = 1.02c_a^2$ (where the wind response to the west Indian Ocean heating switches sign) the results become rather sensitive to γ_c, hence it is hard to assess whether our value is 'correct'. If the high sensitivity to γ_c is not solely due to our very simple convection scheme, our results strengthen the notion that a good representation of convection is important for correct modelling of ENSO and its interaction with the Indian Ocean. With our model we can only show that convection over the Maritime Continent *might* have an important effect. Note that even if in reality the convection effect were too weak to turn the wind response over the Pacific to a pure cool west Indian Ocean into easterlies, it might still lead to a easterly response to a negative IOD, for which the pure Gill response is nearly zero.

It is maybe impossible to judge from observations whether the convection feedback can turn the Pacific wind response to a cool west Indian Ocean into easterlies, because of the

powerful ENSO cycle obscuring the Indian Ocean-induced signals. Therefore experiments with more sophisticated models are needed to check our findings. Kajtar et al. (2016) performed partial decoupling experiments with a relatively low-resolution atmosphere-ocean-GCM. In their Fig. 8a and e, they show that for their fully coupled simulation a composite of positive (negative) IOD years is accompanied by strong westerlies (easterlies) over the Pacific for more than half a year. When suppressing interannual Pacific variability, most of this signal vanishes, but there remains a spatially confined but statistically significant westerly (easterly) signal in late boreal autumn (see their Fig. 8b,f; though the latter signal is only very weak). These signals might be a result of Indian Ocean-induced nonlinear convection over the Maritime Continent. Note, though, that many GCMs still have biases in modelling the IOD Cai and Cowan (2013) which may affect the simulation of such subtle effects as IOD-ENSO interaction.

These results suggest that convection above the Maritime Continent may play an important role in interactions between the Indian Ocean and ENSO; non-locally induced convection might even reverse the wind direction on the atmospheric bridge. It might hence be worthwhile to study these processes with more sophisticated models. This may also be of value for understanding future changes in the Indian Ocean - ENSO interaction, since convection anomalies might be rather sensitive to changes in the warm pool background state.

Chapter 6

On the interaction between the Indian Ocean and ENSO in CESM[1]

6.1 Introduction

From the analysis of observational data in chapter 2 a possible pathway emerged by which the west Indian Ocean might impact ENSO: A cool west Indian Ocean in boreal autumn causes ascent of air above the Maritime Continent due to the Gill response, but as the Maritime Continent is an area with a warm and moist background state, the initial ascent could be nonlinearly amplified sufficiently to cause easterly winds above the west Pacific due to low-level convergence. These easterlies favour the accumulation of warm water in the west Pacific, which in turn is favourable for El Niño development in the course of the next summer-winter. Experiments with the convective Zebiak-Cane model confirmed that in principle convection over the Maritime Continent might be strong enough to generate easterlies over the west Pacific as a reply to west Indian Ocean cooling, but this requires a rather strong convective feedback strength - a free parameter that cannot easily be determined. In addition, the Zebiak-Cane model suggests that SST warm anomalies in the east Indian Ocean should be more efficient in creating easterly wind anomalies over the west Pacific, because in this case the Gill response and the effect of nonlinear convection co-act, rather than cancelling each other out. The notion that the eastern, rather than the western, half of the Indian Ocean determines the impact on ENSO is in line with Izumo et al. (2010, 2015), but contradicts the results in section 2.2, namely, that the correlation Skilful east Indian Ocean SST in autumn and Nino3.4 15months later is insignificant. Since reliable observational data in the Indo-Pacific equatorial region do not yield a very long record (phases of large sampling errors occurring up to the 1940ies according to Izumo et al. (2013)) it appears natural to also use GCM data to test our hypothesis. However, it should be kept in mind that GCMs have systematic biases, for example concerning the amplitude of IOD (Cai and Cowan, 2013) which might affect the subtle interaction between the Indian and Pacific Oceans.

In this chapter, output from control runs of the Community Earth System Model

---

[1]This chapter is based on the article Wieners, C.E., W.P.M de Ruijter, and H.A. Dijkstra: The interaction between the Indian Ocean and ENSO in CESM. Submitted to Climate Dynamics.

(CESM) is analysed, focusing on the Indo-Pacific interaction via the atmospheric bridge.

6.2   Model description and methods

The Community Earth System Model (CESM) contains model components for the oceans, sea ice, land surface, land ice, and the atmosphere (Hurrel et al., 2013). The ocean component is the Parallel Ocean Program (POP, version 2.1) model (Smith et al., 2010), while the atmosphere is modelled by the Community Atmosphere Model (CAM; Neale at al. (2012)). In the simulations used in this study, the radiative forcing (solar, aerosol, and greenhouse gasses) is kept at observed year 2000 values.

Two control runs of CESM are used in this analysis. One of them, the Low Resolution (LR) simulation, is performed with CESM version 1.1.2 with CAM5 at a resolution of $1°$ for the atmosphere and a nominal resolution of $1°$ for the ocean and sea ice (that model uses a curvilinear, tripolar grid); the ocean has 60 non-equidistant depth levels. For this simulation, the model years 400-498 are used. The other simulation (High Resolution or HR) is performed using CESM1.0.4 with CAM4 at a resolution of $0.5°$ for the atmosphere and $0.1°$ for the ocean, with 42 depth levels. Roughly 200 years are available for this simulation. Although the model is not perfectly equilibrated after this time, spin-up related trends flatten out substantially after about 80 years (supplementary material of van Westen and Dijkstra, 2017). It therefore seems justifiable to use model year 93-192 and apply some suitable detrending method, especially since our analysis does not deal with deep sea processes. Data is available as monthly means, and is interpolated on a rectangular grid before use.

For comparison with observations (abbreviated as OBS), the following observational data sets were used: The Sea Surface Temperature (SST) in the years 1948-2016 is provided by the Hadley Centre (Rayner et al., 2003; Met Office Hadley Centre, 2017). Surface wind, Outgoing Longwave Radiation (OLR, taken at the top of the atmosphere), and surface heat flux data for 1948-2016 were taken from the NCEP reanalysis (Kalnay et al., 1996; NOAA/OAR/ESRL PSD , 2017), and for 3D ocean temperature and currents, as well as the wind stress, SODA data for 1948-2010 was used Carton and Giese (2008); SODA (2017).

The data is detrended with a 23 years running mean, similar to what was done in chapter 2. The seasonal cycle is subtracted where appropriate. Often the analysis is carried out for individual calendar month. When studying the impact of the Indian Ocean on ENSO, year 0 is defined as the year in which the relevant Indian Ocean anomaly takes place which might lead to an ENSO event in the winter of year 1-2.

As before, when defining criteria for, say, El Niño years, the following shorthand notation is used: Nino3.4$(ND(1)JF(2)) > 0.9$. This means that an El Niño is defined to occur in the winter of year 1-2 if the Nino3.4 index, averaged over November of year 1 to February of year 2, exceeds 0.9 times the standard deviation of this quantity. A definition in terms of standard deviations, rather than fixed values, is preferable because the amplitude of ENSO variability differs considerably between HR, LR and OBS.

An important tool in this chapter is partial regression. If one regresses a time series y onto several time series x_k $(k = 1, 2, ...)$ which are mutually correlated, this affects the significance levels. As an extreme example, suppose $x_1 = X + \epsilon z$ and $x_2 = X - \epsilon z$ where $\text{std}(X) = \text{std}(z) = 1$ and $\epsilon \ll 1$, and $y = Y + z$. Suppose also that X, Y, and z are uncorrelated. Then x_1 and x_2 are strongly correlated, but while neither x_1 nor x_2 are strongly correlated to y, y is strongly correlated to $x_1 - x_2$. Thus when linearly fitting $y = a_1 x_1 + a_2 x_2 + Res$, one might obtain relatively large coefficients a_1 and a_2 with

$a_1 \approx -a_2$. This effect is taken into account in significance tests by letting the confidence limits depend on the correlations between the x_k. The actual regression coefficients are compared to results obtained from N surrogate data sets $\{\tilde{x}_k\}$ where the correlations among the $\tilde{x}_k$ are the same as for the original x_k. A regression coefficient is considered significant at $s\%$ confidence (two-tailed) if its absolute value is larger than that of $s\%$ of the corresponding surrogate results. When using relatively moderate significance levels like $s = 90$, $N = 1000$ is a reasonable choice.

As we are mainly interested in estimating the relative influence of the x_i on y, rather than the amplitude of the time series, all time series are normalised by their standard deviation prior to performing the regression.

6.3 Indo-Pacific interaction

6.3.1 Preliminary check of basic ENSO and Indian Ocean properties

Prior to investigating the Indo-Pacific connection, the model performance concerning some basic properties of ENSO and the Indian Ocean modes - Indian Ocean Dipole (IOD) and Indian Ocean Basinwide Warming (IOB) - is checked in this section.

Both HR and LR have ENSO and IOD variability with reasonable spatial patterns (Fig. 6.1). During the peak of ENSO (represented by composites of the SST anomaly in December of year 1, Fig. 6.1a-c), both the warm anomaly in the cold tongue and the surrounding cool anomaly, the 'horse shoe pattern', are well represented. For the positive IOD (represented by a composite in September of year 1, Fig. 6.1d-f), CESM (both HR and LR) and OBS all show a spatially relatively extended, but weaker, warm anomaly in the west Indian Ocean and a more localised, strong cool anomaly off Sumatra. The figures show that El Niño tends to co-occur with a positive IOD and vice versa. In CESM, the anomalies are stronger and the eastern one extends more to the east and to the north than in OBS, but little difference is noted between the two CESM versions, HR and LR. The IOB variability (Fig. 6.1g-i) is less well represented in CESM. In OBS, most parts of the Indian Ocean show a modest, but significant warm anomaly, whereas in CESM only the west Indian Ocean and the IODeast region are warm, whereas the northeast is cool. The dominance of IOD over IOB variability in CESM is confirmed by an EOF analysis of Indian Ocean SST (Fig. 6.2): In OBS, the first EOF (Fig. 6.2a, explaining 40% of the variance) shows warming over most of the Indian Ocean, though it is weakest in the IODeast region, while only the second EOF (Fig. 6.2d, 12%) represents IOD variability. In CESM, the IOD determines the first EOF with 34% and 47% of the variance for HR and LR, respectively (Fig. 6.2b,c), while the second mode does not resemble an IOB either.

In order to investigate the strength and seasonality of the various modes of variability, the standard deviation of several indices for each calendar month is plotted in Fig. 6.3. Nino3.4 in CESM has its largest variability in boreal winter, as is the case for OBS. LR overestimates and HR underestimates the ENSO amplitude (e.g., std(Nino3.4) in December takes the values $1.66K$ for LR, $0.83K$ for HR and $1.11K$ for OBS). The variability in Nino1+2, relative to Nino3.4, is underestimated in CESM, especially in LR (i.e., LR El Niño has a comparatively weak signal at the Peruvian coast, while observed El Niños often start with coastal warming in boreal summer). As for OBS, std(IOD) in CESM peaks in autumn, but its peak values are much too high (for October, the values are $1.54K$ for LR, $1.1K$ for HR and $0.42K$ for OBS, i.e. CESM overestimates std(IOD) by

about a factor of three). This is mainly due to the very strong variability in the eastern pole of the IOD (IODeast) in CESM.

Fig. 6.4 shows normalised power spectra of several Indian and Pacific quantities. Both HR and LR reproduce the typical period of around 4 years reasonably well. However, LR has a much more regular spectrum with a single, relatively narrow peak at a period of about 4.3 years. All quantities show this peak, suggesting that ENSO and the Indian Ocean are strongly linked. The HR spectra are less periodic and show two broader peaks, one at 5.7 and one at 3.6 years. The plot for OBS also has two peaks at similar periods, except for IOD which in OBS also has a strong bi-annual peak that lacks in HR and LR.

In OBS, the IOD signal is seasonally strongly confined to boreal autumn; the auto-correlation (Fig. 6.5) for, say, IOD in September is above 0.3 only for lags of up to three months, indicating that IOD events start in boreal summer and end in early winter. For CESM, especially LR, this effect is weaker. In LR, autumn IOD is even positively correlated to next summer's IOD, with a break in early spring. In other words, consecutive IOD events might occur (henceforth referred to as die-hard IOD); often, the first event co-occurs with an ENSO event while the second does not. For more details about the die-hard IOD, see the appendix of this chapter.

While observed El Niños show a considerable diversity and can for example be grouped into central Pacific and east Pacific El Niños, or into eastward and westward propagating events (see chapter 2), no significantly distinct classes of ENSO events can be generated for CESM. When attempting to sort the ENSO events by the criteria used in 2.3.2 (with possible some shift in the exact threshold values), the groups are not significantly different at 90% confidence (not shown). We also tried to detect ENSO flavours by means of an MSSA (see section 2.1.2 for an explanation of the technique. The results are not shown here). HR has two ENSO modes with periods consistent with the spectra in Fig. 6.4b, but very similar spatial patterns. In LR, the second MSSA mode shows eastward propagation of SST patterns, while the first does not. However, the first mode has almost 4 times as much variance as the second one, so apparently the second mode is of minor importance. Due to the lack of ENSO diversity in the model, the question whether Indian Ocean influence affects the ENSO flavour cannot be investigated using CESM.

6.3.2   Correlation-based analysis

Fig. 6.6 shows the correlations between IOD and Nino3.4. Obs shows a strong seasonal dependence. At small lags, IOD peaking in autumn is positively correlated (about 0.65) to the ENSO event lasting from the previous summer to the next spring. For IOD in January-April, the correlation to Nino3.4 is close to zero. However, for CESM, this seasonal dependence is much weaker, correlations at relatively small lags are positive in all seasons, though weakest for IOD in spring. Especially in LR, IOD is also positively correlated to Nino3.4 at negative lags of about 10 months, i.e. a positive IOD is preceded by El Niño. This reflects the 'die-hard IOD' effect mentioned in section 6.3.1, i.e. an IOD event co-occurring with ENSO may be followed by a second IOD event without ENSO.

More importantly, for OBS at lags beyond 1 year, we find a negative correlation at +15 months lag (a negative IOD in summer-autumn is followed by El Niño 1.5 years later). No such strong correlation is found for negative lags longer than a year (IOD following ENSO). Thus at lags exceeding one year, the IOD predicts ENSO better than the other way round, suggesting a possible physical influence from the IOD on ENSO. Similar relations hold for HR. However, in LR we find strong negative correlations both for IOD leading ENSO by 15 months and for ENSO leading the IOD by about 25 months. This makes it doubtful whether the IOD is a useful ENSO predictor in LR - or vice versa.
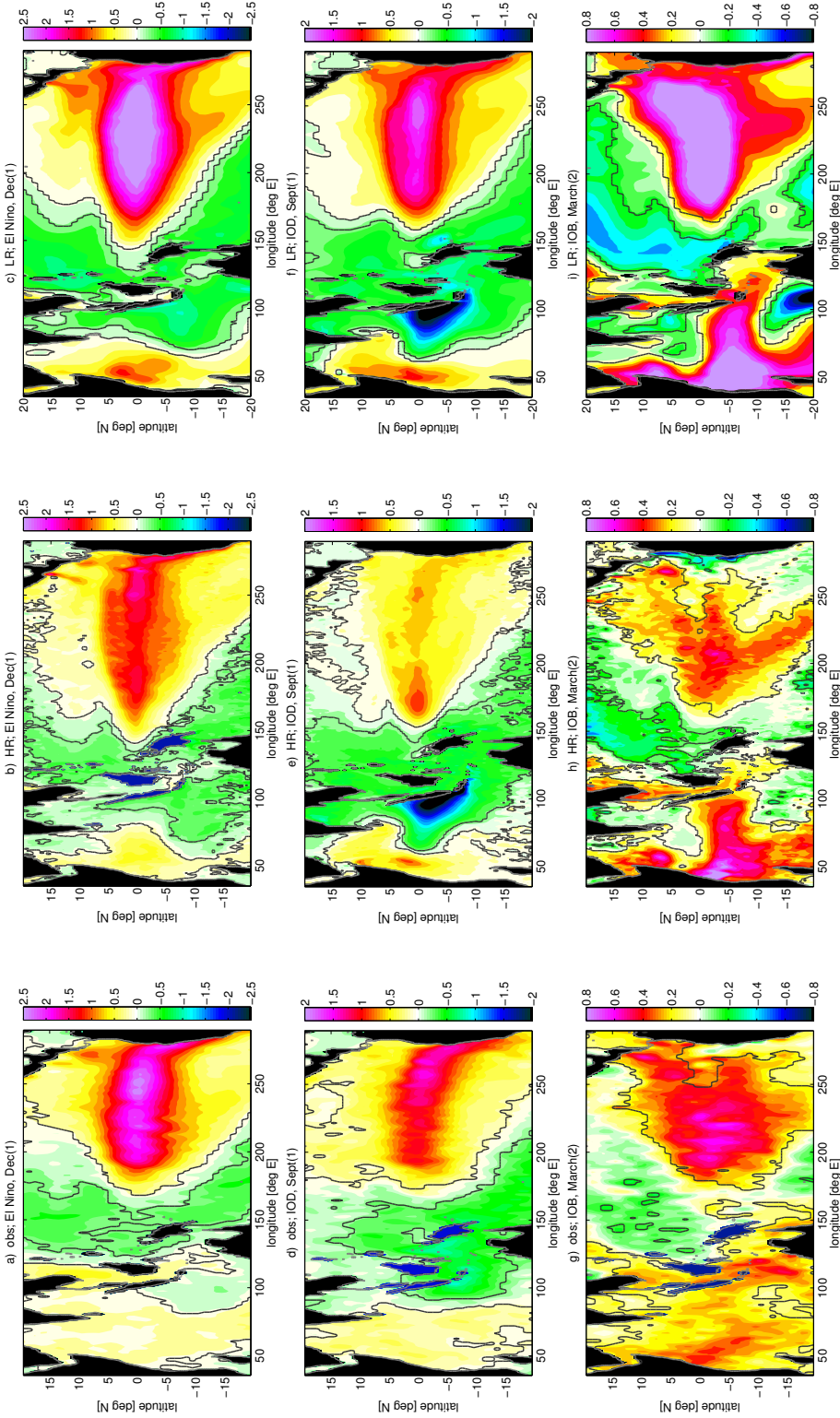
Figure 6.1: *SST Composites of El Niño (top row; plots for dec(1)), IOD (middle row; plots for sept(9)) and IOB (bottom row; plots for March(2)) for OBS (left), HR (middle) and LR (right). The criteria for the composites are: Nino34(ND(1)JF(2)) > 0.9σ for El Niño; IOD(ASON(1)) > 0.9σ for IOD and IOB(FMAM(2)) > 0.9σ for IOB. Black lines encircle areas where the anomaly is significant at 90% confidence.*
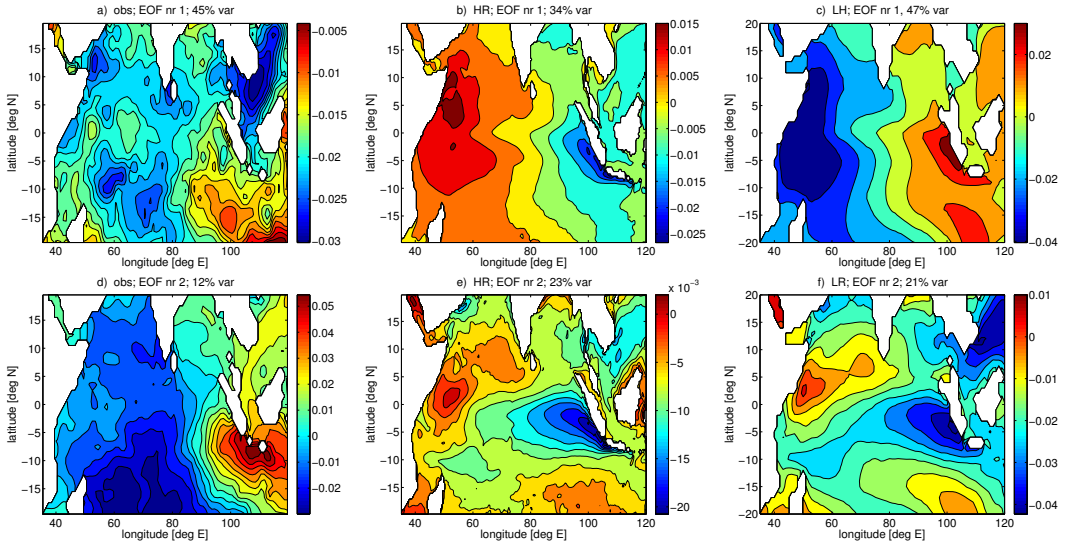
Figure 6.2: *The leading two EOFs of the Indian Ocean SST for OBS (left), HR (middle), and LR (right). Percentages of explained variance are given in the plot titles. The seasonal cycle was subtracted before the analysis, but all calendar month were used. Note that EOFs are only determined up to an overal scaling constant, and that the colour scale (in particular, the zero point) is not the same for all plots.*
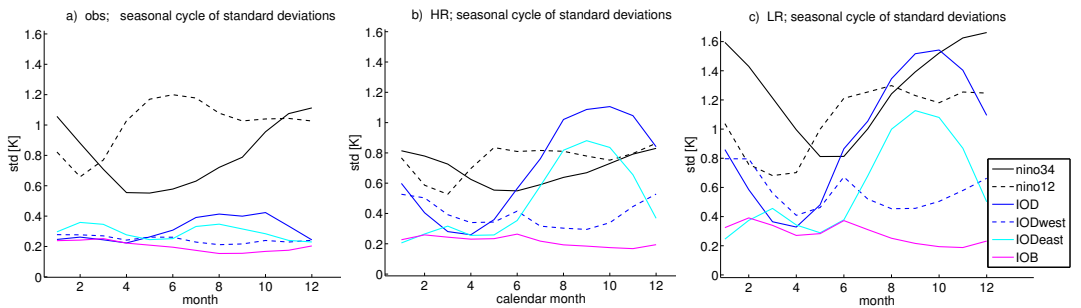

Figure 6.3: *Seasonal cycle of standard deviations of several indices for OBS (left), HR (middle), and LR (right)*
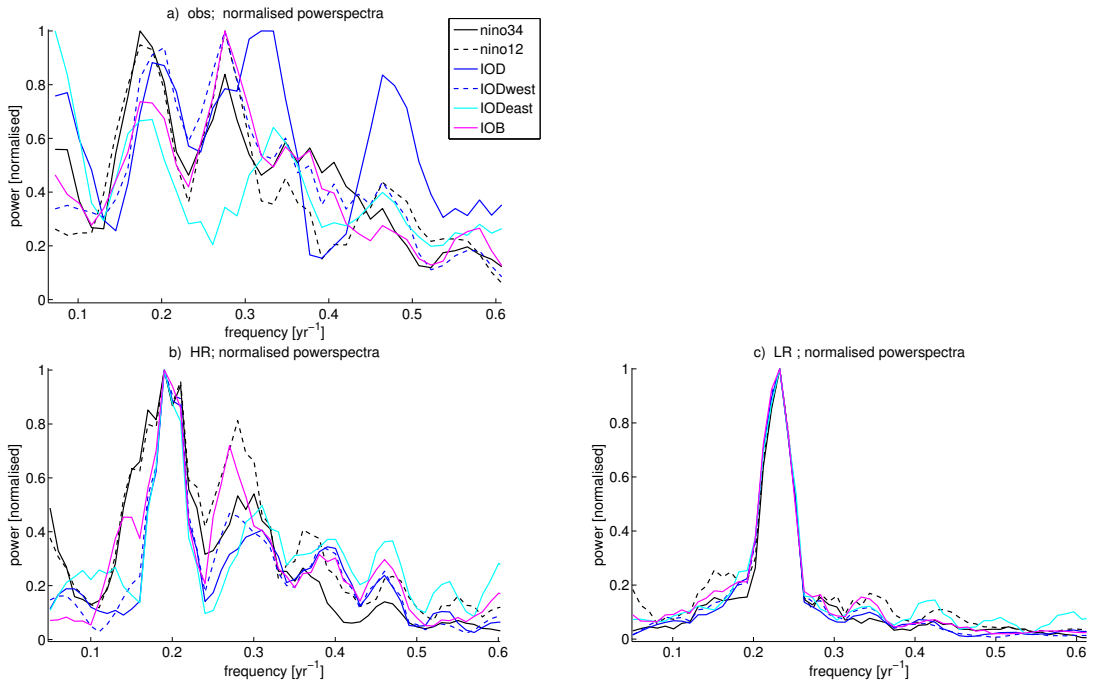
Figure 6.4: *Power spectra of various time series (after subtraction of the annual cycle) for OBS (a), HR (b), and LR (c). All curves were normalised by dividing by their peak value.*
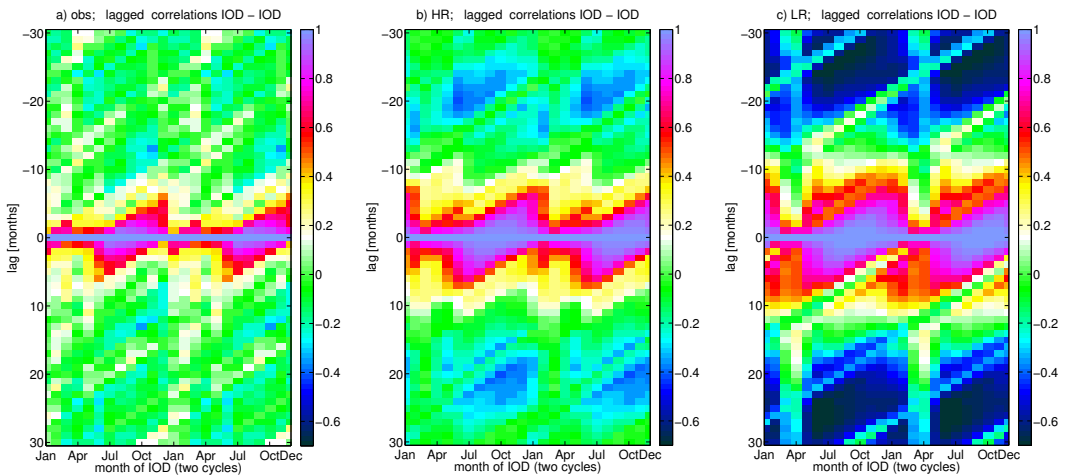

Figure 6.5: *Season-dependent lagged autocorrelation of IOD for OBS (a), HR (b), and LR (c). The x-axis shows the month in which IOD is taken; the y-axis shows the lag in months. The data was detrended before correlating.*
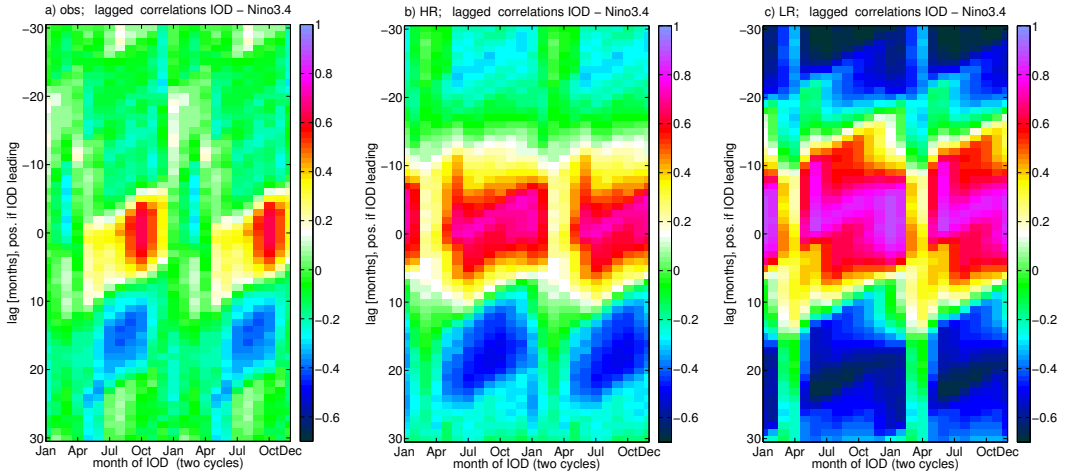
Figure 6.6: *Season-dependent lagged correlations between Nino3.4 and IOD for OBS (a), HR (b), and LR (c). The x-axis shows the month in which IOD is taken; the y-axis shows the lag in months (positive if Nino3.4 is taken at a later time than IOD). The data were detrended before correlating.*

In order to check whether the correlations at lags around 15 months are significant against the null hypothesis that they are a side effect of the stronger correlations at small negative lags and ENSO cyclicity, the common cause test of section 2.2 can be applied. The correlation of z_2 and z_3 is checked against the common influence of z_1, where z_2 is IOD or one of its poles or IOB, z_3 is Nino3.4 taken at lag l_{23} later than z_2, and z_1 (the common cause) is Nino3.4 at lag l_{12} later than z_2. For z_2=IOB, the values $-14 < l_{12} < 0$ were used and for z_2=IOD, we used $-14 < l_{12} < 6$ (all in months). The reason for this choice is that IOD may be linked to a still growing El Niño peaking later than IOD itself, while IOB is thought to be influenced by the previous ENSO.

In observations, IOB, IOD and IODwest in autumn are all negatively correlated to Nino3.4 about 15 months later, and 99% confidence is reached for all these Indian Ocean quantities (see Fig. 6.7). The strongest correlations occur for IODwest. IODeast in autumn is weakly and insignificantly positively correlated to Nino3.4 1.5 years later, suggesting that the west Indian Ocean has a stronger impact on ENSO than the eastern half. The strong negative correlation with IOB seems surprising at the first sight, because one would expect a negative IOB to cause westerlies (Gill response dominating) which hamper warm water accumulation. However, autumn is not the main IOB season, and in general IOB is strongly correlated to IODwest (> 0.83 at lag 0 for all calendar months), likely the IOB signal is dominated by the IODwest in autumn.

For HR, the correlations for IODwest and IOD are similar to those in OBS. As opposed to OBS, the positive correlation between IODeast and Nino3.4 is also significant. A greater influence of IODeast in CESM can possibly be explained by its very strong variability in CESM. A very warm IODeast can cause easterlies over the west Pacific, even if the atmospheric response is a pure Gill response.

For LR, even though correlations are generally higher than for HR, the common cause test mostly gives negative results, suggesting that ENSO is so cyclic here that the Indian Ocean does not yield much independent information about ENSO. This does not mean
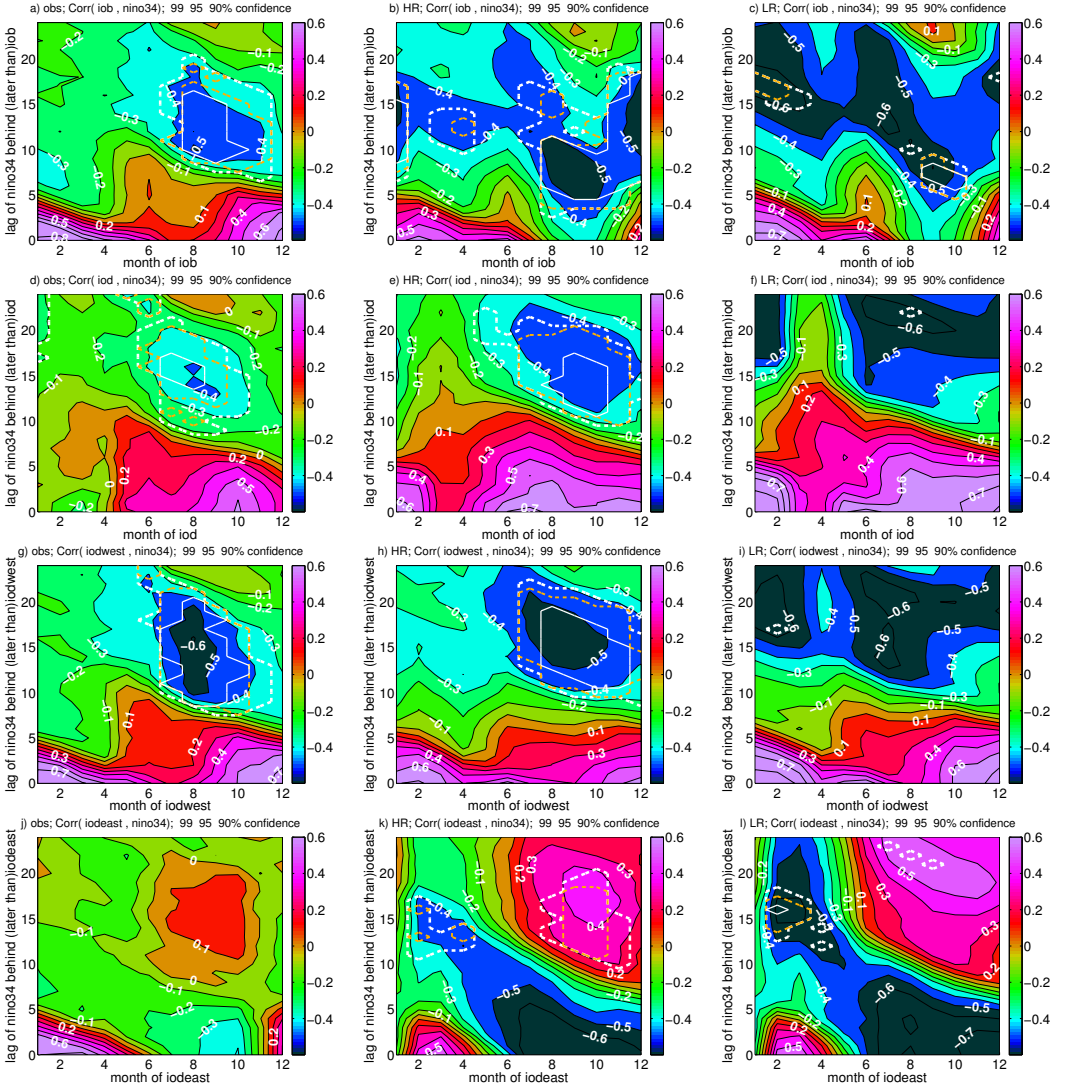
Figure 6.7: *Common cause test for Nino3.4 and IOB (plot a,b,c), IOD (d,e,f), IODwest (g,h,i) and IODeast (j,k,l) in OBS (left column), HR (middle), and LR (right). White dashed, orange dashed and white solid lines encircle values which are significant at 90%, 95%, and 99% confidence, respectively.*

that the Indian Ocean cannot physically influence ENSO. It just means that in LR, knowing the IOD does not help much in predicting ENSO, and the impact of the IOD cannot easily be disentangled from ENSO influence by statistical analysis.

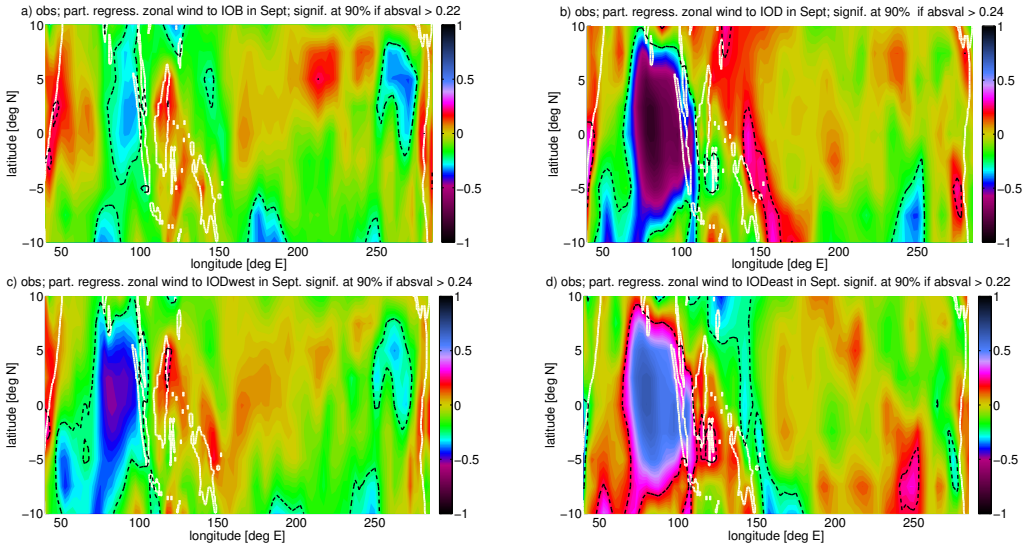### 6.3.3   The Indo-Pacific atmospheric bridge in CESM

Figure 6.8: *Partial regression of observed zonal wind in Sept. onto the following indices at zero lag (regression to Nino3.4 not shown): a) Nino3.4 and IOB, b) Nino3.4 and IOD; c&d) Nino3.4, IODwest (c), and IODeast (d). All data (indices and local field time series) were normalised by their local std before regressing. Black lines encircle regions with 90% confidence (two-tailed). White lines are coastlines.*

Next, an attempt is made to verify that a negative (positive) IOD indeed leads to easterlies over the west Pacific, to assess the role of the two poles of the IOD and investigate the role of convection.

First, the zonal wind in September is regressed onto the IOD or IOB in the same month. In order to filter out the effect of possible co-occurring ENSO events, partial regressions are used. For OBS, it suffices to regress onto IOD (or IOB) and Nino3.4 at zero lag. For CESM, the regression is carried out onto IOD (or IOB) and Nino3.4 at zero lag and Nino3.4 in the previous December (i.e. at -9 months lag), because Nino3.4 in December is significantly correlated to both IOD and the SST in an area around $5°S, 200°E$ in September (remnants of the ENSO-related SST anomaly; not shown), leading to spurious correlations between IOD and the southeast Pacific SST and thus the south Pacific winds. Finally, in order to investigate the relative importance of both IOD poles, partial regressions are carried out onto Nino3.4, IODeast and IODwest (all at zero lag), and Nino3.4 in previous December (only for CESM). Prior to regressing, all time series and fields were normalised by their (local) standard deviation, so that the regression coefficients only contain information on the proportion of explained variance, not the standard deviation of the time series considered. Only the partial regressions onto Indian Ocean quantities are plotted.
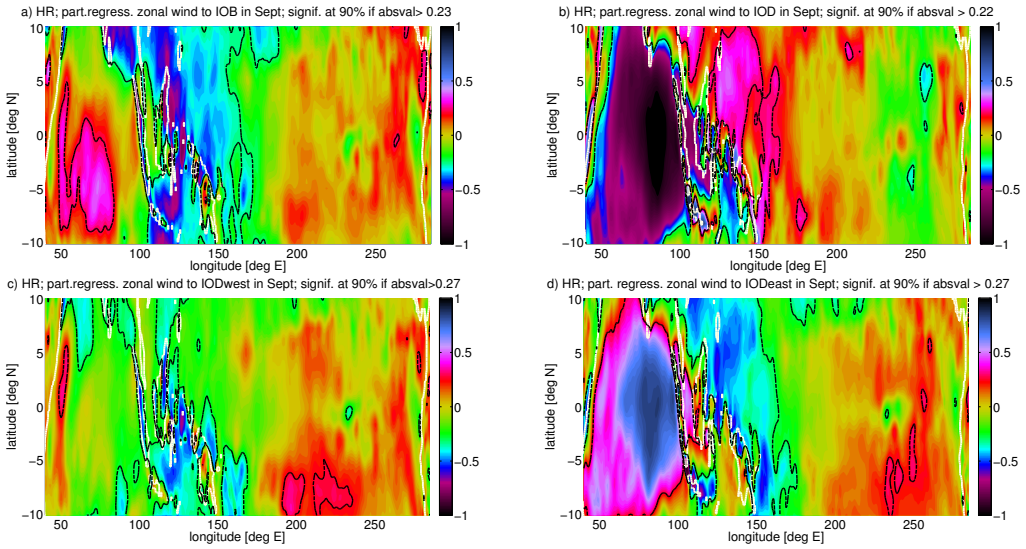
Figure 6.9: *Partial regression of HR zonal wind in September onto the following indices (regression to Nino3.4 not shown): a) Nino3.4 and IOB at zero lag and Nino3.4 9 month before, b) Nino3.4 and IOD at zero lag and Nino3.4 9 month before; c&d) Nino3.4, IOD-west (c), and IODeast (d) at zero lag and Nino3.4 9 months before. All data (indices and local field time series) were normalised by their local standard deviation before regressing. Black lines encircle regions with 90% confidence (two-tailed). White lines are coastlines.*
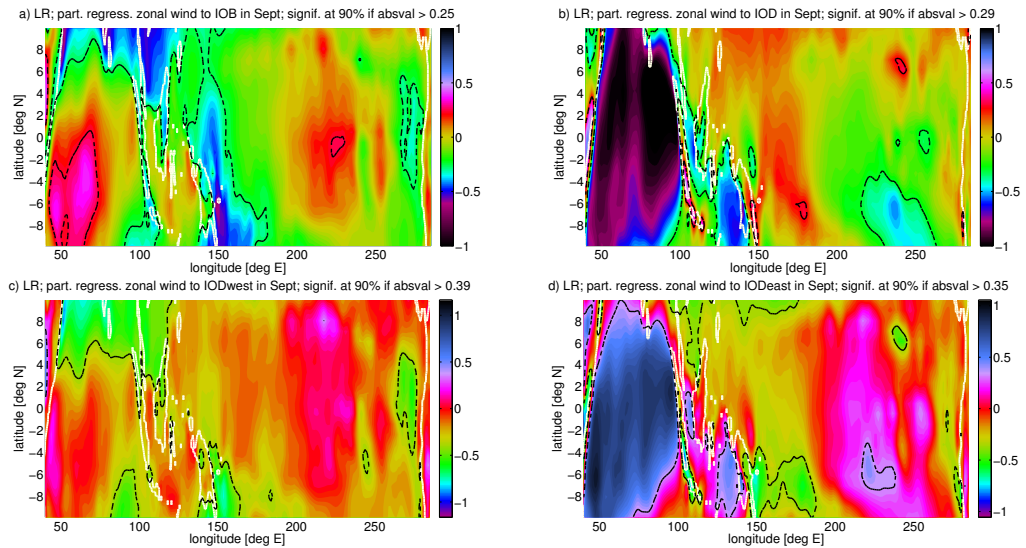
Figure 6.10: *as Fig. 6.9, but for LR instead of HR.*

In OBS (see Fig. 6.8a), the IOB hardly shows any Gill response (the seemingly significant signals in the east Pacific are linked to local SST anomalies; not shown). This might be because in September the IOB variability is comparatively low, so its signal may be hidden by more powerful ones like the IOD. (However, the IOB signal in spring is weak as well (not shown); this might be because IOB is so strongly correlated to ENSO that it is hard to disentangle their relative influence in a partial regression). IOD in OBS (Fig. 6.8b) in September has a significant positive regression with the zonal wind in a relatively narrow stroke in the west Pacific. Significant correlations are also found between May and August (not shown). Though the regression coefficients are of the expected sign (negative IOD is associated with easterlies), they are not very strong. In order to see which IOD pole causes the winds, simultaneous regressions onto Nino3.4 IODwest, and IODeast were also performed (see Fig. 6.8c,d). For IODwest, a region of positive regression coefficients exists in the west Pacific, though they are hardly significant, but they are not negative; thus it might be that convection over the MC cancels the Gill response, but does not surpass it. Recall, though, that in section 2.4.1, while the wind signal associated with a cool west Indian Ocean was found to be weak, the correlation between west Indian SST in summer-autumn and Pacific Warm Water Volume (WWV) a few months later, was found to be significant in the common cause test. While wind data are often noisy, the WWV is expected to provide an integrated measure of the wind in the previous few months. IODeast in OBS is associated with negative regression coefficients in a stroke in the west Pacific. Both poles thus may contribute to the IOD signal, but in general signals are weak and it is difficult to distinguish Indian Ocean-induced winds from winds that are caused by local SST gradients. Whether the data is too short and noisy or whether the impact of the Indian Ocean on the Pacific is just weak, is hard to tell.

In HR and LR, the IOB is associated with negative regression coefficients over the west Pacific, which is in line with Gill response (see Figs. 6.9a and 6.10a). In HR, the IOD shows positive regression coefficients in the west Pacific (Fig. 6.9b), and the signal is stronger than in OBS. In HR, IODeast seems to cause the winds, while IODwest yields no significant positive contribution at all in the west Pacific (Fig. 6.9c,d). This stronger impact of IODeast is in line with the positive results for IODeast in the common cause test, and also with the results obtained with the convective Zebiak-Cane model (see section 5.3), which likewise supports the notion that IODeast has a stronger impact on ENSO than IODwest; but it disagrees to observations, which only show a week, insignificant correlation between IODeast and ENSO at 15 months lag. In LR, winds associated with IOD and its poles are not significant (Fig. 6.10b-d). This may mean that the impact of the Indian Ocean is smaller than in HR (at least relative to the influence of ENSO, which has a high amplitude in LR), or that the strong correlation between ENSO and IOD makes it more difficult to distinguish their wind contributions.

In order to gain insight into the possible impact of the Indian Ocean on convection, the above regression analysis for the IOD and its poles was repeated using Outgoing Longwave Radiation (OLR) instead of the zonal wind. OLR is a measure for convective activity, since vigorous convection leads to high cloud tops which have a low temperature and hence emit less radiation; low OLR thus corresponds to high convective activity. (It should be noted that the "observed" OLR provided by NCEP for the pre-satellite era, i.e. before 1974, is based on reanalysis.)

As mentioned in section 6.2, the OLR field was normalised by the local standard deviation at each point prior to regressing. Thus in an area with low (high) standard deviation, the same regression coefficient corresponds to a lower (larger) absolute value of the OLR signal. Therefore plots were added of the local standard deviations of the OLR

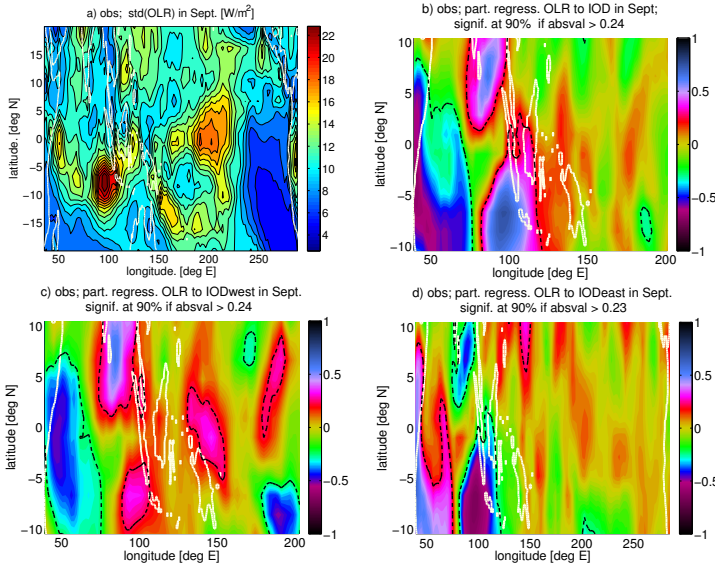Figure 6.11: *a) standard deviation of observed OLR in September. Other plots: Partial regression of observed OLR in September onto the following indices at zero lag (regression to Nino3.4 not shown): b) Nino3.4 and IOD; c&d) Nino3.4, IODwest (c), and IODeast (c). All data (indices and local field time series) were normalised by their local std before regressing. Black lines encircle regions with 90% confidence (two-tailed). White lines are coastlines.*

field (Fig. 6.11a, 6.9a, 6.13a), which vary considerably in space. The highest standard deviations in September are found over the IODeast region, which has both a warm and moist climate and a reasonably strong variability in the temperatures of the underlying sea.

In OBS, the IOD is associated with a dipole pattern in OLR; its eastern pole extends over the Maritime Continent (see Fig. 6.11b). The positive OLR anomaly over the bay of Bengal is not related to a local SST anomaly (not shown) and might thus be induced non-locally. When regressing onto Nino3.4, IODwest and IODeast (Fig. 6.11c,d), one finds that IODwest seems to contribute also to the OLR anomaly over the IODeast region and vice versa. Both poles seem to contribute to the OLR anomalies over the Maritime Continent, though for IODwest the regression coefficients are significant only over a small area. As explained above, the same regression coefficient over the IODeast corresponds to a much larger OLR signal than over IODwest or the Maritime Continent.

For CESM (both HR and LR) one finds again for IOD a dipole pattern over the Indian Ocean (Fig. 6.12b, 6.13b). However, for CESM, the contribution from IODwest is smaller: in HR (Fig. 6.12c), there are some marginally significant regression coefficients in the south Maritime Continent (where IODeast does not have a significant contribution), while for LR no significant signal is present except over the IODwest region itself (Fig. 6.13c). Once again, the strong correlations between IOD (or its poles) and ENSO in LR make it harder to disentangle their impact on OLR.

To summarise, the CESM results do not support the hypothesis that IODwest causes easterlies over the west Pacific due to strong convection above the Maritime Continent. If an atmospheric bridge is present in CESM, it seems to be based on Gill response to
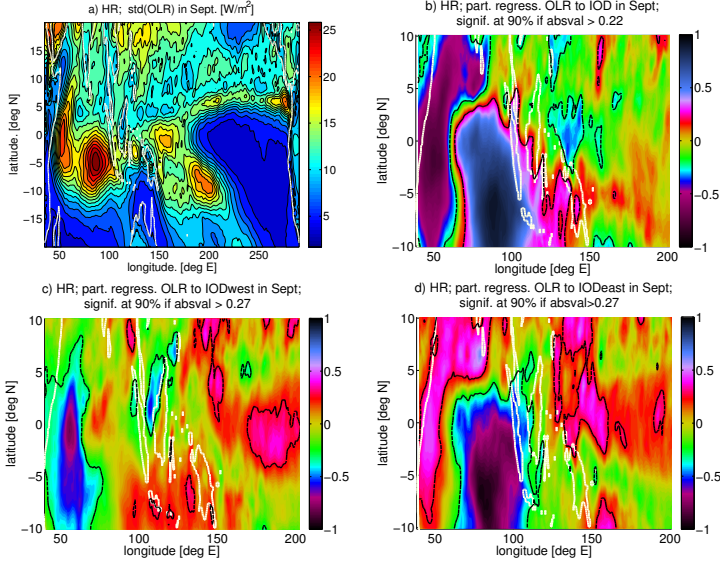
Figure 6.12: *a) standard deviation of HR OLR in September. Other plots: Partial regression of HR OLR in September onto the following indices (regression to Nino3.4 not shown): b) Nino3.4 and IOD at zero lag and Nino3.4 9 month before; c&d) Nino3.4, IODwest (c), and IODeast (d) at zero lag and Nino3.4 9 months before. All data (indices and local field time series) were normalised by their local std before regressing. Black lines encircle regions with 90% confidence (two-tailed). White lines are coastlines.*

Figure 6.13: *As Fig. 6.12, but for LR instead of HR.*

IODeast. On the one hand, this might mean that the results obtained by analysing observational data (in particular the common cause test for IODwest and IODeast) are incorrect, for example due to taking a too short, non-representative time series. On the other hand, it was shown in section 6.3.1 that IOD variability is not reproduced entirely correctly in CESM; in pa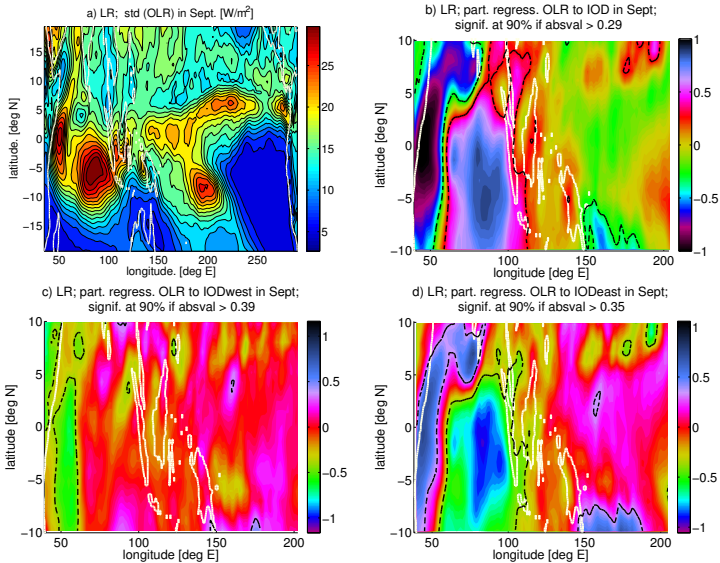rticular, the variability in the IODeast region is far too strong. The artificially large SST variability in this region might lead to an overly large influence of the IODeast on west Pacific winds and thus ENSO.

6.4 IOD bias

As we have seen in section 6.3.1, the autumn IODeast variability in CESM is too strong by about a factor of three, which may cause the influence of IODeast to obscure possible signals from IODwest (section 6.3.3). In this section, the origins of this overly large IODeast signal will be investigated.

In this section (6.4), time series are *not* normalised by their standard deviations when applying linear regressions.

IOD is linked to and probably partly forced by ENSO, but while in HR and LR the ENSO amplitude differs strongly, being too low in HR and too high in LR, both model versions have a similarly strong IOD variability. This suggests that the bias arises within the Indian Ocean, rather than from external ENSO forcing.

In boreal late summer to autumn, southeasterlies prevail along the east coast of Sumatra, allowing coastal upwelling and cooling. In addition, the zonal wind along the equator in the open ocean becomes less positive (i.e. less westerly) or even slightly negative (see Fig. 6.14). In CESM (both HR and LR), the wind along the equator is more negative than in OBS. These conditions resemble to some extent the cold tongue in the east Pacific and allow some Bjerknes-like coupling between zonal wind, thermocline depth, upwelling, and SST, which may be a source of interannual variability in the IODeast area. Important processes determining this variability include:

- the strength of the thermocline depth response to wind stress anomalies,

- the strength of the wind response to SST anomalies,

- the thermocline feedback, which determines how strongly thermocline depth anomalies influence the SST; this depends on the background upwelling at the lower boundary of the mixed layer and on how strongly thermocline variations influence T_{sub}, the temperature just below the mixed layer,

- the upwelling feedback, which determines how strongly upwelling anomalies influence the SST; this depends on the mean gradient between the SST and T_{sub},

- and the thermodynamic damping, i.e. the surface heatflux response to SST anomalies.

The surface heatflux Q is the sum of sensible and latent heat flux and long- and shortwave radiation flux. It is here defined as positive upwards, thus a positive value leads to ocean cooling. The dependence of the heatflux on SST is here represented by the regression of Q onto the index IODeast (Fig. 6.15; for the spatial patterns of the SST, compare the composites in Fig. 6.16). This regression yields much larger values in CESM (both HR and LR) than in OBS, especially south of the equator, away from the coast (the large values around $2°N, 80°E$ in Fig. 6.15d is unrelated to local SST anomalies and does
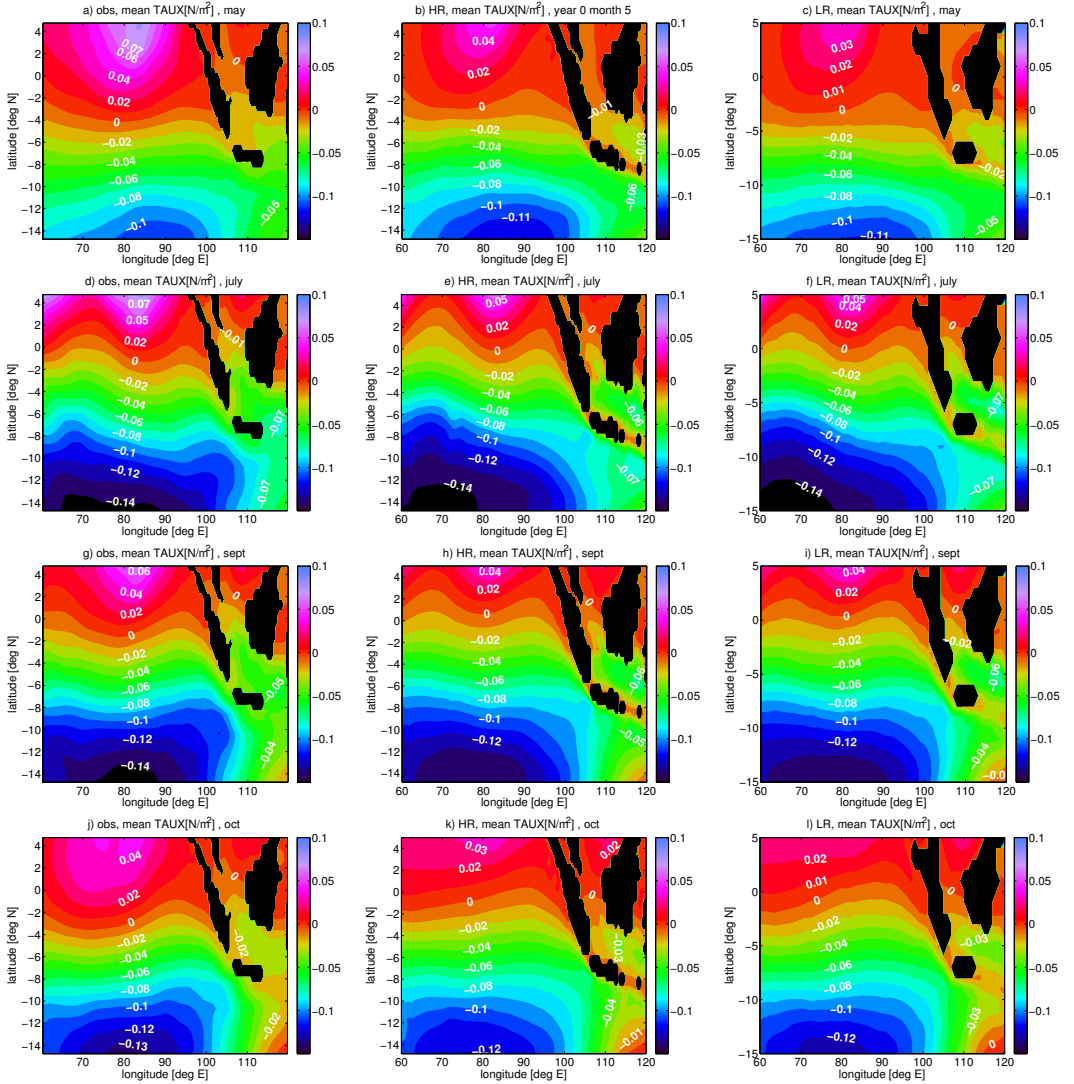
Figure 6.14: *The climatological wind stress in N/m^2 over the east Indian Ocean. Results are shown for OBS (left), HR (middle) and LR (right), in the months May (top row), July (second row), September (third row) and October (bottom row).*
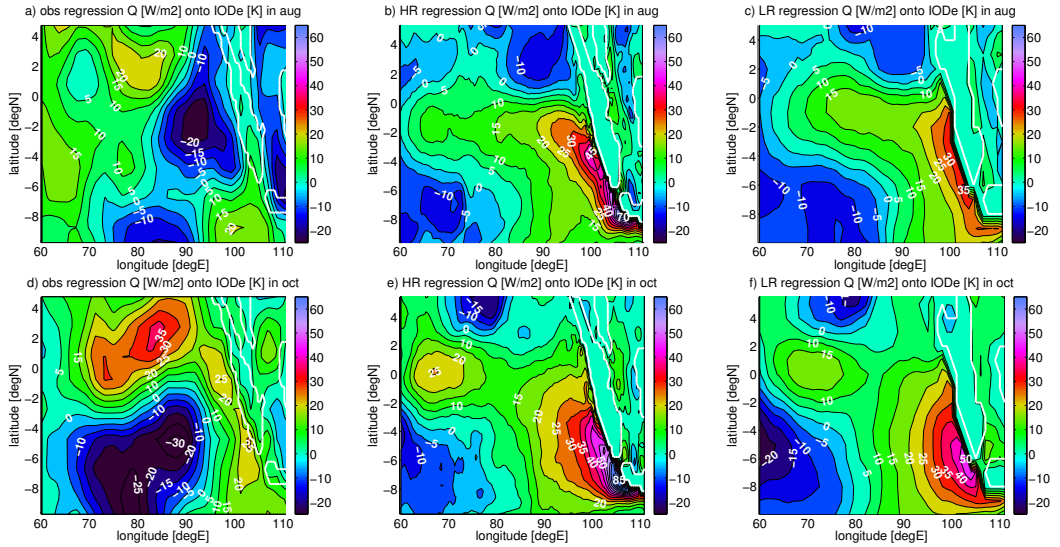
Figure 6.15: *The regression of the surface heat flux (in W/m^2, positive upward) in the east Indian Ocean onto IODeast. Results are shown for OBS (left), HR (middle) and LR (right) in the months August (top row) and October (bottom row). White lines are coastlines.*

Figure 6.16: *Composites of the SST anomalies [K] in cool IODeast years (IODeast(ASON(0)<0.9) in the east Indian Ocean. Results are shown for OBS (left), HR (middle) and LR (right), in August (top row) and October (bottom row). The black line encircles areas where the results differ significantly from zero (90% confidence). Note that in plot e) and f) is mostly hidden by the land or lies outside the plotted area; the cool anomalies in IODe are significant.*
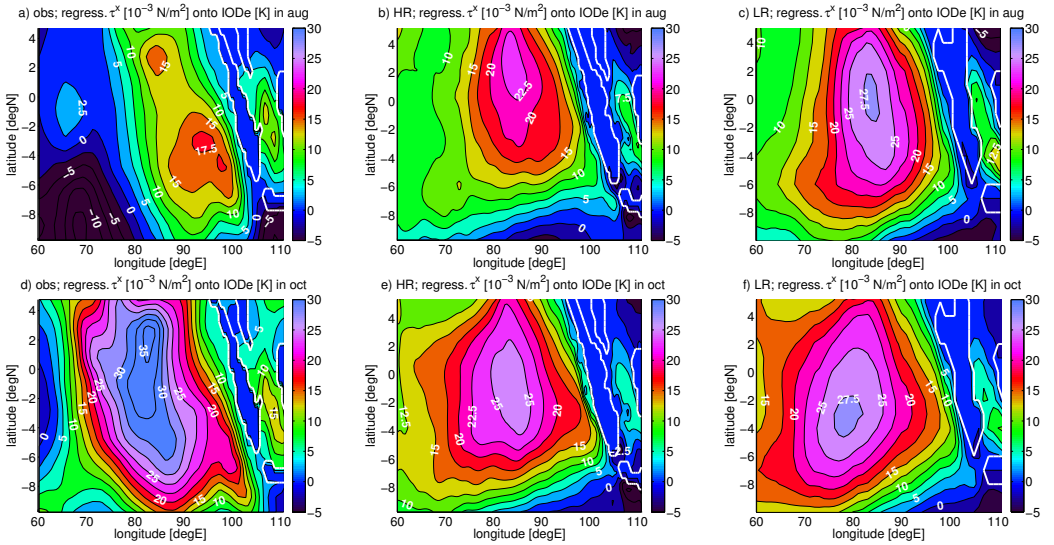
Figure 6.17: *The regression of the zonal wind stress (in $10^{-3} N/m^2$) in the east Indian Ocean onto IODeast. Results are shown for OBS (left), HR (middle) and LR (right), in August (top row) and October (bottom row). White lines are coastlines.*

not contribute to the damping of the IODeast SST signal). The larger extent of IODeast-related heating anomalies in CESM is probably because the SST anomaly also extends further northwest in CESM. This implies that the thermodynamic damping is stronger for CESM than for OBS, so the high IODeast amplitude in CESM is not caused by lack of damping. When computing a correlation between the Q field and IODeast, rather than a regression, CESM yields values well above 0.8 over large parts of the IODeast box west of Sumatra, while in OBS, only 0.6 is reached and only near the coast (not shown). Thus the damping depends less consistently on IODeast for OBS than for CESM - possibly because in CESM the local SST signal is so strong as to dominate over non-local forcing of the heat flux.

The regression of the zonal wind onto IODeast (in the same months) is given in Fig. 6.17. Until September, the regression shows somewhat higher values for CESM, especially LR, than for OBS. In October, OBS yields higher values. The maximum values in CESM (both HR and LR) are shifted northwards with respect to OBS, which is in line with the spatial patterns of the SST. Although it is plausible that a stronger wind response to IODeast SST anomalies early in the IOD season leads to a stronger positive Bjerknes feedback, it is questionable whether this is the main driver for the difference between OBS and CESM, because the wind response between HR and LR also differs considerably, while their SST variability is similar, at least compared to OBS.

To assess the thermocline variability, composites over cool IODeast years (IODeast $(ASON(0))<-0.9$) of the $20°C$ isotherm depth (z20) are made. Fig. 6.18 shows that this isotherm indeed lies within the thermocline. The observed negative z20 anomalies (see Fig. 6.19) during cool IODeast years along the coast are somewhat weaker than those in LR, but similar to or slightly stronger than those in HR, though the area of shallow z20 extends somewhat further northwest in CESM than in OBS. Seeing that the thermocline variability differs most strongly between HR and LR, whereas the SST variability is much higher in both HR and LR than in OBS, the difference in thermocline variability seems

Figure 6.18: *The climatological temperature profile in °C along the equator in the east Indian Ocean. Results are shown for OBS (left), HR (middle) and LR (right), in June (top row), August (middle row) and October (bottom row).*

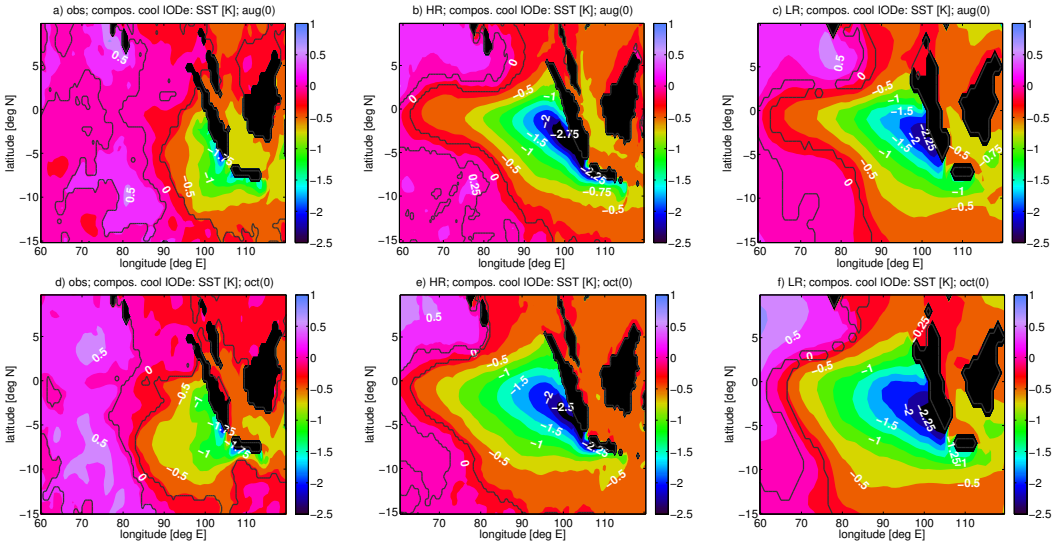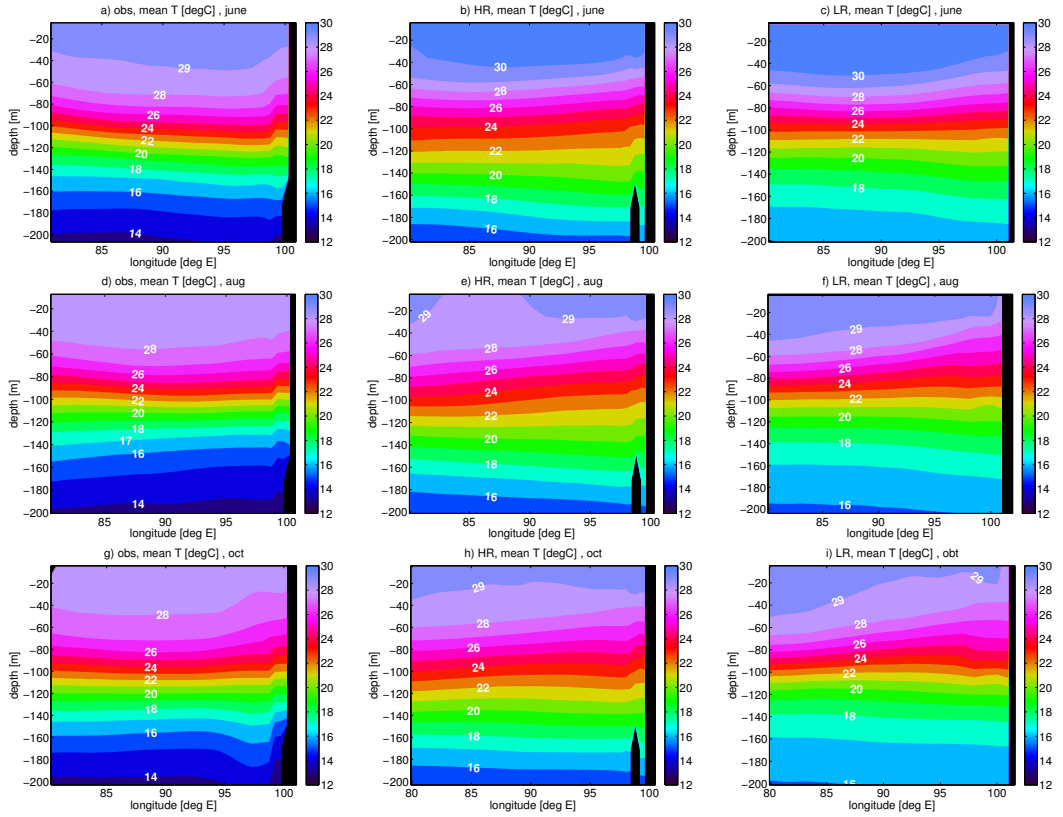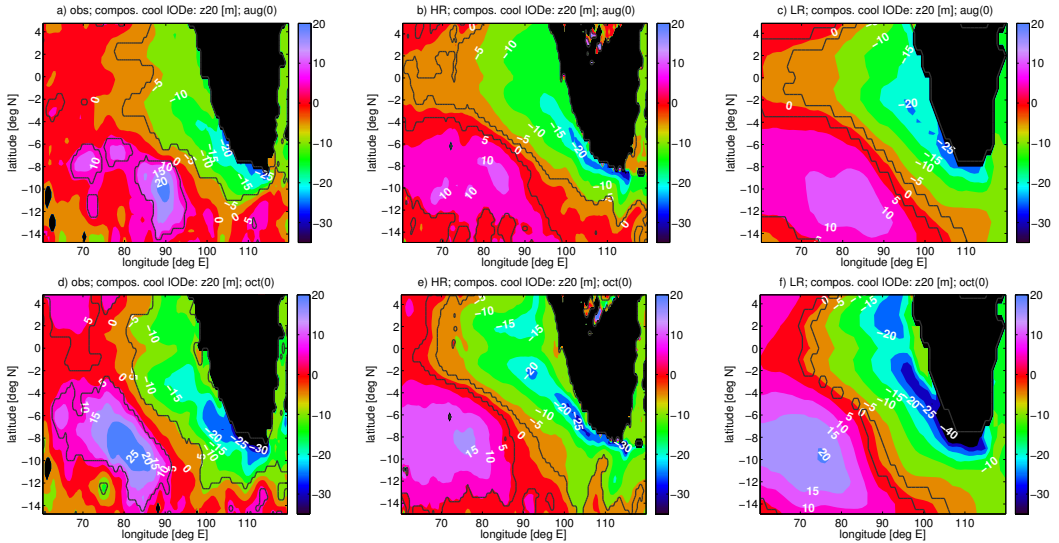Figure 6.19: *Composites of the z20 anomalies [m] in cool IODeast years (IODeast(ASON(0)<0.9) in the east Indian Ocean. Results are shown for OBS (left), HR (middle) and LR (right), in August (top row) and October (bottom row). The black line encircles areas where the results differ significantly from zero (90% confidence).*

not to be the main cause for the difference in SST variability.

Upwelling variability is likewise assessed by taking composites for cool IODeast years (IODeast(ASON(0)<-0.9)) of the vertical velocity (Fig. 6.20). As one would expect, positive upwelling anomalies occur at around 50m depth in cool IODeast years; however, these anomalies are not statistically significant and are actually within one standard deviation. At $6°S$, the upwelling anomalies are even much weaker than at the equator and spatially incoherent (not shown). The upwelling anomalies are of similar strength for LR and OBS, but weaker for HR. Therefore, the difference in upwelling anomalies cannot be the cause for the difference in SST anomalies. The fact that both upwelling and thermocline anomalies, which are related by wind stress anomalies, do not explain the strong IODeast variability between CESM and OBS suggests that the difference in wind response discussed above is a consequence, rather than a cause, of the difference in SST variability.

Now, if the upwelling and thermocline variability is similar for OBS and CESM, the main difference between CESM and OBS must lie in the efficiency at which upwelling and thermocline anomalies influence the surface temperature. One way to achieve this is a strong background upwelling; another one, a strong impact of the thermocline on T_{sub}. Near the equator, where the differences between CESM and OBS SST are particularly large, the mean upwelling (see Fig. 6.21) at around 50m depth is positive in June-October for CESM (both HR and LR), and for July-September in OBS. However, in July-September, the values in OBS are, if anything, stronger than in CESM.

The cool IODeast composites of the temperature anomalies along the equator (see Fig. 6.22) show that at depth, the signal in OBS is not much weaker than in CESM; it just does not reach the surface well. The temperature minimum lies at greater depth in OBS (in August: around 70m, rather than 40m as in CESM), i.e. below the mixed layer, and also below the level where the background upwelling is strongest. The reason for the
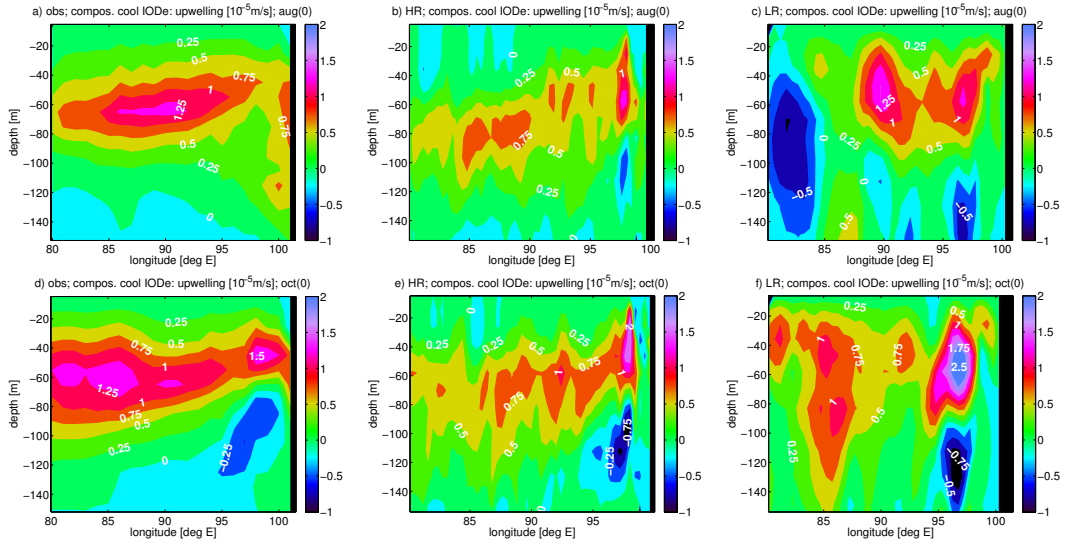
Figure 6.20: *Composites of the upwelling anomalies* $[10^{-5}m/s]$ *in cool IODeast years* *(IODeast(ASON(0)<0.9) along the equator. Results are shown for OBS (left), HR (middle) and LR (right), in August (top row) and October (bottom row). The results are not significant at 90% confidence.*

different depths of the temperature anomaly peaks may be that in CESM, the strongest vertical mean temperature gradients are found at a smaller depths than in OBS (see Fig. 6.18). If one simplistically imagines thermocline depth anomalies to be associated with vertical shifts of the overlying isotherms, then changes in the thermocline depth will cause large temperature changes where the mean vertical gradient is strong. In CESM, the vertical temperature gradient in the upper 70m is stronger than in OBS, especially in boreal summer. At $90°E$, $0°N$, the difference between the SST and the temperature at $70m$ depth in June takes the values: $3.4K$ (LR), $3.8K$ (HR), and $1.3K$ (OBS); in August, the values are: $3.4K$ (LR), $3.8K$ (HR), and $2.1K$ (OBS); and in October: $3.4K$ (LR), $3.0K$ (HR), and $1.9K$ (OBS). The stronger mean vertical temperature gradients in CESM allow upwelling anomalies to have a greater impact on the SST.

Along the coast at $6°S$, the temperature anomalies are likewise at a somewhat larger depth in OBS than in CESM, but reach the surface better. One reason may be that the mean upwelling in OBS extends to a larger depths along $6°S$, allowing subsurface temperature anomalies to affect the SST; another reason is that the vertical temperature gradients in OBS are more pronounced at this latitude than along the equator (not shown).

So the main driver for the bias in IODeast variability is likely a bias in the temperature profile, leading to an exaggerated sensitivity of T_{sub} to thermocline depth anomalies. Yao et al. (2016), who analysed various CESM runs at 2° and 1° resolution by performing regressions of time series obtained by spatially averaging the SST, zonal wind, T_{sub}, and the thermocline depths, likewise find that the largest discrepancy between the observed and model results lies in the sensitivity of T_{sub}, followed by the wind-SST-coupling.
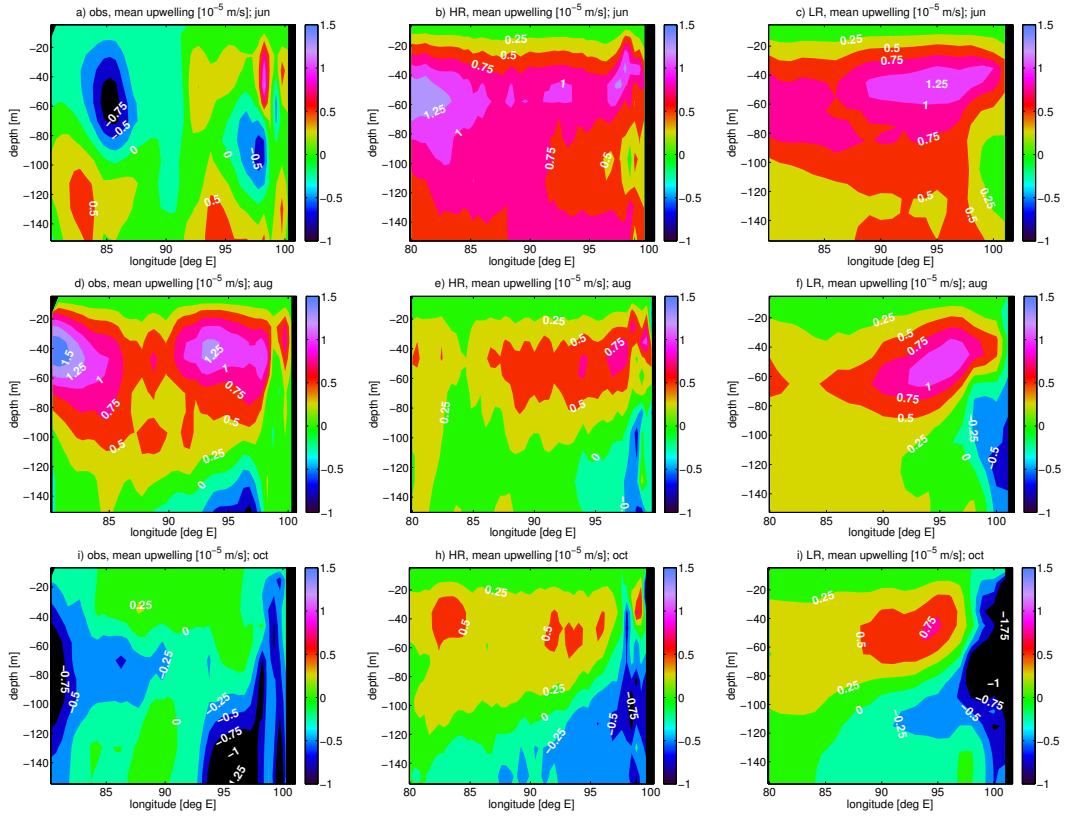
Figure 6.21: *The climatological upwelling in $10^{-5} m/s$ over the east Indian Ocean. Results are shown for OBS (left), HR (middle) and LR (right), in June (top row), August (middle row) and October (bottom row).*
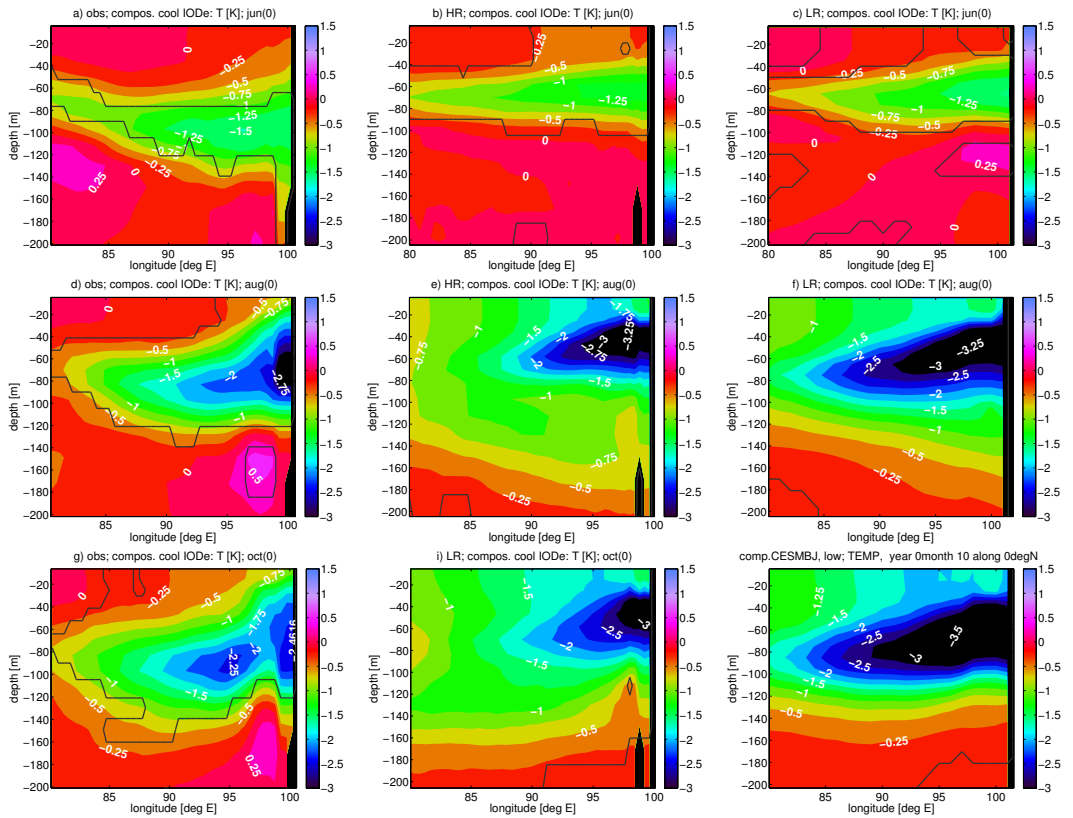
Figure 6.22: *Composites of the temperature anomalies [K] in cool IODeast years (IODeast(ASON(0)<0.9) along the equator. Results are shown for OBS (left), HR (middle) and LR (right), in June (top row), August (middle row) and October (bottom row). The black line encircles areas where the results differ significantly from zero (90% confidence).*

6.5   Summary and Conclusion

It was attempted to use a GCM, namely CESM, to investigate the possible influence of the Indian Ocean on ENSO, and in particular to test whether a cool west Indian Ocean can induce enhanced convection and surface convergence over Indonesia and easterlies over the west Pacific, which in turn lead to a strong west Pacific Warmpool acting as reservoir for next winter's El Niño, as was suggested sections 2.4.1 and 5.2. Using a GCM in addition to observations is particularly attractive because the observed easterly wind signal following a cool IODwest is rather weak in observations, possibly because of noisy data, so a check against longer time series is desirable.

Two CESM simulations were used, one at $1°$ resolution (Low Resolution / LR), and one at $0.1°$ resolution for the ocean and $0.5°$ for the atmosphere (High Resolution / HR). Both capture the spatial pattern and period of ENSO, although LR is too periodic. The IOD is also captured, but its amplitude in autumn is too large. In particular, the standard deviation of the index IODeast in boreal autumn is too large by a factor of about 3 in both HR and LR.

The common cause test (see section 6.3.2) suggests that in the HR simulation, Indian Ocean quantities may add skill to ENSO prediction. In the LR simulation, this does not hold, because ENSO is sufficiently regular that the Indian Ocean adds little independent information. In HR, not only the western pole of the Indian Ocean Dipole (IODwest), but also the eastern pole (IODeast) yields positive results, which disagrees with observations.

No conclusive evidence is found that a cool west Indian Ocean induces easterlies over the west Pacific or strong convergence over the Maritime Continent. Such signals are weak even in observations, but more or less absent in CESM. However, in HR, a warm IODeast can lead to easterlies. (In LR, due to the overly strong correlations between ENSO and Indian Ocean quantities, and the high regularity, it is very hard to disentangle the influence of ENSO and the Indian Ocean by linear techniques like regression).

These findings may suggest that it is in fact the east Indian Ocean which dominates the influence on ENSO, as suggested by Izumo et al. (2010). This would be plausible in the sense that a warm IODeast needs no subtle convection effects to cause a wind reversal over Indonesia, but can cause easterlies over the west Pacific by a plain Gill response. The negative result of the common cause test for IODeast in observations might be an artefact of inaccurate sampling and a relatively short record.

On the other hand, the strong biases CESM exhibits in the Indian Ocean, particularly the exaggerated variability in IODeast, make it doubtful whether the model can realistically reproduce the subtle Indo-Pacific relationships. This bias is partly due to the fact that in CESM, the SST anomaly associated with IODeast variability extends further northwest into the open ocean, covering a greater area within the box over which IODeast is computed. It was found that the main cause for the strong IOD variability is the strong sensitivity of the subsurface temperature (i.e. the temperature of the water that can be upwelled into the mixed layer) to thermocline variations, especially in the equatorial region. This high sensitivity in turn may be due to differences in the mean temperature profile; in CESM, the vertical temperature gradients over the top 70m are considerably stronger than in observations. Therefore a similar vertical displacements of isotherms may cause a stronger temperature anomaly. In addition, in observations, the temperature anomalies associated with a cool IODeast peak at greater depth (where the mean temperature gradients are stronger) than in CESM, which means that in observations, the temperature anomalies overlap less with the zone of strong climatological upwelling, so the temperature anomalies reach the surface less well.

Note that an overly large IOD variability is quite common in GCMs. Cai and Cowan
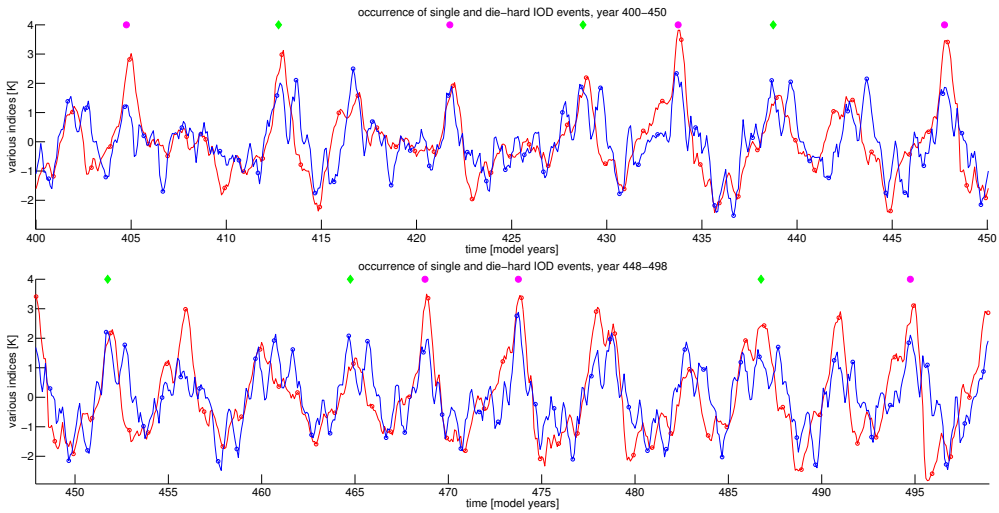
Figure 6.23: *Illustration of the occurrence of single and die-hard IOD events in LR. The red line depicts Nino3.4 (red circles mark December values), the blue line depicts IOD (blue circles mark September values). The filled purple circles and green diamonds mark single IOD events and die-hard IOD events, respectively (for definitions of IOD types, see Fig. 6.24 and 6.25.)*

(2013)find that in many CMIP3 and CMIP5 models, the SST is too sensitive to thermocline variability. However, in that study, it is suggested that unrealistically strong climatological easterlies and an unrealistically shallow east Indian thermocline are the cause. However, in our temperature profiles (Fig. 6.18), the 20 degrees isotherm (used as proxy for the thermocline by Cai and Cowan (2013)) in HR is actually deeper than in OBS. We propose that the whole temperature profile should be considered when investigating the reasons for the high IOD amplitude in GCMs.

It would be interesting to investigate in greater detail why the temperature profiles in CESM (and possible other GCMs) differ from observations. One thing to check would be the parametrisation of vertical mixing, but other processes such as horizontal advection might play a role as well. Understanding the processes determining the temperature profile might help improving future model generations. However, for now we have to conclude that CESM has too strong biases to allow a detailed analysis of the subtle Indo-Pacific coupling. The mechanism suggested in sections 2.4.1 and 5.2 can neither be confirmed nor definitely falsified by analysing CESM data.

Appendix to Chapter 6: A few remarks on the 'Die-hard IOD'

In CESM, especially LR, consecutive IOD events can occur even if the second IOD event does not co-occur with El Niño. These events are termed die-hard IOD here. A die-hard IOD event in autumn of year 0 and year 1 is defined as: IOD(ASON(0))>0.8, IOD(ASON(+1))>0.8, Nino3.4(ND(1)JF(2))<0.3 i.e. two consecutive IOD events occur, and the second one is not linked to a co-developing El Niño. These events are marked

Figure 6.24: *Composites of Single IOD events for LR. A single IOD event in autumn of year 0 is defined as: IOD(ASON(-1))<0.3, IOD(ASON(0))>0.8, IOD(ASON(+1))<0.3, i.e. the IOD event is neither preceded nor followed by another one. The plots show anomalies of the SSH (in m, left column), SST (in K, middle column), and zonal wind (in m/s, right column), for nov(0) (top row), April(1) (middle row), and July(1) (bottom row).*

Figure 6.25: *Composites of die-hard IOD events for LR. A die-hard IOD event in autumn of year 0 and year 1 is defined as:* $IOD(ASON(0))>0.8$, $IOD(ASON(+1))>0.8$, $Nino3.4(ND(1)JF(2))<0.3$ *i.e. two consecutive IOD events occur, and the secon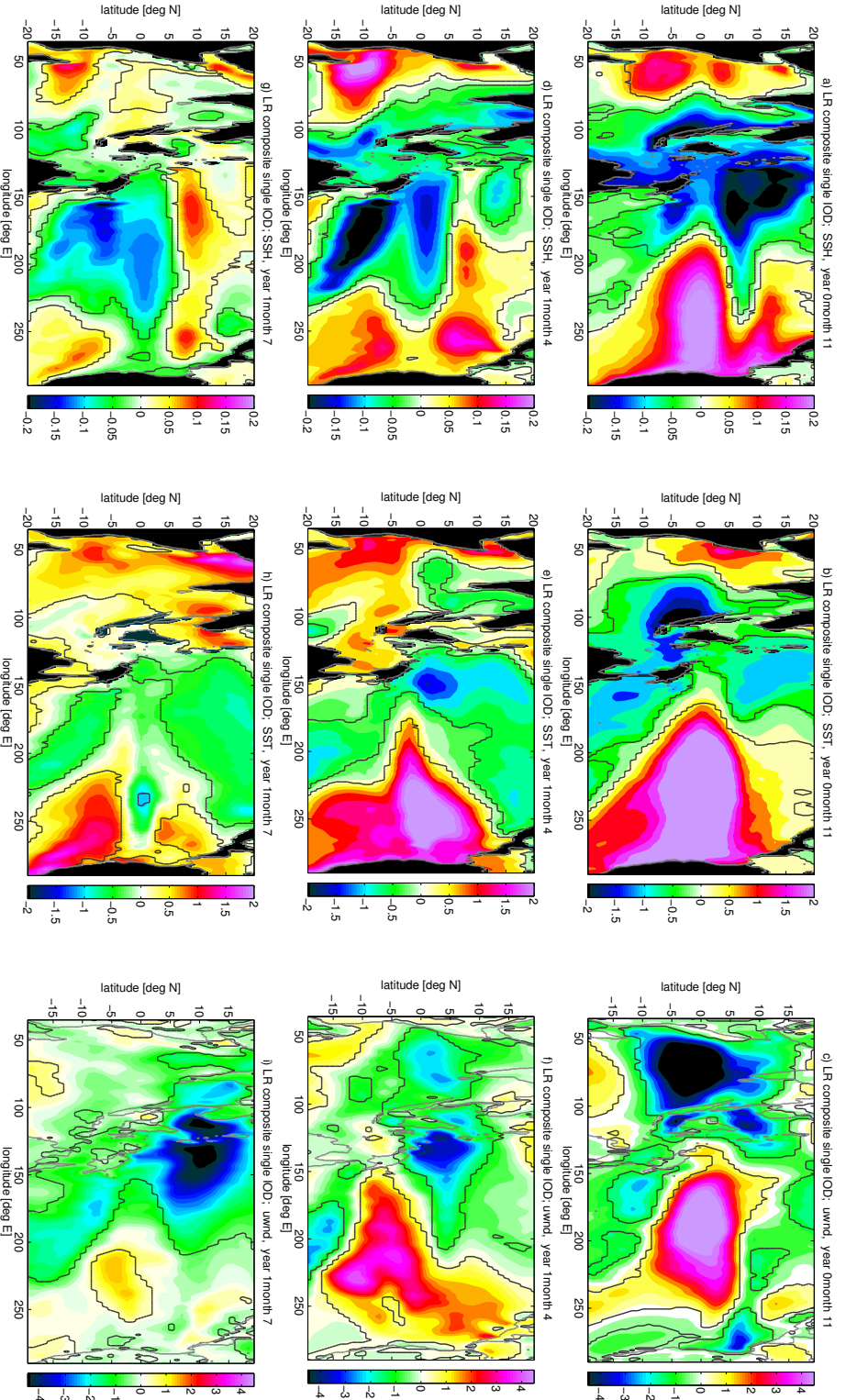d one is not induced by a co-developing El Niño. The plots show anomalies of the SSH (in m, left column), SST (in K, middle column), and zonal wind (in m/s, right column), for nov(0) (top row), April(1) (middle row), and July(1) (bottom row).*
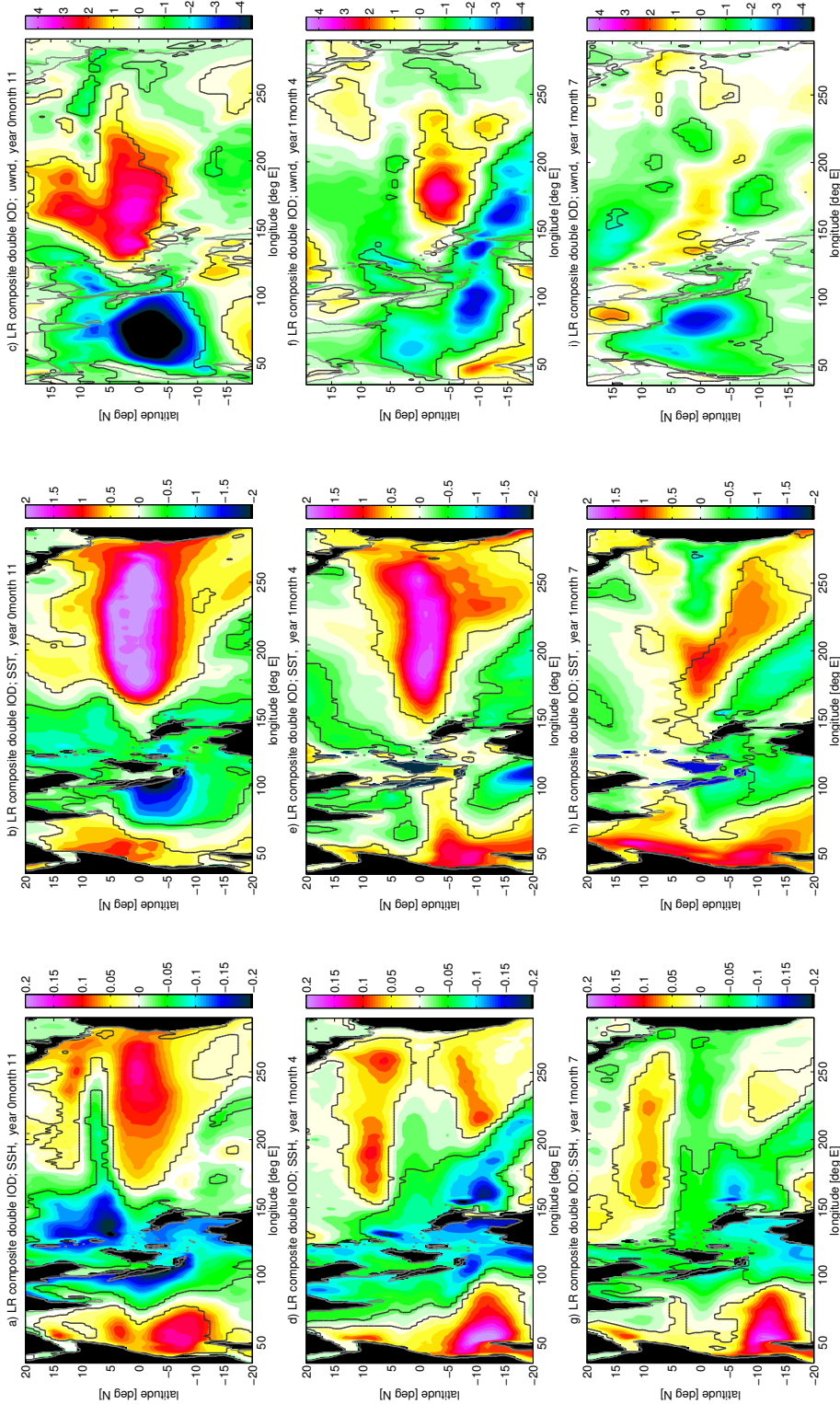
by green diamonds in Fig. 6.23. In contrast, single IOD events in autumn(0) are defined by the following criterium: IOD(ASON(-1))<0.3, IOD(ASON(0))>0.8, IOD(ASON(+1))<0.3, i.e. the IOD event is neither preceded nor followed by another one. These events are marked by purple circles in Fig. 6.23.

Composites of these two IOD types in LR are shown in Fig. 6.24 and 6.25. In boreal autumn of year 0 (here represented by nov(0), see plots a-c), the two composites hardly differ in the Indian Ocean. In the course of winter, the cool SST anomaly IODeast area quickly disappears, and by April(1), the area west of Sumatra shows a moderate warm anomaly, which is slightly stronger in the single IOD composite (see plots e). The die-hard IOD composite shows a significant cool anomaly is present around $15°S, 100°E$, which is much weaker in the single IOD case. The winds over the Indian Ocean are slightly more easterly in the die-hard case. The SSH anomaly is still negative in the IODeast area in both cases (the SST is quite independent of the SSH in boreal spring as the background upwelling lacks). In may and June(1), the negative east Indian SSH anomaly dissolves at the equator (not shown) with a Kelvin-wave like signature.

In July(1), an upwelling Kelvin wave occurs in the die-hard case, leading to a negative SSH anomaly in the equatorial east Indian Ocean. The SST also decreases in this area, since the background upwelling has resumed. Easterly winds are present over most of the Indian Ocean, especially around $0°S, 85E$. The SSH and SST anomaly quickly grow in the next months to form a full-fledged (and statistically significant) positive IOD event. No upwelling Kelvin wave occurs in the single case.

It is hard to prove what triggers the upwelling Kelvin wave in the die-hard case. One explanation may be that the cool anomaly around $15°S, 100°E$ helps to induce easterlies; however, this anomaly lies quite far off the equator, and its origin is not known. On the other hand, it might be that unpredictable wind noise triggers the initial Kelvin wave, and that it is the unrealistically strong Bjerknes feedback in CESM in the Indian Ocean which quickly amplifies an initial SSH and SST anomaly from June or July onwards.

During all six die-hard events, El Niño occurs between the two IOD events (but not after the second IOD, by definition), i.e. an El Niño (in winter(0/1) is followed by an IOD event (autumn(1)). The die-hard IODs occur sufficiently often to cause a positive correlation between Nino3.4 and IOD 9 months later.

Chapter 7

Summary and Outlook

7.1   Summary

The main objective of this study was to understand the influence of the Indian Ocean on the El Niño/Southern Oscillation (ENSO) at interannual time scales, in the hope to enhance the skill of ENSO prediction at lead times beyond the spring predictability barrier (research questions 1 and 2 in section 1.4). In addition, the influence of long-term Indian Ocean warming on ENSO was investigated (question 3).

Question 1) Does interannual variability in the Indian Ocean contain independent information about ENSO at a lag of 1.5 years, e.g. about the probability, the amplitude, or the flavour of the event?   It was found in section 2.2 that El Niño (La Niña) events are often preceded by a cool (warm) anomaly in the southwest Indian Ocean, roughly the Seychelles Dome region or the western pole of the Indian Ocean Dipole (IODwest) in boreal summer-autumn about 1.5 years before the ENSO event. The 'common cause test' shows that this correlation is significantly stronger than one would expect if it were a mere effect of ENSO cyclicity and the impact of ENSO on the Indian Ocean. Interestingly, when repeating this analysis for the region off Sumatra (IODeast), no significant correlation is found, despite the closer proximity to the Pacific. These findings suggest the possibility of a physical influence of the west Indian Ocean on ENSO. In section 2.3.2, it was found that cool Seychelles Dome SST anomalies in particular favour a type of El Niño with strong and early warming in the East Pacific.

Question 2) By which physical mechanism may the summer Seychelles Dome anomalies influence ENSO development at 1.5 years lag?   Further analysis of the observational record inspired us to 'guess a mechanism' for this Indo-Pacific interaction (see section 2.4):

Atmospheric bridge A cool west Indian Ocean is accompanied by easterlies over the Pacific. The easterlies occur too late in the year to force a fully-fledged La Niña, but they cause an accumulation of warm water in the west Pacific, 'recharging the warm pool', which favours El Niño development in the next season (see section 2.4.1).

State-dependent noise A cool west Indian Ocean is followed by an enhanced intraseasonal wind variability over the west Pacific in the following winter to spring. Wind variability in boreal spring, in turn, can excite El Niño development (see section 2.4.2).

Both mechanisms can co-act. They favour in particular east Pacific (EP) El Niño events starting with an early warming near the South American coast (see section 2.3.2), presumably because EP El Niños require a larger warm water volume than central Pacific (CP) El Niños (Kao and Yu, 2009). In addition, in boreal spring the climatological SST gradients are weak, thus a westerly wind burst will not lead to large eastward temperature advection - which would heat the central Pacific - but to a downwelling Kelvin wave, whose warming effect is largest near the coast (Vialard et al., 2001).

The atmospheric bridge mechanism requires additional research for two reasons. First, the observational evidence is not very strong: The west Pacific easterly wind signal accompanying a cool west Indian Ocean is rather weak (only 80% confidence after removing ENSO influence, see section 2.4.1). On the other hand, the correlation between west Indian Ocean temperature and the Warm Water Volume (which acts to some extend as an integrated measure of the wind in the last few month) is significantly negative in the common cause test at around 5 month lead time, so maybe the wind data is just too noisy to detect the wind response properly. Second, easterly winds to the west of a cool anomaly contradict the Gill response (cool anomalies should be accompanied by near-surface wind divergence). We proposed that an amplification of the Gill-induced uplift over the Maritime Continent by convective heating might cause a sufficiently strong surface convergence as to overcome the Gill response and induce easterlies over the west Pacific.

To test this hypothesis and 'compute the consequences of our guess', an intermediate complexity model was employed, namely an extension of the Zebiak-Cane model version by Van der Vaart et al. (2000) described in chapter 3. While the original model only includes the tropical Pacific Ocean and has a linear atmosphere based on a pure Gill response, we added a simplified Indian Ocean without internal dynamics but prescribed, ENSO-dependent SST patterns and a convective feedback term over the very moist warm pool area of the east Indian Ocean and the Maritime Continent (see section 3.5). Within this model it is indeed possible to obtain an easterly wind contribution over the west Pacific as response to west Indian Ocean cooling (see section 5.2). However, this requires a sufficiently strong convection feedback strength parameter γ_c. The correct value for this parameter cannot be inferred from the model itself, so it may be that the convective effect is overestimated.

In addition, the model suggests that a warm east Indian Ocean should create much stronger easterlies than a cool west Indian Ocean (section 5.3). This is because the east Indian Ocean lies underneath a very moist atmosphere where strong convection anomalies can occur. Thus the Gill response, namely an uplift over the east Indian Ocean, is amplified and leads to an even stronger surface convergence - as opposed to the west Indian Ocean case, where the Gill response and the non-local convection counteract each other. Although physically plausible, this result seems to contradict the previous finding in section 2.2 that the west Indian Ocean adds more predictive skill to ENSO predictions.

The dominant Indian Ocean modes of SST variability are the Indian Ocean Basinwide warming (IOB) and the IOD. Their effect on ENSO is investigated in section 5.4. In our model, the IOB has the strongest impact on Pacific winds, mainly because of its strong Gill response. Positive (warm) IOB events are the dominant response of the Indian Ocean to El Niño and peak a few months after El Niño (Klein et al., 1999), inducing easterlies which accelerate the switch to La Niña. Therefore IOB variability reduces the period and the amplitude of ENSO, as has also been found in studies based on observations and GCMs (Kug and Kang, 2006; Kug et al., 2006; Santoso et al., 2012; Kajtar et al., 2016). The IOD, however, was often thought to have little impact on ENSO, because

the Gill response to both poles nearly cancels. However, as both a cool IODwest and a warm IODeast induce enhanced convection over the Maritime Continent, a negative IOD event can lead to a substantial easterly wind response over the Pacific. Positive IOD events typically peak a few months before El Niño, inducing additional westerlies which re-enforce the ongoing El Niño event. Therefore the IOD variability increases the ENSO amplitude. However, the net effect of the Indian Ocean on the spectral properties of ENSO is dominated by the IOB, partly because of its larger wind response, and partly it is more strongly correlated to ENSO, making its impact occur more reliably at a fixed ENSO phases. On the other hand, the relative independence of the IOD makes it a better predictor of individual ENSO events (IOB being so strongly determined by ENSO that it does not add independent information (Xie et al., 2009; Izumo et al., 2013)).

Having shown that our suggested mechanism of the atmospheric bridge may work in principle, it should be 'tested against nature' - preferably a long record, but not the one from which we originally guessed our hypothesis. Since obviously no such observational record is at hand, two 100 year long simulations of CESM at constant forcing were analysed in chapter 6, one at 1° resolution (Low Resolution/LR) and one at 0.1° in the ocean and 0.5° in the atmosphere (High Resolution/HR). In the LR simulation, ENSO is too periodic (see section 6.3.1), so although Indo-Pacific correlations are strong, the Indian Ocean cannot add much skill to predict the unrealistically regular ENSO. The common cause test therefore yields negative results (see section 6.3.2). In HR, the test finds a significant negative correlation between IODwest and ENSO at around 15 months lag, but likewise a positive correlation for IODeast and ENSO. Using a partial regression approach (see section 6.3.3), no significant easterly wind response to a cool IODwest is found in HR, while the response to a warm IODeast is significant. Thus the CESM results seem to falsify our hypothesis. However, it is unclear whether CESM is capable of modelling Indo-Pacific interactions correctly, because the model has considerable biases. In particular, the SST variability in the IODeast box in boreal autumn is too large by a factor of about 3 (see section 6.3.1). This overly strong variability might mask signals from the west Indian Ocean. The reason for the strong IODeast variability seems to be an exaggerated sensitivity of the subsurface temperature - and thus, the SST - for thermocline anomalies (see section 6.4). This is due to the fact that the vertical temperature gradient in the top 70m is too large in CESM, which allows large temperature variations at depths where the climatological upwelling is strong. These anomalies are then easily advected to the surface.

Question 3) How do long-term changes in Indian Ocean SST affect ENSO stability and flavour? In particular, could there be a connection between Indian Ocean SST trends and the frequency of Central Pacific (CP) El Niños? The Indian Ocean may not only influence ENSO through its interannual variability, but also by long-term temperature trends, as was investigated in chapter 4, using a linear atmosphere version of the Indo-Pacific Zebiak-Cane model (see section 3.4). It was found in section 4.3 that an IOB-like constant warming yields a mean easterly wind contribution over the Pacific which leads to a stronger climatological thermocline slope and SST gradient and stronger mean upwelling. This in turn affects ENSO stability and flavour. The ENSO cycle is destabilised (i.e. the amplitude increases) because at least for small Indian Ocean temperature changes, all destabilising components of the Bjerknes feedback increase. A stronger mean upwelling gives thermocline anomalies a stronger impact on the SST; a shallower thermocline increases the impact of upwelling anomalies; increased mean zonal SST gradients allow a greater influence of zonal current anomalies.

The spatial pattern of ENSO is also influenced. Westerly wind anomalies are strongest west of a warm anomaly, therefore during El Niño, the eastward zonal currents (leading to temperature advection) and the upwelling anomalies are also largest to the west of the SST anomaly. This effect tends to pull the warm anomaly towards the central Pacific. However, in our model, the subsurface temperature T_{sub} is prescribed to be most sensitive to thermocline variations at values $h = 30m$, i.e. when the thermocline is 30m above the reference level. Thus for relatively small mean thermocline slopes, T_{sub} is most sensitive in the very east of the Pacific; this keeps ENSO-related temperature anomalies near the coast. For strong mean thermocline gradients, saturation occurs, i.e. T_{sub} is very cold in much of the east Pacific and not sensitive to thermocline anomalies, and the location of the strongest SST anomalies becomes more determined by the location of the upwelling anomalies. These results offer a possible explanation for the observed increased frequency of CP El Niños in recent decades: They might be related to the strong Indian Ocean warming in the same time span. However, as the T_{sub} parametrisation is rather simplified, it is not clear a priori whether the saturation effect plays as strong a role in the real ocean as in the Zebiak-Cane model.

Within the Zebiak-Cane model, interannual variability in the Indian Ocean has little impact on ENSO flavour (see section 4.4). Note that the Zebiak-Cane model does not exhibit ENSO diversity but has only one ENSO mode, the spatial shape of which depends mainly on the background state.

7.2   Outlook

The results presented in this study give rise to plenty of open questions and possibilities for further investigations.

First of all, it is still not clear whether convection anomalies induced above Indonesia by a cool west Indian Ocean are really strong enough to lead to a substantial easterly wind response over the Pacific. Or, in the notation of the Zebiak-Cane model, the realistic value of γ_c is not known. The strong observed correlation between IODwest and ENSO might still be an artefact of inaccurate or too short observational records, and GCMs are likely too biased to model the Indo-Pacific interactions reliably. Apart from waiting 50 years for more observational data, a solution could be to perform a dedicated experiment with an atmospheric GCM, for example by prescribing climatological conditions in the Pacific, but specific SST anomalies over the Indian Ocean (e.g. resembling the IOD and its isolated poles), to check the convective and wind response over the Maritime Continent and the Pacific. This procedure has the advantage that overly large IODeast variability in the ocean model is eliminated. Another alternative might be to use a full atmosphere-ocean GCM, but prescribe the SST evolution over the Indian Ocean.

The observations of the Warm Water Volume seem to support the notion that a cool west Indian Ocean induces easterlies over the Pacific. However, it cannot be excluded that the strong negative correlation between IODwest and Warm Water Volume at around months lag is caused by other factors than west Pacific winds, such as variability in the Indonesian Throughflow (Yuan et al., 2011, 2013). Unfortunately, owing to the complex geometry around the Maritime Continent, accurate and long observational records of the Indonesian Throughflow are hard to obtain.

Another aspect which should be investigated further is the discrepancy in the temperature profiles between CESM and the SODA data. The temperature profile in the upper ocean probably depends on vertical mixing, although other factors might play a role, for example horizontal advection. If the processes determining the temperature profile can

be isolated, it might be possible to reduce the model bias, for example by adjusting the parametrisation of the vertical mixing. This might not only apply to CESM, but also to other GCMs. Cai and Cowan (2013) have found an overly strong SST-z20 dependence for many CMIP3 and CMIP5 models, although they do not analyse the temperature profiles in detail.

The results concerning the dependence of the spatial pattern of ENSO on the climatology rely partly on the simplistic T_{sub} parametrisation of the Zebiak-Cane model. It should be tested with more sophisticated models or against observations whether a 'saturation effect' exists, i.e. whether the impact of extreme thermocline anomalies on the overlying SST levels off. Or, more generally, it should be investigated how the relative importance of the Bjerknes feedback terms depend on the background state. In principle, observations might provide some clues here: One could compare ENSO events during the cold and warm phase of the Pacific Decadal Oscillation. However, the observational record is probably too short for this. Alternatively, one could conduct sensitivity experiments with a coupled GCM by adding a constant "external" zonal wind stress over the equatorial Pacific.

Two-way Indo-Pacific coupling might also take place at longer than ENSO time scales. Lee et al. (2015) suggest that the recent strengthening of the easterlies over the equatorial Pacific lead to an enhanced transport of warm water into the Indian Ocean via the Indonesian Throughflow (see also Vranes et al. (2002)). On the other hand, this heat import might lead to surface warming in the Indian Ocean, which in turn induces easterly winds over the Pacific (see section 4.3). Therefore a positive feedback might exist between Pacific easterlies and Indian Ocean SST. It would be interesting to investigate whether a long-term oscillation exists, possibly linked to the Pacific Decadal Oscillation. This might also be relevant in the light of the recent global warming hiatus, as Meehl et al. (2013) and England et al. (2014) argue that enhanced Pacific easterlies will strengthen both the zonal circulation (upwelling of cool water in the cold tongue and subduction of warm water in the west Pacific) and the meridional circulation (upwelling of cold water along the equator and subduction of warm surface water in the subtropics), leading to surface cooling and ocean heat uptake. As mentioned, part of this heat will end up in the Indian Ocean according to Lee et al. (2015).

An aspect of the CESM simulations to which little attention was payed in chapter 6 is the different spectral properties of ENSO between HR and LR. The standard deviation of Nino3.4 in December in LR is too large, while it is too low in HR. The two model versions differ by a factor of two. In addition, the ENSO cycle is more periodic in LR. The latter might seem intuitively plausible: In HR, more small-scale processes are resolved which can act as noise, making ENSO less regular. One such process might be Tropical Instability Waves (TIW), which are thought to warm the cold tongue, in particular during La Niñas, and thus reduce the ENSO amplitude and increase the skewness of ENSO (Graham, 2014). The same study also finds large differences in TIW-induced heat transport between a 1° and a 0.25° resolution model, suggesting that high resolution models are needed to adequately capture the impact of TIWs. While the difference in ENSO amplitudes between HR and LR is in line with the expected influence of TIWs, the difference in skewness is not, as Nino3.4 in LR is more positively skewed than in HR (not shown). Other small-scale processes which are relevant for ENSO and might be represented differently in the two model versions are Westerly Wind Bursts, for example associated with the Madden-Julian-Oscillation. Unfortunately, most of the CESM data is only available as monthly averages, which is too coarse a time resolution to allow an analysis of noise processes, but daily output exists for 10 model years, which might be sufficient to gain

some insights into these processes. On the other hand, it might also be that the difference between the ENSO amplitudes in HR and LR is due to large-scale processes. Therefore it might be fruitful to carry out an analysis similar to the one in section 6.4. The difference in periodicity between HR and LR may also be explained by a difference in ENSO stability: A slightly damped system in which oscillations are excited by noise tends to be less regular than a system with self-sustained oscillations slightly modified by noise.

Daily CESM output could also be used to gain more insight into the possible influence of the (west) Indian Ocean on Pacific wind noise, so as to test the state-dependent noise mechanism of section 2.4.2. In particular, it should be investigated whether the IOD or IODwest indeed influences the Madden-Julian Oscillation (MJO), as suggested by Izumo et al. (2009) and Wilson et al. (2013) and our own findings in section 2.4.2. It might be possible to set up dedicated model experiments to test the mechanisms suggested by Izumo et al. (2009) and Wilson et al. (2013), although it probably will not work to simply prescribe certain SST patterns (e.g. an IOD-like anomaly), as the MJO is a coupled ocean-atmosphere process. To investigate whether enhanced (reduced) moisture convergence over the IODeast during negative IOD years indeed strengthens (weakens) the MJO, one might try enhancing the SST and/or low-level moisture content over the IODeast by a nudging method (i.e. still permitting intraseasonal variability associated with the MJO). To investigate whether enhanced air-sea coupling in the Seychelles Dome region (associated with a shallow thermocline and enhanced upwelling during positive IOD events) strengthen the MJO, one might use a low-pass filter to extract a slowly varying background state (i.e. filtering out intraseasonal signals) of the surface heat and moisture flux in that region from a control simulation and then perform a perturbed simulation where the surface heat and moisture flux in the Seychelles dome region is set to the background state.

It would be foolish to claim that the mighty Pacific dog, El Niño, is actually wagged by its Indian tail. The (west) Indian Ocean does clearly not *dictate* the state of ENSO 1.5 years in advance; a short look at the plain correlations shows this. In the complex interplay between the Indian and Pacific Oceans, the Pacific is the dominant player. Still, the Indian Ocean might feed back on ENSO, and taking into account the internal - ENSO-independent - variability of the Indian Ocean might improve ENSO predictions. If our hypothesis is right - which we may not know until some more decades of data are added to the observational record - ENSO forecasts with empirical models might benefit from including the west Indian Ocean SST, and forecasts with dynamical models might be improved by ensuring that the initial conditions in this region are accurate.

Bibliography

Allen, M. R., and A. W. Robertson, 1996: Distinguishing modulated oscillations from coloured noise in multivariate datasets. Climate Dyn., 12, 775–784.

Allen, M. R. and L. A. Smith, 1996: Monte Carlo SSA: Detecting irregular oscillations in the presence of colored noise. J. Climate, 9, 3373–3404.

Anderson, D.L.T. and J. P. J. McCreary, 1985: On the role of the Indian Ocean in a coupled ocean-atmosphere model of El Niño and the Southern Oscillation. Journal of the Atmospheric Sciences, 44(22), 2439-2442

Annamalai, H., S.-P. Xie, J. P. J. McCreary, and R. Murtugudde, 2005: Impact of Indian Ocean sea surface temperature on developing El Niño. Journal of Climate, 18(2), 302–319

Annamalai, H., S. Kida, and J. Hafner, 2010: Potential Impact of the Indian Ocean-Indonesian Seas on El Niño. Geophysical Research Letters, 40(6), 1200-1205.

Ashok, K., S. K. Behera, S. A. Rao, H. Weng, and T. Yamagata, 2007: El Niño Modoki and its possible teleconnection. J. Geophys. Res., 112, C11007.

Australian Bureau of Meteorology, 2017. The data is provided at their website http://poama.bom.gov.au/ocean_monitoring.shtml and was retrieved in June 2017.

AVISO/SSALTO, 2014: MSLA heights in delayed time. Accessed November 2014. [Available online at http://www. aviso.altimetry.fr/en/data/products/sea-surface-height-products/ global/msla-h.html.]

Barnett, T. P., 1984: Interaction of the monsoon and Pacific trade wind system at interannual time scales. Part III: The tropical band. Mon. Wea. Rev., 112, 2388–2400.

Barnett, T. P., M. Latif, E. Kirk, and E. Roeckner, 1991: On ENSO physics. J. Climate, 4, 487–515

Barnston, A. G., M. K. Tippett, M. L. L'Heureux, S. Li, and D. G. DeWitt, 2012: Skill of real-time seasonal ENSO model predictions during 2002–11: Is our capability increasing? Bull. Amer. Meteor. Soc., 93, 631–651.

Bejarano, L. and F.-F. Jin, 2008: Coexistence of equatorial coupled modes of ENSO. J. Climate, 21, 3051–3067.

Cai, W. and T. Cowan, 2013: Why is the amplitude of the Indian Ocean Dipole overly large in CMIP3 and CMIP5 climate models? Nature, 443(7109), 324-328.

Carton, J. A., and B. S. Giese, 2008: A reanalysis of Ocean climate using simple Ocean data assimilation (SODA), Mon. Weather Rev., 136, 2999–3017.

Cessi, P. and F. Paparella, 2001: Excitation of basin modes by ocean-atmosphere coupling. Geophys. Res. Lett., 28, 2437– 2440.

Chang, P., Y. Fang, R. Saravanan, L. Ji, and H. Seidel, 2006: The cause of the fragile relationship between the Pacific El Niño and the Atlantic Niño. Nature, 443, 324–328.

Chen, D. and M. A. Cane, 2008: El Niño prediction and predictability. J. Comput. Phys., 227, 3625–3640.

Clarke, A. J., 2003: Improving El Niño prediction using a space-time integration of Indo-Pacific winds and equatorial Pacific upper ocean heat content. Geophys. Res. Lett., 30, 1399.

Dayan, H., T. Izumo, J. Vialard, M. Lengaigne, and S. Masson, 2014: Do regions outside the tropical Pacific influence ENSO through atmospheric teleconnections? Climate Dynamics, 1–19.

Deser, C., A. S. Phillips, and M. A. Alexander, 2010: Twentieth century tropical sea surface temperature trends revisited. Geophys. Res. Lett., 37, L10701.

Dijkstra, H. A., and J. D. Neelin, 1995: Ocean–atmosphere interaction and the tropical climatology. Part II: Why the Pacific cold tongue is in the east. J. Climate, 8, 1343–1359.

Dommenget, D., V. Semenov, and M. Latif, 2006: Impacts of the tropical Indian and Atlantic Oceans on ENSO. Geophys. Res. Lett., 33, L11701.

Dommenget D, and Y. Yu, 2016: The seasonally changing cloud feedbacks contribution to the ENSO seasonal phase-locking. ClimDyn 47,3661–3672.

Eisenman, I., L. Yu, and E. Tziperman, 2005: Westerly wind bursts: ENSO's tail rather than the dog? J. Climate, 18, 5224–5238.

England, M.H. and co-authors, 2014: Recent intensification of wind-driven circulation in the Pacific and the ongoing warming hiatus. Nature Climate Change 4, 222–227 (2014)

Fedorov, A. V., and S. G. Philander, 2000: Is El Niño changing? Science, 288, 1997–2002.

Frauen, C., and D. Dommenget, 2012: Influences of the tropical Indian and Atlantic Oceans on the predictability of ENSO. Geophys. Res. Lett., 39, L02706.

Gadgil, S., P. V. Joseph, and N. V. Joshi, 1984: Ocean-atmosphere coupling over monsoon regions. Nature, 312(5), 141-143.

Gill, A. E., 1980: Some simple solutions for heat-induced tropical circulation. Quarterly Journal of the Royal Meteorological Society, 106(449), 447–462.

Gill, A.E., 1983: The 1982–83 climate anomaly in the equatorial Pacific. Nature, 306, 229–234

Graham, T., 2014: The importance of eddy permitting model resolution for simulation of the heat budget of tropical instability waves. Ocean Modelling 79 (2014) 21–32

Guilyardi, E., 2006: El Niño – mean state – seasonal cycle interactions in a multi-model ensemble. Climate Dyn., 26, 329– 348.

Ham, Y. G., J. S. Kug, and J. Y. Park, 2013: Two distinct roles of Atlantic SSTs in ENSO variability: North tropical Atlantic SST and Atlantic Niño. Geophys. Res. Lett., 40, 4012–4017.

Harrison, D. E., and P. S. Schopf, 1984: Kelvin-wave-induced anomalous advection and the onset of surface warming in El Niño events. Mon. Wea. Rev., 112, 923–933.

Hurrell, J. W. and co-authors, 2013: The community earth system model: a framework for collaborative research, Bulletin of the American Meteorological Society, 94(9), 1339–1360.

Izumo, T., S. Masson, J. Vialard, C. de Boyer Montégut, S. K. Behera, G. Madec, K. Takahashi, and T. Yamagata, 2009: Low and high frequency Madden–Julian oscillations in austral summer: Interannual variations. Climate Dyn., 35, 669–683.

Izumo, T., J. Vialard, M. Lengaigne, C. de Boyer Montégut, S. K. Behera, J.-J. Luo, et al., 2010: Influence of the state of the Indian Ocean Dipole on the following year's El Niño. Nature Publishing Group, 3(3), 168–172.

Izumo, T., M. Lengaigne, J. Vialard, J.-J. Luo, T. Yamagata, and Madec, G., 2013: Influence of Indian Ocean Dipole and Pacific recharge on following year's El Niño: interdecadal robustness. Climate Dynamics, 42(1-2), 291–310.

Izumo, T., J. Vialard, H. Dayan, M. Lengaigne, and I. Suresh, 2015: A simple estimation of equatorial Pacific response from windstress to untangle Indian Ocean Dipole and Basin influences on El Niño. Climate Dynamics, 46(7), 2247–2268.

Jansen, M. F., D. Dommenget, and N. S. Keenlyside, 2009: Tropical atmosphere–ocean interactions in a conceptual framework. J. Climate, 22, 550–567.

Jin, F. F., 1997a: An equatorial ocean recharge paradigm for ENSO. Part I: Conceptual model. J. Atmos. Sci., 54, 811–829.

Jin, F. F., 1997b: An equatorial ocean recharge paradigm for ENSO. Part II: A stripped-down coupled model. J. Atmos. Sci., 54, 830–847.

Kajtar J. B., A. Santoso, M.H. England, and W. Cai, 2015: Indo-Pacific climate interactions in the absence of an Indonesian Throughflow. J Clim 28:5017–5029

Kajtar, J. B., A. Santoso, M.H. England, and W. Cai, 2016: Tropical climate variability: interactions across the Pacific, Indian, and Atlantic Oceans. Climate Dynamics, 1–18.

Kalnay, E., and Co-authors, 1996: The NCEP/NCAR 40-Year Reanalysis Project. Bull. Amer. Meteor. Soc., 77, 437–471.

Kao, H.-Y., and J.-Y. Yu, 2009: Contrasting Eastern-Pacific and Central-Pacific types of ENSO. J. Climate, 22, 615–632.

Keen, R. A., 1982: The role of cross-equatorial tropical cyclone pairs in the Southern Oscillation. Mon. Wea. Rev., 110, 1405–1416.

Keller, H. B. (1977). Numerical solution of bifurcation and nonlinear eigenvalue problems. Applications of bifurcation theory.

Kessler, W. S., M. J. McPhaden, and K. M. Weickmann, 1995: Forcing of intraseasonal Kelvin waves in the equatorial Pacific. J. Geophys. Res., 100, 10613–10632.

Kessler, W. S., and R. Kleeman, 2000: Rectification of the Madden–Julian oscillation into the ENSO cycle. J. Climate, 13, 3560–3575.

Kirtman, B. P., 1997: Oceanic Rossby wave dynamics and the ENSO period in a coupled model. J. Climate, 10, 1690–1704.

Kleeman, R., 2008: Stochastic theories for the irregularity of ENSO. Philos. Trans. Roy. Soc. London, 366A, 2509–2524.

Klein, S. A., B. J. Soden, and N. C. Lau, 1999: Remote sea surface temperature variations during ENSO: Evidence for a tropical atmospheric bridge. J. Climate, 12, 917–932.

Kug, J. S., and I.-S. Kang, 2006: Interactive feedback between ENSO and the Indian Ocean. Journal of Climate, 19(9), 1784–1801.

Kug, J. S., T. Li, S.-I. An, I.-S. Kang, J.-J. Luo, S. Masson, and T. Yamagata, 2006: Role of the ENSO–Indian Ocean coupling on ENSO variability in a coupled GCM. Geophysical Research Letters, 33(9), L09710–4.

Kug, J. S., F.-F. Jin, and S.-I. An, 2009: Two types of El Niño events: Cold tongue El Niño and warm pool El Niño. J. Climate, 22, 1499–1515.

Kug, J. S., K. P. Sooraj, T. Li, and F. F. Jin, 2010: Precursors of the El Niño/La Niña onset and their interrelationship. J. Geophys. Res., 115, D05106.

Kug, J. S., and Y. G. Ham, 2011: Are there two types of La Nina? Geophys. Res. Lett., 38, L16704.

Larkin, N. K., and D. E. Harrison, 2005: On the definition of El Niño and associated seasonal average U.S. weather anomalies. Geophys. Res. Lett., 32, L13705.

Latif, M., and T. P. Barnett, 1995: Interactions of the tropical oceans. J. Climate, 8, 952–964.

Lee, S.-K., W. Park, M. O. Baringer, A. L. Gordon, B. Huber, and Y. Liu, 2015: Pacific origin of the abrupt increase in Indian Ocean heat content during the warming hiatus. Nat. Geosci., 8, 445–449.

Lübbecke, J. F., and M. J. McPhaden, 2014: Assessing the Twenty-First-Century Shift in ENSO variability in terms of the Bjerknes stability index. J. Climate, 27, 2577–2587.

Luo, J.-J., R. Zhang, S.K. Behera, Y. Masumoto, F.-F. Jin, R. Lukas, and T. Yamagata, 2010: Interaction between El Niño and Extreme Indian Ocean Dipole. Journal of Climate, 23(3), 726-742.

Luo, J. J., W. Sasaki, and Y. Masumoto, 2012: Indian Ocean warming modulates Pacific climate change. Proc. Natl. Acad. Sci. USA, 109, 18 701–18 706.

Madden, R. A., and P. R. Julian, 1971: Detection of a 40–50 day oscillation in the zonal wind in the tropical Pacific. J. Atmos. Sci., 28, 702–708.

McPhaden, M. J., X. Zhang, H. H. Hendon, and M. C. Wheeler, 2006: Large scale dynamics and MJO forcing of ENSO variability. Geophys. Res. Lett., 33, L16702.

McPhaden, M. J., T. Lee, and D. McClurg, 2011: El Niño and its relationship to changing background conditions in the tropical Pacific Ocean. Geophys. Res. Lett., 38.

Meehl, G.A., A. Hu, J.M. Arblaster, J. Fasullo, and K.E. Trenberth, 2013: Externally Forced and Internally Generated Decadal Climate Variability Associated with the Interdecadal Pacific Oscillation, Journal of Climate, 26, 7298–7310

Meijer, H. G. E., F. Dercole, and B. Oldeman, 2009: Numerical Bifurcation Analysis. In R. A. Myers (Ed.), Encyclopedia of Complexity and Systems Science (pp. 6329-6352). [10.1007/978-0-387-30440-3_373] New York: Springer Verlag.

Meinen, C. S., and M. J. McPhaden, 2000: Observations of warm water volume changes in the equatorial Pacific and their re- lationship to El Niño and La Niña. J. Climate, 13, 3551–3559.

Met Office Hadley Centre, 2012: Hadley Centre Sea Ice and Sea Surface Temperature data set (HadISST). Met Office Hadley Centre. [Available online at http://www.metoffice.gov.uk/ hadobs/hadisst/.] Data retrieved in 2012.

Met Office Hadley Centre, 2017: Hadley Centre Sea Ice and Sea Surface Temperature data set (HadISST). Met Office Hadley Centre. [Available online at http://www.metoffice.gov.uk/ hadobs/hadisst/.] Data retrieved in February 2017.

Mitchell, J. M., B. Dzeerdzeevskii, H. Flohn, W. L. Hofmeier, H. H. Lamb, K. N. Rao, and C. C. Wallen, 1966: Climatic change. WMO Tech. Note 79, 79 pp.

Neale, R. B., and Coauthors, 2012: Description of the NCAR Community Atmosphere Model (CAM 5.0). NCAR Tech. Note TN-486, 274 pp

NOAA/OAR/ESRL PSD, 2014: NCEP/NCAR Reanalysis 1: Summary. Accessed February 2014. [Available online at http://www.esrl.noaa.gov/psd/data/gridded/data.ncep.reanalysis. html.]

NOAA/OAR/ESRL PSD, 2017: NCEP/NCAR Reanalysis 1: Summary. Accessed February and September 2017. [Available online at http://www.esrl.noaa.gov/psd/data/gridded/data.ncep.reanalysis. html.]

NOAA/PMEL Tropical Atmosphere Ocean Project, 2014: Upper ocean heat content and ENSO. Accessed November 2014.[Available online at http://www.pmel.noaa.gov/tao/elnino/ wwv/.]

Neelin, J. D., D. S. Battisti, A. C. Hirst, F. F. Jin, Y. Wakata, T. Yamagata, and S. E. Zebiak, 1998: ENSO theory. J. Geophys. Res., 103, 14 261–14 290.

Philander, S. G., 1990: El Niño, La Niña, and the Southern Oscillation. Academic Press, 289 pp.

Philip, S., and G. J. van Oldenborgh, 2006: Shifts in ENSO coupling processes under global warming. Geophys. Res. Lett., 33, L11704.

Plaut, G., and R. Vautard, 1994: Spells of low-frequency oscillations and weather regimes in the Northern Hemisphere. J. Atmos. Sci., 51, 210–236.

Rayner, N. A., and Coauthors, 2003: Global analyses of sea surface temperature, sea ice, and night marine air temperature since the late nineteenth century. J. Geophys. Res., 108, 4407.

Roxy, M. (2013). Sensitivity of precipitation to sea surface temperature over the tropical summer monsoon region|and its quantification. Climate Dynamics, 4(5-6), 1159-1169.

Saji, H. N., B. N. Goswami, P. N. Vinayachandran, and T. Yamagata, 1999: A dipole mode in the tropical Indian Ocean. Nature, 401(6), 360–363.

Saji, H. N., S.-P. Xie, and T. Yamagata, 2006: Tropical Indian Ocean variability in the IPCC twentieth-century climate. Journal of Climate, 29(11), 4397-4417.

Santoso, A., M.H. England, M. H., and W. Cai, 2012: Impact of Indo-Pacific Feedback Interactions on ENSO Dynamics Diagnosed Using Ensemble Climate Simulations. Journal of Climate, 25(21), 7743-7763.

Santoso, A., S. McGregor, F. F. Jin, W. Cai, H. M. England, S. I. An, M. J. McPhaden, and E. Guilyardi, 2013: Late-twentieth-century emergence of the El Niño propagation asymmetry and future projections. Nature, 504, 126–130.

Schott, F. A., S. P. Xie, and J. P. J. McCreary, 2009: Indian Ocean circulation and climate variability. Rev. Geophys., 47, RG1002.

Shinoda, T. , H. H. Hendon, and M. A. Alexander, 2004: Surface and subsurface dipole variability in the Indian Ocean and its relation with ENSO. Deep Sea Research Part I: Oceanographic Research Papers, 51(5), 619–635

Smith, R. D., and Coauthors, 2010: The Parallel Ocean Program (POP) reference manual: Ocean component of the Community Climate System Model (CCSM) and Community Earth System Model (CESM). Los Alamos National Laboratory Tech. Rep. LAUR-10-01853, 141 pp. [Available online at www.cesm.ucar.edu/models /cesm1.0/pop2/doc/sci/POPRefManual.pdf.]

SODA data, 2017: the data is provided at http://dsrs.atmos.umd.edu/DATA/soda_2.2.4/?C=D;O=A; accessed on 18th of September 2017.

Tozuka, T., T. Yokoi, and T. Yamagata, 2010: A modeling study of interannual variations of the Seychelles Dome. J. Geophys. Res., 115, C04005.

Tziperman, E., S. E. Zebiak, and M. A. Cane, 1997: Mechanisms of seasonal–ENSO interaction. J. Atmos. Sci., 54, 61–71.

Van der Vaart, P. C. F., H. A. Dijkstra, and F.-F. Jin, 2000: The Pacific cold tongue and the ENSO mode: A unified theory within the Zebiak–Cane model. J. Atmos. Sci., 57, 967–988

Van der Vaart, P. C. F., 1998: Nonlinear tropical climate dynamics (PhD thesis)

Vialard, J., C. Menkes, J. P. Boulanger, P. Delecluse, E. Guilyardi, M. J. McPhaden, and G. Madec, 2001: A model study of oceanic mechanisms affecting equatorial Pacific sea surface temperature during the 1997–98 El Niño. J. Phys. Oceanogr., 31, 1649–1675.

Vranes, K., A. L. Gordon, and A. Ffield, 2002: The heat transport of the Indonesian Throughflow and implications for the Indian Ocean heat budget. Deep-Sea Research II 49 (2002) 1391–1410.

Wang, C., R. H. Weisberg, and J. I. Virmani, 1999: Western Pacific interannual variability associated with the El Niño-Southern Oscillation. J. Geophys. Res., 104, 5131–5149.

Watanabe, M., and Jin, F.-F. (2002). Role of Indian Ocean warming in the development of Philippine Sea anticyclone during ENSO. Geophysical Research Letters, 29(10), 116-1 - 116-4.

Watanabe, M., 2008: Two regimes of the equatorial warm pool. Part I: A simple tropical climate model. J. Climate, 21, 3533– 3544.

Weller, E., S. K. Min, W. Cai, F. W. Zwiers, Y. H. Kim, and D. Lee, 2016: Human-caused Indo-Pacific warm pool expansion. Sci. Adv., 2, e1501719.

van Westen, R.M. and H.A. Dijkstra, 2017: Southern Ocean Origin of Multidecadal Variability in the North Brazil Current. Geophys. Res. Letters, accepted

White, W. B., and D. R. Cayan, 2000: A global El Niño-Southern Oscillation wave in surface temperature and pressure and its interdecadal modulation from 1900 to 1997. J. Geophys. Res., 105, 11223–11242

Wiedermann, M., A. Radebach, J. F. Donges, J. Kurths, and R. V. Donner (2016), A climate network-based index to discriminate different types of El Niño and La Niña, Geophys. Res. Lett., 43, 7176–7185

Wilson, E. A., A. L. Gordon, and D. Kim, 2013: Observations of the Madden Julian oscillation during Indian Ocean dipole events. J. Geophys. Res. Atmos., 118, 2588–2599.

Wright, P. B., 1986: Precursors of the Southern Oscillation. Int. J. Climatol., 6, 17–30.

Wyrtki, K. (1975). El Niño—The Dynamic Response of the Equatorial Pacific Ocean to Atmospheric Forcing. Journal of Physical Oceanography, 5(4), 572–584.

Wyrtki, K., 1985: Water displacements in the Pacific and the genesis of El Nino cycles. J. Geophys. Res., 90, 7129–7132.

Xie, S. P., H. Annamalai, F. A. Schott, and J. P. J. McCreary, 2002: Structure and mechanisms of south Indian Ocean climate variability. J. Climate, 15, 864–878.

Xie, S.-P., K. Hu, J. Hafner, H. Tokinaga, Y. Du, G. Huang, G., and T. Sampe, 2009: Indian Ocean Capacitor Effect on Indo-Western Pacific Climate during the Summer following El Niño. Journal of Climate, 22(3), 730–747.

Yao, Z., Y. Tang, D. Chen, L. Zhou, X. Li, T. Lian, and S. U. l. Islam 2016: Assessment of the simulation of Indian Ocean Dipole in the CESM—Impacts of atmospheric physics and model resolution, J. Adv. Model. Earth Syst., 8, 1932–1952.

Yeh, S.-W., J.-S. Kug, B. Dewitte, M.-H. Kwon, B. P. Kirtman, and F.-F. Jin, 2009: El Niño in a changing climate. Nature, 461, 511–514.

Yokoi, T., T. Tozuka, and T. Yamagata, 2008: Seasonal variation of the Seychelles Dome. J. Climate, 21, 3740–3754.

Yu, J. Y., and S. T. Kim, 2010: Three evolution patterns of central-Pacific El Niño. Geophys. Res. Lett., 37, L08706.

Yuan, D., J. Wang, T. Xu, P. Xu, Z. Hui, X. Zhao, Y. Luan, W. Zheng, and Y. Yu, 2011: Forcing of the Indian Ocean dipole on the interannual variations of the tropical Pacific Ocean: Roles of the Indonesian Throughflow. J. Climate, 24, 3593–3608.

Yuan D, H. Zhou, and X. Zhao, 2013: Interannual climate variability over the tropical Pacific Ocean induced by the Indian Ocean dipole through the Indonesian Throughflow. J Clim 26:2845–2861

Zebiak, S. E. (1986). Atmospheric Convergence Feedback in a Simple Model for El Niño. Monthly Weather Review, 114(7), 1263-1271.

Zebiak, S. E., and M. A. Cane, 1987: A model El Niño–Southern Oscillation. Mon. Wea. Rev., 115, 2262–2278.

Zebiak, S. E., and Co-authors, 2015: Investigating El Niño-Southern Oscillation and society relationships. Wiley Interdiscip. Rev.: Climate Change, 6, 17–34.

Zhang, C., 2005: Madden-Julian oscillation. Rev. Geophys., 43, RG2003.

List of publications

Chapter 2 is based on the article

Wieners, C.E., W.P.M de Ruijter, W. Ridderinkhof, A. von der Heydt, and H.A. Dijkstra, 2016: Coherent tropical Indo-Pacific interannual climate variability. J. Climate, 29, 4269-4291

Chapter 4 is based on the article

Wieners, C.E., W.P.M de Ruijter, and H.A. Dijkstra, 2017: The influence of the Indian Ocean on ENSO stability and flavour. J. Climate, 30, 2601– 2620

Chapter 5 is based on the article

Wieners, C.E., H.A. Dijkstra, and W.P.M de Ruijter, 2017: The Influence of Atmospheric Convection on the Interaction between the Indian Ocean and ENSO. J. Climate

Chapter 6 is based on the article

Wieners, C.E., W.P.M de Ruijter, and H.A. Dijkstra: The interaction between the Indian Ocean and ENSO in CESM. Submitted to Climate Dynamics

Acknowledgements

In many respects, a PhD project resembles ENSO. The period is similar, and one is bound to run into some predictability barriers and other nasty and delightful surprises. More importantly, it requires both noise and deterministic terms to keep it going.

Will de Ruijter provided the noise term: a stream of fascinating ideas, speculations, and inspiring suggestions - enough to fill at least two more PhD projects. Will, it was always enlightening, and great fun, to brainstorm with you about El Niño and the Seychelles Dome, but also about all other regions in the seven seas, and about how science works. While I occasionally got mildly obsessed with significance-testing, you taught me that sometimes one may follow one's intuition and even make some wild speculations, and told me: 'The sea - for me, there is some romance to it!' Romanticism aside, you have also given me a lot of useful, instructive feedback and suggestions about designing model experiments, transforming results into papers, and a lot more. Thank you also for your many efforts towards making IMAU a place where it is a pleasure to work, for your hospitality during the ocean group canoeing barbecues, and for taking me under your wing on the sunlit conference venue in Goa during my first-ever stay outside Europe! And thank you, Els de Ruijter, for an unforgettable afternoon exploring Panaji.

Henk Dijkstra provided the deterministic part: deep physical insight combined with a great knowledge about and delight in the technical aspects of the work - from MSSA to flux-corrections in the Zebiak-Cane model - as well as keeping a clear overview when I threatened to loose my way in the 30-dimensional ZC parameter space ('Claudia, you are a bit chaotic. Try one thing at a time!'). Thank you, Henk, for your honest and always constructive criticism, and the enthusiasm with which you shared your insights. Sometimes you emitted such a torrential current of facts and ideas that only your good sense of humour saved me from information overflow - the moment you had to laugh gave me a brief respite to reset my overwhelmed brain. It was always a great pleasure to work with you. And thank you for rescuing me from tremendous trouble during the Valsavarenche summer school, when I had to pay my hotel room but could neither remember the code of my brand-new credit card, nor get any money from that ramshackle cash dispenser down in the village, nor communicate with the Italian hotel owner...

Both of you were always prepared to help me and answer my questions, but also let me try out things myself - or, as Will put it: 'If ideas bubble up in your head, you should pursue them - and I trust that there is sufficient bubbling!'

I would like to thank Frank Selten for his thorough introduction to the ECearth model. Even though our experiments do not appear in this thesis, I have learned a lot about the complex and capricious nature of GCMs. Thank you, Anna von der Heydt, for introducing me to the Zebiak-Cane model when I tried to use the absence of my promotors to take a break from data analysis. Anna's competent guidance and Inge van Tongeren's great enthusiasm made it a pleasure to play with the state-dependent noise in the ZC-model. Michael Kliphuis, thank you for providing all sorts of CESM data, and your kind help with nagging NAG library issues and those other IT troubles which occasionally harassed me - although many of them probably qualify as PICNIC (Problem In Chair, Not In Computer). I would also like to thank Huib de Swart for getting me into IMAU. Without your great course on ocean waves in spring 2012, I might still be languishing somewhere, trying to solve dry quantum theory problems - your lectures made me take the plunge into the deep wet ocean!

I would like to thank my room mates at BBL 664 (The Jungle Room) for your tolerance with my odd habits of crunchingly consuming up to 5 apples a day and muttering to my computer. Thanks, Erik Ensing, for your artistic drawings of 'puzzled penguins' (we still

didn't dare to wipe the whiteboard), and Bing Yuan, for your gentle humour and your introductions to Chinese culture. André Jüling, thank you for bringing so much lively chlorophyll into our room, and for confidently taming those creatures over which I have lamentably little authority: two nasty beamers, Henk's monster screens, and a group of summer school students whom I nearly lost during an excursion to Zeeland.

Dear oceanographers - Sandra Brunnabend, Jan Viebahn, Dewi Le Bars, Qingyi Feng, Alexis Tantet, Lisa Hahn-Woernle, Inti Pelupessy, Michiel Baatsen, Erik Mulders, Fiona van der Burgt, René van Westen, Daniele Castellana, André Jüling, Mark Dekker, Peter Nooteboom, Erik van Sebille, David Wichmann, and Philippe Delandmeter - on many Thursdays we had a kleine werkbespreking in BBL 661... thank you very much for giving me feedback on my research, and in turn sharing your work! I have learnt a lot from you.

Sandra, I really enjoyed our travels from the civilised Utrecht via the crowded Naschmarkt in Vienna and the forests of Bonn to our lonely campsite in the foggy Fire Fissure (Eldgjá), surrounded by shy sheep and lava. Michiel, thank you for many, many weather predictions (if I got wet on my bike trips, it was my own fault) and thorough and humorous discussions on channel rats, whales' mouths and punhole eyes (pin not intended...). René, thank you for some fruitful exchange about MSSA and CESM - and for providing me the experience that tandem bikes are not as frighteningly erratic and unstable as I always thought. Qingyi, thank you for your kind help with the difficult step from the safe job of teasing El Niño to the complex maze of coordinating a master course. Thank you, Daniele, for sharing your insights on how to cook pasta properly (though I'll never achieve your standard) and how to measure diffusion with Swedish fermented herring. And thank you, Getachew, for your contagious good humour, Femke, for your introductions to the political aspects of climate science, and Lisa, for your PhD anniversary dinners. Maarten, Narcissa, Rianne, Anna, Frans and Daniele, thanks for joining the tea and coffee choir - it was a pleasure to rehearse and perform with you.

Felix Beckebanze, Anna Kruseman, Roeland van der Vijsel, and André, I will never forget our hilarious evenings with Käsespätzle, Glühbirnen - stoofperen, I mean - and obligatory linguistic confusion.

Outside IMAU, I would like to thank my father for his interest and keen questions about my project (although they typically started with 'Of course, I am just a layman', you would surely have given me a hard time if you were my opponent during my PhD defence...), my mother for poetic discourses in times of computational hardships, my sister Marianne for her unfailing willingness to keep 'aloof theoreticians' down to earth - and smiling - by means of gentle teasing, and my boyfriend Lars for eagerly listening to my daily Zebiak-Cane stories in every gradation from euphoria to despair, and for being a faithful beacon in all sorts of haze.

It is thanks to all of you that - unlike El Niño, who will probably forever remain a nasty, tantrum-driven little boy - this thesis gained some degree of maturity!

Curriculum Vitae

Claudia Elisabeth Wieners was born on April 26th 1989 in Frankfurt am Main, where she also went to school and passed the final exam in June 2008. Wishing to know which fundamental forces hold the world together, she did a Bachelor's degree in Physics (October 2008-August 2011), still in Frankfurt. But as she had been fascinated by the Netherlands - a country held dry by dikes! - for years, she moved to Utrecht (still 2m above mean sea level...) to do a Master's degree in Theoretical Physics. However, after a year she found Theoretical Physics a bit too dry and switched to oceanography (which is not dry by definition), by also following the Meteorology, Physical Oceanography and Climate programme. In October 2013 she completed both master programmes by writing a thesis on the stochastic aspects of El Niño, under the supervision of Henk Dijkstra and Deb Panja. Feeling that she was not yet done with the Noisy Christ-child El Niño, she gladly accepted a PhD position on the interaction between the Indian Ocean and ENSO, supervised by Will de Ruijter and Henk Dijkstra.

In November 2017 she started a postdoc on complex systems with Henk Dijkstra. Back to the theoretical physics roots?